UNIVERSITY OF Southampton

Microstructure and properties of low-carbon steels processed by high pressure torsion

by

KHALED S. HUSAIN

Engineering Materials Group

Engineering and the Environment

University of Southampton

Thesis for the Degree of Doctor of Philosophy

August 2015

Supervisors:

Prof. Marco J. Starink

Dr. Nong Gao

Abstract

In this study, low-carbon steel (0.1 wt.% C) in ferritic-pearlitic (FP) and ferritic-martensitic (FM) initial states were processed by high pressure torsion (HPT) up to 10 turns under a pressure of 6 GPa at room temperature (RT). The HPT-processed FM samples were tempered at 150^{o}C to 550^{o}C. The microhardness monotonically increased with the number of turns up to 10 turns. After 10 turns, the microhardness had increased to 3 times that of the initial state for both the FP and FM samples. The microhardness of the individual phases, ferrite and martensite, in the FM processed samples increased with strain. The nanoindentation measurement of the ferrite in the FP processed samples revealed that the ferrite nanohardness increased with the number of turns up to 10 turns. The microhardness was maintained when the FM sample processed up to 4 turns and tempered at 450^{o}C while the microhardness slightly increased when tempering at 350^{o}C. Similarly, the ferrite in the FM sample processed up to 4 turns and tempered at 350^{o}C had a nanohardness value higher than that of the sample tempered at 250^{o}C: this can be attributed to the limited formation of cementite particles in the ferrite matrix.

Optical and scanning electron microscopy (SEM) revealed that cementite fragmentation in the FP samples started after 4 turns of HPT processing and increased with the number of turns, or strain. SEM investigation revealed the formation of cementite particles when the FM sample processed up to 4 turns and tempered at 450^{o}C: these cementite particles coarsened when tempering at 550^{o}C. The transmission electron microscopy (TEM) investigation of the microstructure in the FM processed samples revealed that the microstructure was characterised by high internal stresses and dislocation density. The dislocation cells evolved during the HPT processing up to 10 turns and the fraction of high angle grain boundaries increased with the number of turns. X-ray diffraction (XRD) analysis revealed that no appreciable lattice parameter (a) expansion occurs during the HPT processing of the ferrite of the FP samples. The lattice parameter of the ferrite of the FM processed samples increased with the number of turns, or strain. The lattice parameter of the ferrite of the FM sample processed up to 4 turns and tempered at 450^{o}C was equal to that of pure α-iron which suggests that the cementite particles formed at the expense of the decomposition of the supersaturated Fe-C solid solution in ferrite.

It is well documented in the literature that the strength or hardness significantly increases with the number of turns during HPT processing. However, so far no attempt has been made to predict the strength of low-carbon steels after HPT processing. In this

study, the X-ray line profile analysis (XLPA) using the multiple whole profile fit (MWP-fit) was used, as an alternative tool to TEM, to determine the dislocation density in the HPT-processed samples. A model that incorporates both the dislocation and grain boundary strengthening was proposed to predict the strength of the HPT-processed samples. In this model, other strengthening contributions such as solid solution and Orowan strengthening due to different structures such as pearlite, martensite, and carbide particles in the ferrite matrix were taken into account. The strength/hardness model proposed in this study was applied to predict the strength/hardness of six low-carbon steel (0.1 wt.% C) samples in the ferritic-pearlitic or ferritic-martensitic initial states processed by HPT up to 1, 4, and 10 turns. Furthermore, the strength/hardness model was also applied to predict the strength of FM samples processed by HPT and tempered at different temperatures. The strength/hardness model proposed in the current study can be used to predict the strength of all the investigated samples to a good accuracy with an average error of ±8%.

Academic Thesis: Declaration of Authorship

I, Khaled S. A. Husain

declare that this thesis and the work presented in it are my own and has been generated by me as the result of my own original research.

Microstructure and properties of low-carbon steels processed by high pressure torsion

I confirm that:

1. This work was done wholly or mainly while in candidature for a research degree at this University;

2. Where any part of this thesis has previously been submitted for a degree or any other qualification at this University or any other institution, this has been clearly stated;

3. Where I have consulted the published work of others, this is always clearly attributed;

4. Where I have quoted from the work of others, the source is always given. With the exception of such quotations, this thesis is entirely my own work;

5. I have acknowledged all main sources of help;

6. Where the thesis is based on work done by myself jointly with others, I have made clear exactly what was done by others and what I have contributed myself;

7. Either none of this work has been published before submission, or parts of this work have been published as: [please list references below]:

Signed:

Date: 18/01/2016

1. K.S. Husain, N. Gao, and M.J. Starink, Hardening of low-carbon steel by high pressure torsion, (in progress).

Acknowledgements

I would like to express sincere gratitude to my supervisors, Prof. Marco J. Starink and Dr. Nong Gao for their continuous guidance and encouragement throughout my course of work.

I would like to thank Bahrain Defence Force for their financial support and the University of Southampton for partial funding during my course of work.

I wold like to express the deepest sense of gratitude to Prof. Jeno Gubicza for his online support and Dr. Richard Cook for his great help in the nanoindentation experiment.

I would also like to take this opportunity to thank both Dr. David Walker (University of Warwick) and Dr. Mark Light (University of Southampton) for their help in the X-ray diffraction test. I would like to express my sincere appreciation to the all technicians and staff that helped in this work.

Finally, I would like to acknowledge the support of my family members and especially my mother. Special thanks go to my wife for being patient during my course of work.

Table of Contents

List of Tables

List of Figures

Acronyms and Symbols

List of Acronyms

ARB	Accumulative roll bonding
ASTM	American Society for Testing and Materials
ATP	Atom Probe Tomography
BCC	Body-centred cubic structure
BCT	Body-centred tetragonal structure
CEC	Cyclic extrusion and compression
CHPT	Continuous high pressure torsion
CMWP	Convolutional Multiple Whole Profile
CS	Carbon steel
CSV	Carbon steel contain vanadium
DP	Dual-phase steel
DSA	Dynamic strain ageing
EBSD	Electron back scatter diffraction
ECAP	Equal-channel angular pressing
EDS	Energy dispersive spectroscopy
FEM	Finite element method
FG	Fine grain material
FM	Ferritic-martensitic
FP	Ferritic-pearlitic steel
FWHM	Full width at half maximum
GND	Geometrically necessary dislocation
HAB	High-angle grain boundaries
HPT	High pressure torsion
HREM	High resolution electron microscopy
HSLA	High-strength low alloy steel
IF	Interstitial free steel
ISE	Indentation size-effect
LAB	Low-angle grain boundaries
MDF	Multi-directional forging
MWP-fit	Multiple Whole Profile-fit program
NS	Nanostructure materials
NS+P	Nanostructure material contain precipitates
SAD	Selected area diffraction

SEI	Secondary Electron Imaging
SEM	Scanning electron microscopy
SPD	Severe plastic deformation
SSD	Statistically stored dislocation
TE	Twist extrusion
TEM	Transmission electron microscopy
UFG	Ultra-fine grain
UTS	Ultimate tensile strength
WEL	White etching layer
XLPA	X-ray line profile analysis
XRD	X-ray diffraction
YS	Yield strength

List of Symbols

a	Lattice parameter of the investigated sample or steel
a_{ind}	Radius of the contact area at the peak load
a_o	The lattice parameter of pure alpha-iron
A	Constant depends on the arrangement and density of dislocation
A_B	Area fraction of the soft bulk material
A_{c}	Contact area at peak load
A_{GB}	Area fraction of the hardened layer of the grain boundaries
A_{r}	Residual projected area
$A1$	The lower critical temperature on the iron-iron carbide phase diagram
$A3$	The upper critical temperature on the iron-iron carbide phase diagram
b	Burgers vector
C_{T}	Factor relates the yield strength to the microhardness in Tabor relation
c/a	The ratio of the two axes having different length in the martensite BCT structure
CL	Confidence limit
C	Average contrast factor of dislocations
$\overline{C}_{h00}$	Average dislocation contrast factor for the *h00* reflection
d	Mean grain size
d_{part}	Average particle diameter
D	Interparticles spacing
D_{HAB}	Average size of grain boundaries with high misorientation
e	maximum strain
f	Volume fraction of cementite particles

f_{an}	Fraction of annihilated dislocations
f_P	Volume fraction of pearlite
f_{part}	Volume fraction of second phase particles
G	Shear modulus
h	Indentation depth
h_{max}	Maximum depth of indentation
H_{i}	Initial thickness of HPT disk
H_{HPT}	Thickness of HPT disk
H_{f}	Final thickness of HPT disk
H^N	Hardness obtained by nanoindentation
Hv	Vickers microhardness
k	Hall-Petch constant
$k(\varepsilon)$	Hall-Petch constant at certain strain
K_{C}	Proportionality constant of carbon
Kα1	X-ray characteristic emission resulted from electron transition from the second orbit of the L shell to K shell
Kα2	X-ray characteristic emission resulted from electron transition from the third orbit of the L shell to K shell
L	Fourier variable (frequency)
L_{gen}	Generated dislocation linelength
L_{gb}	Dislocation linelength at grain boundary
L_{ig}	Dislocation linelength in grain
m	The median
M	Taylor factor
M_{Dis}	Dislocation arrangement parameter
N	Number of HPT turns
N_{cycles}	Number of accumulative roll bonding cycles
N_{Dis}	Number of dislocation in a pile-up at the grain boundary
N_{f}	Number of fields
N_{L}	Number of particles intercepted per unit length of test line
N_{passes}	Number of passes during equal-channel angular pressing process
O	Stands for higher order terms in K^2C in Equation 2.37
P	Compressive applied pressure during HPT processing
P_{max}	Maximum load
P_{o}	The number of grid points
P_{p}	Number of points in the second phase (pearlite)
P_{T}	Total number of grid points
q	Constant depends on the type of dislocation which exists in the

	investigated sample (edge or screw)
r	Distance from the centre in HPT disk
r_{part}	Average particle radius
R^2	Correlation coefficient of fitted datum points
R_{e}	Outer cut-off radius of a dislocation
s	Space between two adjacent dislocation loops
sd	Standard deviation
S	Elastic unload stiffness
S_{v}	The area of boundaries per unit volume
$\langle t \rangle_{\mathrm{vol}}$	Volume-weighted mean column-length
V_{m}	Volume fraction of martensite
V_{p}	Volume fraction of pearlite
X_{C}	Carbon content in ferrite [wt. %]
X_{i}	Number of point in the second phase per number of grid points
$\overline{X}$	Mean volume fraction of the second phase
$\langle X \rangle_{\mathrm{area}}$	Area weighted mean crystallite size
$\Delta\sigma_{\mathrm{ppt}}$	The increment in strength due to precipitates
β^{D}	Breadth due to strain
β^{S}	Breadth due to size
γ	Austenite
γ_{PR}	Poisson's ratio of the matrix
γ_{ss}	Shear strain
θ	Bragg-angle of reflection *hkl*
θ_{ind}	The angle between the surface of the conical indenter and the plane of the surface
ρ	Dislocation density
ρ_{GND}	The density of the geometrically necessary dislocations
ρ_{cells}	Dislocation density in cells
ρ_{SSD}	The density of the statistically stored dislocations
σ	Flow stress of a material
σ_{B}	Flow stress of the bulk material
σ_{c}	The flow stress of a composite material consists of a hardened layer of grain boundaries and soft bulk material
σ_{D}	Stress due to dislocation strengthening
σ_{SS}	Stress due to solid solution
σ_{FP}	Flow stress of ferritic-pearlitic steel
σ_{GB}	Flow stress of the hardened layer of the grain boundaries
$\sigma_{\mathrm{GB+D}}$	Stress due to grain boundary and dislocation strengthening

σ_{PAR}	Stress due to second phase particles
σ_{P}	Flow stress of pearlite
σ_{o}	The friction stress of the matrix
σ_{v}	Variance of the size distribution
σ_{y}	The yield strength
σ_{α}	Flow stress of ferrite
$\sigma(\varepsilon)$	Flow stress of a material at certain strain
α	Ferrite
α-Fe	Alpha-iron phase
Δa	The increment in the lattice parameter of the alpha-iron
σ	The variance of the size distribution
τ_{c}	The critical shear stress above which the dislocation will glide pass the grain boundary
τ_{e}	The effective shear stress
τ_{p}	The shear stress at the head of the pile-up
φ	Die channel angle in the equal-channel angular pressing tool
Φ	The misorientation angle between two adjacent boundaries
ψ	Outer corner angle in the equal channel angular pressing tool
β	Breadth due to size and strain
ε	Equivalent strain
η	Constant taken as 0.9 for spherical crystallite shape
λ	Wavelength of X-ray
λ_{part}	Free mean path
μ	Constant (0.3-0.4)

CHAPTER 1

1. Introduction

During the last few decades, material scientists have been conducting intensive studies in order to develop materials with superior mechanical properties such as high strength and good ductility. Several strengthening methods were found to be effective in increasing the strength of a material such as grain refinement, work hardening, solid solution, and precipitation strengthening.

During the last two decades, two approaches were developed and used to produce ultrafine-grain materials (materials with grain size of less than ~ 1 μm) and they are often called "bottom-up" and "top-down" approaches [1]. In the "bottom-up" approach, the solid material is produced by assembling individual atoms or nanoparticulate solids. Examples of this procedure include gas condensation [2] and ball-milling with subsequent consolidation [3]. Although this approach allows the production of extremely small grains, it has several disadvantages: the size of the finished product is very small, contamination is very likely, and some degree of residual porosity is possible [4, 5]. In the "top-down" approach, a bulk, fully-dense solid with a relatively coarse grain is processed through application of a large strain to produce ultrafine-grained materials [4, 5]. The latter approach is often termed 'severe plastic deformation' (SPD) processing. Recently, several SPD techniques have been developed such as equal-channel angular pressing (ECAP), high-pressure torsion (HPT), accumulative roll bonding (ARB), cyclic extrusion and compression (CEC), twist extrusion (TE), and multi-directional forging (MDF). When using these SPD techniques to process metals, higher strain can be achieved when compared with the conventional processing, and consequently a higher degree of grain refinement is achieved. The ECAP and ARB techniques are the most preferred techniques in industrial application since they have the ability to produce industry-sized products. However, HPT is the most effective SPD technique in refining the grain size of a material since higher accumulative strain can be imposed on the processed sample [6].

Steel alloys are used in the structural and automotive industry more than any other alloys. Different steel alloys were developed to satisfy the industrial application requirements such as high-strength low alloy (HSLA) steel, interstitial free (IF) steel, and dual-phase (DP) steel. DP steel attracted researchers due to its unique characteristics such as low and continuous yielding, high initial work hardening rate, high tensile strength, and large elongation to failure. On the other hand, ferritic-pearlitic (FP) steel is, generally, still the dominant alloy used due to its low cost and good formability.

Many studies in the literature used ECAP and HPT to process non-ferrous alloys such as aluminium (Al) and copper (Cu) alloys. In contrast, few studies used ECAP to process steel alloys and even lesser studies used HPT to process ferritic-pearlitic (FP) or ferritic-martensitic (FM) steels. During HPT processing, extreme strains, especially at high number of turns, are imposed on the deformed material which results in submicron and nano scale structure with a high density of defects that is difficult to resolve. Transmission electron microscopy (TEM) is generally not able to determine the dislocation density and, hence, an alternative tool is needed to determine the dislocation density such as X-ray line profile analysis (XLPA). Although XLPA can be considered as an alternative tool to TEM for determining the dislocation density, deep understanding and special caution are needed when using XLPA. There is lack of studies investigating the properties of severely deformed low-carbon steel in the ferritic-pearlitic and ferritic-martensitic initial states. Additionally, the reason behind the significant increase in strength of SPD-processed steel is not clear yet and no attempt was made to predict the final strength of such HPT processed steels.

The first aim of the present work is to study the microstructural evolution during the HPT processing of two low-carbon steel samples in the FP and FM initial states. The second aim of the present work is to propose a model predicting the strength of the FP, and FM samples processed by HPT up to different number of turns and this cannot be achieved without determining the dislocation density first. The third aim of this study is to extend the proposed model to predict the strength of FM steel processed by HPT and tempered at different temperatures.

The thesis is structured as follows. Chapter 2 provides the literature review. Chapter 3 presents the main methods used in the experimental work that was performed in this study and Chapter 4 details the experimental results. A thorough analysis of the results is presented and discussed in Chapter 5 which also includes comparisons between the experimental results from the current study and the results reported in the literature. In Chapter 6, the proposed strength/hardness model is

presented in details and applied to the FP, FM, and FM samples processed by HPT and tempered at different temperatures. In Chapter 7, conclusions for this work were drawn where the author also highlights the most important outcomes, and future works are summarized in Chapter 8.

CHAPTER 2

2. Literature Review

In this chapter, a thorough literature review is presented. In the first section, a general overview of severe plastic deformation is presented including the description of the principles of the ECAP, HPT, and ARB techniques. A summary of mechanical properties of SPD-processed materials is also presented in this section. Section 2.1 also reviews some applications of SPD processed materials. The position of this section (i.e. at the beginning of the thesis) is very important since the reader has to be familiar with the experimental procedures performed in the current study as well as with the microstructure and properties of SPD-processed materials. The basic characteristics of the materials used in the current study are presented in Section 2.2. Section 2.3 provides an explanation of the strengthening mechanisms which contributed to the total strength of the HPT-processed steels that were used in this study. In Section 2.4, an overview of SPD processing of steels was given. In Section 2.5, the basic principle of the nanoindentation technique and the so-called "indentation size effect (ISE)" (observed during a nanoindentation test) are presented. Furthermore, examples using nanoindentation to characterise SPD-processed steels are presented in this section. Two methods of X-ray line profiles analysis are presented and some examples using these techniques to characterise SPD processed steels are given in Section 2.6. A brief summary of the literature review is provided in Section 2.7.

2.1 Severe Plastic Deformation

Severe plastic deformation is a metal forming process where the sample is exposed to a very large strain which results in grain refinement without significant changes in the shape and dimension of the processed sample [4]. SPD enhances the strength of the material and maintains a reasonable ductility, under certain SPD conditions, while in conventional thermomechanical processing, the strength is enhanced but the ductility deteriorates [7]. The structures obtained by the thermomechanical process are generally of cellular type with low angle grain boundaries, while those obtained by SPD

are in many cases ultra-fine grain boundaries with high misorientation. In addition, the SPD process is more efficient in terms of grain refinement compared to the conventional process.

The SPD process generally produces ultra-fine grain (UFG) materials with an average grain size of less than 1 μm in diameter. If the average grain size lies within the submicrometer range (100-1000 nm), then it is called a submicron structure while it is called a nanocrystalline structure if it lies within the nanometre range (less than 100 nm). The capability of the SPD process to produce a material that is 100% dense, contamination-free, and large enough to be used in industrial applications makes SPD a very attractive process for researchers to develop materials with enhanced mechanical properties that are suitable for industry applications [8]. Several SPD processing methods have been developed such as equal-channel angular pressing, high pressure torsion, accumulative roll bonding, cyclic extrusion and compression, twist extrusion, repetitive corrugation and straightening, and multi-directional forging. In the following sections, the HPT, ECAP, and ARB will be discussed since they are the most important methods amongst the SPD techniques.

2.1.1. High-Pressure Torsion (HPT)

2.1.1.1. Principle of high-pressure torsion

The HPT tool is depicted in Figure 2.1 where two anvils, upper and lower, contain a circular cavity of the same geometry and dimension [4, 9, 10]. For most HPT anvils the sample fitting the cavities has a disk shape with a diameterr of ~ 10 mm and a thickness of 0.8 to 1 mm. The HPT sample is first placed in the lower anvil's cavity; then, the lower anvil is raised up. The HPT sample is subjected to a constant compressive pressure, *P*, of several GPa and simultaneously to an increasing shear strain resulting from the rotation of the lower anvil [4]. A burr is formed at the edge of the sample between the two anvils. This burr prevents the two anvils from contacting each other and helps build up a hydrostatic pressure by confining the free flow of the material out of the HPT tool [11].

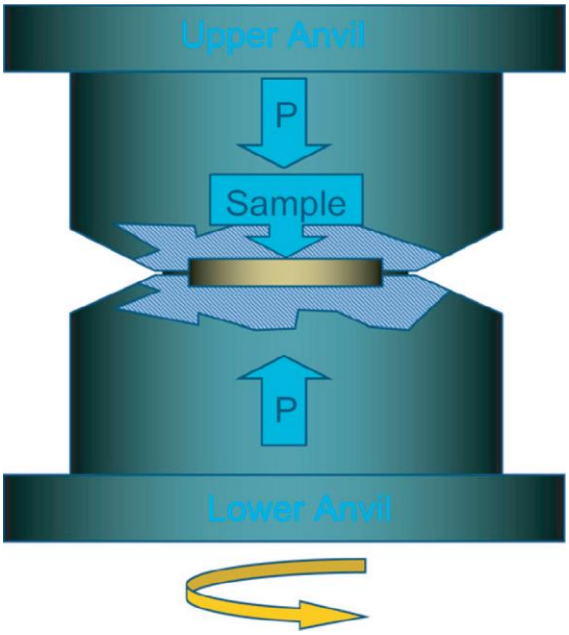

Figure 2.1 Schematic illustration of a typical HPT tool [9].

The shear strain (γ_{ss}) imposed on the HPT sample during the HPT processing is given by [12]:

$$\gamma_{ss} = \frac{2\pi N r}{H_{HPT}} \qquad 2.1$$

where N is the number of rotations, r is the distance from the axis of rotation, and H_{HPT} is the thickness of the sample. The equivalent strain according to the von Mises yield criterion is given by [13] :

$$\varepsilon = \frac{\gamma_{ss}}{\sqrt{3}} \qquad 2.2$$

For small to medium strains, Equation 2.2 is correct but in the case of very high strains, where $\gamma_{ss} \geq 0.8$, the equivalent strain is given by [14]:

$$\varepsilon = \left(\frac{2}{\sqrt{3}}\right) ln \left[\left(1 + \frac{\gamma_{ss}^2}{4}\right)^{\frac{1}{2}} + \left(\frac{\gamma_{ss}}{2}\right)\right] \qquad 2.3$$

Incorporating the decrease in thickness of the disk, another relationship is derived [15]:

$$\varepsilon = ln\left[1 + \left(\frac{\varphi.r}{H_{\mathrm{f}}}\right)^2\right]^{\frac{1}{2}} + ln\left(\frac{H_{\mathrm{i}}}{H_{\mathrm{f}}}\right) \qquad 2.4$$

where $\varphi = 2\pi Nr$, H_{i} and H_{f} are the initial and the final thicknesses of the HPT disk. Equation 2.4 can be further simplified since $\frac{\varphi.r}{H_{\mathrm{f}}} \gg 1$, which yields [16]:

$$\varepsilon = ln\left(\frac{\varphi.r}{H_{\mathrm{f}}}\right) + ln\left(\frac{H_{\mathrm{i}}}{H_{\mathrm{f}}}\right) = \ln\left(\frac{\varphi.r.H_{\mathrm{i}}}{H_{\mathrm{f}}^2}\right) = ln\left(\frac{2\pi NrH_{\mathrm{i}}}{H_{\mathrm{f}}^2}\right) \qquad 2.5$$

It follows from Equation 2.5, the strain is proportional to the distance from the axis of rotation, or the disk centre, and the number of turns. Theoretically, the strain at the centre of the disk is zero and increases as the distance increases to reach a maximum value at the edge of the sample. Furthermore, as the number of turns increases, the strain at the centre remains zero while the strain at the edge increases significantly since both the distance from the centre and the number of turns increase and significant strain variation is observed between the centre and the edge. The microstructure is correlated to the strain and hence inhomogeneous microstructures are expected across the HPT disk especially at a high number of turns. Surprisingly, there are only few experiments that support the theortical variation in strain across the HPT disk [11, 17]. However, more experiments suggest that gradual homogeneity in the microstructure and microhardness develops across the HPT disk as the number of turns increases [9, 13, 18].

The HPT process has many advantages: first, it has the ability to extemely refine the grain size of coarse grained materials; second, there is no significant change in the overall dimensions and shape of the processed sample; finally, it has the ability to consolidate metallic powder [4]. However, the HPT process has several disadvantages: first, the sample has to have a disk shape which may be inefficient or unsuitable for many industrial applications; second, the disk size is relatively small, and in most cases, limited to a maximum diameter of 10 mm and a thickness of 1 mm; finally, microstructure variations develop across the disk since the strain imposed on the sample is proportional to the distance from the centre of the disk.

2.1.1.2. Unconstrained and constrained HPT

HPT can be conducted in 2 main modes: unconstrained and constrained. In unconstrained HPT, as shown in Figure 2.2a [4], the material flows freely under the applied pressure during the deformation, while in constrained HPT there is no outward flow of the material as shown in Figure 2.2b [4]. This means that the material deforms in the presence of a back-pressure. In reality, it is very difficult to achieve the constrained condition, which makes researchers use what is known as a quasi-constrained condition where there is limited outward flow of material as shown in Figure 2.2c [4].

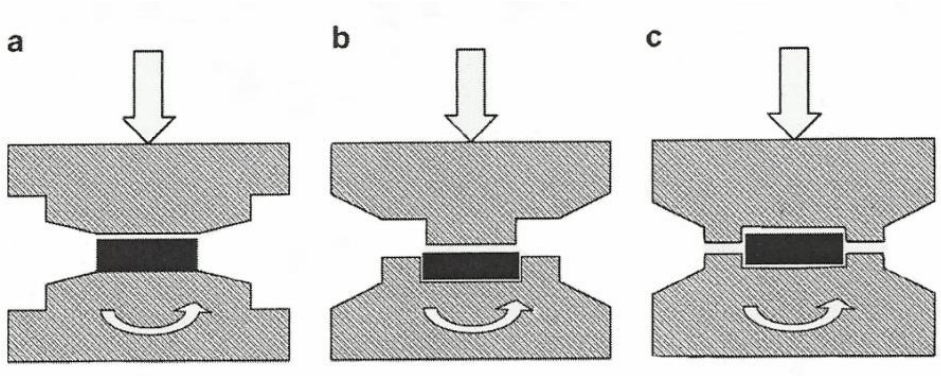

Figure 2.2 Schematic illustration of (a) unconstrained (b) constrained and (c) quasi-constrained HPT processes [4].

2.1.1.3. Experimental parameters affecting HPT

The number of turns and applied pressure influence the properties of HPT-processed samples. Zhilyaev et al. [19] studied the effect of the number of rotations on the microhardness of a nickel (Ni) sample processed by HPT at room temperature under a pressure of 6 GPa through 1 and 7 turns and the microhardness results are depicted in Figure 2.3. After 1 turn of HPT processing, there is a noticebale difference in the microhardness values between the centre and the edge of the Ni processed sample as shown in Figure 2.3. After 7 turns of HPT processing, the difference in the microhardness values between the centre and the edge becomes smaller. Furthermore, the authors processed the Ni sample by HPT up to 5 turns under different pressures, 1 and 9 GPa. The microhardness results are dipicted in Figure 2.4. Processing under low pressure, 1 GPa, resulted in a difference in the microhardness between the centre and

the edge of the Ni processed sample. This difference tended to be smaller when processing under a pressure of 9 GPa.

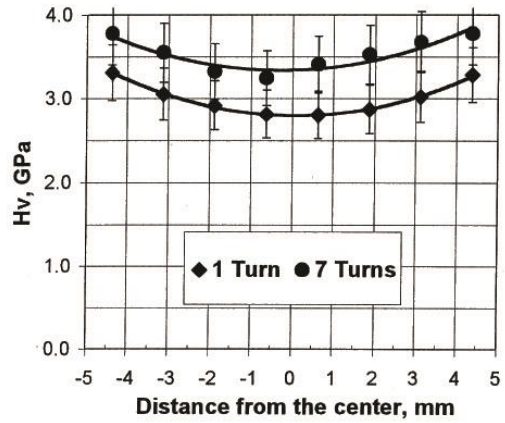

Figure 2.3 Microhardness vs. the number of turns of Ni sample processed by HPT up to 1 and 7 turns under a pressure of 6 GPa [19].

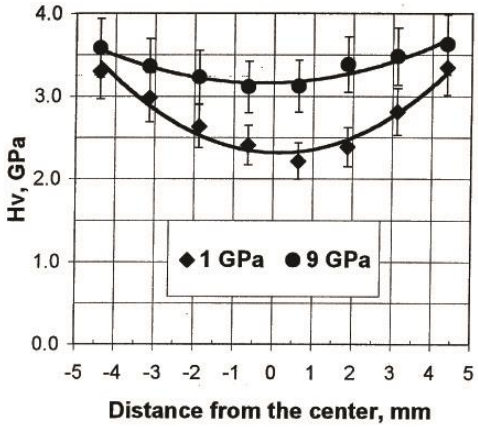

Figure 2.4 Microhardness vs. the number of turns of Ni sample processed by HPT up to 5 turns under a pressure of 1 and 9 GPa [19].

2.1.2. Equal-channel angular pressing

The ECAP process uses a special die containing a channel which has a uniform cross section along its length [20]. The channel is bent through an angle φ while the outer arc of curvature, where the two parts of the channel intersect, is represented by an angle ψ as shown in Figure 2.5 [20-23].

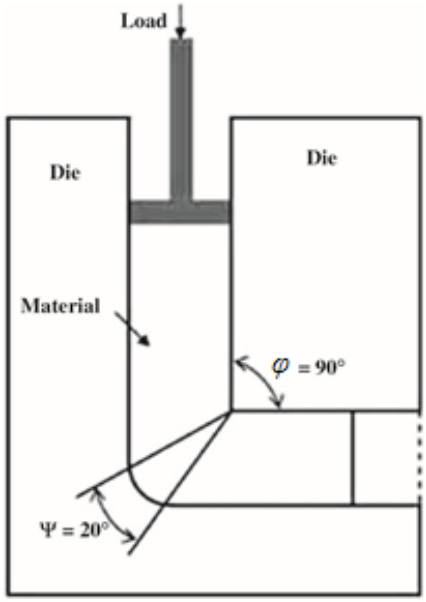

Figure 2.5 Schematic illustration of equal-channel angular pressing facility [23].

The sample should have a round or square cross section (depending on the channel cross section). The diameter of the cross section, in the case of round cross sections, or the diagonal, in the case of a square cross section, is generally less than 20 mm, while the maximum length of the sample is generally 100 mm [7]. The sample is simply pressed through the channel by a plunger as shown in Figure 2.6 [24]. The sample undergoes predominantly shear deformation when it reaches the intersection plane of the two channels.

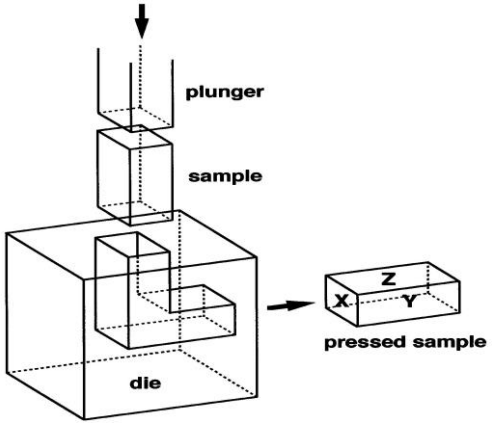

Figure 2.6 Schematic illustration of ECAP facility [24].

The total strain (ε) imposed on the sample is given by [25]:

$$\varepsilon = \frac{N_{\text{passes}}}{\sqrt{3}}\left[2\cot\left(\frac{\varphi}{2}+\frac{\psi}{2}\right)+\psi\,\text{cosec}\left(\frac{\varphi}{2}+\frac{\psi}{2}\right)\right] \qquad 2.6$$

where N_{passes} is the number of passes through the die. It is clear from the equation above that the strain imposed on the sample depends mainly on both angles φ and ψ. When φ=90^o and ψ=0^o as shown in Figure 2.6, the total strain is $\sim$ 1 after one pass. Using this kind of configuration is preferred when pressing ductile material like aluminium and copper-based alloys but it becomes difficult when pressing hard materials like titanium alloys [26]. In this case, increasing the angle φ or increasing the deformation temperature is advised. Tungsten samples were successfully processed up to 8 passes at 1000^{o}C in combination with an angle φ=110^o [27].

Four main routes of ECAP processing have been developed [22, 25, 28-30]. In route A, the sample is not rotated between passes, whereas in route C the sample is rotated about its axis by 180^o between consecutive passes. In route B_A, the sample is rotated by 90^o in an alternate direction between consecutive passes, and in route B_C, the sample is rotated by 90^o in the same direction between consecutive passes [22, 25, 28-30]. These routes are illustrated in Figure 2.7 [31]. It has been reported that the optimum route to develop a microstructure of equi-axed grains with high-angle boundaries is route B_C [5].

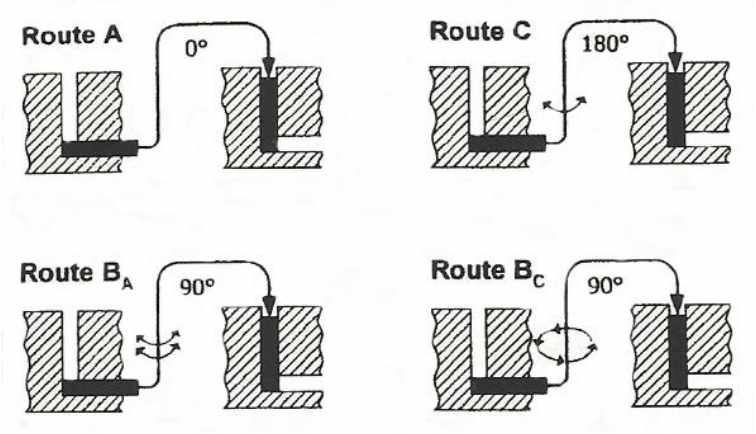

Figure 2.7 Schematic illustration of different ECAP routes [31].

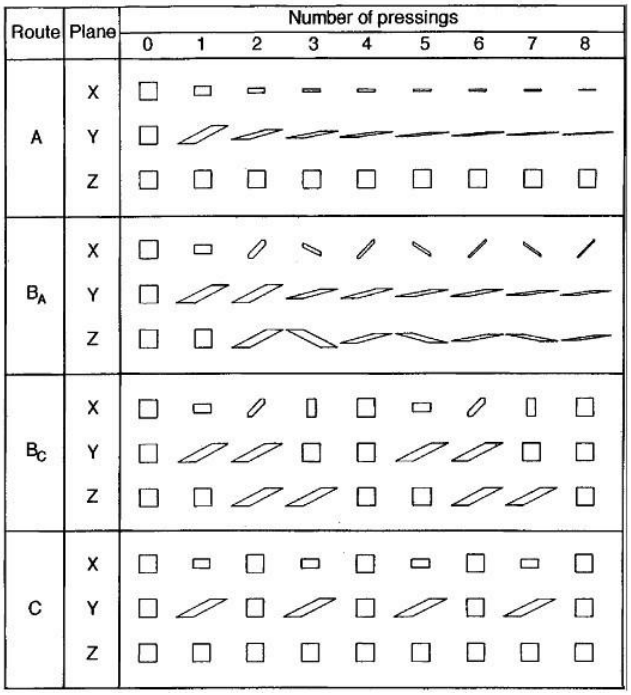

Figure 2.8 Schematic illustration of element distortion as a function of ECAP passes for routes A, B_A, B_C, and C [29].

It is apparent from Figure 2.8 that route C and B_C have the ability to maintain the original shape of the element after each two and four passes, respectively. When the processed material by ECAP is sufficiently ductile, the process can be conducted at room temperature. During the ECAP process, there is an increase in temperature, but this does not have any major effects on the structure's evolution. In contrast, when processing a hard-to-deform material, the material should be processed at elevated temperatures in order for the material to gain some ductility [26]. Optimum processing temperatures should be precisely selected since a high temperature will lead to dynamic recovery and grain growth, whereas a low temperature will cause microscopic or even macroscopic shear cracks during the ECAP process [26].

2.1.3. Accumulative Roll Bonding

In the Accumulative Roll Bonding (ARB) process, sheets of the same thickness are stacked and simultaneously rolled as shown in Figure 2.9 [6]. After rolling, the sheet is cut into two halves and stacked together again. Before each stacking, surface treatment is carried out on the contact faces. This includes degreasing and wire brushing in order to enhance the bonding between the two sheets [6, 32-34]. This operation which includes rolling, cutting, brushing, and stacking can be repeated several times so that a large strain is accumulated in the rolled sheet which leads to grain refinement. Heating

the sheet to a temperature below the recrystallization temperature is also possible in order to achieve enhanced bonding and to lower the required rolling force [6]. When the reduction in thickness is 50% during one cycle of the ARB process, the von Mises equivalent strain (ε) is 0.8 and $0.8N_{cycles}$ for N_{cycles} cycles of ARB [6, 33]. One of the important advantages of ARB processing is that a conventional rolling mill can be used and no further special equipment are needed. ARB has another advantage over other SPD techniques and that is its ability for producing large-scale products which makes it more attractive for industrial applications. Recently, several successful ARB experiments were documented using different materials. The microstructure obtained by ARB characterised by lamellae structure oriented in the rolling direction. With increasing the number of cycles, the microstructure develops to have more ultrafine grains with high misorientation. Furthermore, ARB-processed materials exhibit similar strength and ductility to the other SPD-processed materials [33, 34].

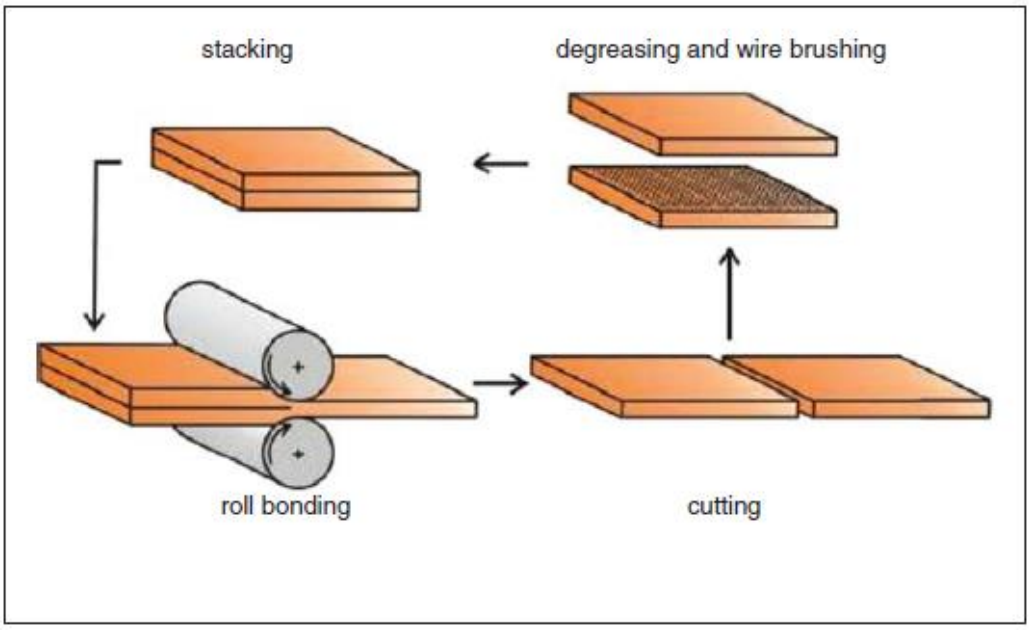

Figure 2.9 Schematic illustration of the ARB process [6].

2.1.4. Properties of SPD-processed materials

2.1.4.1. Strength and ductility

The ECAP and HPT processes are widely used since they have the ability to produce ultrafine grains lying in the lower submicron or nanometer range. It is well-known that

the strength of a material is often related to the mean grain size according to Equation 2.7, which is known as the Hall-Petch relation [35, 36]:

$$\sigma_y = \sigma_o + kd^{-1/2} \qquad 2.7$$

where σ_y is the yield strength, σ_o is the friction stress needed to move individual dislocations, d is the mean grain size, and k is a constant. It follows from Equation 2.7 that the increment in yield strength is inversely proportional to the square root of the grain size. Hence, one expects significant increase in the strength of a material processed by SPD and this is found by many researchers [37-39]. In the same regard, it was observed that the strength increases as the number of passes increases, in the case of ECAP processing, or as the number of turns increases, in the case of HPT processing, while the ductility decreases as the strain increases and this behaviour is similar to the one illustrated in Figure 2.10 [30].

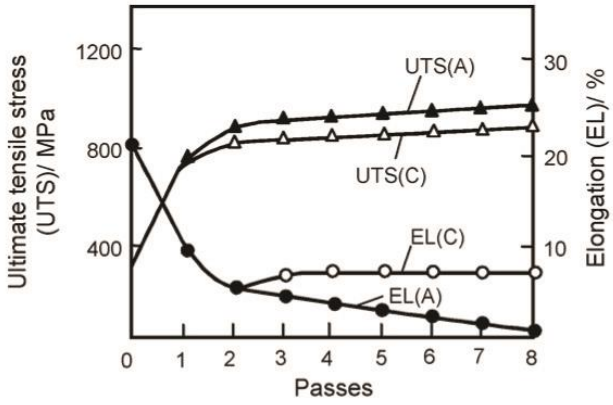

Figure 2.10 The effect of number of passes on the ultimate tensile strength and the elongation to failure of Armco iron processed by ECAP up to 8 passes. A and C refer to route A and C, respectively [30].

Horita et al. [40] obtained similar results when they processed 6 Al-alloys by ECAP up to different equivalent strains as shown in Figure 2.11 and Figure 2.12 [40]. There is a significant increase in the strength and drastic drops in the elongation to failure after an equivalent strain of 1.

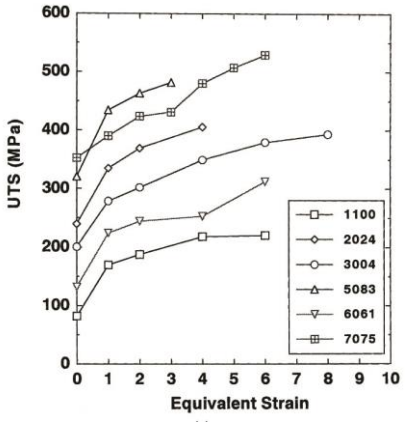

Figure 2.11 Ultimate tensile stress (UTS) vs. the equivalent strain in six Al-alloys processed by ECAP [40].

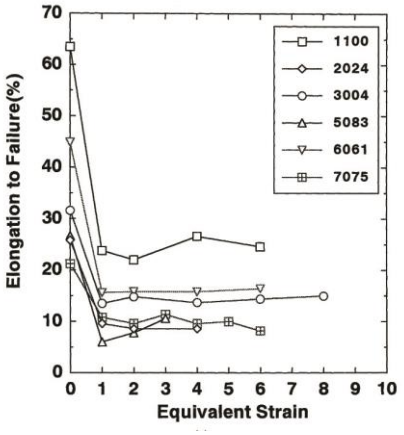

Figure 2.12 Elongation to failure vs. the equivalent strain in six Al-alloys processed by ECAP [40].

The low ductility observed in SPD-processed materials is the result of early necking during deformation. Increasing the work hardening rate would help delay necking and consequently higher ductility will be obtained. The reason behind the low rate of work hardening observed in SPD-processed maerials is that these materials contain high density of dislocations and soon reach a saturation level of dislocation density. Reaching the saturation level of dislocation density implies more difficulty in accomodating more dislocations and hence deforming the material becomes harder [8]. When the grain size is reduced to a certain size, the grain interior becomes dislocation free and instead the dislocations emitted from one grain boudnary dissapear at another grain boundary and no accumulation of dislocations is associated with the processing leading to a low rate of work hardening [8].

On the other hand, another hypothesis emerged when studying the strength and ductility of SPD-processed materials suggesting that these materials possess a combination of high strength and good ductility. Valiev et al. [41] sucessully obtained an excellent combination of strength and ductility when they processed pure Cu by ECAP and pure Ti by HPT up to 16 passes and 5 turns, respectively. Valiev et al. [41] suggested that in order for a material to exihibit a good combination of strength and ductility, the material should be processed under sufficient large strain, (i.e. beyond a certain strain value). The authors attributed the good ductility to the new deformation mechanism, grain boundary sliding, which operates at extreme large strains. The authors added that the grain boundary sliding mechanism is facilitated by many microstructural features, such as fine grains with high misorientation, and non-equilibrium grain boundaries. Furthermore, Horita et al. [40] compared the strength of an Al-3004 alloy processed by ECAP and the same alloy cold rolled to an equivalent strain of $\sim$ 3. The strength

increases linearly with strain for both methods as illustrated in Figure 2.13. However, the elongation to failure, or ductility, drops to ~ 14 % beyond a strain of ~ 1 for the ECAP-processed sample and no additional reduction was recorded at further strain while the reduction in ductility continued with further strain for the cold rolled sample as shown in Figure 2.14 [40].

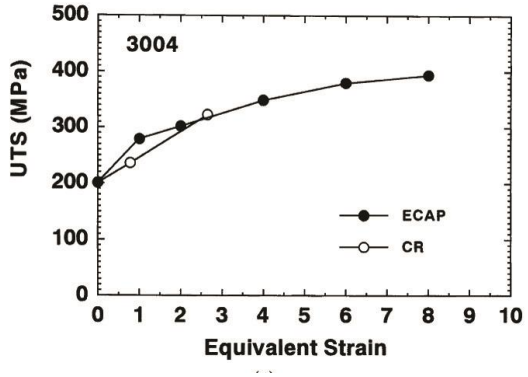

Figure 2.13 Stress-strain curve of 3004 aluminium-based alloy in two conditions: cold rolled and processed by ECAP [40].

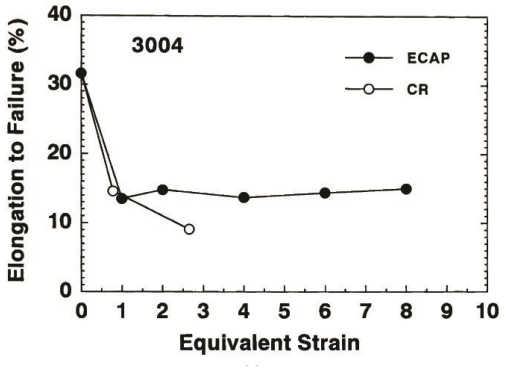

Figure 2.14 Elongation vs. the equivalent strain of 3004 aluminium-based alloy in two conditions: cold rolled and processed by ECAP [40].

2.1.4.2. Thermal stability of SPD-processed materials

The microstructure of SPD-processed materials is characterised by refined grains with high misorientation, high dislocation density, and non-equilibrium grain boundaries. Hence, the microstructure is in a high-energy, non-equilibrium state. At elevated temperatures, these microstructures can easily undergo grain growth [8]. In order to fully gain the advantage of SPD techniques, it is important to preserve the ultrafine grained micorstructure produced by these techniques at high temperatures.

Horita et al. [40] investigated the thermal stability of six Al alloys after ECAP processing up to different equivalent strain by annealing at 100, 200 and 300^{o}C for 1 hour. For 100^{o}C annealing, the alloys maintained their ultrafine grain microstructure. For 200^{o}C annealing, inspite of the clear evolution of grain boundaries, no grain growth was observed and reduction in the dislocation density was recorded as well. For 300^{o}C annealing, two alloys, 2024 and 7075, out of the six alloys retained their submicrometer grains while grain growth was observed in the rest of the six alloys. Horita et al. [40] ascribed the limited grain growth to the existence of the fine particles in these two alloys. Stolyarov et al. [42] studied the thermal stability of pure Ti deformed by two-step

processing through TEM investigation and microhardness test on the processed sample. In the first step, the Ti sample was processed by warm ECAP up to 8 passes; in the second step, the as-pressed Ti sample was cold-rolled to a total reduction of 35-73%. The TEM investigation of the processed sample followed by annealing at 400°C for 30 min revealed that the dislocation density was reduced and the morphology of the grains changed from irregular shapes to equi-axed ones without any evidence of grain growth. Stolyarov et al. [42] conducted the microhardness test on two samples processed by warm ECAP and cold-rolled to a total reduction of 35 and 55%. The sample cold-rolled to a 55% reduction in thickness had a microhardness slightly higher than that of the sample cold-rolled to a 35% reduction in thickness. When annealing the cold-rolled samples, the authors observed that the microhardness tended to increase before reaching 300°C but no clear explanation for this increase was given by the authors. However, a noticeable drop in the microhardness was observed around 400°C.

The above studies suggest that the microstructure of the two Al-alloys, 2024 and 7075, processed by ECAP in Horita et al.'s [40] investigation is thermally stable up to 300°C while the microstructure of the Ti sample processed by ECAP and cold-rolled in Stolyarov et al.'s [42] investigation is thermally stable up to 400°C. This indicates that the microstructure of the SPD-processed materials is thermally stable to a large extent but further investigations are still needed to confirm these findings.

2.1.5. Applications of SPD

SPD-processed materials are, in general, used whenever a material with high strength is needed or a thickness reduction is important. SPD-processed materials are used in structural, electrical, hydrogen storage materials, and many other applications. Some examples of these applications will be briefly discussed. Titanium alloys are used widely in biomedical applications due to their biocompatibility with living organisms. However, Ti alloys contain small amounts of alloying elements such as aluminium (Al) and vanadium (V) which are toxic if they leave the alloy and spread in the body. Due to this fact, there is a trend to use pure Ti but it was found that pure Ti is not strong enough to bear the applied loads in the body. SPD techniques allow the production of pure Ti with high strength that is suitable for biomedical applications. Latysh et al. [43] successfully produced nanostructure pure Ti using ECAP and thermomechanical treatment. This nanostructure pure Ti was used in the production of different kinds of implant screws as shown in Figure 2.15.

High-strain rate superplasticity has been successfully used for forming complex shaped articles, such as pistons, using nanostructured Al 1420 alloy, Figure 2.16 [44]. This opens new windows for the production of complicated shaped components in short time. In the electrical field, the use of pure Al is limited due to its low strength. It was possible to overcome this limitation by processing an Al-alloy, AA6060, by HPT at 180^{o}C to produce a homogenous ultrafine-grained Al-alloy [45]. Bobruk et al. [45] argued that dynamic strain ageing (DSA) took place during the HPT processing at this temperature and resulted in a reduction in both the dislocation density and the concentration of the alloying elements in the Al matrix and second-phase precipitates were formed. Both the strength and electrical conductivity were improved while the latter was very close to that of pure Al [45].

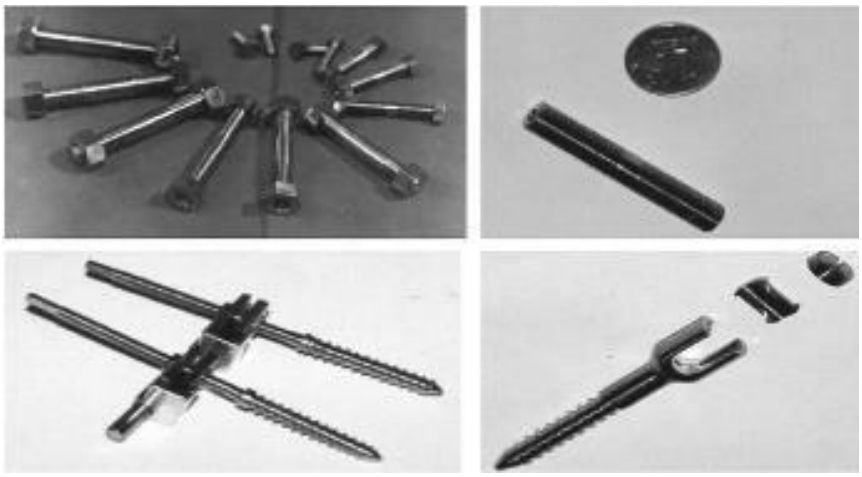

Figure 2.15 Different types of implant screws made of nanostructured pure Ti [43].

Figure 2.16 Piston manufactured from nanostructured Al 1420 alloy used in small internal combustion engine [44].

SPD processing also contributes to the development of hydrogen storage materials. Processing ball-milled $Mg_{70}Ni_{30}$ by HPT increases the maximum absorption capacity by 30-50% and this increase is attributed to the formation of extra sites and lattice defects at the grain boundaries [46].

2.2 Steels

Steel alloys are widely used in the automotive, structural, pipe line, and civil structures (e.g. bridges) sectors. When processing multi-phase steel using SPD, complex deformation mechanisms occur. Changes in the microstructure that can take place during the SPD process of steels include cementite dissolution, cementite formation, and carbon segregation at the grain/subgrain boundaries. In the following, ferritic-pearlitic and ferritic-martensitic steels will be discussed.

2.2.1. Ferritic-pearlitic steel

2.2.1.1. Ferritic-pearlitic steel characteristics

The microstructure of the ferritic-pearlitic steel consists of soft ferrite matrix and hard dispersed colonies of pearlite as shown in Figure 2.17. The pearlite colonies consist of lamellae structures of cementite and ferrite as shown in Figure 2.18. The soft ferrite supplies the FP steel with ductility while pearlite supplies strength. The higher the carbon content in the FP steel, the more pearlite is formed and hence the higher overall strength will be. In the low-carbon steel where the pearlite volume fraction is expected to be small, the pearlite contribution to the overall strength is still small. FP steel is produced more than any other steel alloy and is widely used in structural applications due to its good formability and low cost.

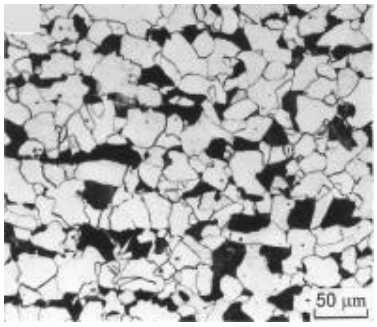

Figure 2.17 Optical micrographs showing the microstructure of low-carbon FP steel (0.15 wt.% C) where the light colour represents the ferrite and the dark represents the pearlite [47].

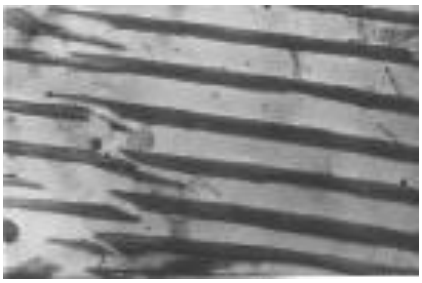

Figure 2.18 TEM bright-field image showing the lamellae structure of pearlite in low-carbon steel (0.15 mass.% C) [48].

2.2.1.2. The strength of the ferritic-pearlitic steel

The strength of the FP steel is strongly correlated to its microstructure which consists of continuous matrix ferrite and hard pearlite colonies. Since the pearlite supplies the FP steel with strength, an increase in the volume fraction of the pearlite leads to an increase in the strength. An increase in the strength of any of the two phases (ferrite or pearlite) or both will lead to an increase in the overall strength of the FP steel. The overall flow stress of FP steel is often described by the rule of mixtures [49]:

$$\sigma_{\mathrm{FP}} = (1 - f_{\mathrm{P}})\sigma_{\alpha} + f_{\mathrm{P}}\sigma_{\mathrm{P}} \qquad 2.8$$

where σ_{FP} is the flow stress of the FP steel, σ_{α} and σ_{P} are the flow stresses of the ferrite matrix and pearlite, and f_{P} is the volume fraction of pearlite. It can be seen from Equation 2.8 that the overall flow stress of the FP steel can be calculated based on the individual flow stress and the volume fraction of each phase (ferrite and pearlite). Suh et al. [48] proposed a model using the finite element method (FEM) to predict the flow stress of FP steel. The authors incorporated a previous Swift relation to calculate the individual stress of each phase, ferrite and pearlite. The Swift relation is a function of the chemical composition of the steel alloy, the carbon content in ferrite, ferrite grain size, interlamella spacing, and the volume fraction of cementite in pearlite. The calculated flow stress was lower than the measured stress. The authors investigated the microstructure using TEM and found that dislocations developed at the ferrite/pearlite interface and in ferrite where no significant change in the pearlite was observed. Accordingly, the authors assumed that only ferrite deformed plastically during the yield elongation. Thus, a better flow stress of the FP steel was predicted when the authors recalculated the flow stress taking into consideration the important effect of ferrite during the yield elongation. Karlsson and Linden [49] studied the flow stress of low carbons steel [0.2 wt.% C] in the FP initial state. The volume fraction of pearlite in the FP steel is 25%. Karlsson and Linden [49] claimed that the overall yield strength of the FP steel is similar to that of the ferrite matrix. Furthermore, the authors used the concept of the geometrically necessary dislocations (GNDs) to describe the flow stress of the ferrite matrix and good agreement between the calculated and the measured flow stress was observed. It is worth noting that the authors described the flow stress of the ferrite based on the geometrically necessary dislocations and independent of the ferrite grain size.

2.2.2. Ferritic-martensitic steel

2.2.2.1. Ferritic-martensitic steel characteristics

The FM steel consists of soft, continuous matrix (ferrite), and hard, brittle particles (martensite islands). Before discussing the characteristics of the FM steel, it is important to briefly explain how the FM steel is produced. Low-carbon steel or low-alloy steel is annealed in the ferrite-austenite region (α + γ), i.e. between the lower and upper critical temperature (*A1* and *A3*) on the iron-iron carbide phase diagram as shown in Figure 2.19. The alloy, a low-carbon or low-alloy steel, is held for several minutes to allow the formation of the austenite in the ferrite matrix. Here, it is worth stressing that the higher heating temperature, the higher the volume fraction of austenite formed. The formed austenite transforms into martensite when quenching to room temperature and hence the final microstructure consists of ferrite and martensite. The martensite has a body-centred tetragonal (BCT) structure due to the expansion in the c-axis and relative contracting in the a-axis, which occurs when the interstitial carbon atoms occupy the octahedral sites in martensite. Xiao et al. [50] argued that this tetragonality only exists if the carbon content is higher than 0.6 wt.%. The tetragonality in martensite has been widely studied and a general accepted relationship between the carbon content and the c/a ratio has been established [51, 52]:

$$c\ (\mathrm{A}^o) = a_\mathrm{o} + (0.116 \pm 0.002)X_\mathrm{C} \qquad 2.9$$

$$a(\mathrm{A}^o) = a_\mathrm{o} - (0.013 \pm 0.002)X_\mathrm{C} \qquad 2.10$$

$$\frac{c}{a} = 1 + (0.046 \pm 0.001)X_\mathrm{C} \qquad 2.11$$

where X_C is the carbon content in wt.% and a_o is the lattice parameter of α-iron (0.28664 nm [53, 54]). Based on the relationships established by Kurdjumove and Khachaturyan [51, 52], Xiao et al. [50] hypothesised that $c = a$ (Equation 2.9 and Equation 2.10) if the carbon content is less than or equal to 0.18 wt.%. Furthermore, Xiao et al. [50] established a general relationship to predict the value of c in martensite for plain carbon steels as:

$$c\ (\mathrm{A}^o) = 2.8664 + (0.020 \pm 0.002)X_{\mathrm{C}} \qquad 2.12$$

The FM steel exhibits a combination of high strength and good ductility when compared to other steel alloys containing the same carbon content and this combination can be attributed to the composite-like microstructure: ferrite matrix reinforced by hard martensite particles. The martensite islands supply the FM steel with the strength, while the ferrite supplies it with the ductility [55]. The FM steel is characterised by high strength, good ductility, high work hardening rate at the initial stage of the deformation, continuous yielding, and a low yield to tensile strain ratio [56].

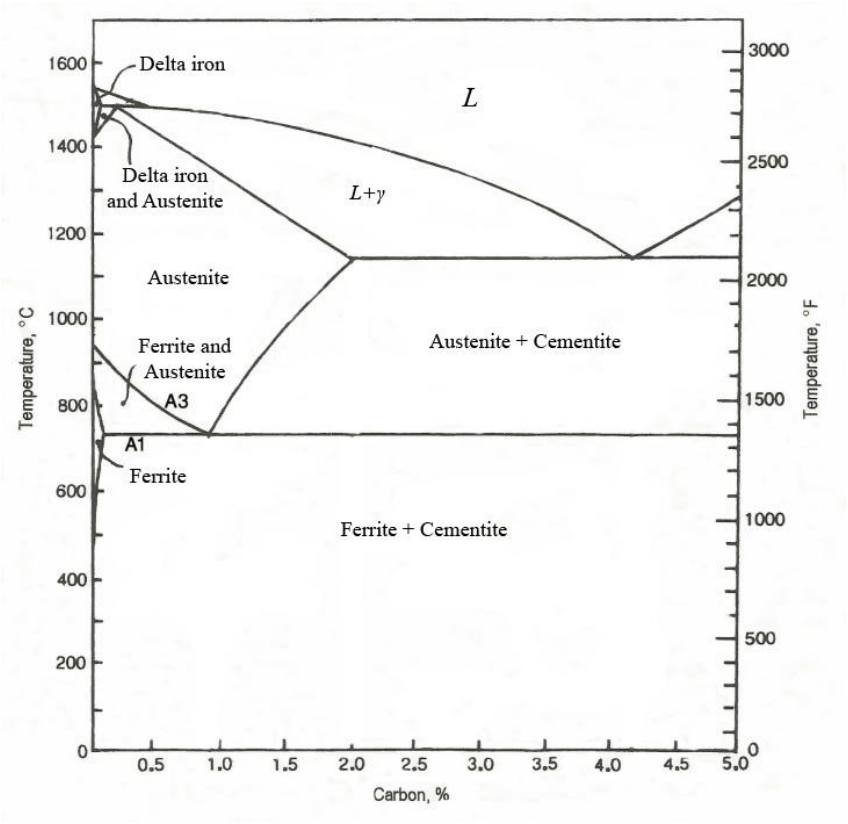

Figure 2.19 Iron-iron carbide phase diagram [57].

2.2.2.2. The strength of the ferritic-martensitic steel

The strength of a material is correlated to its microstructure. The microstructure of the FM steel is complex due to the possible existence of more than two phases in it. The microstructure of the FM steel can contain retained ferrite (formed during intercritical

annealing), retained austenite, epitaxial ferrite (formed by epitaxial growth on the retained ferrite during quenching), and different types of carbides [58]. Thus, one can expect different deformation mechanisms and stress-strain behaviour during a tensile test of FM steel due to the complexity in the microstructure mentioned above.

Hwang et al. [59] studied the effect of the ferrite grain size on the yield and tensile strength in two low-carbon FM steel (0.15 wt.% C) samples by conducting a tensile test at room temperature. The low-carbon steel samples were homogenised in the single phase region (γ) at different holding temperatures to achieve different ferrite grain sizes after the austenite-ferrite transformation. On the other hand, the low-carbon steel samples were intercritically annealed at the two-phase regions ($\alpha + \gamma$) at different holding temperatures to achieve different volume fractions of martensite. Hwang et al. [59] observed an increase in the yield and tensile strength as the ferrite grain size decreased. The yield strength of two FM samples containing the same martensite volume fraction (V_m), 30%, but different ferrite grain sizes of ~ 13 and 23 μm, were 468 and 408 while the tensile strength of the same samples were 669, and 592 MPa, respectively. Moreover, the authors observed that the yield strength increased as the volume fraction of martensite (V_m) increased. The yield strength of two FM samples having similar ferrite grain sizes, ~ 22 μm, with different martensite volume fractions (V_m), ~ 33 and 53%, were 408 and 505 while the tensile strength of the same samples were 592 and 794 MPa, respectively. Pouranvari [60] heat treated low-carbon steel (0.11 wt.% C) at different temperatures in the two-phase region ($\alpha + \gamma$) to achieve different volume fractions of martensite in the low-carbon steel samples. Pouranvari [60] conducted tensile test on the samples containing different volume fractions of martensite (V_m) at room temperature. The author found out that the yield and ultimate tensile strength increased as the martensite volume fraction (V_m) increased; however, the ultimate tensile stress remained constant at $V_m \sim 70\%$ and he attributed this steady-state in the tensile stress to the decrease in the martensite hardness resulting from the decrease in the carbon content in the martensite as the volume fraction of martensite (V_m) increased. Liedl et al. [61] obtained similar results when they conducted a tensile test on three FM steel samples containing 6, 11, and 18% of martensite. The authors observed an increase in the yield strength as the martensite volume fraction (V_m) increased as shown in Figure 2.20.

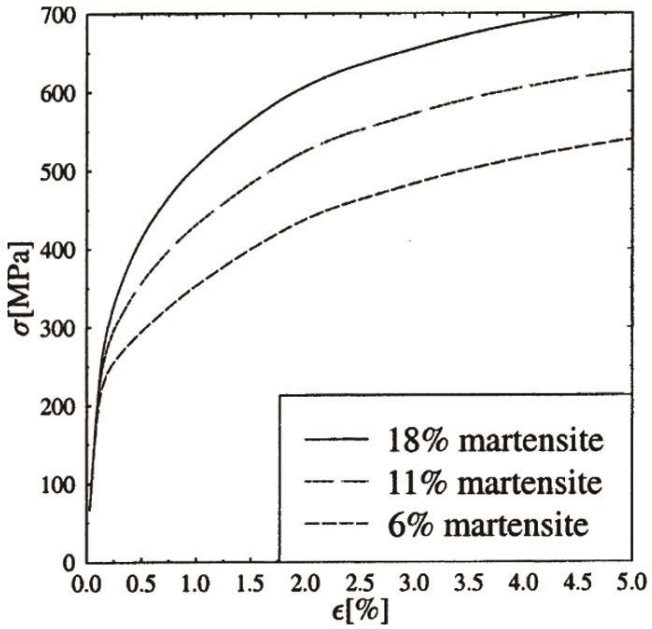

Figure 2.20 Stress-strain curve of FM steel with different volume fractions of martensite [61].

Liedl et al. [61] attributed the high rate of work hardening at the initial stage of the deformation to the formation of a hardened skeleton, from the ferrite phase, connecting the martensite islands during the quenching process. Korzekwa et al. [58] studied the relationship between the strength and the microstructure when conducting a tensile test on dual-phase steel (0.063 wt.% C). The stress-strain curve depicted in Figure 2.21 is, in general, characterised by continuous yielding in addition to high rate of work hardening at the initial stage of the deformation. The authors observed that the stress-strain curve, shown in Figure 2.21, cannot be described by a single parabolic function but instead three parabolic functions are needed to describe the whole stress-strain curve of the dual-phase steel used in Korzekwa et al.'s [58] investigation. In stage I, the authors observed a high dislocation density in the ferrite adjacent to the martensite. The austenite-martensite transformation results in volume expansion which in turns causes plastic deformation in the ferrite adjacent to the martensite. Consequently, a high density of unpinned dislocations is created in the ferrite adjacent to the martensite as shown in Figure 2.22. These dislocations are assumed to be mobile, or at worst case, partly mobile, which facilitates the early deformation or in other words the deformation is initiated in the ferrite adjacent to the martensite. Furthermore, the distribution of these dislocations varies from place to place [58, 61]. In stage II, the authors [58] observed the evolution of cell structures, again, in ferrite adjacent to the martensite. In stage III, well defined structures evolved and tended to be smaller near the martensite. In this regard, Kadkhodapour et al. [56] confirmed the existence of geometrically

necessary dislocations (GNDs) in the ferrite adjacent to the martensite leading to local hardening in the ferrite matrix by conducting nanoindentation tests on a commercially dual-phase steel as shown in Figure 2.23.

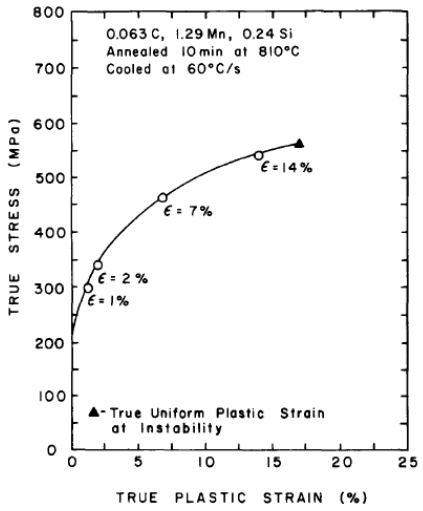

Figure 2.21 Stress-strain curve of low-carbon dual-phase (or FM) steel (0.063 wt.% C) [58].

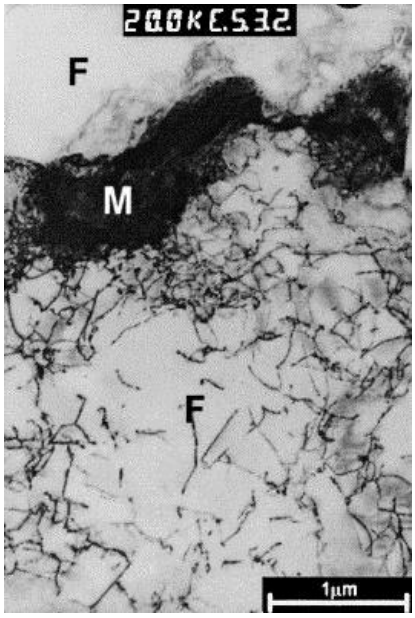

Figure 2.22 TEM micrograph showing the microstructure of FM steel where the ferrite appears as light coloured while the martensite appears as dark coloured [61].

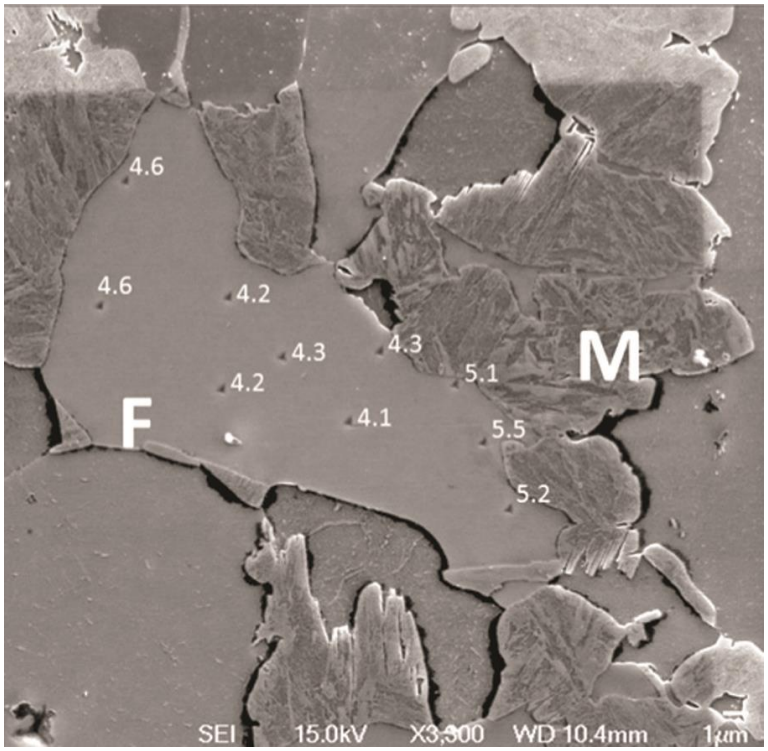

Figure 2.23 Nanoindentation test on commercially FM steel [56].

2.2.3. Tempered FM steel

2.2.3.1. Tempered FM steel characteristics

The martensitic, or as-quenched, steel is characterised by high strength and reduced ductility. Heating the martensitic steel to a temperature close to or below the lower critical transformation temperature, *A*1, is referred to as tempering process [55]. During tempering process, the toughness and ductility of the martensitic steel are enhanced but often at the expense of the high hardness. However, a combination of good strength and ductility can be obtained if low tempering temperature is chosen. Several parameters such as tempering temperature, tempering time, and the chemical composition will affect the formed microstructure after the tempering process. The tempering process undergoes three to four overlapped stages and forms recrystallized ferrite grains and cementite particles at the end. During stage I (up to 250^{o}C), carbon clustering and precipitation of transition carbide, ε-carbide, occurs [62]. During stage II (up to 300^{o}C), decomposition of any existed retained austenite occurs. During stage III (above 300^{o}C), formation of cementite, Fe_3C, and equi-axed ferrite grains [62]. Typical microstructure

of martensitic steel (0.13 wt. %C) tempered at 250°C is shown in Figure 2.24 where the microstructure consists of ferrite matrix and tempered martensite.

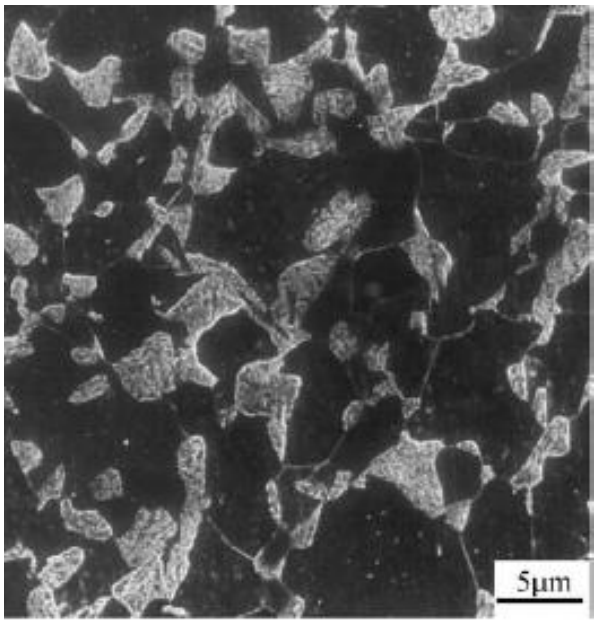

Figure 2.24 Scanning electron microscopy (SEM) micrograph showing the microstructure of FM steel (0.13 wt.% C) tempered at 250°C [63].

2.2.3.2. The strength of tempered FM steel

Tempering process affects the mechanical properties such as toughness, strength, and ductility of the tempered FM steel. Gunduz [64] studied the microstructure changes and strength variation in FM steel (0.17 wt.% C) tempered at 100°C to 600°C. The author did not observe significant changes in the microstructure or tensile behaviour when tempering up to 200°C. The stress-strain curve of the as-quenched sample was characterised by continuous yielding while this was not the case when the tempered samples were tensile tested. The author also observed that the ultimate tensile strength (UTS) decreased with tempering temperature and recorded only a slight decrease in the yield strength (YS) with tempering temperature. On the other hand, the elongation increased with tempering temperature.

Salemi and Abdullah [65] tempered martensitic steel (0.34 wt.% C) at 200°C to 600°C. After conducting tensile tests on the tempered samples, Salemi and Abdullah [65] observed that both the ultimate tensile strength and yield strength decreased as the tempering temperature increased as shown in Figure 2.25. Furthermore, the yield

strength decreased at lower rate than the ultimate tensile strength. The authors also observed slight increase in the elongation as the tempering temperature increased.

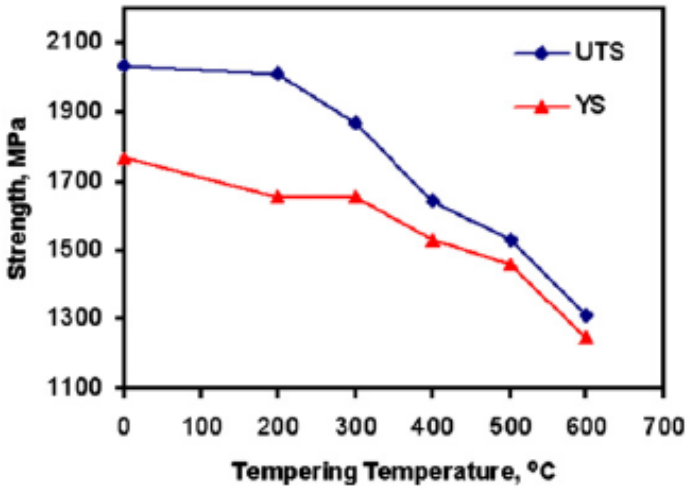

Figure 2.25 The ultimate tensile strength and yield strength of tempered martensitic steel (0.34 wt.% C) as a function of tempering temperature [65].

Fang et al. [63] tempered FM steel (0.13 wt.% C) at 150°C to 450°C. The authors did not observe marked changes in the microstructure when they tempered the martensitic steel at 150°C. Increasing the tempering temperature to 250°C, the microstructure changed and consisted mainly of ferrite and tempered martensite. The authors conducted a tensile test on the tempered samples. The stress-strain curve of the as-quenched sample was characterised by continuous yielding while discontinuous yielding was observed for the tempered samples. The authors recorded no significant changes in the yield strength when tempering at 150°C to 450°C as shown in Figure 2.26. However, the ultimate tensile strength decreased with the tempering temperature. Furthermore, the elongation increased as the tempering temperature increased.

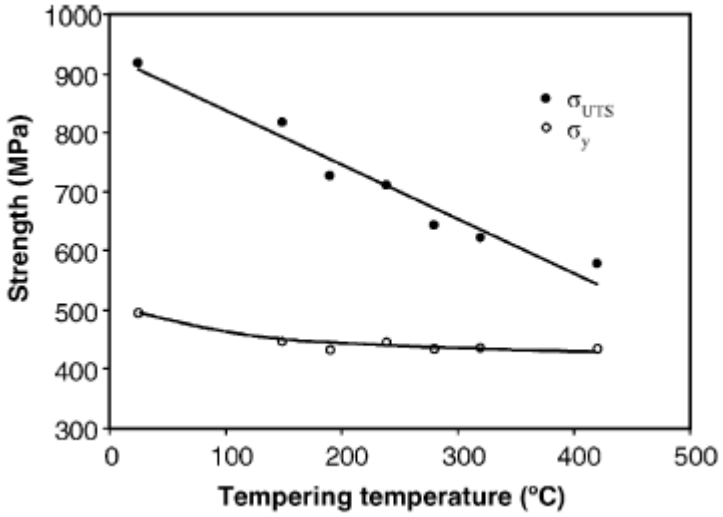

Figure 2.26 The ultimate tensile strength and yield strength of tempered FM steel (0.13 wt.% C) as a function of tempering temperature [63].

2.3 Strengthening mechanisms

Different strengthening mechanisms are commonly used to increase the strength of a material. The following sections will discuss some of these strengthening mechanisms.

2.3.1. Solid solution strengthening

The introduction of solute atoms to occupy the interstitial or substitutional positions in solvent-atom lattice will increase the strength of an alloy. A solid solution is referred to as a substitutional solid solution when both the solvent and solute atoms are of a similar size. In a substitutional solid solution, solute atoms occupy the lattice points within a solvent-lattice structure. A solid solution is referred to as an interstitial solid solution when solute atoms are much smaller than solvent atoms in size and occupy the interstitial positions within a solvent-lattice structure [66]. Common interstitial atoms include carbon, nitrogen, oxygen, hydrogen, and boron. The tendency to form a solid solution increases when a solute and solvent do not have a strong chemical affinity for one another. Otherwise, they will form metallic compounds. Due to differences of shear moduli and size between solute and solvent atoms, a stress field is created around a solute atom. These fields around the solute atoms restrict dislocation motion in a matrix, and consequently, additional stresses are required to overcome these stress fields in order for a dislocation continue moving in the matrix [55].

In steel alloys, although ferrite has limited solubility for carbon, a small amount of carbon (~ 0.1 wt.%) has a significant effect on increasing ferrite strength as shown in Figure 2.27 [67]. Nitrogen also has a similar effect on the yield strength of ferrite.

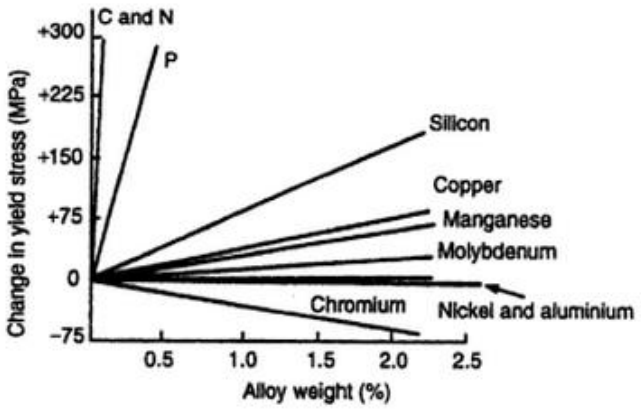

Figure 2.27 Effect of alloying elements on the yield strength of ferrite [67].

When alloying elements such as carbon, nitrogen, silicon, and manganese are introduced in a ferrite matrix to form a solid solution, the lattice parameter of the ferrite increases. The following relation allows for the prediction of carbon concentration in ferrite due to the expansion of the ferrite lattice parameter [68, 69]:

$$X_{\mathrm{C}}(wt.\%) = \frac{(a - 2.8664 + 0.0006 \text{ x } wt.\% \ Si - 0.0006 \text{ x } wt.\% \ Mn)}{0.039} \qquad 2.13$$

where a is the lattice parameter of the ferrite in angstroms. Substitutional solutes such as Si and Mn also have a strong effect on ferrite strength when added in high concentrations, whereas chromium has a weak effect on ferrite strength as shown in Figure 2.28 [70].

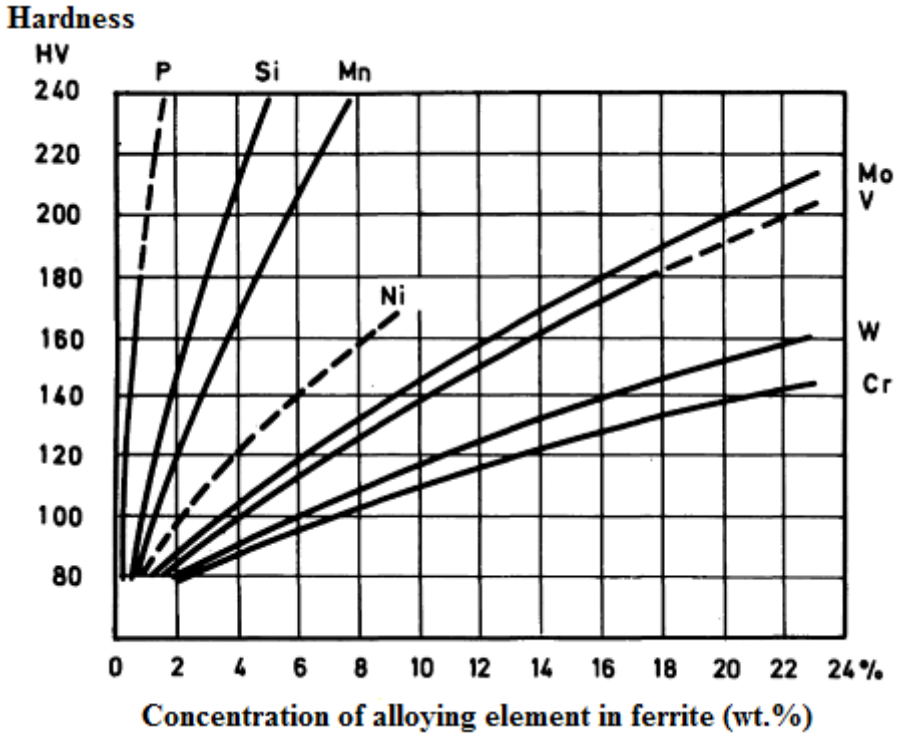

Figure 2.28 Hardness of ferrite (Hv) as a function of alloying element concentrations (wt.%) [70].

The substitutional solute Mn has a similar role to the interstitial solute C in increasing the lattice parameter and strength of ferrite when added to steel alloys. Li et al. [54] studied the effect of Mn on the hardness of ferrite in Fe-Mn alloys with different amounts of Mn. The lattice parameter of the ferrite in the Fe-Mn alloys was found to

increase as the Mn content increases as shown in Figure 2.29 [54]. The authors [54] observed a linear increase in the hardness of the ferrite with the Mn content as shown in Figure 2.30 [54]. The grain size of the ferrite in the Fe-Mn alloys was in the range of 50-300 μm, and hence, the authors hypothesised that the grain boundary strengthening was marginal. The authors ascribed the increase in the hardness to the lattice strain within the ferrite matrix which resulted from the existence of the substitutional solute Mn.

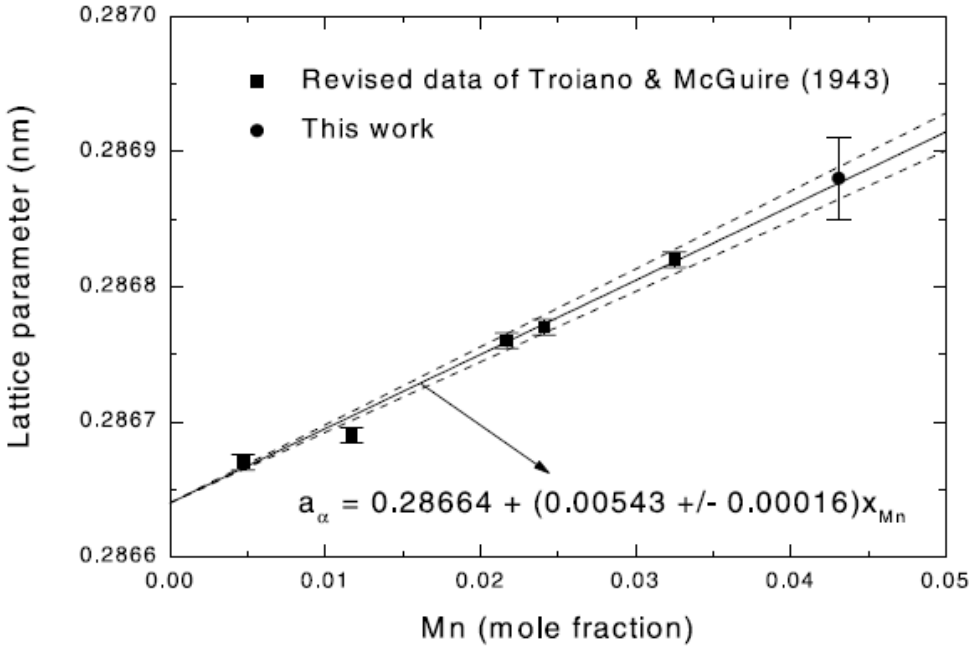

Figure 2.29 The lattice parameter of the ferrite as a function of the Mn content in Fe-Mn alloys. The authors of [54] multiplied the data in [71] by 0.1002056 nm.

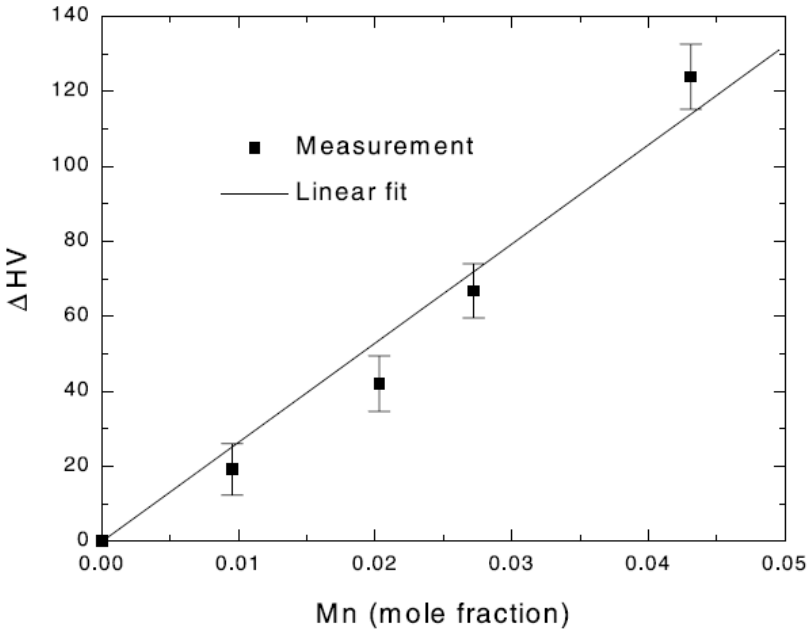

Figure 2.30 Increase in hardness of the ferrite as a function of the Mn content in Fe-Mn alloys [54].

The stress-strain curve of low-carbon steel exhibits a sharp transition from elastic to plastic deformation instead of a continuous transition (Figure 2.31) [72]. In Figure 2.31, the stress gradually increases with the elastic strain until it reaches a sharp transition point (upper yield point). The stress then suddenly drops to a lower point, known as the lower yield point. The material deforms plastically under constant stress which is also referred to as yield-point elongation or Luders extension (Figure 2.31), followed by the flow stress rising and the material work hardening.

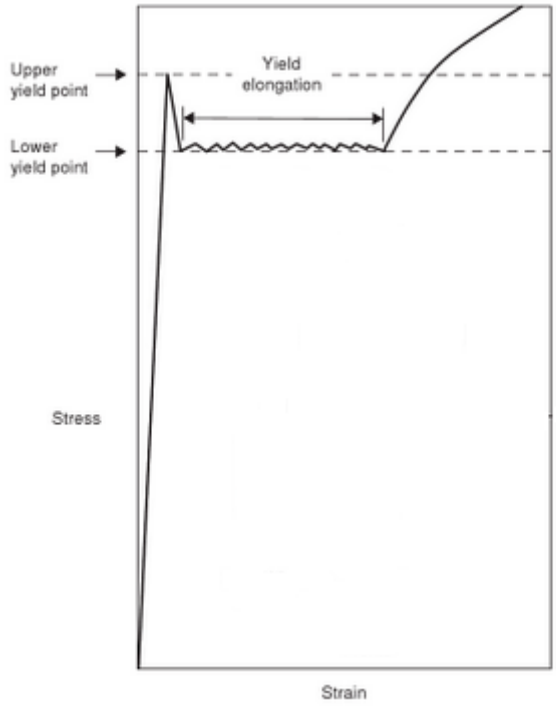

Figure 2.31 Yield-point behaviour in plain carbon steel during tensile test [72].

Cottrell and Bilby [73] proposed the first explanation of the yield-point phenomenon observed in the stress-strain curves of low-carbon steel and other alloys. The authors hypothesised that interstitial solute atoms, such as carbon atoms, diffuse into the cores of dislocations, and consequently, atmospheres around the dislocations are created. Given this situation, dislocations are locked in positions for which high stresses are required to unlock these dislocations which results in the existence of the upper yield point. However, lower stresses are required to move the unlocked dislocations, which results in the existence of a lower yield point [73].

The role of a solid solution in increasing the strength of an alloy has also been observed in nanocrystalline materials. Rupert et al. [74] used sputter deposition to produce nanocrystalline Ni-W alloys. Performing nanoindentation tests on the nanocrystlline Ni-W alloys, they observed that nanohardness increased as the solute content increased from 0 to 20 at.%. When the W content was 20 at.%, nanohardness was found to increase by 3.1 GPa. Furthermore, Matsui et al. [75] used electrodeposition to produce nancrystalline Ni. Matsui et al. [75] studied the effect of interstitial carbon and substitutional sulfur on the strength of the nanocrystalline Ni. The authors found that interstitial carbon produced a large misfit in the Ni matrix while no significant changes were observed for the substitutional sulfur. When the carbon content was at 0.78%, the strength due to the interstitial solid solution was estimated to be 0.42 GPa.

During large plastic deformation, the interstitial solid solution could be formed in the matrix. Hono et al. [76] and Lojkowski et al. [77] observed cementite dissolution and the formation of interstitial solid solution in a ferrite matrix during the cold-drawing and heavy plastic deformation of pearlitic steel at the wheel-rail contact surface, respectively.

2.3.2. Strengthening due to grain size reduction and dislocation density

Following the Hall-Petch relation [35, 36], Equation 2.7, several models have been proposed to explain the linear relationship between stress and the reciprocal of the square root of grain size (d). These models will be briefly discussed.

2.3.2.1. Pile-up model

In this model, the grain centre of a given grain is considered to be the dislocation source that generates dislocations and sends them out to pile-up at the grain boundary as shown in Figure 2.32a. After the piling-up of a number N_{Dis} of dislocations at the grain boundary, stress concentrations build up at the head of the dislocation pile-up. These stress concentrations are a function of the dislocation number N_{Dis} in the pile-up. The stress at the head of a pile-up must exceed a certain critical shear stress τ_{c} in order for a slip to continue past the grain boundary. It is important to note that the larger the grain size, the larger the number of dislocations that can be accommodated. Hence, the larger the grain size is, the larger stress or shear stress at the tip of the pile-up. Thus, it can be concluded that the larger the grain size, the quicker and easier yielding can occur [55, 66]. Eshelby et al. [78] estimate the shear stress at a head of the pile-up (τ_{p}) as follows:

$$\tau_{\mathrm{p}} = N_{\mathrm{Dis}}\tau_{\mathrm{e}} \qquad 2.14$$

where τ_{e} is the effective shear stress. Cottrell [79] hypothesises that a dislocation source is activated in an adjacent grain when the critical shear stress is exceeded at the head of the pile-up.

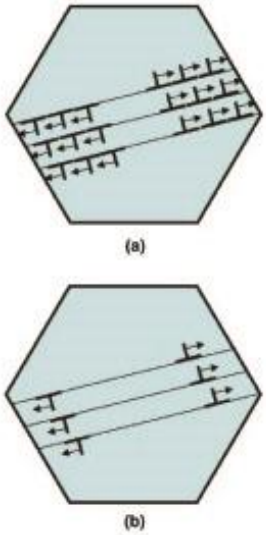

Figure 2.32 Schematic illustration of dislocation pile-up in (a) coarse grain and (b) nanocrystalline material [80].

2.3.2.2. Dislocation density model

In this model, a linear relationship between stress and the square root of dislocation density, ρ, is considered. Ashby [81] proposes that strengthening due to dislocation involves two distinct kinds of dislocations: statistically stored dislocations (SSDs) and geometrically necessary dislocations (GNDs). SSDs are created by uniform deformation (Figure 2.33a) and they trap each other, which results in hardening of a material. Furthermore, voids and overlaps are created between adjacent grains as shown in Figure 2.33b. Ashby [81] also hypothesises that inhomogeneous strains are created between adjacent grains (also called strain gradients) which result in the generation of GNDs. GNDs eliminate voids and correct overlaps to reproduce fitted and continuous grains as shown in Figure 2.33c and Figure 2.33d.

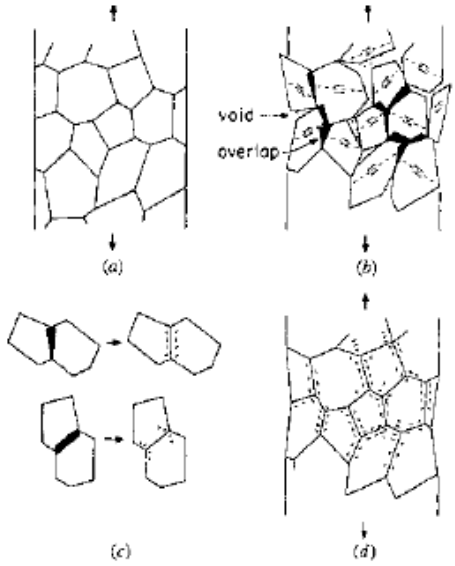

Figure 2.33 Ashby's model: (a) uniform deformation of polycrystal (b) generation of voids and overlaps (c and d) correction of voids and overlaps by introducing the GNDs. SSDs are not shown [81].

2.3.2.3. Composite flow stress model

Meyers and Ashworth [82] developed this important model (later known as the core and mantle model) to express the flow stress of a material. They ascribe the existence of incompatibility between each adjacent grain in a material to the elastic anisotropy. This incompatibility plus shear strain resulting from applied stress during deformation generate GNDs at grain boundaries. A composite-like microstructure comprising a continuous network of a work-hardened layer of grain boundaries and discontinuous islands of soft bulk material is formed. The flow stress of a composite material (σ_c) can be described as follows [82]:

$$\sigma_c = A_B\sigma_B + A_{GB}\sigma_{GB} \qquad 2.15$$

where A_B and A_{GB} are the area fractions of the bulk material and the grain boundary layer, respectively, and σ_B and σ_{GB} are the flow stresses of the bulk material and the grain boundary layer, respectively. The fraction of the area of the work-hardened grain boundary layer increases as grain size decreases as shown in Figure 2.34b. Hence the second term on the right side of Equation 2.15 will dominate. The core and mantle

model proposed by Meyers and Ashworth [82] was later extended to the investigation of nanocrystalline materials as low dislocation densities within the grain interior (core) and high dislocation densities at the grain boundary (mantle) were observed in such materials.

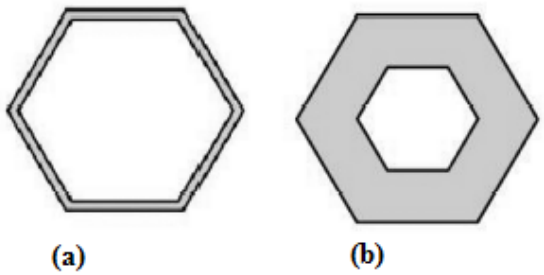

Figure 2.34 Schematic illustration showing the mantle and core model in (a) coarse grain and (b) fine grain materials [80].

When the grain size decreases below a critical size, according to the pile-up model, dislocation pile-up becomes very difficult and may contain only one dislocation as shown in Figure 2.32b. The Hall-Petch relation has been found to be applicable to predict the strength of a material when the grain size is greater than 100 nm. Valiev et al. [13] produced Armco iron with a grain size of 100 nm using HPT. Valiev et al. [13] applied the Hall-Petch relation to predict the yield strength of the Armco iron from its grain size and found it to be very close to the measured strength. The authors therefore concluded that the Hall-Petch relation is applicable down to a grain size of 100 nm. Based on the experimental data in the literature, Morris and Morris [83] claim that the classical theory behind the Hall-Petch effect (i.e. the pile-up or core-mantle theory) can be applied even to materials with grain sizes of 50 nm. When the grain size drops below 25 nm, however, strength generally does not follow a Hall-Petch relation with no increase in yield strength observed [84]. This phenomenon is often referred to as the inverse Hall-Petch effect. The mechanisms behind the inverse Hall-Petch effect will not be discussed here, as it is beyond the scope of the current study.

The hardness against the inverse of the square root of the grain size of steels with different grain sizes are plotted in Figure 2.35 [85]. In general, the steels in Figure 2.35 are produced by powder milling and grouped into coarse and ultrafine grain groups. It can be seen from Figure 2.35 that the Hall-Petch effect extends from coarse grain to very fine grain (which is roughly 5-6 nm).The ultrafine grain group, however, has a Hall-Petch slope lower than that of the coarse grain group.

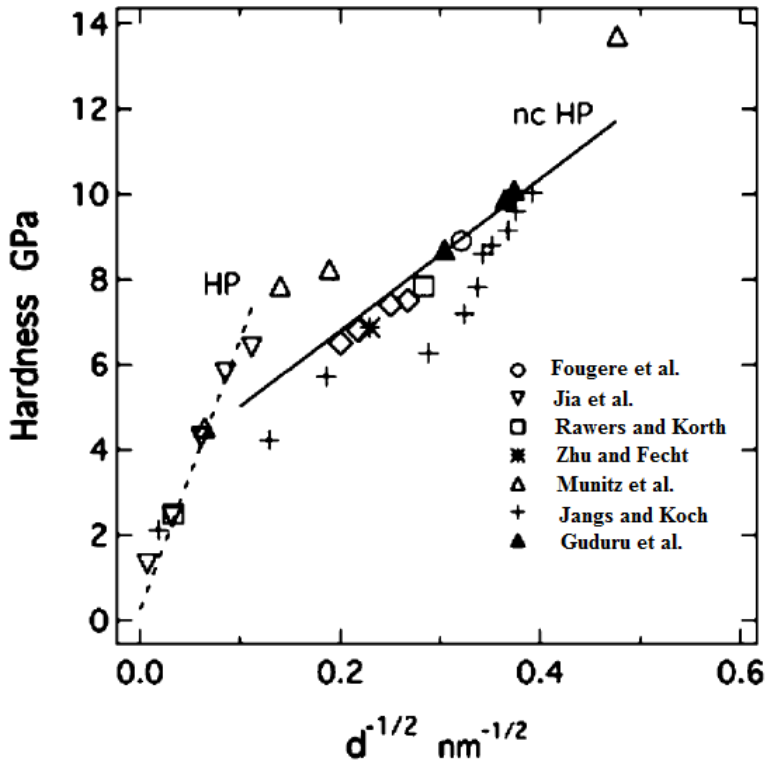

Figure 2.35 Representation of the Hall-Petch relation in milled steels [85-91]. This figure is adapted from [85].

In general, interstitial solute affects the Hall-Petch parameters and particularly the slope *k*. Takeda et al. [92] measured the yield stress of pure iron with different amount of interstitial solute, such as carbon and nitrogen, during tensile tests. The study also included interstitial free steel. The authors plotted the yield stresses vs. the inverse of the square root of the grain sizes of these irons as shown in Figure 2.36. The Hall-Petch slope (*k*) can be seen to increase as the carbon content increases (Figure 2.36a), though there is little increase in this regard when the nitrogen content increases (Figure 2.36b).

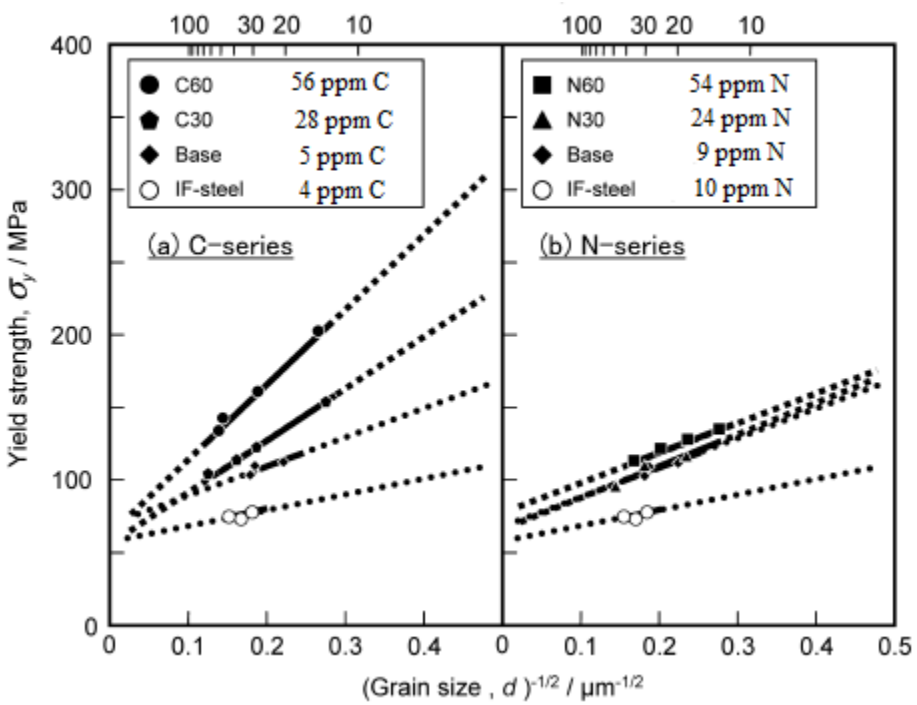

Figure 2.36 Representation of Hall-Petch relation in (a) carbon group and (b) nitrogen group [92].

During the SPD process, large strain is imposed on the sample leading to structural refinement in the submicron or nanometer range. In most metals, dislocation cells and cell blocks are formed at low strain. These cell blocks have thick walls and low misorientations. With increasing strain, these cells are refined and wall thickness is reduced, which is accompanied by an increase in misorientation. At high strain, the majority of the formed substructures at the initial stage of deformation are transformed into equi-axed ultrafine grains with high misorientation and non-equilibrium boundaries [13, 17, 93].

A review of the literature revealed that three main approaches have been developed for studying the strength of a material. These are briefly described below.

The first approach: researchers who have followed this approach consider grain size reduction to be the dominant contributor to the strength of a material. Valiev et al. [13] attributed the high strength of ultrafine-grained Armco iron processed by HPT up to five turns to grain size reduction (Section 2.3.2.3). Valiev et al. [13] found that the Hall-Petch relation can still be used even when the grain size reaches 100 nm. Lesuer et al. [94] ball milled ferrous-based alloys for short periods of time and found nano-scale subgrains to develop during the milling process. These subgrains were preserved during the subsequent consolidation and warm working. Lesuer et al. [94] observed that yield

strength is a function of the reciprocal of subgrain size. This dependency, however, breaks down at sub-grain size of 150 nm.

The second approach: researchers of this approach consider both grain size reduction and dislocation density to contribute to the strength of a material. Hansen [95] studied the flow stress of polycrystalline metals (Ni) during tensile test. Hansen estimated the dislocation density as $\sim 1.5S_{\mathrm{v}}\Phi/b$ where S_{v} is the area of boundaries per unit volume and Φ is the misorientation angle. Based on this approximation and taking into account that the majority of the low-angle grain boundary (LAGB) evolved into high-angle grain boundaries (HAGB) at large strain, Hansen [95] derived the following expression for flow stress at a certain strain $\sigma(\varepsilon)$:

$$\sigma(\varepsilon) = \sigma_{\mathrm{o}} + \mu M G\sqrt{1.5b(S_{\mathrm{v}}\theta)_{\mathrm{LAGB}}} + k(\varepsilon)D_{\mathrm{HAGB}}^{-1/2} \qquad 2.16$$

Where μ is constant, M is the Taylor factor, G is the shear modulus, b is the Burgers vector, $k(\varepsilon)$ is constant at the certain strain, and D_{HAGB} is the average size of grains with high misorientation. Similarly, Qiao et al. [93] proposed a model that involves grain boundary and dislocation strengthening.

Kamikawa et al. [96] investigated strengthening mechanisms when processing pure Al by ARB up to six cycles. The authors observed that not only a grain boundary strengthening mechanism took place during the ARB process but other mechanisms, such as dislocation strengthening, did as well. Their transmission electron microscopy (TEM) and electron back scatter diffraction (EBSD) investigation revealed the existence of different microstructural elements which were accounted for in studying the strength of the ARB-processed sample. These structural elements were: (a) high-angle grain boundaries (>15°) of the grain size D_{HAGB} and their contribution to strengthening will be calculated as Hall-Petch strengthening, (b) dislocation cell boundaries of low angle misorientation (≤2°) and their strengthening contribution will be proportional to the square root of the dislocation density ρ_{cells}, (c) the remaining dislocation boundaries will be treated as high angle grain boundaries, and (d) dislocations exist between grain boundaries and their strengthening contribution will be proportional to the square root of their density, ρ. The authors derived the following expression for yield strength (σ_{y}):

$$\sigma_{\mathrm{y}} = \sigma_{\mathrm{o}} + kD_{\mathrm{HAGB}}^{-1/2} + \mu M G b\sqrt{\rho + \rho_{\mathrm{cells}}} \qquad 2.17$$

The third approach: the researches who follow this approach hypothesise dislocation strengthening to be the main contributor to the strength of a material, with the Taylor relation (Equation 2.18) commonly being used to predict strength. Gubicza et al. [97] attributed the high strength of pure Al, Al1Mg, and Al3Mg alloys processed by ECAP up to eight passes to dislocation density which was measured using X-ray diffraction (XRD) line broadening. Gubicza et al. [97] found the strength values measured in their mechanical tests are in good agreement with those calculated using the Taylor equation:

$$\sigma = \sigma_o + \mu M G b \rho^{1/2} \qquad 2.18$$

Karlsson and Linden [49] conducted an extensive study on FP steel (0.2 wt.% C) and concluded that the yield strength of FP steel is nearly the same as that of a ferrite matrix. The flow stress of the investigated FP steel can be described by a rule of mixture if the flow stresses of the ferrite and pearlite are known. Importantly, Karlsson and Linden [49] looked at the dislocation density as the main strengthening contributor to the yield strength of the ferrite and used the Taylor relation (Equation 2.18) to calculate the ferrite's yield strength. Dingley and McLean [98] conducted a tensile test on pure iron (99.97%) and claimed the flow stress of the pure iron tensile tested to be a function of dislocation density independent of grain size. Malik and Lund [99] predicted the yield strength of martensitic steel (0.4 wt.% C) tempered at different temperatures in relation to dislocation density while taking into account Orowan strengthening as well. Sarkar et al. [100] processed an interstitial-free (IF) steel (0.0027 wt.% C) by ECAP up to 4 passes using rout A. Sarkar et al. [100] calculated the dislocation density of the ECA-pressed sample using XRD. The authors predicted the strength of the ECA-pressed sample using the Taylor relation (Equation 2.18), which depends mainly on dislocation density, and found a good agreement between the predicted and the measured strength.

2.3.3. Strengthening due to second-phase particles

The strength of a material increases when its dislocation motion is impeded by obstacles, such as grain boundaries, immobile dislocations, or second phase particles. Second phase particles come in different forms, such as precipitates that are formed during the ageing process, carbides or nitrides, or inclusions. There are two factors that affect strengthening due to precipitation: particle size (d_{part}) and interparticle spacing (D). The nature of the particle/matrix interface can be coherent, semi-coherent, or

incoherent. Coherent precipitates are weak precipitates in nature, whereas incoherent precipitates are strong. A moving dislocation cuts through weak particles, which results in the creation of new particle/matrix interfaces. In contrast, when a dislocation moves in its slip plane and encounters two particles with interparticle spacing *D*, the dislocation will bow as shown in Figure 2.37. The dislocation will then continue moving forward until it reaches a critical curvature. When the critical shear stress is exceeded, the dislocation becomes unstable and will expand to leave a loop around the particles which is known as an Orowan loop [101]. On the other side of the particles, the two segments of the dislocation have opposite signs and annihilate each other, while the original dislocation will continue moving forward. The number of loops increases as more dislocations are encountered by the original Orowan loops, resulting in more resistance to the dislocation motion [66].

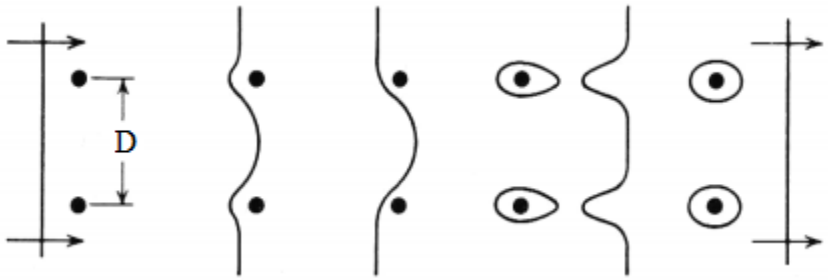

Figure 2.37 Schematic illustration showing the different stages of the Orowan loop mechanism [66].

Several versions of the Orowan equation have been developed to predict increments of strength due to precipitation or particle strengthening ($\Delta\sigma_{\text{part}}$) [102-104]. Kelly and Nicholson [104] restated the Orowan relations to have the following form:

$$\Delta\sigma_{\text{part}} = \frac{\phi G b}{\pi D} ln \frac{D}{2b} \qquad 2.19$$

And

$$\phi = \frac{1}{2}\left[1 + \frac{1}{1-\gamma_{\text{PR}}}\right] \qquad 2.20$$

where γ_{PR} is the Poisson's ratio of the matrix (for steel, γ_{PR}=0.33 [66]) and D is the edge-to-edge spacing of the nearest adjacent particles in a slip plane, which can be determined by the following relation [103]:

$$D = \left(\left(\frac{2\pi}{3f_{\text{part}}} \right)^{1/2} - \left(\frac{8}{3} \right)^{1/2} \right) . \frac{d_{\text{part}}}{2} \qquad 2.21$$

where d_{part} and f_{part} is the diameter and volume fraction of the second phase particles, respectively. Fullman [102] suggested the following relation to predict the free mean path (λ_{part}) of the second phase particles:

$$\lambda_{\text{part}} = \frac{1 - f_{\text{part}}}{N_{\text{L}}} \qquad 2.22$$

where N_{L} is the number of particles intercepted per unit length of a test line. Baldwin and Edelson [105] used the mean free path (λ_{part}) and the volume fraction of the second phase particles (f_{part}) to predict the diameter of the second phase particle (d_{part}) as follows:

$$d_{\text{part}} = \frac{3f_{part}\lambda_{\text{part}}}{2(1 - f_{\text{part}})} \qquad 2.23$$

Few studies exist in the literature investigating the effect of the second-phase particles on the strength of SPD-processed materials. Strengthening caused by the presence of second-phase particles in UFG or nanocrystalline materials occurs in a similar manner to conventional coarse-grained materials, where these particles impede the motions of dislocations. Moon et al. [106] studied the Orowan strengthening in four carbon steel alloys denoted as A, B, C, and D. Both alloy A and B contained carbon content of 0.1 and 0.15 wt.% with no alloying element. Alloy C contained Ti, while alloy D contained Ti and Nb. Moon et al. [106] studied the microstructure using TEM and energy dispersive spectroscopy (EDS) and found that alloy C contained TiN, whereas alloy D contained TiN, TiC, NbN, and NbC particles. The authors measured the

interparticle spacing of the particles and found that alloy D had smaller interparticle spacing. They measured the nanohardness of the investigated carbon steel alloys A-D using nanoindenation technique. The nanohardness value of D was the highest value measured, whereas alloys A and B had the lowest nanohardness values. The authors attributed the highest nanohardness values measured for alloy C and D to the Orowan strengthening resulting from the nitride and carbide particles of these alloys. Furthermore, alloy D was found to have a higher nanohardness value than C, which was ascribed to the lower value of the interparticle spacing of particles in alloy D.

Zhao et al. [107] studied the effect of second-phase particles (precipitates) on the strength of an Al-7075 alloy processed by cryogenic rolling and aged at a low temperature. After cryogenic rolling, a nanostructure (NS) had formed with an average size of 100 nm, whereas the formation of coherent, semi-coherent, and non-coherent precipitates took place after the ageing process and this nanostructure was denoted as (NS+P). The presence of the precipitates improved both the yield and tensile strength of the aged alloy as shown in Figure 2.38. Furthermore, the uniform elongation of the aged alloy increased by more than twice compared to the as-rolled sample. The authors ascribed the high strength and improved uniform elongation obtained in the NS+P case to the presence of the precipitates.

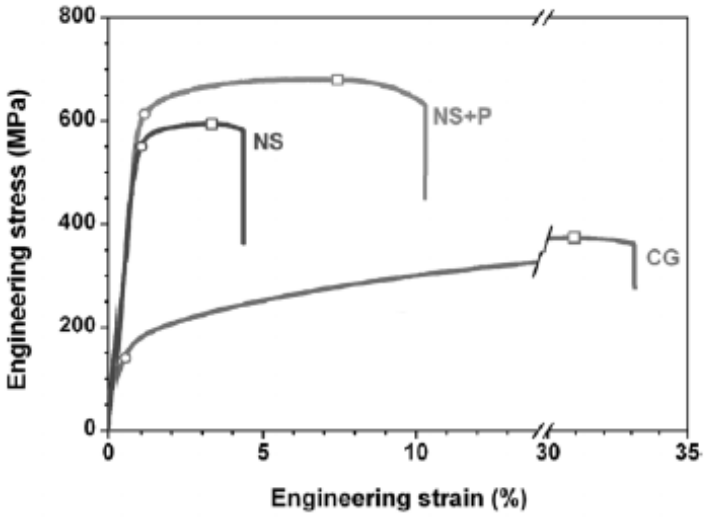

Figure 2.38 The engineering stress-strain curve of Al-7075 cryogenically rolled and aged at a low temperature [107].

Zimmerman et al. [108] studied the effect of the second-phase particles on the strength of Ni-SiC composite. The authors produced a nanocrystalline Ni matrix

reinforced by second-phase particles (SiC) by pulse electrodeposition. The formed nanocrystalline Ni matrix had a grain size of 10-15 nm, while the second-phase particles had an average size of 0.4 μm. The authors observed an improvement in the microhardness of the nanocomposite Ni-SiC material compared to the conventional Ni-SiC material with coarse grains. The tensile test also revealed an increase in tensile strength of the nanocrystalline Ni-SiC composite which can reach a value that is twice as much as the strength of the conventional Ni-SiC composite. The ductility of the nanocrystalline Ni-SiC composite also improved when compared to the ductility of the coarse-grained pure Ni. However, both the strength and ductility of the nanocrystalline Ni-SiC composite began to decrease when the volume fraction of the second-phase particles (SiC particles) was more than 2%.

Moriss and Moriss [83] used the Orowan looping mechanism to study strengthening due to second phase particles in a copper matrix. Figure 2.39 shows the Orowan loops surrounding the second phase particles embedded in the copper matrix [83]. The authors claimed that below a particle size of 20 nm, dominant strengthening was due to second phase particles, while strengthening due to grain size was less important. The authors also observed that the strengthening due to the second phase particles tended to be slow as the particle size became very fine, which they attributed to the possible shearing of particles.

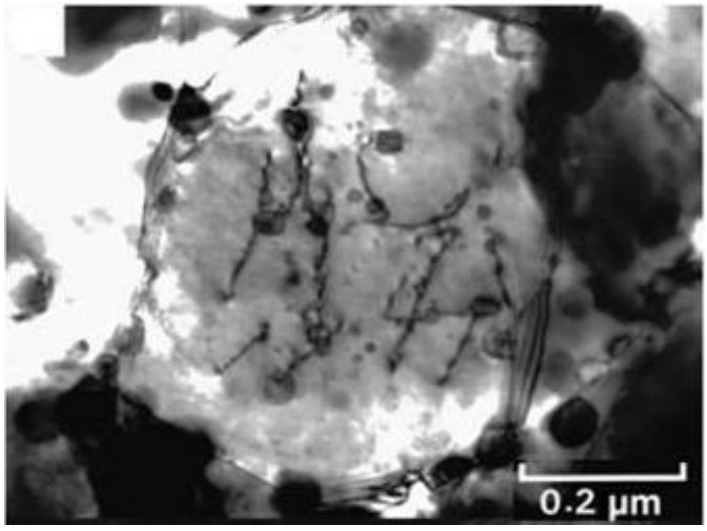

Figure 2.39 TEM bright-field image showing the microstructure of a Cu matrix with embedded second phase particles [83].

2.4 Severe plastic deformation of steel

2.4.1. Severe plastic deformation of ferritic-pearlitic steel

During the SPD processing of FP steels, the ferrite grains are deformed and the original grains are subdivided into subgrains with low misorientation. The newly formed subgrains decrease in size and higher misorientation evolves with further strain and finally the formation of well equi-axed ultrafine grains with high misorientation takes place at high strain [13, 109]. Park et al. [110] observed the evolution of fairly equi-axed ferrite grains with an average grain size of ~ 0.2 μm, as shown in Figure 2.40, when processing low-carbon steel (0.15 wt.% C) by ECAP up to 4 passes using route C. Fukuda et al. [109] observed the formation of an array of subgrains with low misorientation in low carbon-steel (0.08 wt.% C) after 1 and 2 passes of ECAP processing using route C. After 3 passes of the ECAP process, Fukuda et al. [109] observed the evolution of equi-axed grains with high misorientation and the microstructure becoming homogeneous. In contrast, Wang et al. [37] observed the evolution of parallel bands of elongated ferrite grains, as shown in Figure 2.41, when processing low-carbon steel (0.15 wt.% C) by ECAP up to 10 passes using route C.

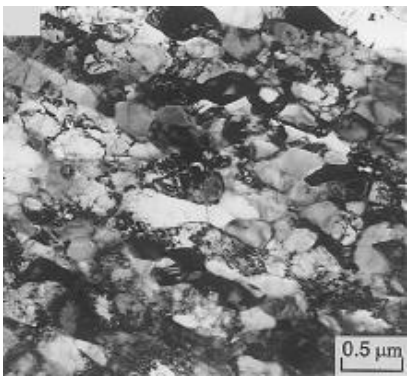

Figure 2.40 TEM bright-field image showing the microstructure of low-carbon steel (0.15 wt.% C) after 4 passes of ECAP processing using route C [110].

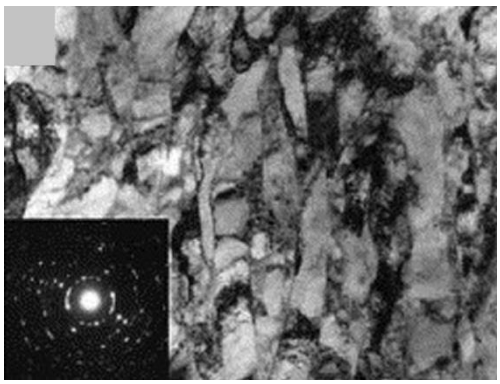

Figure 2.41 TEM bright-field image showing the microstructure of low-carbon steel (0.15 wt.% C) after 10 passes of ECAP processing using route C [37].

Dobatkin et al. [111] produced a nanocrystalline structure with a mean size of ~ 95 nm when processing low-carbon steel, 10G2FT, by HPT up to 5 turns. The pearlite colonies were elongated and thinned at low strain. It is important to note that during

pearlite thinning, both the cementite thickness and the interlamellar spacing were reduced. Further thinning and fragmentation of cementite occurred as the strain increases [112]. Partial or complete dissolution of the cementite took place at higher strain as reported by several researchers [39, 113-115].

2.4.2. The strength of ferritic-pearlitic steel processed by SPD

The high strength of SPD-processed materials is documented in the literature. FP steel processed by SPD exhibited high strength which can be mainly attributed to the formation of high dislocation density in addition to the reduction of the lamellae spacing in the pearlite. Wang et al. [37] conducted a tensile test on low-carbon steel (0.15 wt.% C) processed by ECAP up to 4, 6, and 10 passes. The tensile test results are depicted in Figure 2.42. It can be seen from Figure 2.42 that both the yield and ultimate tensile strength increases with the number of passes, and both surpass 1200 MPa after 10 passes. However, the elongation to failure decreases drastically after 4 passes and then increases again after 6 and 10 passes. Park et al. [110] investigated the tensile test characteristics of FP steel (0.15 wt.% C) processed by ECAP up to 4 passes and observed significant increases in both the yield and tensile strength after 4 passes but no strain hardening was observed during the tensile test. Fukuda et al. [109] studied the tensile test characteristics of low-carbon steel (0.08 wt.% C) processed by ECAP up to 3 passes and observed an increase in the ultimate tensile stress, greater than 800 MPa after 3 passes, and a significant increase in the yield strength after 1 pass only but the yield strength remained constant with further straining as shown in Figure 2.43. Fukuda et al. [109] compared their tensile test results with results from the literature where low-carbon steels were ECAP-processed [110, 116]. The elongation to failure in Fukuda et al.'s [109] study is larger than those obtained by other researchers. The authors ascribed the higher elongation to failure they obtained to the strain path, route B_C, used during the ECAP processing.

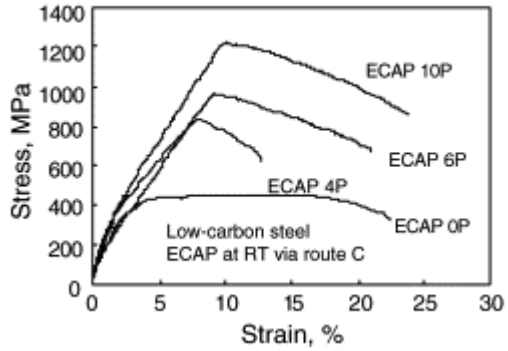

Figure 2.42 Stress-strain curves of low-carbon steel (0.15 wt.% C) samples processed by ECAP up to 4, 6, and 10 passes via route C [37].

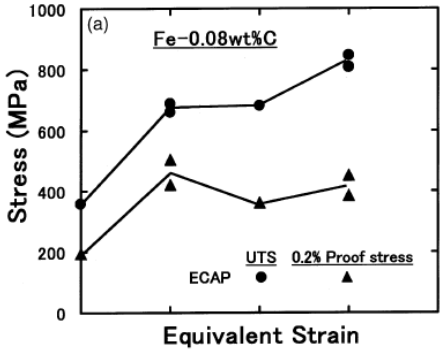

Figure 2.43 A plot of 0.2 proof stress and ultimate tensile stress vs. the equivalent strain of low-carbon steel (0.08 wt.% C) processed by ECAP up to 3 passes [109].

Park et al. [38] studied the tensile characteristics of two low-carbon steel samples: one with vanadium (CSV) while the second without vanadium (CS). Park et al. [38] processed the two samples by ECAP up to 4 passes at 623^{o}K using route C. Tensile tests were conducted on both samples and the results are depicted in Figure 2.44. The yield and tensile strength of the sample with vanadium (CSV) were higher than those of the sample without vanadium (Figure 2.44). Moreover, the elongation to failure of the sample with vanadium (CSV) is larger than that of the sample without vanadium (CS). The authors attributed the high dislocation density observed in the microstructure of the CSV sample after ECAP processing to the existence of the vanadium. These dislocations facilitate the diffusion of the dissolved carbon atoms since they act as easy and open channels and hence nano-sized cementite particles are formed and uniformly distributed along the ferrite grain boundaries. The vanadium plays another important role during the ECAP process; it aids retarding the grain growth of the ferrite grains and hence smaller ferrite grains were obtained. The authors attributed the improved tensile test characteristics (Figure 2.44) to the unique microstructure of the CSV processed sample.

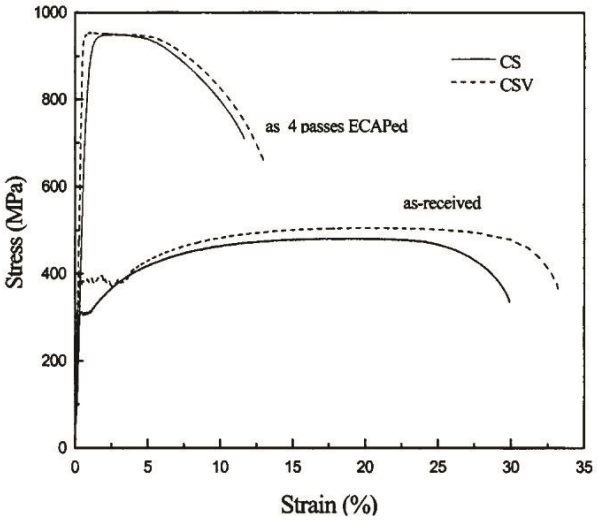

Figure 2.44 Stress-strain curves of low-carbon steels with vanadium (CSV) and without vanadium (CS) processed by ECAP up to 4 passes [38].

Dobatkin et al. [111] found out that the microhardness of the low-carbon steel sample, mentioned in Section 2.4.1, has increased by 3 times when processed at the ferritic-pearlitic initial state. Bayramoglu et al. [117] conducted a microhardness test on a low-carbon steel (0.17 wt.% C) sample processed by HPT up to 1, 3, 5, and 6 turns at 300^{o}C. Bayramoglu et al. [117] observed an increase in the microhardness as the number of turns increased; this increase continued until the fifth turn. After 6 turns, a reduction in the microhardness was observed and they ascribed this reduction to the dynamic recovery during the HPT processing at 300^{o}C. Zrnik et al. [39]successfully conducted both hardness and direct tensile tests on medium-carbon steel (0.45 wt.% C) processed by HPT up to 6 turns at 400^{o}C. Zrnik et al. [39] observed a significant increase in the microhardness after 6 turns of HPT processing; however, softening was observed after the fourth turn. The authors attributed the softening to the dynamic recovery. Furthermore, an inhomogeneous microstructure and microhardness were observed regardless of the number of turns. The authors observed that the tensile strength increased with the number of turns as shown in Figure 2.45. After 6 turns, the tensile stress reached a value higher than 1700 MPa.

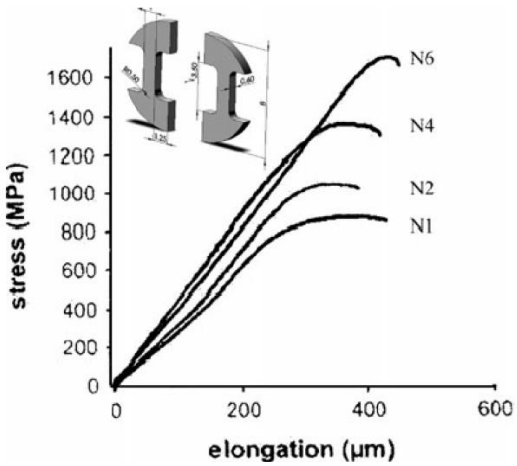

Figure 2.45 Stress vs. elongation of medium-carbon steel (0.45 wt.% C) processed by HPT up to 6 turns at 400°C [39].

Ivanisenko et al. [115] measured the microhardness at a distance of 3 mm from the centre of a pearlitic steel sample (0.6-0.8 wt.% C) processed by HPT up to 7 turns and found it to be ~ 11 GPa. Cardona et al. [118] processed a low-carbon triple-alloyed steel (0.2 wt.% C) by HPT up to 5 turns under a pressure of 6 GPa at room temperature. The authors recorded a microhardness of 400 and 620 Hv at the centre and the edge of the sample processed up to 5 turns, respectively, as shown in Figure 2.46. After 5 turns of HPT processing, the microhardness distribution is still inhomogeneous across the disk and the authors suggested that higher pressure or higher number of turns is required in order to achieve homogenous microstructure and microhardness across the disk.

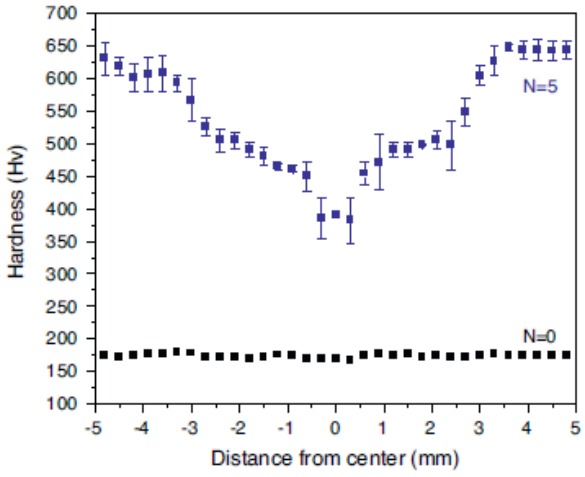

Figure 2.46 The microhardness (Hv) of the low-carbon triple-alloyed steel processed by HPT up to 5 turns vs. the distance from the centre [118].

2.4.3. Severe plastic deformation of ferritic-martensitic steel

Few studies have been conducted to study SPD processing of FM steels. It is well-known that SPD is very effective in reducing the grain size of most metals and alloys and this includes FM steels. Grain refinement takes place on both the ferrite phase and the martensite particles. Two approaches were developed using SPD to produce UFG FM steel. One approach involves processing FP steel by SPD, or thermomechanical processing, to obtain UFG ferrite with fine or spherodized cementite, intercritical annealing for short time (~ 10 min), and quenching to room temperature. The second approach relies on processing low-carbon steel in its FM initial state by SPD to obtain UFG FM steel. Calcagnotto et al. [119] used the first approach to produce UFG FM steel by deforming FP steel samples at different temperatures, 550^{o}C and 700^{o}C, followed by intercritical annealing at 730^{o}C for 3 min. Following this approach, Calcagnotto et al. [119] successfully produced fine grained (FG), 2.4 μm, and UFG, 1.2 μm, FM steel as shown in Figure 2.47. Similarly, Son et al. [120] successfully obtained UFG FM steel using the first approach when processing low-carbon steel by ECAP at 500^{o}C up to 4 passes followed by intercritical annealing at 730^{o}C for 10 min. After ECAP processing, a ferrite grain size ~ 0.2-0.5 μm with high dislocation density while cementite thinning and some kind of spheroidisation were observed in the pearlite. After the intercritical annealing, the ferrite and the martensite had a grain size of 1 μm as shown in Figure 2.48.

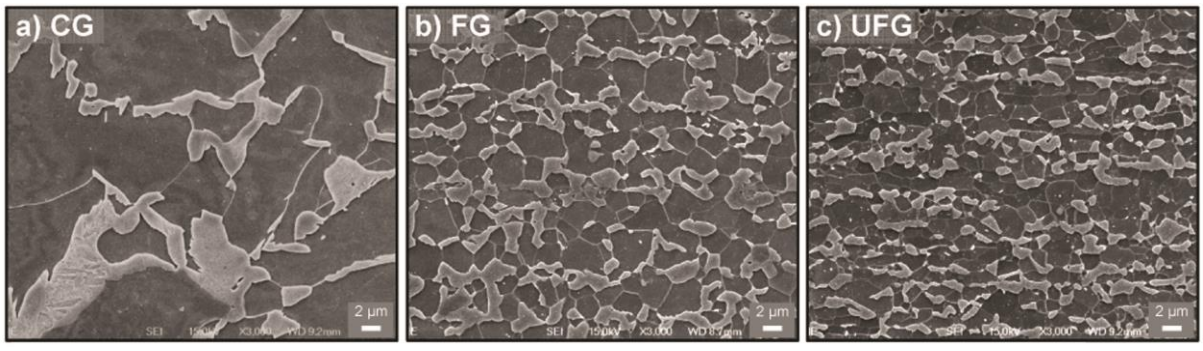

Figure 2.47 SEM images showing the microstructure of (a) coarse grain (b) fine grain and (c) ultrafine grain FM steel [119].

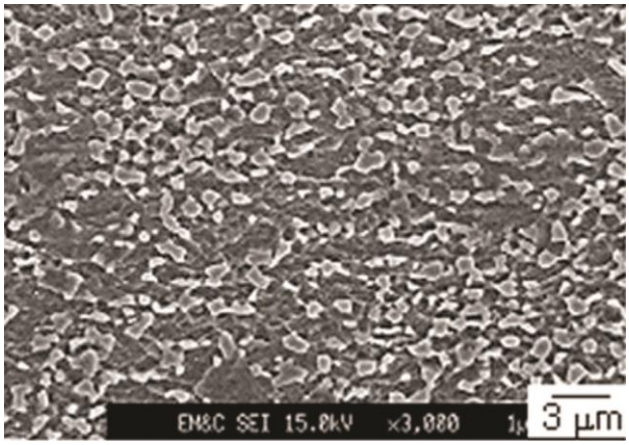

Figure 2.48 SEM image showing the microstructure of low-carbon steel (0.15 wt.% C) processed by ECAP at 500°C up to 4 passes and annealed at 730°C for 10 min [120].

Dobatkin et al. [111] used the second approach to achieve grain refinement in FM steel by processing two low-carbon steel samples, 09G2S and 10G2FT, in their ferritic-martensitic initial state by HPT up to 5 turns at 20°C. Dobatkin et al. [111] obtained a nanocrystalline structure of ~ 65 nm in the case of 10G2FT and even smaller in the case of 09G2S. The microstructure was characterised by the presence of oriented cellular nanostructures with individual equi-axed nano-grains.

2.4.4. The strength of ferritic-martensitic steel processed by SPD

Coarse-grained FM steel is characterised by a high stress rate at the initial stage of the deformation and relatively high uniform elongation. The ability of SPD to produce UFG FM steel with similar tensile characteristics as those of coarse-grained FM steel counterparts was investigated by several researchers. Calcagnotto et al. [119] conducted a tensile test on two materials, FG and UFG FM samples, mentioned in Section 2.4.3. The corresponding stress-strain curve is depicted in Figure 2.49. Surprisingly, the stress-strain curves of the fine and ultrafine grained FM steels still have the same tensile characteristics as those of the coarse grained FM steels: continuous yielding and high initial strain hardening rate. Also, there is a significant increase in the yield and tensile strength of the fine and ultrafine grained FM steel samples.

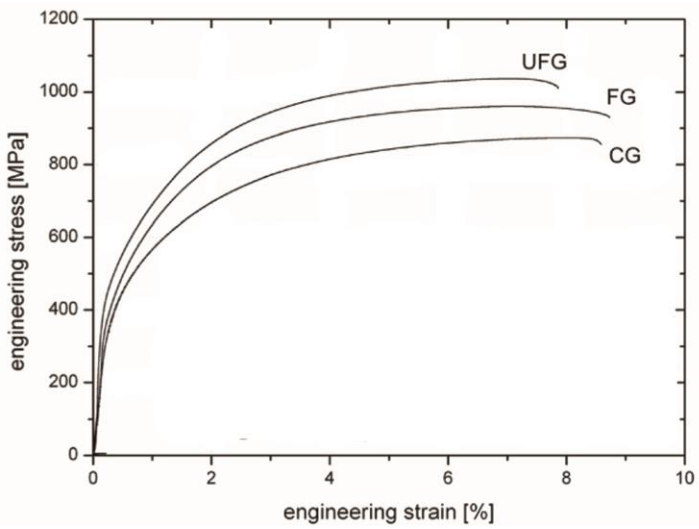

Figure 2.49 Stress-strain curve of coarse grained (CG), fine grained (FG), and ultrafine grained (UFG) FM steel (0.17 wt.% C) [119].

Similarly, ultrafine-grained FM steels containing different amounts of vanadium processed by ECAP up to 4 passes exihibited different stress-strain behavior than the SPD-processed materials [120]. The stress-strain curve of the ultrafine grained FM steel, in Son et al.'s [120] investigation, was characterised by high strain hardening rate at the initial stage of the deformation which is similar to the behavior of coarse-grained FM steel as shown in Figure 2.50. Furthermore, ultrafine-grained FM steel tends to exihibit elongation to failure similar to its coarse-grained dual phase steel counterpart.

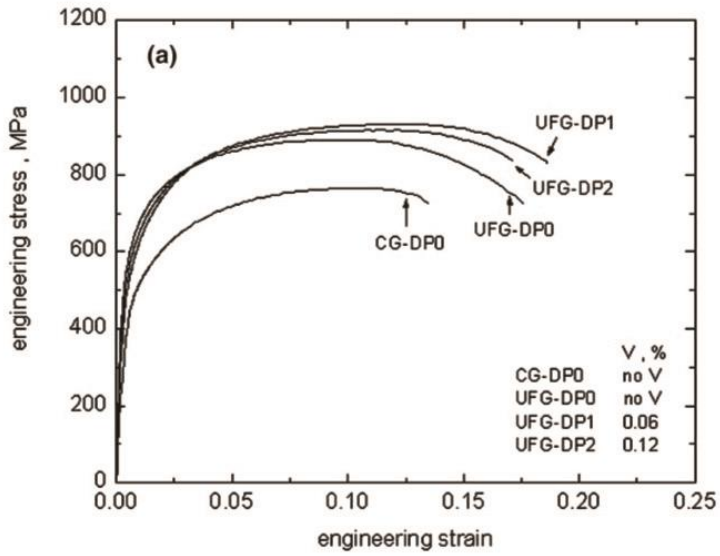

Figure 2.50 Engineering stress-strain curve of FM (or dual-phase) steel containing different amounts of vanadium [120].

Dobatkin et al. [111] conducted a microhardness test on two low-carbon FM steel samples, 09G2S and 10G2FT, processed by HPT at room temperature up to 5 turns. Dobatkin et al. [111] found that the microhardness of the two FM samples has increased by 1.5-2 times compared to the initial microhardness.

When the SPD-processed sample is relatively large, similar to ECAP-processed samples, it is easy to study the tensile characteristics such as yield strength, ultimate tensile, and elongation to failure by conducting direct tensile tests. However, when the processed sample is small, similar to HPT-processed samples, it becomes difficult to conduct direct tensile tests and instead most researchers conduct microhardness tests across the HPT sample. Furthermore, researchers often relate the microhardness (Hv) to the yield strength (σ_y) through the empirical relationship, also known as Tabor relationship [121]:

$$Hv \approx C_T \sigma_y \qquad 2.24$$

where C_T is constant. Different C_T values in the literature have been suggested by several researchrs. Tabor [121] suggested a value of 2.9 for C_T in Equation 2.24 when steel was investigated. Cahoon et al. [122] and Zhang et al. [123] suggested a value of 3 and 3.5 for C_T when steel was investigated, respectively. Speich and Warlimont [124] suggested a higher value, ~ 4, for C_T when low-carbon martensitic steel and Fe-Ni alloys were investigated.

2.4.5. Severely plastically deformed FM steel tempered at different temperatures

There are few studies in the literature investigating the tempering process of severely plastically deformed FM steel. In this section, a breif explanation of some of these studies will be presented. Tsuji et al. [125] cold-rolled a martensitic steel (0.13 wt.% C) up to 50% reduction in thickness, and then tempered the rolled martensitic sample at 773^{o}K for 1.8 ks. The authors used TEM to study the microstructure of the tempered sample and observed that the microstructure was characterised by equi-axed and ultrafine grains at this high temperature as shown in Figure 2.51. The structural element had a mean size of $\sim$ 180 nm.

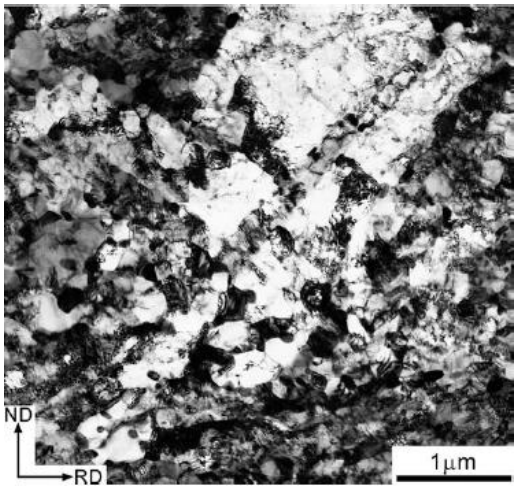

Figure 2.51 TEM bright-field image showing the microstructure of tempered martensitic steel (0.13 wt.% C) at 773°K for 1.8 ks. [125].

Lan et al. [126] cold-rolled a martensitic steel (0.17 wt.% C) up to 50% reduction in thickness, and then tempered the rolled martensitic sample at 450°C to 650°C for 60 min. The authors used TEM to study the microstructure changes during the tempering process at different temperatures. When tempering at 450°C, the lath structure observed in the as-rolled martensitic steel sample could no longer be seen (Figure 2.52a) and no significant changes in the dislocation density and dislocation cells sizes were observed. The authors also observed an evolution of equi-axed grains with sharp grain boundaries when tempering at 550°C as shown in Figure 2.52b. Furthermore, fine cementite particles formed (indicated by arrows in Figure 2.52b) at this tempering temperature.

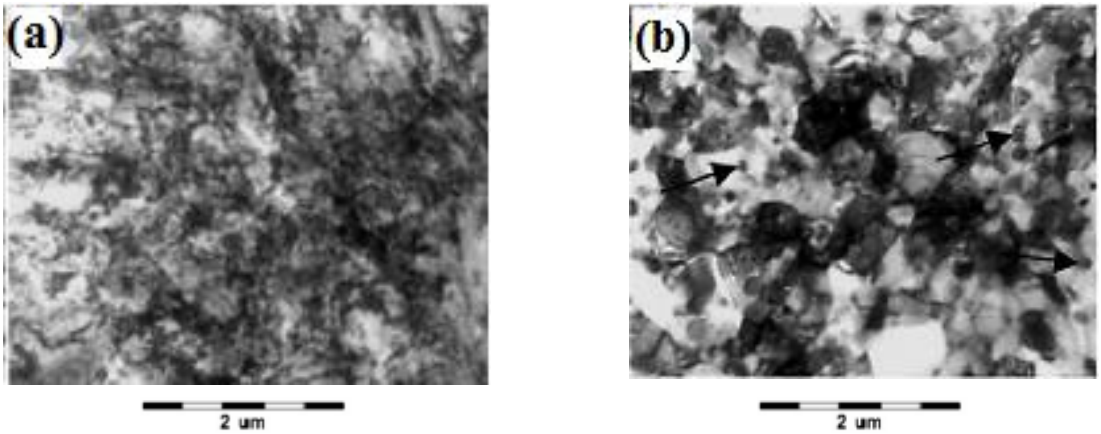

Figure 2.52 TEM bright-field image showing the microstructure of the martensitic cold-rolled sample (0.17 wt.% C) tempered at (a) 450°C and (b) 550°C for 60 min [126].

Astafurova et al. [127] processed martesitic steel sample (0.1 wt.% C), quenched from 1180°C, by HPT up to 5 turns. Later, the HPT-processed martensitic sample was tempered at 500°C for 1 hr. The authors studied the microstructure of the tempered sample using TEM and observed almost complete recovery of the martensitic structural element, such as lath (Figure 2.53). The authors observed that the structural element had semi equi-axed subgrains/grains with a mean size of 150 to 300 nm. The authors also observed grain growth in several regions and two different types of carbide were formed at this tempering temperature. The authors claimed that the long-range stress, observed in the as-deformed sample, was completely relaxed.

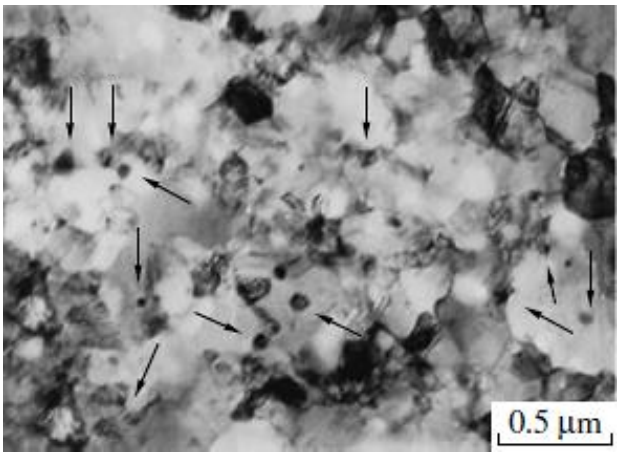

Figure 2.53 TEM bright-field image showing the microstructure of martensitic steel processed by HPT up to 5 turns and annealed at 500°C. The arrows are pointing to carbide particles. [127].

2.4.6. The strength of SPD-processed FM steel tempered at different temperatures

Tsuji et al. [125] conducted a tensile test on the martensitic steel sample rolled up to 50% reduction in thickness (Section 2.4.5) and tempered at different temperatures. The sample tempered at 773°K to 823°K had a combination of good strength and good elongation as shown in Figure 2.54.

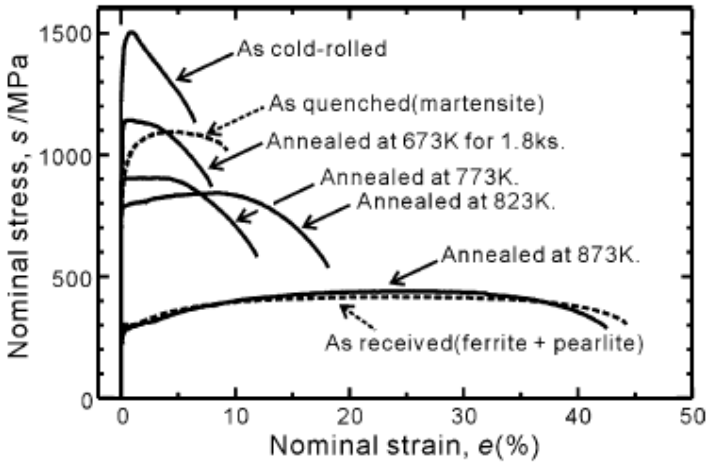

Figure 2.54 Stress-strain curves of martensitic steel samples (0.13 wt.% C) rolled up to 50% reduction in thickness and tempered at different tempering temperatures for 1.8 ks [125].

Lan et al. [126] conducted a microhardness test on the martensitic sample that was rolled up to 50% reduction in thickness (Section 2.4.5) and tempered at different temperatures. The results of the microhardness test are depicted in Figure 2.55. It can be seen from Figure 2.55 that the hardness was preserved up to 550°C and then started to drop quickly. Astafurova et al. [127] measured the hardness in the as-deformed sample as 8.6 GPa while it was 7.4 and 5.1 GPa in the tempered sample at 400°C and 500°C, respectively.

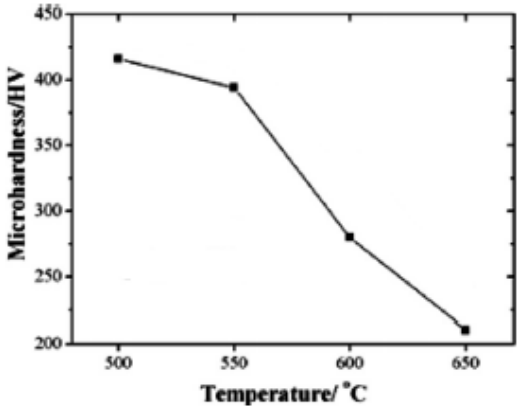

Figure 2.55 The microhardness (Hv) of martensitic steel samples (0.17 wt.% C) rolled up to 50% reduction in thickness and tempered at different temperatures vs. the tempering temperature [126].

2.5 Nanoindentation

Over the last ten years, the nanoindentation technique has become an important tool to study and characterise the mechanical properties of individual phases in an alloy. In this section, the basic principle of nanoindenation will be briefly discussed. In addition, the common phenomenon of indentation size effect (ISE) which is often observed during nanoindentation tests will also be discussed.

2.5.1. The basic principle of nanoindentation

During a nanoindentation test, a predefined load is applied on a diamond indenter that is in contact with a test sample. The indenter is pushed into the sample until a predefined maximum load or depth is reached. The maximum load is kept constant for a few seconds and then the indenter is withdrawn. The indenter can be of different geometries, such as conical or spherical. The three-sided Berkovich indenter is often used in nanoindentation tests due to its ability to produce well-defined plastic deformation during a test. The loads and their correspondent depths of penetration (also known as displacements) are simultaneously recorded and a load-displacement curve is generated (Figure 2.56) [128, 129]. Oliver and Pharr [128] used the contact area at load (A_c) instead of the residual projected area (A_{res}) after complete withdrawn of the indenter when calculating the nanohardness of a tested sample. The authors estimated the contact area at load (A_c) from the load-displacement curve that is generated during the nanoindenation test (for complete derivation of A_c from load-displacement curve see [128]).

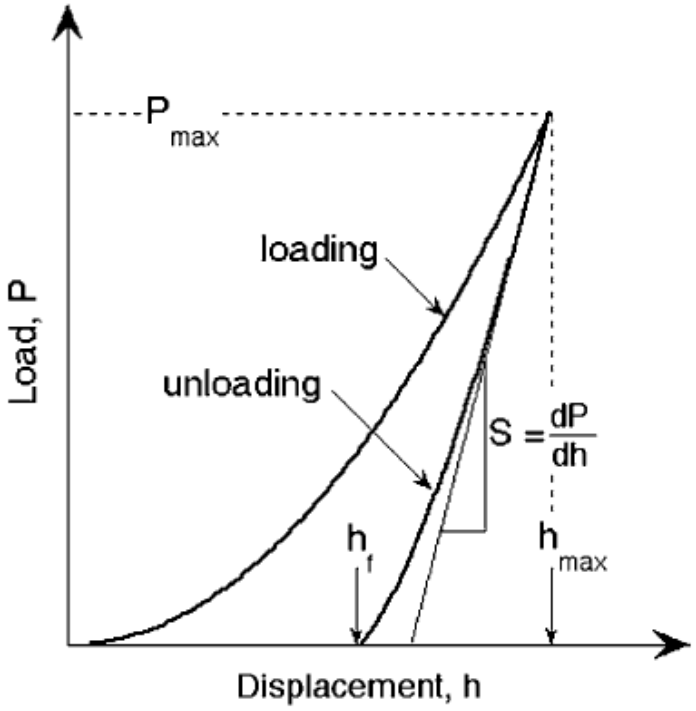

Figure 2.56 A typical load-displacement curve that is generated during nanoindentation test [128].

Using Oliver and Pharr method [128], the nanohardness of a tested sample can be found as follows:

$$H^N = \frac{P_{\max}}{A_c} \qquad 2.25$$

where $P_{\max}$ is the load at peak. The Oliver and Pharr method [128] is a very useful method to estimate the nanohardness of a tested material from the load-displacement curve without the need to image the residual projected area after the complete unloading of the indenter. However, while the Oliver and Pharr method [128] is simple and has been widely adopted for estimating the nanohardness, it has two limitations: first, the method only incorporates the Berkovich indenter and to the neglect of other indenter geometries, such as spherical indenters, and second, the method accounts only for the sink-in process at the contact periphery and does not account for possible pile-up processes in soft materials. In 2004, attempts were made to expand the application of the method to include spherical indenters, as well as to account for pile-up processes [129].

2.5.2. Indentation size effect

Several researchers [130-132] have observed that nanohardness increases as indentation depth decreases during nanoindentation tests, which is known as the indentation size effect (ISE). Nix and Gao [130] proposed a model to relate hardness to indentation depth *h* using the concept of GNDs, while taking into account SSDs as well. The authors assumed that circular loops of GNDs are generated when an indenter is pushed into a sample. The GNDs in Figure 2.57 have a Burgers vector *b* that is normal to the plane of the surface.

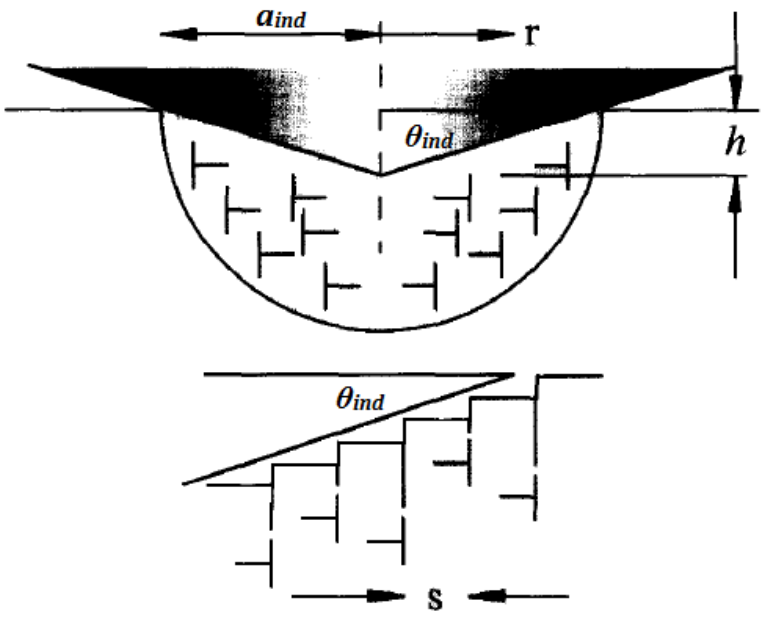

Figure 2.57 Schematic illustration showing the configuration of geometrically necessary dislocations when a conical indenter is pushed into a sample during a nanoindenation test [130].

In Figure 2.57, the angle between the surface of the conical indenter and the plane of the surface is denoted as θ_{ind}, the radius of the contact area as a_{ind}, and the displacement of the indenter as *h*. Nix and Gao [130] assumed that the individual dislocation loops are equally spaced (Figure 2.57), and hence, the space between two adjacent dislocation loops (*s*) can be found from the following relation:

$$\tan\theta_{\text{ind}} = \frac{h}{a_{\text{ind}}} = \frac{b}{s}\ , s = \frac{ba_{\text{ind}}}{h} \qquad 2.26$$

Accordingly, Nix and Gao [130] derived the density of the GNDs as follows:

$$\rho_{\text{GND}} = \frac{3}{2bh}\tan^2\theta_{\text{ind}} \qquad 2.27$$

Using the Taylor relation, the shear strength was estimated as follows [130]:

$$\tau = \mu Gb\sqrt{\rho_{\text{GND}} + \rho_{\text{SSD}}} \qquad 2.28$$

where ρ_{GND} is the density of the geometrically necessary dislocations, ρ_{SSDs} is the density of the statistically stored dislocations, and the other parameters are as defined in Equation 2.16. Nix and Gao [130] assumed that the von Mises flow rule is valid ($\sigma = \sqrt{3}\tau$), using a value of 3 for Tabor's factor to convert the flow stress to hardness:

$$H^N = 3\sigma \qquad 2.29$$

Using Equation 2.26 to Equation 2.29, the hardness of the indented sample was estimated as follows [130]:

$$\frac{H^N}{H_{\text{o}}} = \sqrt{1 + \frac{h^*}{h}} \qquad 2.30$$

Where

$$H_{\text{o}} = 3\sqrt{3}\mu Gb\sqrt{\rho_{\text{SSD}}} \qquad 2.31$$

where H_{o} is the hardness (depending only on SSDs), and

$$h^* = \frac{81}{2} b\mu^2 \tan^2\theta_{\text{ind}} \left(\frac{G}{H_o}\right)^2 \qquad 2.32$$

It is clear from Equation 2.27 and Equation 2.30 that both the density of the GNDs and nanohardness are inversely proportional to indentation depth. Qian et al. [131] conducted nanoindentation tests on fused silica, copper, stainless steel, nickel, and titanium and observed the ISE of all of these materials (except the fused silica). Qian et al. [131] attributed the ISEs observed during the nanoindentation tests to two factors: one, the contact area at peak load A_c is always smaller than the residual projected area A_r, and two, the assumption was made by the authors [128] that the elastic part of the unloading curve (in the load-displacement curve) that describes the elastic/plastic indentation process was imprecise. When the authors [131] compared the results of the microhardness and the nanoindenation tests, they found that the nanoindenation results were 10% to 30% higher than those obtained from the microhardness tests.

2.5.3. Characterization of SPD-processed steels by nanoinentation technique

It is well-known that the nanoindentation technique is very useful tool to study the behaviour or response of one particular phase when there are more than one phase in an alloy. From this point and up in this thesis, the term “nanohardness” will be used for the hardness obtained by the nanoindentation technique while the term “microhardness” will be used for the hardness obtained by the Vickers microhardness test. Hayashi et al. [133] tempered a martensitic steel (0.16 mass.% C) at 200°C to 500°C and conducted a nanoindentation test on these tempered martensitic steel samples. The authors observed that the nanoindent in the ferrite had a larger size than that in martensite (Figure 2.58) which suggested that the martensite resisted the deformation more than the ferrite did. The authors also observed several discontinuities, or pop-ins, in the load-displacement curve of the ferrite: they [133] attributed the pop-in behaviour to dislocation nucleation in a dislocation-free zone (Figure 2.59). The authors [133] measured a nanohardness of 2.8 and 7.2 GPa for the ferrite and martensite , respectively , in the martensitic sample tempered at 200°C.

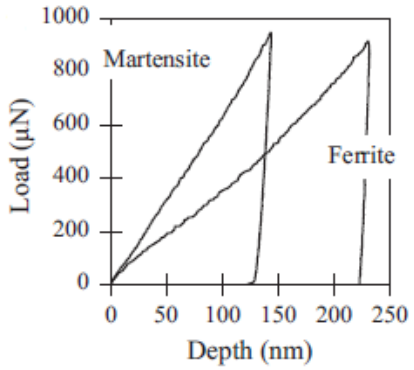

Figure 2.58 Load-displacement curves of ferrite and martensite in a martensitic steel (0.16 mass% C) tempered at 350°C [133].

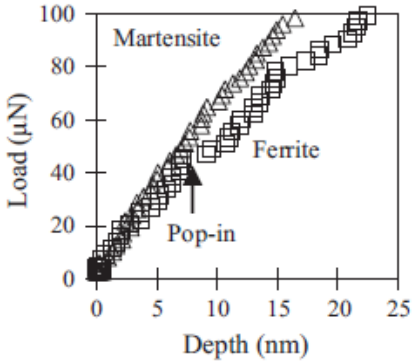

Figure 2.59 A magnified parts of the load-displacement curves of ferrite and martensite in a martensitic steel (0.16 mass% C) tempered at 350°C [133].

Ghassemi-Armaki et al. [134] studied the microstructure and properties of a martensitic steel sample tensile tested up to a strain of 0.5, 5.0, and 7% using TEM, SEM, tensile tests, nanoindentaion tests, and micropillars compression tests. Ghassemi-Armaki et al. [134] observed inhomogeneous distribution of nanohardness in the ferrite where the nanohardness of the ferrite close to the ferrite/martensite interface was higher than that of the ferrite at the centre of the grain in the as-received sample. The authors attributed the high nanohardness of the ferrite close to the ferrite/martensite interface to the existence of high number of GNDs at the ferrite/martensite interface resulted from austensite-to-martensite transformations. The authors measured a mean nanohardness of 2 GPa for the ferrite in the as-received sample and this nanohardness increased to 3.5 GPa in the sample tensile tested up to 7%. The authors observed that the ferrite at the grain centre hardened with strain up to 7%, while the ferrite close to the ferrite/martensit interface softened with strain. The authors believed that the GNDs at the ferrite/martensite interface were mobile, and hence, glided to the centre during the deformation where they interacted with the immobile dislocations.

Fereiduni and Banadkouki [132] studied the effect of the ferrite volume fraction and morphology on the mechanical properties of the ferrite in a dual-phase steel (0.38 wt.% C). Instead of direct quenching, they isothermally held the samples at 600°C for 20, 30, and 45 sec and then oil quenched the samples. Later, all the samples were tempered at 600°C for 30 min. Holding the sample for a small period of time, 20 sec, resulted in a small fraction of ferrite and fine ferrite grains. Increasing the holding time to 30 and 45 sec resulted in higher fraction of ferrite and a mixture of polygonal and quasi-poloygonal ferrite. Fereiduni and Banadkouki [132] recorded a nanohardness of 481, 416, and 387 Hv for the samples held at 600°C for 20, 30, and 45 sec, respectively.

The authors added that these nanohardness values were overestimated due to the so-called indentation size effect (ISE). The authors concluded that holding the sample at 600°C for just 20 sec resulted in a thin layer with fine grains of ferrite and high fraction of martensite, 93%, which in turn yielded the highest nanohardness, 481 Hv.

Taylor et al. [135] studied the validity of the nanohardness as a reliable technique, such as the Vickers microhardness, to investigate the properties of a material in eight carbon-steel alloys. All these steel alloys were in the FM initial state and had different chemical compositions. The difference in the chemical composition in these steel alloys resulted in variation in the microstructure such as ferrite grain size, martensite islands sizes, and the volume fraction of each phase (ferrite and martensite). The authors averaged 225 nanoindentation measurements in each steel alloy and considered it as the average nanohardness of the alloy. The nanoindentation measurements close to the ferrite/martensite interface were excluded when calculating the individual nanohardness of the ferrite and martensite. The authors conducted a Vickers microhardness test on each steel alloy and came up with a good relation between the nanohardness, obtained by nanoindentation, and the Vickers microhardness of each material (Figure 2.60), which suggested that nanoindention is a reliable technique in studying the properties of a material. The authors also observed a good relation between the yield strength (YS) of each steel alloy, obtained by tensile test, and the nanohardness of the ferrite, obtained by the nanoindentation, as shown in Figure 2.61. They [135] claimed that the good relation between the YS and ferrite nanohardness (Figure 2.61) is consistent with the general notion that the ferrite governs the yielding behaviour in dual-phase steels.

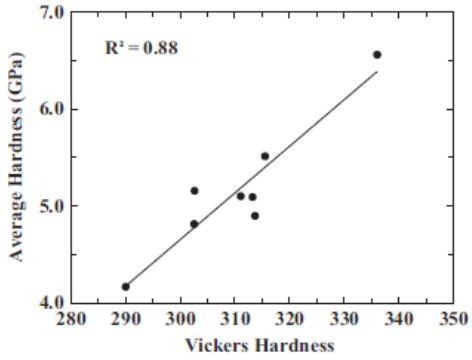

Figure 2.60 The relation between the nanohardness and the Vickers microhardness of eight steel alloys with different chemical compositions [135].

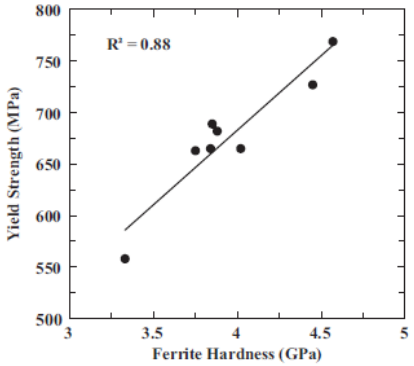

Figure 2.61 The relation between the YS and the ferrite nanohardness of eight steel alloys with different chemical compositions [135]

2.6 XRD line profiles analysis

The microstructure of a material can be investigated by direct methods such as SEM or TEM, or by indirect methods such as XRD line profiles analysis [136]. During the last few decades, it was proven that XRD line profiles analysis (XLPA) is a useful tool when studying the microstructure of a material and especially nanocrystalline materials. Assuming that line broadening occurs mainly due to size, strain, and instrumental broadening, the instrumental broadening removal is the first step in the analysis to make sure that the broadening is solely due to the structure (size and strain). Two common methods are usually used in the XRD line profiles analysis (XLPA). The first method is based on the full width at half maximum (FWHM) or the integral breadth (Williamson-Hall method) [137] while the second is based on the Fourier coefficient of the profile (Warren-Averbach method) [138].

Recently, novel software was developed based on the *ab initio* theoretical functions to evaluate the size and strain contributions in a broadened profile [136, 139, 140]. The software is called Multiple Whole Profile-fit (MWP-fit). In the following sections, a brief discussion will be given for the Williamson-Hall method and the MWP-fit.

2.6.1. Williamson-Hall method

Guinier [141] established the well-known relationship when he assumed that line broadening is due to finite crystallite size and negligible strain broadening:

$$\langle t \rangle_{\mathrm{vol}} = \frac{\eta\lambda}{FWHM * \mathrm{COS}\theta} \qquad 2.33$$

where $\langle t \rangle_{\mathrm{vol}}$ is the volume-weighted mean column-length, η is a constant taken as 0.9 for spherical crystallite shape, θ is Bragg-angle of reflection *hkl*, and λ is the wavelength of X-ray. Stokes and Wilson [142] defined the maximum strain (e) as:

$$e = \frac{\beta^{\mathrm{D}}}{4\tan\theta} \qquad 2.34$$

where β^{D} is the breadth due to strain. When the line broadening is due to size (β^{S}) and strain broadening, the linear addition rule of the two broadening contributions (size and strain) is often considered [142]:

$$\beta = \beta^{S} + \beta^{D} \qquad 2.35$$

Equation 2.35 is strictly applied when both the size and strain profiles have the Lorentzian shape. Based on the fact that the size and strain are diffraction-order-independent/dependent in the reciprocal space, respectively, Williamson and Hall proposed the following relation [137]:

$$\Delta K = \frac{0.9}{\langle t \rangle_{\mathrm{vol}}} + 2\,\langle \varepsilon^2 \rangle^{1/2} K \qquad 2.36$$

where $\Delta K = \cos\theta . \Delta(2\theta)/\lambda$, $\Delta(2\theta)$ is the FWHM of the diffraction peak (in radians), $\langle \varepsilon^2 \rangle^{1/2}$ is the mean-square strain, $K = 2\sin\theta/\lambda$. When plotting ΔK vs. K (in Equation 2.36), it is possible to separate the two broadening contributions (size and strain) from each other. A straight line is obtained when the datum points are fitted in the classical Williamson-Hall plot [137]. The intercept of the straight line with the y-axis (ΔK) is ($0.9/\langle t \rangle_{vol}$), while the slope of the straight line is the mean-square strain. A classical Williamson-Hall plot of an extruded copper is depicted in Figure 2.62 [143].

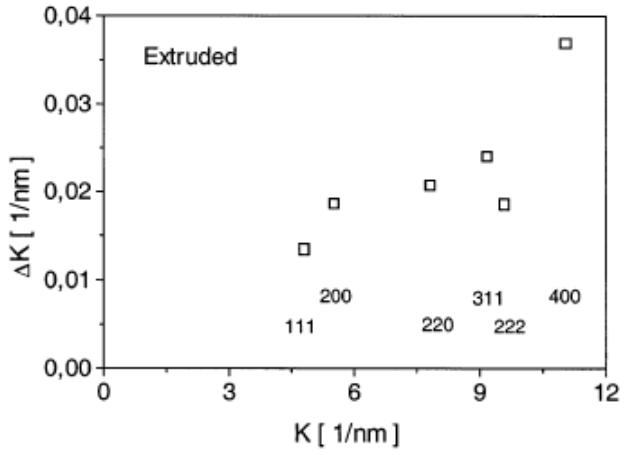

Figure 2.62 The classical Williamson-Hall plot of an extruded copper sample [143].

Williamson and Hall proposed their relation (Equation 2.36) based on two assumptions: linear addition of the size and strain is valid and the mean-square strain ($\langle\varepsilon^2\rangle^{1/2}$) is independent of the crystallographic orientation [137]. It has been shown that neither the FWHM nor the integral breadth in the classical Williamson-Hall plot are monotonous function of K (Figure 2.62) and this phenomenon is referred to as strain anisotropy. Assuming the main source of the strain broadening is dislocations, Ungar and Borbely [144] accounted well for the strain anisotropy by introducing the dislocation contrast factor, C. Ungar and Borbely [144] proposed a relation which is also known as the modified Williamson-Hall relation and has the following form [144]:

$$\Delta K = \frac{0.9}{\langle t\rangle_{vol}} + AKC^{\frac{1}{2}} + O(K^2C) \qquad 2.37$$

where A is a constant that depends on the arrangement and density of dislocation, C is the average contrast factor of dislocations, and O stands for higher order terms in K^2C. For an untextured material having cubic structure, the average contrast factor of dislocations (C) can be calculated according to the following relation [145]:

$$C = \overline{C}_{h00}(1 - qH^2) \qquad 2.38$$

where

$$H^2 = \frac{h^2k^2 + h^2l^2 + k^2l^2}{(h^2 + k^2 + l^2)^2} \qquad 2.39$$

where $\overline{C}_{h00}$ is the average dislocation contrast factor for the *h00* reflection, q is a constant depending on the type of dislocations (edge or screw). For steel, $\overline{C}_{h00}$ is numerically calculated and found to be ~ 0.3 for edge and screw dislocation while $q \sim$ 1.28 and 2.67 in the case of edge and screw dislocation, respectively [146]. Neglecting the higher order terms in Equation 2.37 and assuming a Gaussian peak profile shape exists, ΔK^2 equals the sum of the squares of the first and second terms in the right side of Equation 2.37. Then, inserting Equation 2.38 in the quadratic form of Equation 2.37 and rearranging will yield the following relation:

$$\frac{(\Delta K)^2 - \xi}{K^2} = A\overline{C}_{h00}(1 - qH^2) \qquad 2.40$$

where $\xi = (\frac{0.9}{\langle t \rangle_{vol}})^2$. Thus, the value of q can be determined from the measured profile according to Equation 2.40. The intercept of the linear regression, obtained when plotting the left hand side of Equation 2.40 vs. H^2, with the x-axis yields $1/q$. The strain anisotropy in Figure 2.62 (where ΔK is not a monotonous function of K) is well accounted for when the average contrast factor of dislocations, C, has been introduced and perfect fit was obtained as shown in Figure 2.63.

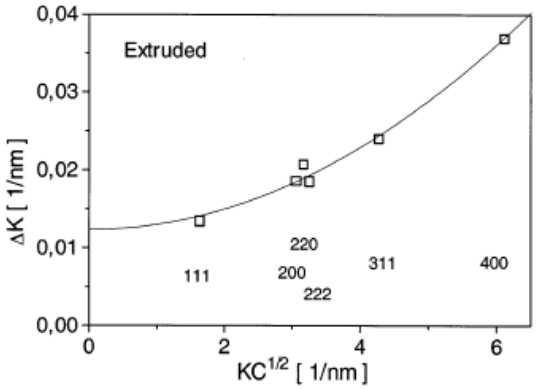

Figure 2.63 The modified Williamson-Hall plot of an extruded copper sample [143].

2.6.2. Multiple Whole Profile-fit

Recently, a computer program called MWP-fit has been developed to study the microstructure of a sample [136, 139, 140, 146]. Before using the MWP-fit program, input files should be prepared by a special program called MKDAT [139, 140] which has been specially designed for this purpose (preparing the input files). Each input file includes one *hkl* reflection since the MWP-fit program uses individual *hkl* reflection during the fitting process. The input files preparation process includes: instrumental correction, background subtraction, transformation from 2θ to K ($K = 2\sin\theta/\lambda$), and overlapped peaks separation (for details see [139]). During the fitting process, the measured intensities of each *hkl* reflection in the pattern are Fourier transformed and normalized according to the maximum intensity. Later, they are fitted by the theoretical Fourier coefficients (product of the size and strain Fourier coefficients), for further details see [139]. During the fitting process, the crystallite is assumed to have a

spherical shape and log-normal size distribution functions while strain broadening is mainly due to dislocations. The user of the MWP-fit program should provide the following: the crystal structure of the material, the lattice constant, the Burgers vector, and $\overline{C}_{h00}$. After the fitting process, the program (MWP-fit) provides the user with the fitting result. The result includes: the median (m), the variance of the size distribution (σ_v), the outer cut-off radius (R_e), the dislocation density (ρ), and the parameter of the dislocation contrast factor (q). A plot showing the measured and the theoretical fitted Fourier transformed profiles is given in the results which gives an indication of the fitting accuracy as shown in Figure 2.64.

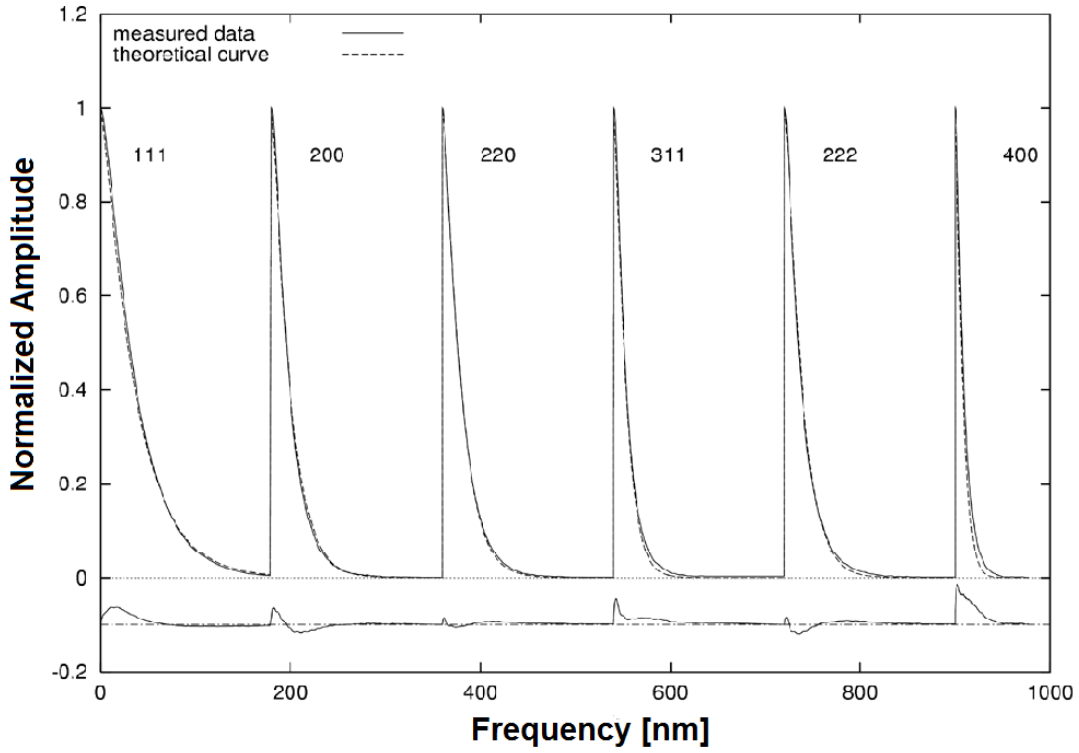

Figure 2.64 A plot showing the measured and fitted Fourier transformed profiles for a severely deformed copper sample vs. the Fourier variable (L). The graph was plotted by the MWP-fit program [139].

Wilkens [147, 148] introduced the dislocation arrangement parameter (M_{Dis}) which can be obtained from the relation:

$$M_{\mathrm{Dis}} = R_e\sqrt{\rho} \qquad 2.41$$

where R_e is the effective outer cut-off radius of dislocations. Wilkens [148] suggested that the correlation in the dislocation distributions is strong when the dislocation arrangement parameter (M_{Dis}) has a small value while the correlation is weak when M_{Dis} has a large value. The area weighted mean crystallite size value ($\langle X \rangle_{area}$) can be calculated according to the relation [149]:

$$\langle X \rangle_{area} = m.\exp(2.5\sigma_v^2) \qquad 2.42$$

2.6.3. Characterizaion of severely plastically deformed steels by XLPA

There are several XLPA methods such as Williamson-Hall, Warren-Averbach, and Multiple Whole Profile (MWP) fitting. The Williamson-Hall method is a simple and direct method so has been used widely in the literature while both Warren-Averbach and MWP are indirect methods and contain complexity to a large extent. Chacraborty et al. [150] cold-drew pearlitic steel (0.8 wt.% C) up to a strain of 1.4 and investigated the microstructure using XRD. The cementite reflections were detected during the XRD test and this can be attributed to the high volume fraction of cementite in the investigated sample. However, the cementite peaks became weak with increasing strain suggesting that the cementite dissolution increases with strain. Chacraborty et al. [150] successfully used Rietveld analysis to study the cementite dissolution during the drawing process and concluded that the cementite dissolution was more than 50% at a drawing strain of 1.4. The lattice parameter did not change with strain which suggests that the carbon atoms which left the cementite did not occupy the interstitial sites in ferrite to form solid solution. The authors used the modified Williamson-Hall method to determine the dislocation density and the nature of the dislocation evolved during the drawing process. The authors successfully eliminated the strain anisotropy observed in the classical Willamson-Hall plot (Figure 2.65) by introducing the dislocation contrast factor or plotting the so-called modified Williamson-Hall plot (Figure 2.66). The authors determined the dislocation density in the ferritic-pearlitic sample cold-drawn up to a strain of 1.4 as 8×10^{15} m^{-2} while the fraction of the screw dislocation was found to be 60%.

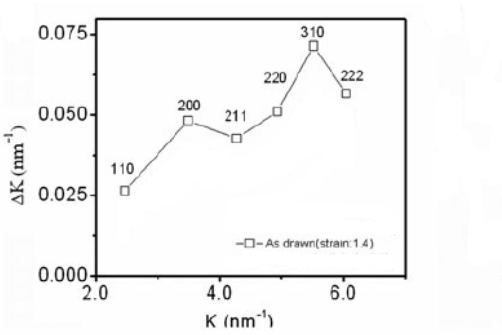

Figure 2.65 The classical Williamson-Hall plot of a pearlitic steel (0.8 wt.% C) cold-drawn up to 1.4 [150].

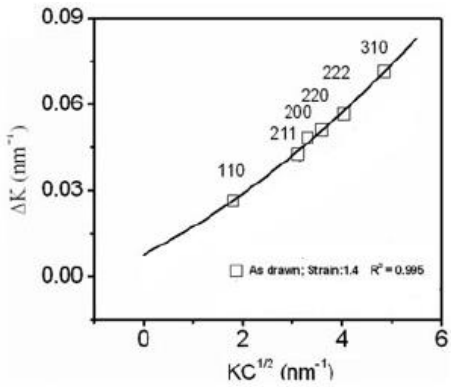

Figure 2.66 The modified Williamson-Hall plot of a pearlitic steel (0.8 wt.% C) cold-drawn up to 1.4 [150].

Nedjad et al. [151] processed Maraging steel, in the FM initial state, by equal channel angular pressing (ECAP) up to 4 passes at room temperature using route B_C. Nedjad et al. [151] conducted XRD test on the deformed Maraging steel and only ferrite reflections were detected during the test, while no martensite reflections were detected and this can be attributed to the low fraction of martensite in the investigated sample. The authors used the Williamson-Hall method in the analysis and observed strong anisotropy when plotting the classical Williamson-Hall plot as shown in Figure 2.67. The authors accounted for the strain anisotropy that was observed in the classical Williamson-Hall plot (Figure 2.67) by introducing the dislocation contrast factor and an improved linear dependency was obtained as shown in Figure 2.68. The authors studied the nature of the dislocations evolved during the ECAP processing and concluded that the screw dislocation was prevailing during the ECAP processing and they attributed this dominance to the easy annihilation of edge dislocation during the early stages of deformation.

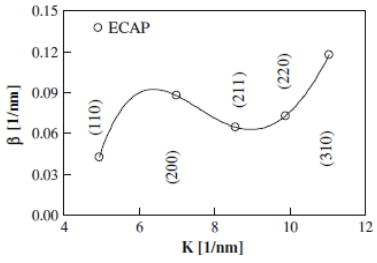

Figure 2.67 The classical Williamson-Hall plot of Maraging steel processed by ECAP up to 4 passes using rout B_C [151].

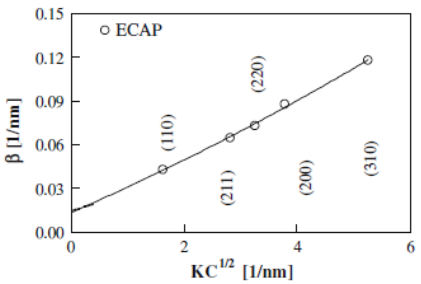

Figure 2.68 The modified Williamson-Hall plot of Maraging steel processed by ECAP up to 4 passes using rout B_C [151].

Sarkar et al. [100] processed an interstitial-free (IF) steel (0.0027 wt.% C) by ECAP up to 4 passes using rout A. Sarkar et al. [100] used the Williamson-Hall and the variance method to study the microstructure of the processed IF steel. The authors observed a decrease in the crystallite size with the strain (Figure 2.69), while an increase in the dislocation density with the strain (Figure 2.70).

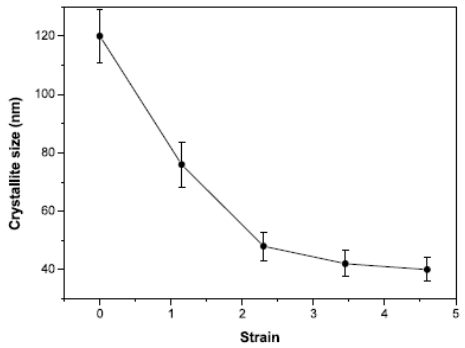

Figure 2.69 The crystallite size (nm) of an IF steel processed by ECAP up to 4 passes vs. the strain [100].

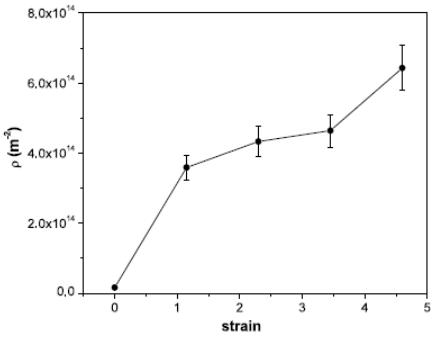

Figure 2.70 The dislocation density (m^{-2}) of an IF steel processed by ECAP up to 4 passes vs. the strain [100].

The Williamson-Hall method is a very useful tool to qualitatively study the microstructure of a material and particularly the volume-weighted mean column length. The Williamson-Hall method has been used widely in the literature due to its simplicity [100, 150, 151]. However, the strain constant in Equation 2.37 depends on both the outer cut-off radius and the dislocation density and not only on the dislocation density. The researchers using the Williamson-Hall method often assume a value for the outer cut-off radius which, in reality, leads to a high possible error associated with the value of the dislocation density calculated following this strategy. In order to obtain more reliable value of the dislocation density, it is preferred to use a method based on the Fourier transform such as Warren-Averbach or MWP method.

2.7 Summary of literature review

In Section 2.1, the principles of the ECAP and ARB were briefly explained whereas the principle of the HPT was explained in more details since it is the processing method used in the current study. The different types of HPT and the experimental parameters that affect the HPT process were also briefly discussed. Reviewing several studies in the literature that study the thermal stability of severely plastically deformed materials and the application of SPD processed materials were also conducted in this section. The characteristics and the strength of the different types of steels (FP, FM, and tempered steel) were explained in Section 2.2. The various strengthening mechanisms contribute to the strength of steels and the three models explaining the dependency in the Hall-Petch relation are discussed in Section 2.3. Also the three approaches for modelling the strength of the severely plastically deformed materials were reviewed in Section 2.3 and accordingly this section was considered to be the base for the strength/hardness model proposed in the current study. Examples of severely plastically deformed steels such as FP, FM, and tempered steels were presented in Section 2.4. In the same regard, the strength of these severely plastically deformed steels was also discussed in this section. The basic principle and the importance of the nanoindentation technique in characterising the properties of the individual phases in an alloy were discussed in Section 2.5. In Section 2.6, two methods of the X-ray line profiles analysis were presented and some examples of severely plastically deformed steels characterised by these methods were given.

Determining the dislocation density in a microstructure that is characterised by high dislocation density and ill-defined grain boundaries using transmission electron microscopy is almost impossible. In this case, using line profiles analysis to determine the dislocation density becomes necessary. However, a deep understanding of the concept behind these XPLA methods is needed to obtain reliable results. The HPT processing of steel samples results in significant increase in the strength of the processed samples but no model was proposed yet to predict the increase in the strength after the HPT processing using the dislocation density obtained by the XLPA. There is also a lack of information on modelling the strength of tempered FM steel originally deformed by HPT.

CHAPTER 3

3. Experimental work

3.1 Material

A hot rolled low-carbon steel strip obtained from Tata Steel was used in this experiment. The chemical composition of the material is given in Table 3.1. The finishing rolling temperature for the low-carbon steel strip was 840°C followed by air cooling for 8 sec and finally water quenching to the coiling temperature of less than 250°C. The final product is a dual phase (ferritic-martensitic) steel strip. Furthermore, the as-received FM steel strip was annealed at 1100°C for 90 min then air cooled to room temperature. The annealed strip has a ferritic-pearlitic microstructure.

Table 3.1 The chemical composition (wt.%) of the material used in the current work.

C	Si	Mn	P	S	Al	N	Fe
0.1	0.1	1.55	0.015	0.005	0.045	0.003	balance

3.2 HPT processing and tempering

For all HPT processing, the disk samples were machined from the rolled and/or heat treated steel (at 1100°C for 90 min). Each disk sample had a diameter of 10 mm and a thickness of 1.2 mm. The samples were mechanically ground until the target thickness was reached. The samples and the two anvils of the HPT tool were carefully cleaned with alcohol. HPT processing was conducted using the HPT facility at the University of Southampton, Figure 3.1.

Figure 3.1 HPT facility at the University of Southampton [152].

3.2.1. Processing FP and FM samples

The FP and FM samples were mechanically ground to reach a final thickness of 1mm. The FP and FM samples were then processed by HPT at room temperature under a pressure of 6 GPa up to 1, 4, and 10 turns.

3.2.2. Tempering the FM processed samples at different temperatures

The FM processed samples were tempered at different temperatures for different tempering times as described in Table 3.2. Later, the tempered samples were air cooled to room temperature.

Table 3.2 Tempering parameters (temperature and time) used in the current study.

Sample	Tempering temperature (°C)	Tempering time (min)
FM processed samples	150 and 250	120
	350, 450, and 550	90

3.3 Hardness: Microhardness and nanoindentation tests

3.3.1. Microhardness test of the FP samples

The FP samples were manually ground up to 4000 grit using SiC paper and polished to a mirror-like state using a 1 μm diamond disk. Microhardness measurements were taken across the disk using 300g force and a dwell time of 15 sec. Three measurements were recorded for each position and the average of these three measurements was calculated.

3.3.2. Microhardness test of the FM samples and FM processed samples tempered at different temperatures

The as-received, FM samples, and FM processed samples tempered at different temperatures (150^{o}C to 550^{o}C) were prepared and tested under the same conditions mentioned in Section 3.3.1. A second microhardness test was performed on the FM samples processed up to 1, 4, and 10 turns to measure the microhardness of the individual phases (ferrite or martensite). In this test, the as-received and FM samples were mechanically prepared then etched with 2% nital for 45 to 60 sec. Only a 10 g load and dwell time of 15 sec were used for the test. With the aid of the FM-300 microhardness testing machine and using the etched samples, each phase was individually indented at the centre and the edge of the investigated samples. Three microhardness readings were taken and the average of these readings was calculated.

3.3.3. Nanoindentation test of the FP samples

The sample annealed at 1100^{o}C for 90 min (FP undeformed sample) and the FP processed samples were prepared for the nanoindentation test by following the same procedures mentioned in Section 3.3.1, then etched with 2% nital for 40 to 60 sec. The nanoindention test was conducted using the Micro Materials Ltd. Vantage System nanoindentation device, at the University of Southampton (Figure 3.2). A three-sided pyramidal Berkovich indenter was used in the test. For the test, an initial load of 0.01 mN was applied with a loading/unloading rate of 1.0 mN/s. Once the maximum load is reached, it was held for 30 sec. During the nanoindenation test, a maximum depth of 500 and 350 nm was set for the ferrite and pearlite, respectively. The Oliver and Pharr

method [128] was used in all indentation tests to calculate the nanohardness. Eight individual indentations were made on each phase (ferrite or pearlite) of the sample annealed at 1100°C for 90 min (FP undeformed sample) and the FP samples processed up to 1 and 4 turns. The eight indentations were made at the edge (4 mm from the centre) of the FP processed samples, whereas they were randomly made for the sample annealed at 1100°C for 90 min (FP undeformed sample). The indentations that fell in the required phase were included in the analysis, while those falling between the two phases were rejected. Furthermore, any indentation with an inconsistent load-displacement curve was excluded as well. Based on this criteria, the nanohardness of each phase was taken as the average of six out of eight indentations. A matrix of 2x4 indentations were made at the edge (4 mm from the centre) of the FP sample processed up to 10 turns. Among the eight indentations in the matrix, five were found in the ferrite matrix. The average of the ferrite nanohardness in the FP sample processed up to 10 turns was taken as the average of these five indentations. During the nanoindentation measurement, overlapped plastic zones were avoided by leaving a relatively large distance (40 μm) between any two adjacent indentations.

Figure 3.2 Micro Materials Ltd. Vantage System nanoindentation device, at the University of Southampton [153].

3.3.4. Nanoindentation test of the FM samples

The as-received and the FM processed samples were prepared for the nanoindentation test by following the same procedures descibed in Section 3.3.2. The nanoindention test was conducted using the NanoTest system nanoindentation device, at the University of Southampton. For the test, an initial load of 0.03 mN was applied with a loading/unloading rate of 0.5 mN/s. Once the maximum load is reached, it was held for 10 sec. The maximum load was 100 mN and a 7 x 7 matrix of indentations was made at a distance of 3 mm from the centre yielding 49 indentations on each tested sample. Overlapped plastic zones were avoided by leaving enough distance, ~ 30 μm, between any two adjacent indentations.

3.3.5. Nanoindentation test of the FM processed samples tempered at different temperatures

The nanoindentation test of the FM sample processed up to 4 turns and tempered at 250^{o}C and 350^{o}C was performed under the same conditions mentioned in Section 3.3.3. Eight individual indentations were randomly made on the ferrite at the centre of the samples tempered at 250^{o}C and 350^{o}C. The average nanohardness of the ferrite in the investigated samples was taken as the average of six out of eight indentations (see also Section 3.3.3). A matrix of 2x4 indentations were made at the edge (4 mm from the centre) of the samples tempered at 250^{o}C and 350^{o}C. The overall nanohardness of the investigated samples was taken as the average of the eight indentations in the matrix.

3.4 Optical and Scanning Electron Microscopy

Samples for optical and scanning elelctron microscopy, were prepared under the same conditions mentioned in Section 3.3.1 and subsequently etched with 2% nital for 40 to 60 sec. The SEM device used is a JSM 6500F thermal field emission scanning electron microscope at the University of Southampton. The SEM device has an accelerating voltage of 0.5 to 30 kV and a magnification up to 500,000. Secondary Electron Imaging (SEI) mode was used for the microstructure investigation.

3.5 Transmission Electron Microscopy

For TEM investigations, the as-received and FM samples processed up to 1, 4, and 10 turns were mechanically ground to a thickness of about 50-70 μm. All of the investigated samples were cut out to disks having a diameter of 3 mm. The samples were electropolished using a twin-jet polishing facility using a solution of 5% perchloric acid and 95% of methanol at -40°C and a voltage of 40 V. After thinning, a Jeol 3010 transmission electron microscope, shown in Figure 3.3, operating at 300 kV was used to examine the prepared foils. Selected area diffraction (SAD) patterns were recorded using an aperture with a diameter of 1.75 μm.

Figure 3.3 Jeol 3010 transmission electron microscope, University of Southampton [154].

3.6 X-ray diffraction

XRD profiles for the as-received, the sample annealed at 1100°C for 90 min (FP undeformed sample), all processed samples (FP and FM), and tempered samples were recorded using a Rigaku SmartLab X-ray diffractometer at the University of Southampton (Figure 3.4 and Figure 3.5). The Rigaku SmartLab X-ray diffractometer is equipped with Cu K_α radiation of 0.154 nm wavelength. The XRD patterns were recorded from $2\theta = 40^o$ to 120^o with a step size and scan speed of 0.02^o and 2 deg/min, respectively. However, a scan speed of 1 deg/min was used in the case of the as-received and FM samples scanning.

Figure 3.4 Rigaku SmartLab X-ray diffractometer, at the University of Southampton [155].

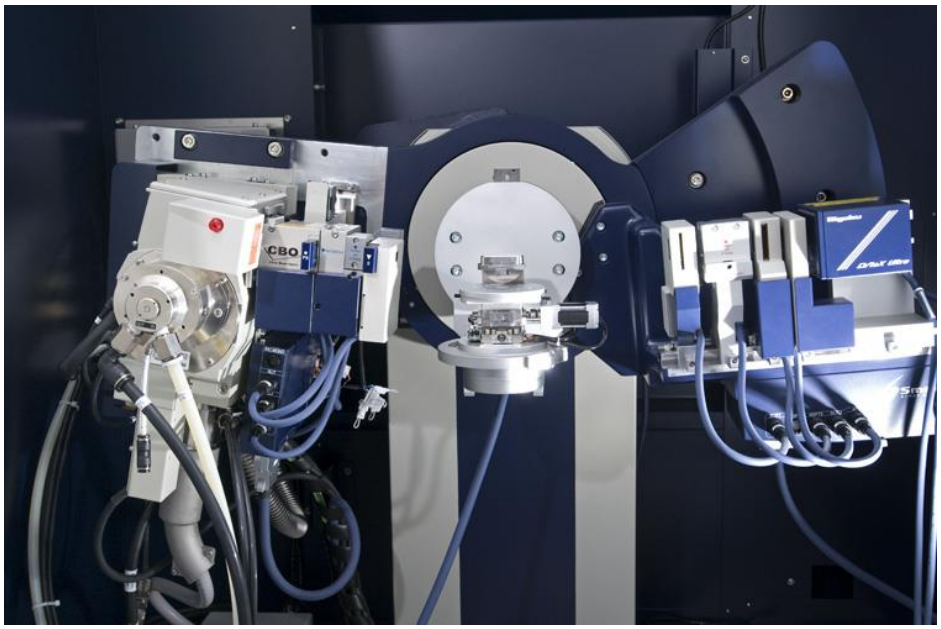

Figure 3.5 Rigaku SmartLab X-ray diffractometer from inside, at the University of Southampton [156].

CHAPTER 4

4. Results and analysis

4.1 HPT processing

Since the hardness of the as-received sample is high (~ 206 Hv), slippage is likely to occur during the HPT process, especially when processing under low pressure. Therefore, two primary tests were conducted to investigate any possible slippage that may occur during the experiment. In the first test, the FM sample had a thickness of 0.85 mm and a line was drawn on each side of the disk. Each line starts from the centre and ends at the circumference of the disk with the ending points on top of each other. In the first attempt, the HPT process was conducted at room temperature under a pressure of 1 GPa up to 1 complete turn. In the second attempt, the sample was processed by HPT at room temperature under a pressure of 1 GPa and up to 4 turns. In the third attempt, the sample was processed by HPT at room temperature under a pressure of 1 GPa and up to 10 complete turns.

In the second test, both the thickness of the sample and the applied pressure were increased to become 1 mm and 6 GPa, respectively. Further HPT processes were conducted to check the effect of the changes made to the sample thickness and the applied pressure.

Again, in the first attempt, the sample was processed by HPT at room temperature under a pressure of 6 GPa and up to 1 complete turn. In the second attempt, the sample was processed by HPT at room temperature under a pressure of 6 GPa and up to 4 turns with no lines drawn on the sample. After the HPT process, the sample was removed from the anvil and the lines were drawn on both sides of the sample. Then the sample was processed again up to 1 complete turn. In the third attempt, the sample was processed by HPT at room temperature under a pressure of 6 GPa and up to 10 turns.

In the first test to investigate slippage, the sample had a thickness of 0.85 mm and was processed under a pressure of 1 GPa at room teperature. In the first attempt, the two lines were still visible with a minor shift in their position which indicates that slippage took place during the process. In the second attempt, the two lines disappeared or only fine traces of them could be seen and a shift in their position was visible which

indicates that slippage took place during the process. Finally, in the third attempt, the two lines disappeared completely.

In the second test to investigate slippage, the sample had a thickness of 1 mm and was processed under a pressure of 6 GPa at room temperature. In the first attempt, the two lines were still visible in their initial position, which indicates that there was no slippage. In the second attempt, the two lines were still visible and were in their position, which indicates that no slippage occurred after the fourth turn in spite of the increased hardness. In the third attempt, the two lines disappeared. The main experiments were conducted under the conditions of the second test (a thickness of 1 mm and pressure of 6 GPa) to ensure that there is no slippage during the HPT processing.

After the HPT process, the thickness of the FP samples processed by HPT up to 1, 4, and 10 turns decreased to 0.91, 0.85, and 0.83 mm, respectively. On the other hand, the thickness of the FM samples processed to 1, 4, and 10 turns decreased to 0.91, 0.88, and 0.85 mm, respectively.

4.2 Hardness tests results

4.2.1. Microhardness test results of the FP samples

The sample annealed at 1100^{o}C for 90 min (FP undeformed sample) had a microhardness value of ~ 146 Hv. The microhardness at the centre of the FP sample processed up to 1 turn was ~ 241 Hv, while it was ~ 422 Hv at the edge as shown in Figure 4.1. Increasing the number of turns to 4 turns was accompanied by an increase in the microhardness of the FP sample to reach ~ 334 Hv at the centre and ~ 480 Hv at the edge as shown in Figure 4.1. Increasing the number of turns further to 10 turns increased the microhardness of the FP sample to ~ 399 Hv at the centre and ~ 597 Hv at the edge as shown in Figure 4.1.

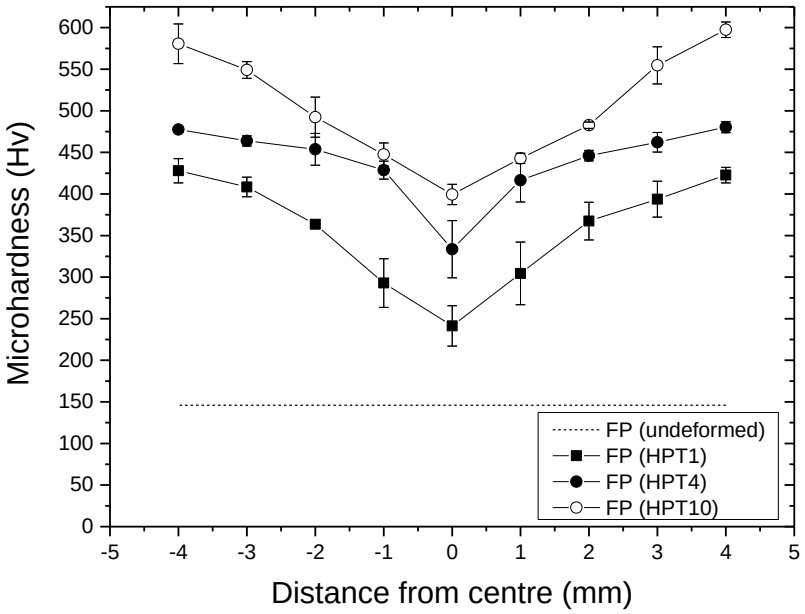

Figure 4.1 The Vickers microhardness (Hv) vs. the distance from the centre of the FP samples processed by HPT up to 1, 4, and 10 turns. Also, the average Vickers microhardness of the sample annealed at 1100°C for 90 min (undeformed) was plotted for reference.

The strain imposed on the FP samples versus the distance from the centre of the disk (calculated using Equation 2.4) is shown in Figure 4.2. The microhardness versus the effective strain of the FP samples after different number of turns of the HPT processing is depicted in Figure 4.3.

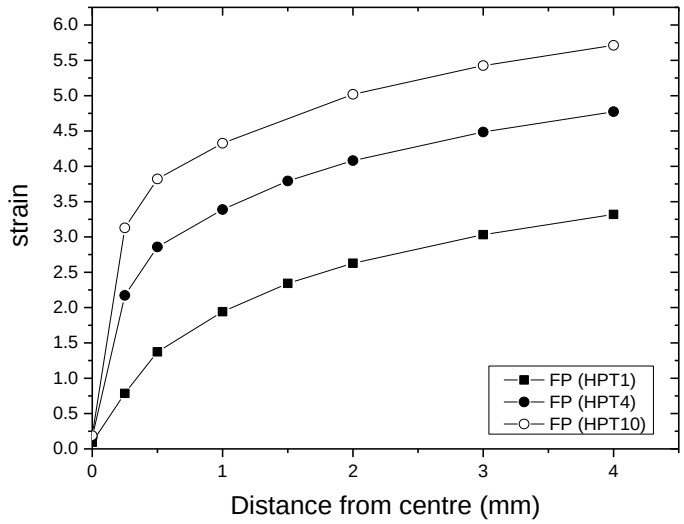

Figure 4.2 The effective strain vs. the distance from the centre of the FP samples processed by HPT up to 1, 4, and 10 turns.

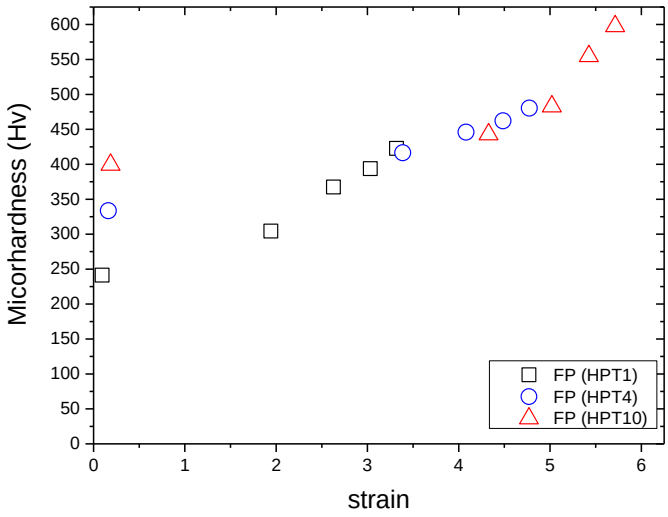

Figure 4.3 The Vickers microhardness (Hv) vs. the effective strain of the FP samples after 1, 4, and 10 turns of HPT processing

4.2.2. Microhardness test results of the FM samples

The as-received sample had a microhardness value of ~ 206 Hv. The microhardness at the centre of the disk of the FM sample processed up to 1 turn increased to reach ~ 290 Hv as shown in Figure 4.4, while the microhardness reached ~ 464 Hv at the edge of the disk. Increasing the number of turns to four increased the microhardness at the centre of the FM sample to ~ 404 Hv, while the microhardness at the edge reached ~ 534 Hv which is higher, again, than the microhardness at the centre and the edge of the FM sample processed up to 1 turn as shown in Figure 4.4. As the number of turns is further increased to 10 turns, the microhardness increased at the centre of the FM sample to ~ 472 Hv, while it reached ~ 596 Hv at the edge as shown in Figure 4.4.

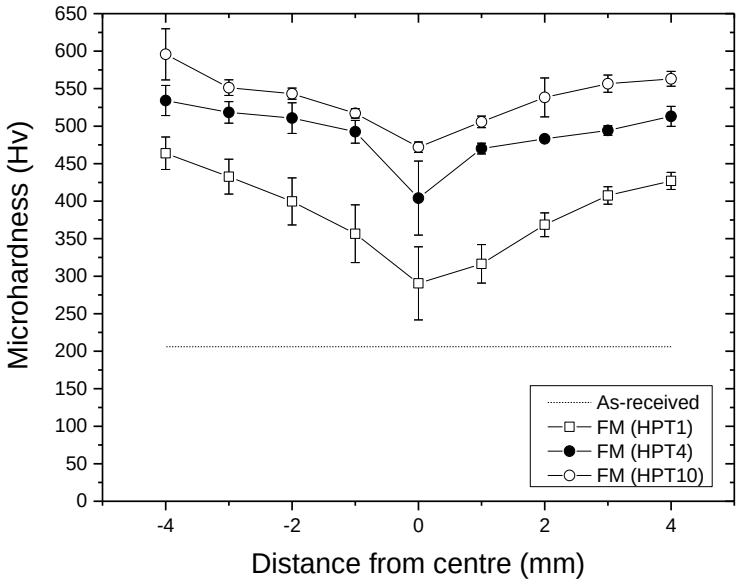

Figure 4.4 The Vickers microhardness (Hv) vs. the distance from the centre of the FM samples processed by HPT up to 1, 4, and 10 turns.

The strain imposed on the FM samples versus the distance from the centre of the disk (calculated using Equation 2.4) is shown in Figure 4.5. The microhardness versus the effective strain of the FM samples after different number of turns of the HPT processing is depicted in Figure 4.6.

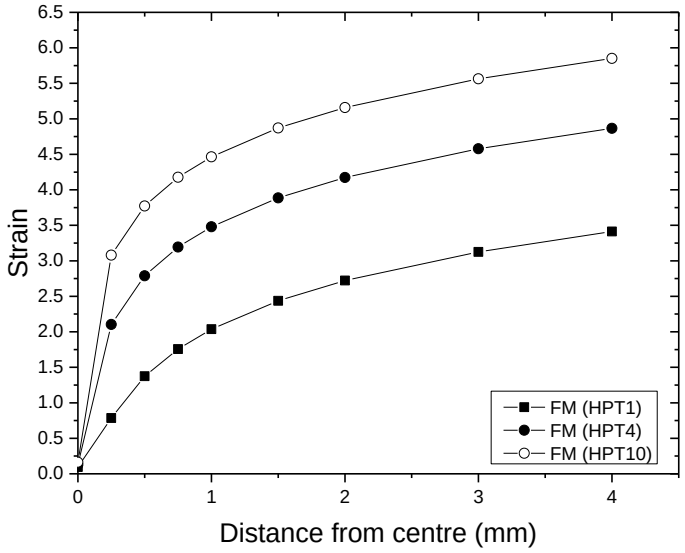

Figure 4.5 The effective strain vs. the distance from the centre of the FM samples processed by HPT up to 1, 4, and 10 turns.

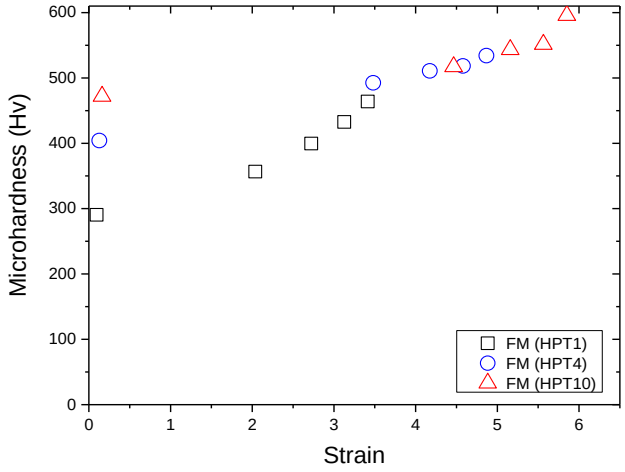

Figure 4.6 The Vickers microhardness (Hv) vs. the effective strain of the FM samples after different number of turns of the HPT processing.

In the second set of microhardness tests, the microhardness of the individual phases, ferrite or martensite, present in the FM sample were investigated using the FM-300 microhardness testing machine. The averaged microhardness results are listed in Table 4.1. Figure 4.7 shows one indentation in ferrite and one indentation in martensite (indicated by black arrows) at the centre of the disk of the FM sample processed up to 10 turns.

Table 4.1 The Vickers micorhardness results of the ferrite and martensite in the as-received and the FM samples processed by HPT up to 1, 4, and 10 turns.

Sample	**Position**	**Ferrite hardness (Hv)**	**Martensite hardness (Hv)**
As-received	-	225 ± 3	316 ± 34
HPT (N=1)	Centre	303 ± 12	370 ± 11
	Edge	443 ± 8	505 ± 15
HPT (N=4)	Centre	468 ± 9	529 ± 8
	Edge	522 ± 10	567 ± 9
HPT (N=10)	Centre	536 ± 5	570 ± 5
	Edge	638 ± 21	641 ± 12

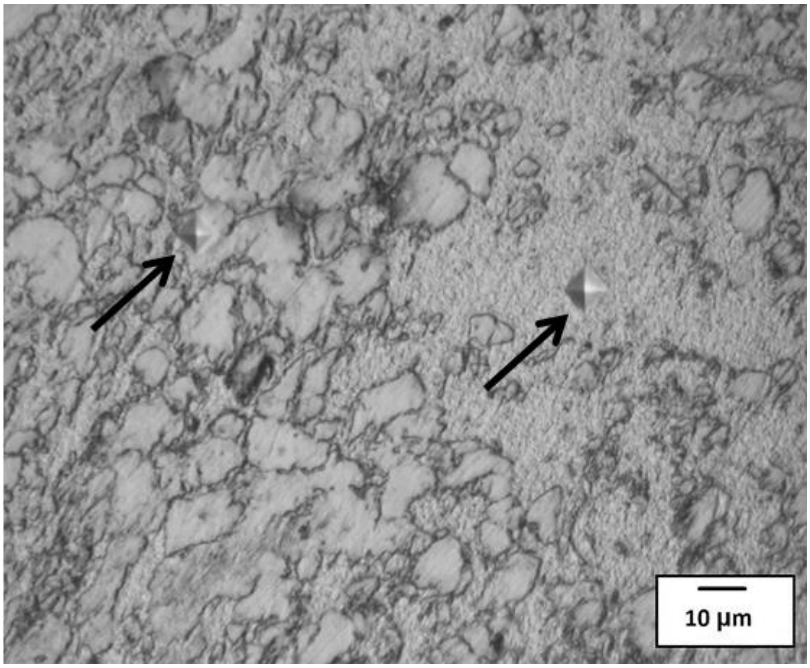

Figure 4.7 Representative optical micrograph showing one microhardness impression in the ferrite and one in martensite (indicated by black arrows) at the centre of the FM sample (0.1 wt.% C) processed up to 10 turns and etched with 2% nital.

4.2.3. Microhardness test results of the FM processed samples tempered at different temperatures

The Vickers microhardness vs. the distance from centre of the disk of the samples tempered at 250°C, 350°C, and 450°C are shown in Figure 4.8 to Figure 4.10. There was no significant change in the microhardness after tempering the FM processed samples at 250°C for 120 min (Figure 4.11). However, there was a slight increase in the microhardness when tempering the FM processed samples at 350°C for 90 min (Figure 4.11). After tempering the FM processed samples at 450°C for 90 min, no significant reduction in the microhardness was recorded as shown in Figure 4.11. Tempering the FM processed samples at 550°C for 90 min, the hardness significantly decreased to have a hardness value close to that of the as-received sample (Figure 4.11).

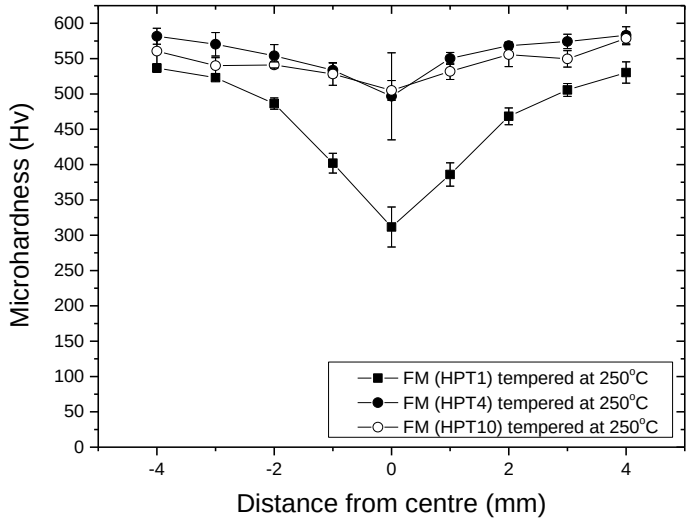

Figure 4.8 The Vickers microhardness (Hv) vs. the distance from the centre of the FM processed samples tempered at 250°C for 120 min.

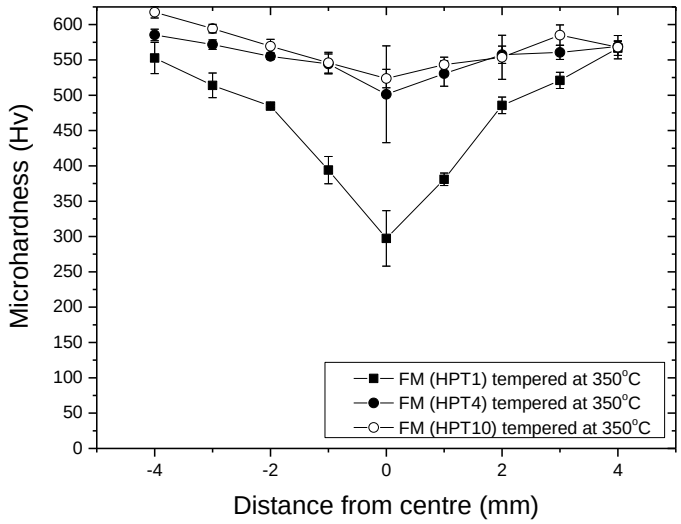

Figure 4.9 The Vickers microhardness (Hv) vs. the distance from the centre of the FM processed samples tempered at 350°C for 90 min.

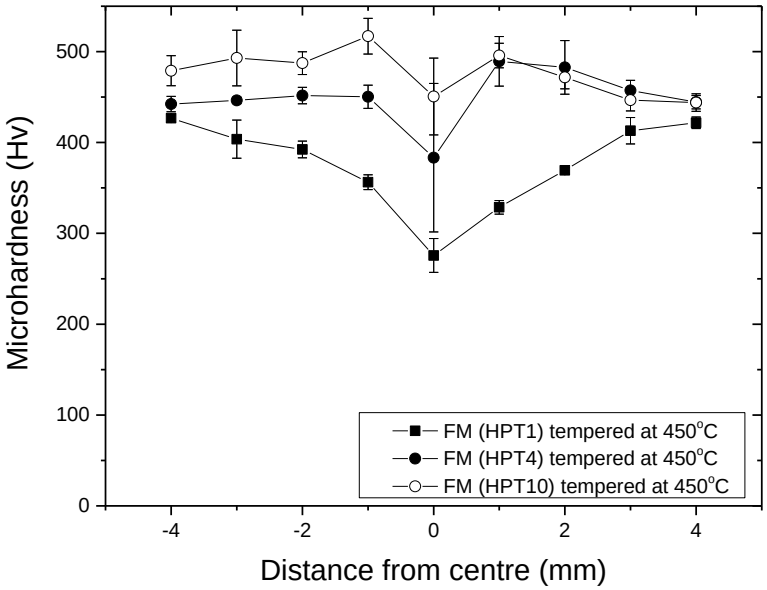

Figure 4.10 The Vickers microhardness (Hv) vs. the distance from the centre of the FM processed samples tempered at 450°C for 90 min.

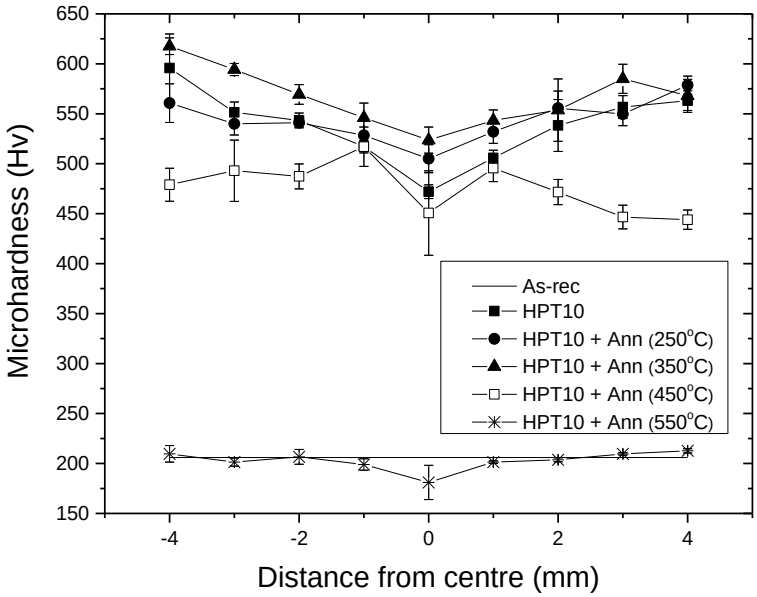

Figure 4.11 The Vickers microhardness (Hv) vs. the distance from the centre of the as-received, FM sample processed up to 10 turns, and FM sample processed up to 10 turns and tempered at 250°C to 550°C.

4.2.4. Nanoindentation results of the FP samples

As mentioned earlier, the hardness obtained by the nanoindentation test will be denoted as nanohardness to differentiate it from the microhardness which is obtained by the Vickers microhardness test. The Oliver and Pharr method [128] was used to calculate the nanohardness of the FP processed samples. It is very clear from Figure 4.12 that the nanohardness of the ferrite of the FP processed samples increased as the number of turns increased. Similarly, the nanohardness of the pearlite of the FP processed samples increased as the number of turns increased as shown in Figure 4.13. The impression of one indentation in the ferrite and pearlite is shown in Figure 4.14 and Figure 4.15, respectively.

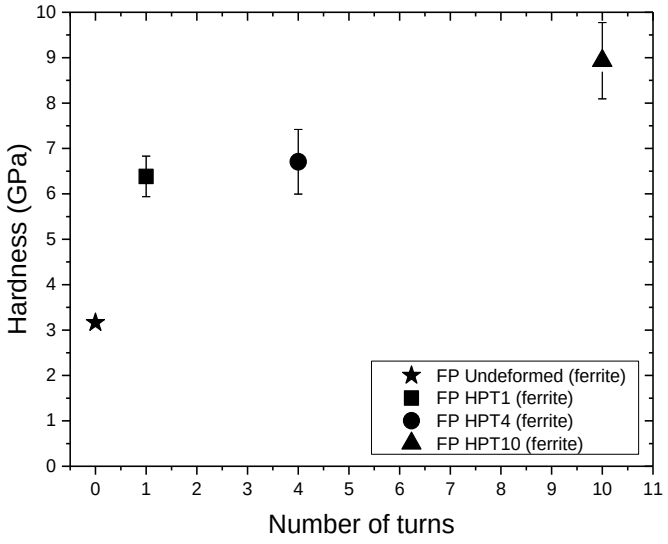

Figure 4.12 The nanohardness of the ferrite at the edge of the FP samples processed up to 1, 4, and 10 turns vs. the number of turns. Also, the average nanohardness of the ferrite in the sample annealed at 1100°C for 90 min (undeformed) is plotted for reference.

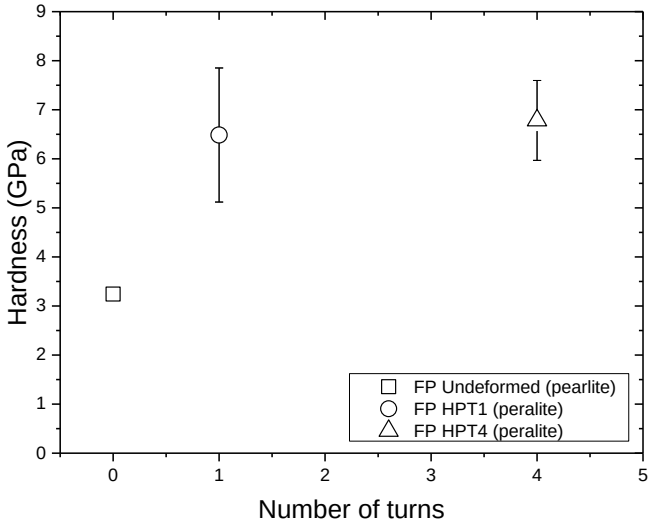

Figure 4.13 The nanohardness of the pearlite at the edge of the FP samples processed up to 1 and 4 turns vs. the number of turns. Also, the nanohardness of the pearlite in the sample annealed at 1100°C for 90 min (undeformed) is plotted for reference.

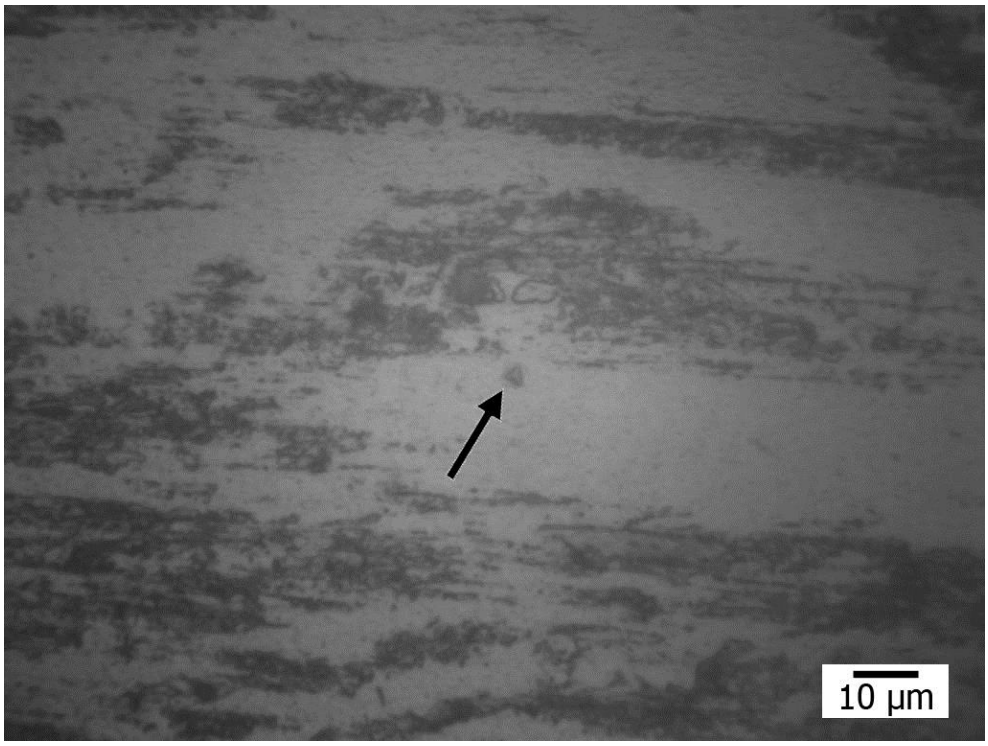

Figure 4.14 Representative optical micrograph showing the impression of one indentation in the ferrite at the edge of the FP sample processed up to 1 turn and etched with 2% nital.

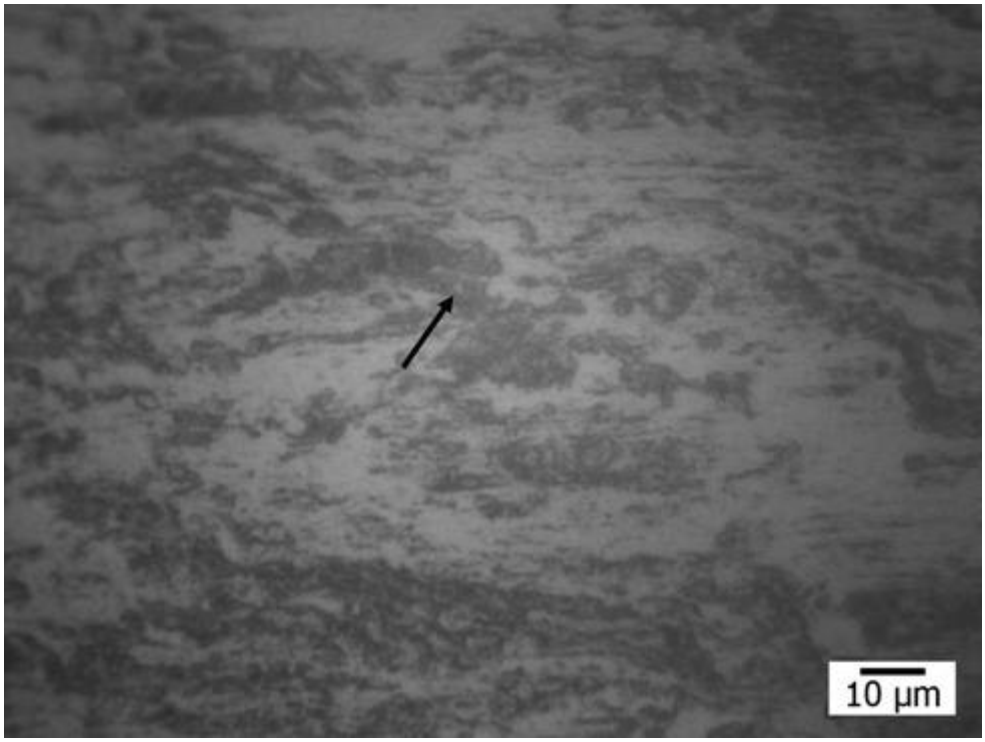

Figure 4.15 Representative optical micrograph showing the impression of one indentation in the pearlite at the edge of the FP sample processed up to 4 turns and etched with 2% nital.

4.2.5. Nanoindentation results of the FM samples

The results of the nanoindentation tests of the FM samples processed by HPT can be statistically analysed by sorting the 49 nanoindentation values from small to large and plotting them against the total number of nanoindentations as shown in Figure 4.16. The overall nanohardness of the FM processed samples increased with the number of turns up to 4 turns. The minimum and maximum nanohardness values recorded for the FM sample processed up to 1 turn (as an example) were 3.8 and 5.05 GPa, respectively. In the second microhardness test (Table 4.1), the ferrite at the centre of the FM sample processed up to 1 turn had a microhardness value of 303 Hv (3 GPa), while the martensite at the edge of the same sample had a microhardness value of 505 Hv (5 GPa), suggesting that both the nanohardness and microhardness values of the FM sample processed up to 1 turn are comparable. The nanohardness and microhardness values continued to be comparable for up to 4 turns (Figure 4.15 and Table 4.1), while deviating at 10 turns. It is believed that the discrepancy between the nanohardness and microhardness measurements of the FM sample processed up to 10 turns is due to the position of the nanoindentation measurements, (i.e. the nanoindentation readings were taken at a distance of less than 3 mm from the centre of the disk). During the

nanoindentation test of the FM processed samples, the indentation size effect (ISE) was not observed, which may be due to the large indentation depth (1 μm) that was used during the test.

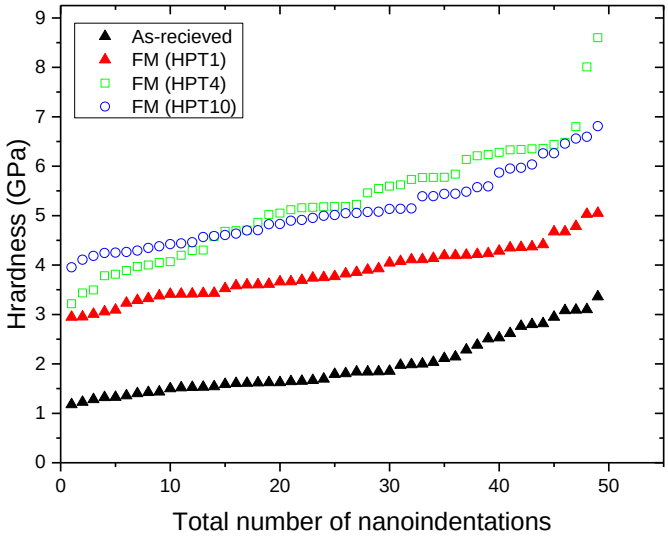

Figure 4.16 The nanohardness (GPa) vs. the total number of nanoindentations after sorting the nanoindentation results in ascending order.

4.2.6. Nanoindentation results of the FM processed samples tempered at different temperatures

The ferrite at the centre of the FM sample processed by HPT up to 4 turns and tempered at 250°C for 120 min had an average nanohardness of ~ 6.4 GPa as illustrated in Table 4.2. The ferrite nanohardness at the centre of the disk was ~ 7.5 GPa when the FM sample was processed up to 4 turns and tempered at 350°C for 90 min as illustrated in Table 4.2. The overall nanohardness of the tempered sample increased from 8 to 9 GPa when the tempering temperature increased from 250°C to 350°C as illustrated in Table 4.3.

Table 4.2 The nanohardness of the ferrite in the FM sample processed up to 4 turns and tempered at 250°C for 120 min and at 350°C for 90 min.

Sample	Position	Ferrite nanohardness (GPa)
FM (HPT4) tempered at 250°C	Centre	6.4 ± 0.3
FM (HPT4) tempered at 350°C	centre	7.5 ± 0.5

Table 4.3 The overall nanohardness of the FM sample processed up to 4 turns and tempered at 250°C for 120 min and at 350°C for 90 min.

Sample	Position	Nanohardness (GPa)
FM (HPT4) tempered at 250°C	Edge	8 ± 0.5
FM (HPT4) tempered at 350°C	Edge	9 ± 0.9

4.3 Microstructure

4.3.1. Optical microscopy and SEM results of the FP samples

Annealing the FM steel strip at 1100°C for 90 min followed by air cooling to room temperature resulted in a ferritic-pearlitic (FP) microstructure as shown in Figure 4.17. The microstructure consists mainly of coarse ferrite grains (appearing grey) and a low volume fraction of pearlite (appearing black). The pearlite colonies consist of cementite lamellae and pearlitic ferrite as shown in Figure 4.18. The volume fraction of the ferrite and pearlite in the sample annealed at 1100°C for 90 min (FP undeformed sample) was determined by the point count method [157]. Due to the variation in the volume fraction of the ferrite and pearlite from one area to another in the undeformed sample, the point count method was applied to three different areas and the three results were averaged and considered as the average volume fraction of the ferrite and pearlite in the undeformed sample. The average volume fraction of the pearlite in the sample annealed at 1100°C for 90 min (FP undeformed sample) was ~ 0.10 ± 0.04. The determination

procedures of the volume fraction of pearlite using the point count method for one area (as an example) are illustrated in Appendix A.

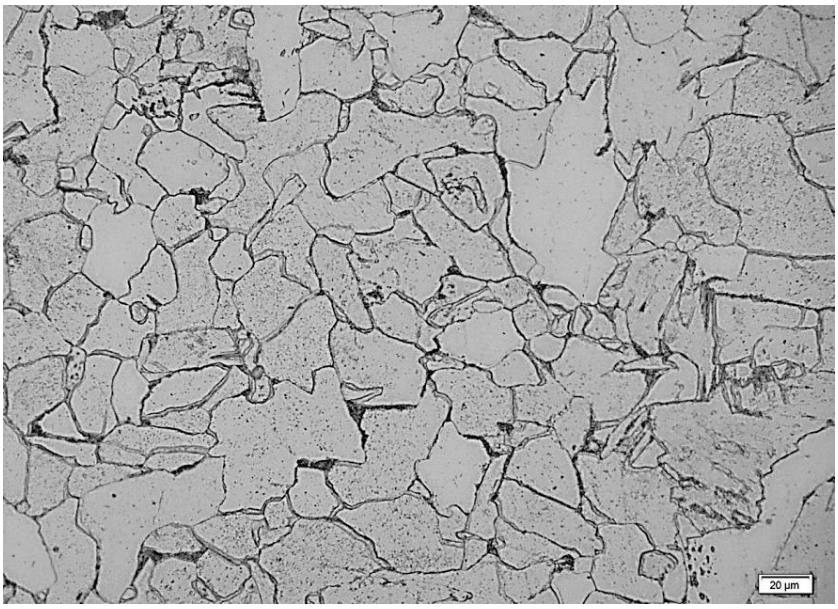

Figure 4.17 Optical micrograph showing the microstructure of the sample annealed at 1100°C for 90 min (0.1 wt.% C) and etched with 2% nital.

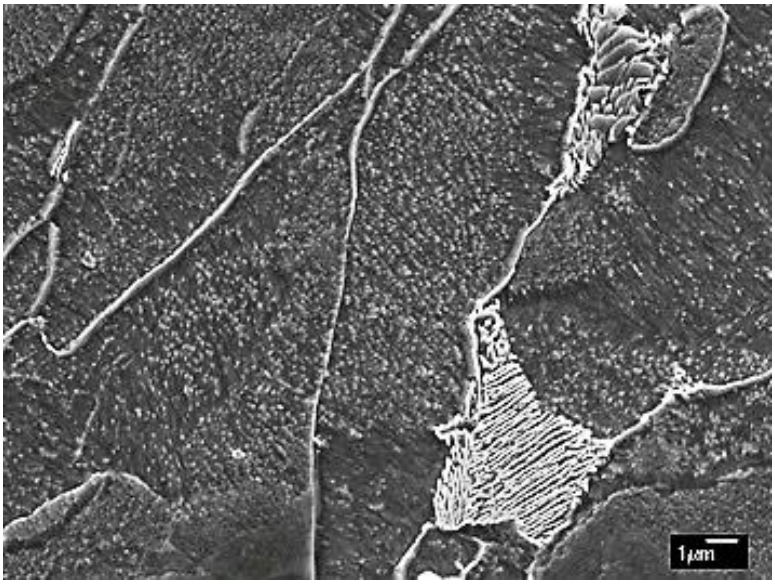

Figure 4.18 SEM micrograph (SEI mode) showing the lamellae structure in the pearlite colony at the centre of the FP sample (0.1 wt.% C) processed by HPT up to 1 turn and etched with 2% nital.

After 1 turn, there was no significant change in the microstructure at the centre of the FP sample where the grain boundaries were still visible as shown in Figure 4.19a and Figure 4.19b. However, in Figure 4.19b a slight grain refinement can be observed at the centre of the FP sample processed up to 1 turn. At the edge of the FP sample processed up to 1 turn, the pearlite colonies show a higher degree of deformation when compared with those at the centre. In general, the pearlite colonies at the edge of the FP sample processed up to 1 turn are elongated in the deformation direction as shown in Figure 4.20.

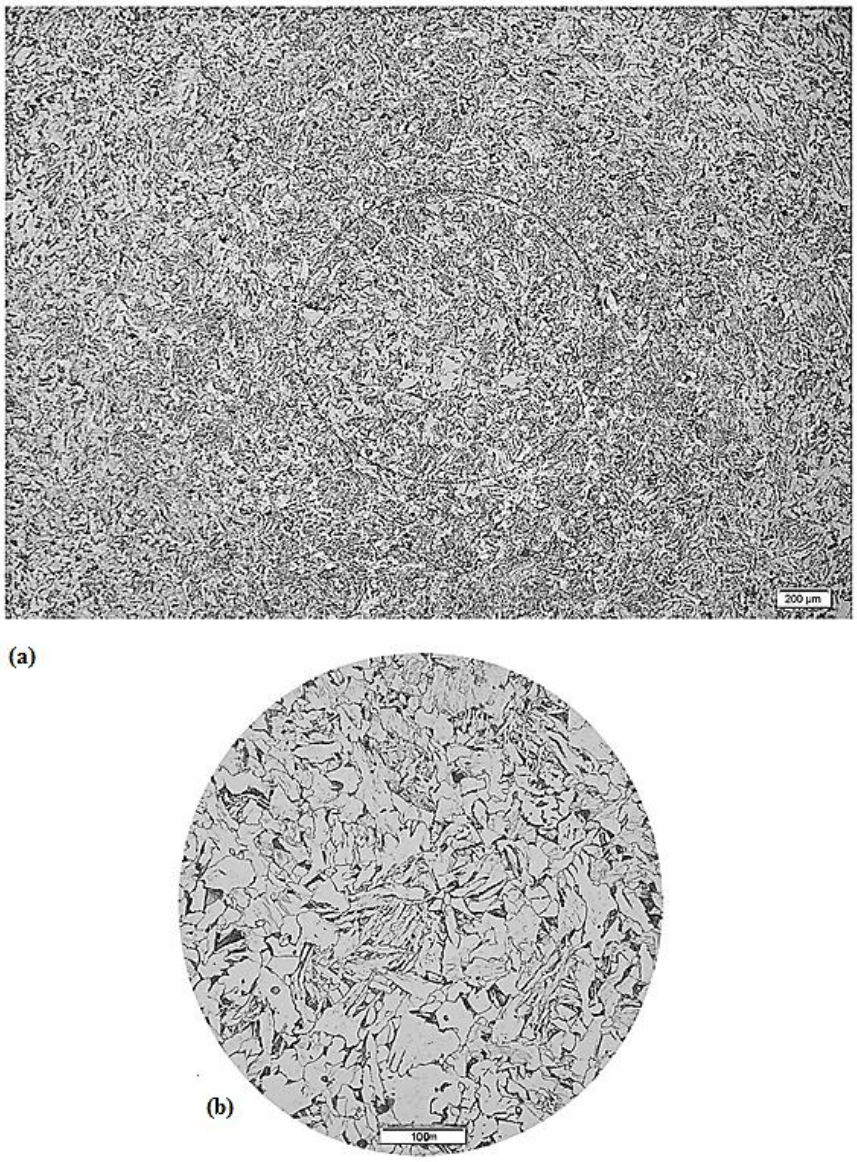

Figure 4.19 Optical micrograph (a) showing the microstructure of the FP sample (0.1 wt.% C) processed by HPT up to 1 turn and etched with 2% nital at low magnification (b) a magnified view of the region in the dashed black circle in Figure 4.18a.

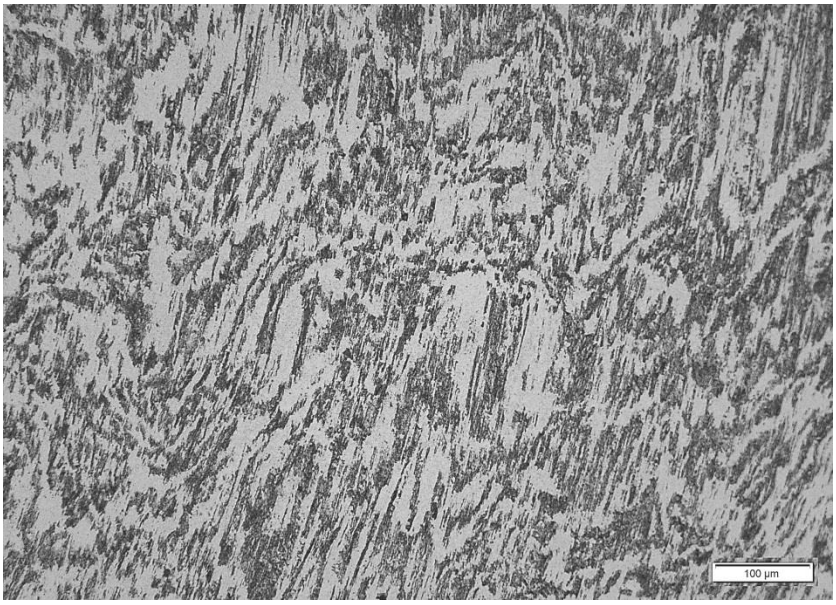

Figure 4.20 Optical micrograph showing the microstructure at the edge of the FP sample (0.1 wt.% C) processed by HPT up to 1 turn and etched with 2% nital.

After 4 turns, the ferrite grain boundaries were still visible at the centre of the disk, while the pearlite colonies continued to maintain their regular morphology as shown in Figure 4.21a and Figure 4.21b. As the distance from the centre or the strain increased, the ferrite grain boundaries became invisible and the pearlite colonies elongated in the deformation direction as shown in Figure 4.21a. At the edge of the FP sample processed up to 4 turns, the ferrite grain boundaries could no longer be seen while the pearlite colonies deformed heavily and fragmented into small pieces (or particles) of cementite as shown in Figure 4.22. However, few pearlite colonies can still be seen but heavily deformed and elongated in the deformation direction as shown in Figure 4.22.

After 10 turns, the ferrite grain boundaries were invisible at the centre of the disk (Figure 4.23) unlike the case in the FP samples processed up to 1 and 4 turns. Furthermore, no pearlite colonies with their regular morphology can be seen at the centre or the edge of the disk. Instead, a swirl appearance at the centre is visible. A fibrous microstructure was also observed at 2.5 mm from the centre in another sample processed up to 10 turns (not shown here). The cementite elongated at the centre (Figure 4.23) and heavily fragmented at the edge of the disk as shown in Figure 4.24.

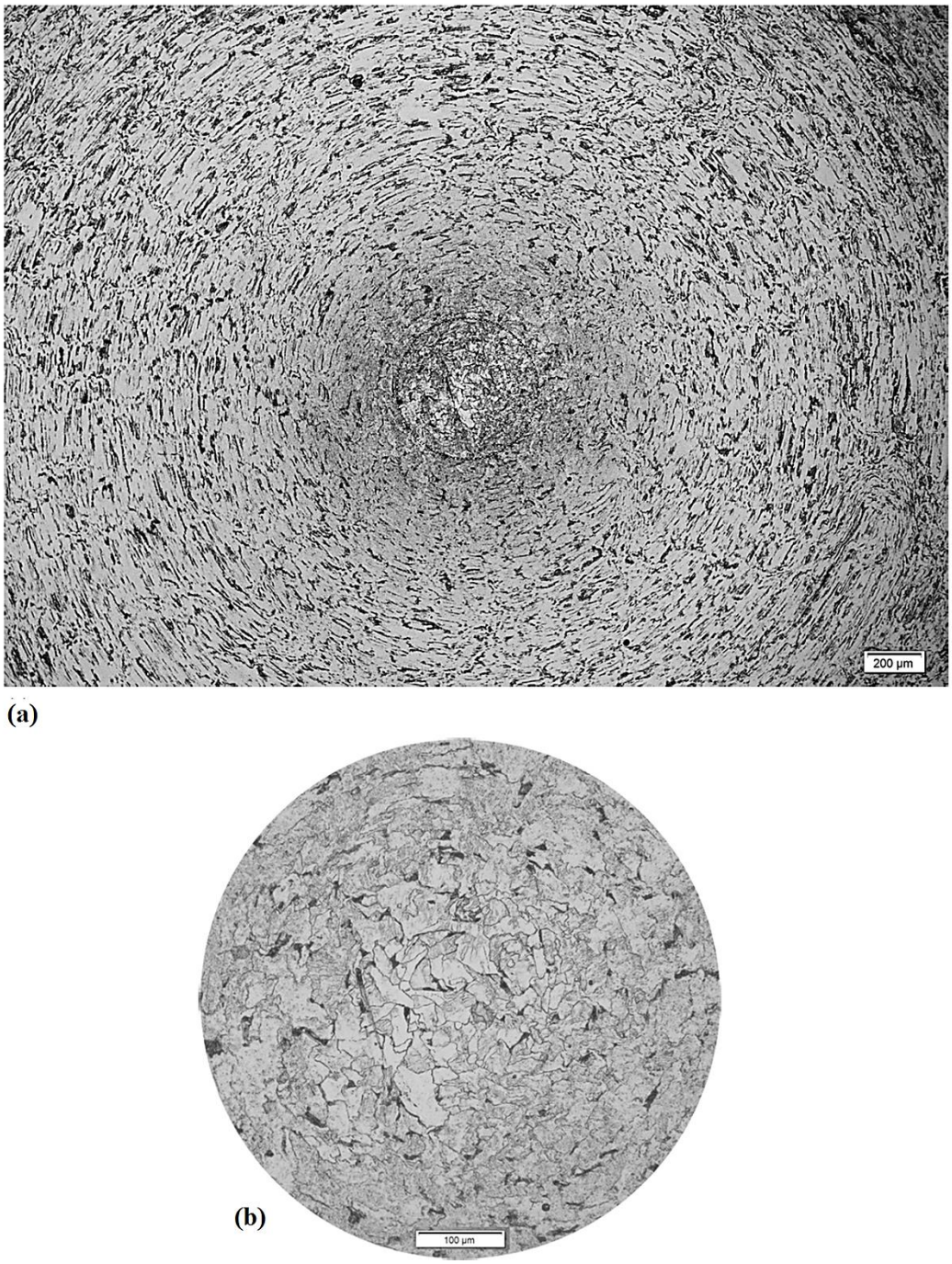

Figure 4.21 Optical micrograph (a) showing the microstructure of the FP sample (0.1 wt.% C) processed by HPT up to 4 turns and etched with 2% nital at low magnification (b) a magnified view of the region in the dashed black circle in Figure 4.20a.

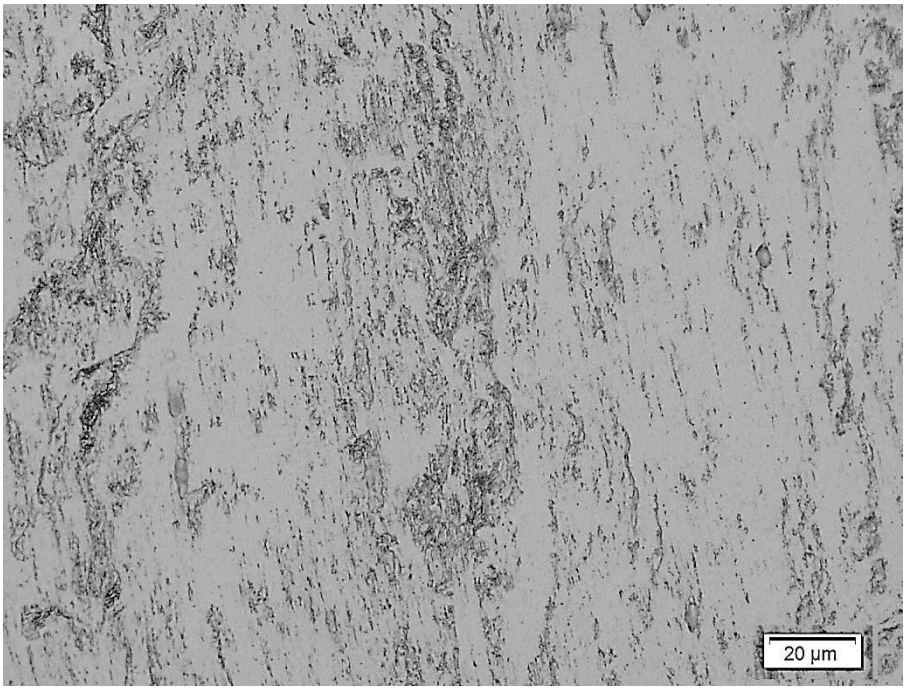

Figure 4.22 Optical micrograph showing the microstructure at the edge of the FP sample (0.1 wt.% C) processed up to 4 turns and etched with 2% nital.

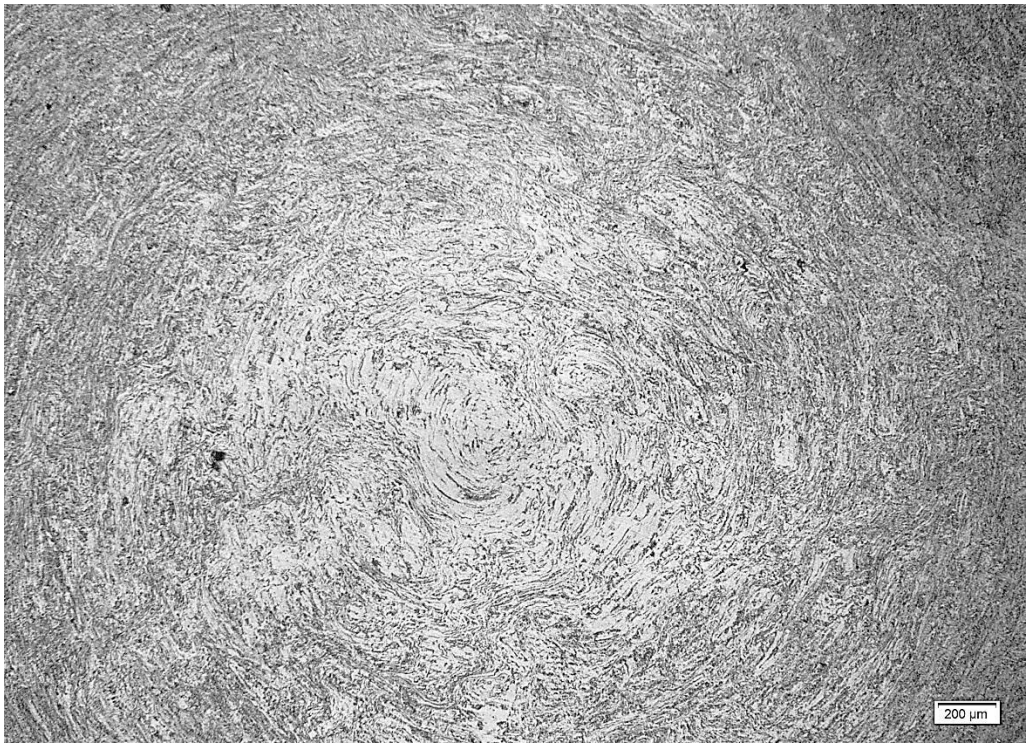

Figure 4.23 Optical micrograph showing the microstructure at the centre of the FP sample (0.1 wt.% C) processed up to 10 turns and etched with 2% nital.

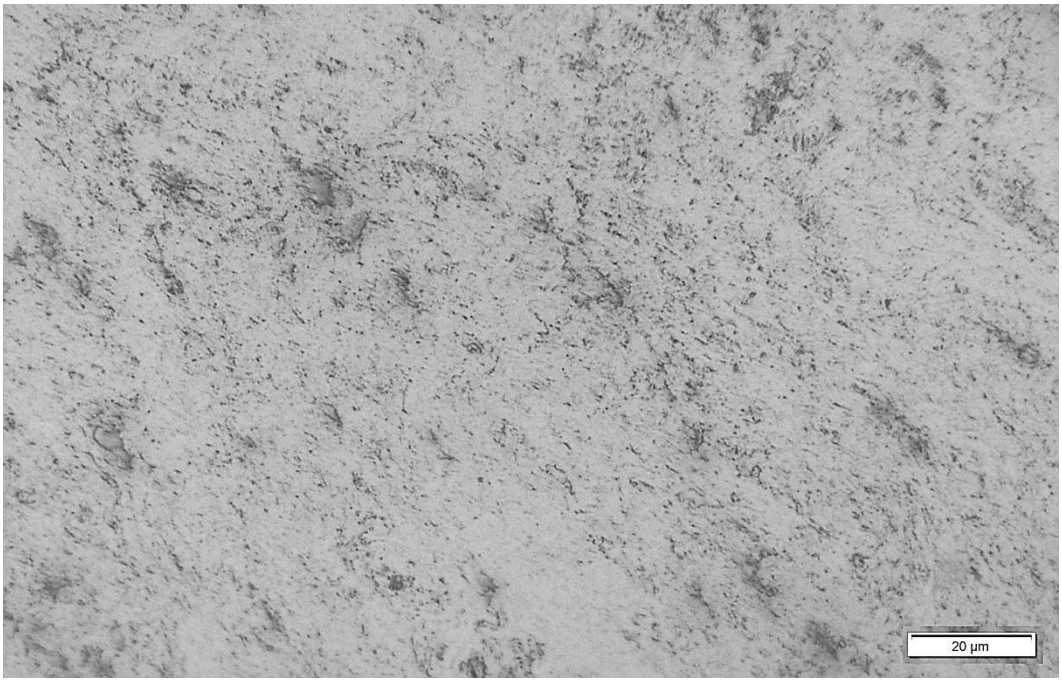

Figure 4.24 Optical micrograph showing the microstructure at the edge of the FP sample (0.1 wt.% C) processed up to 10 turns and etched with 2% nital.

4.3.2. Optical microscopy and SEM results of the FM samples

The as-received sample had a microstructure that consisted of a ferrite matrix and martensite islands as shown in Figure 4.25. The volume fraction of the martensite in the as-received sample was determined by the point count method [157]. Due to the variation in the volume fraction of the martensite in the as-received sample from one area to another, the point count method was applied to three different areas and the three results were averaged and considered as the average volume fraction of martensite. The average volume fraction of the martensite in the as-received sample was found to be as ~ 0.15±0.05.

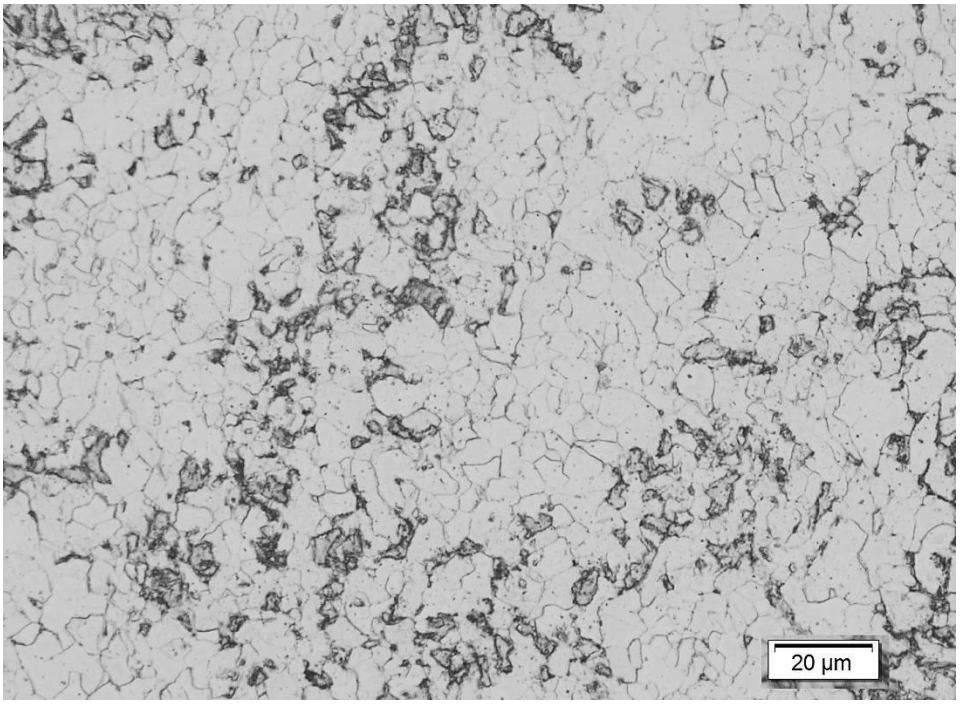

Figure 4.25 Optical micrograph showing the microstructure of the as-received sample (0.1 wt.% C) etched with 2% nital.

The microstructure at the centre of the FM sample processed up to 1 turn is shown in Figure 4.26. Although grain refinement took place at the centre of the FM sample processed up to 1 turn, it is still possible to see the ferrite grain boundaries. The microstructure at the edge of the FM sample processed up to 1 turn is shown in Figure 4.27. The grain boundaries are not visible anymore and only traces of deformation could be observed. The second phase, the martensite phase, elongated in the deformation direction and fragmented into small islands of ~ 4-6 µm.

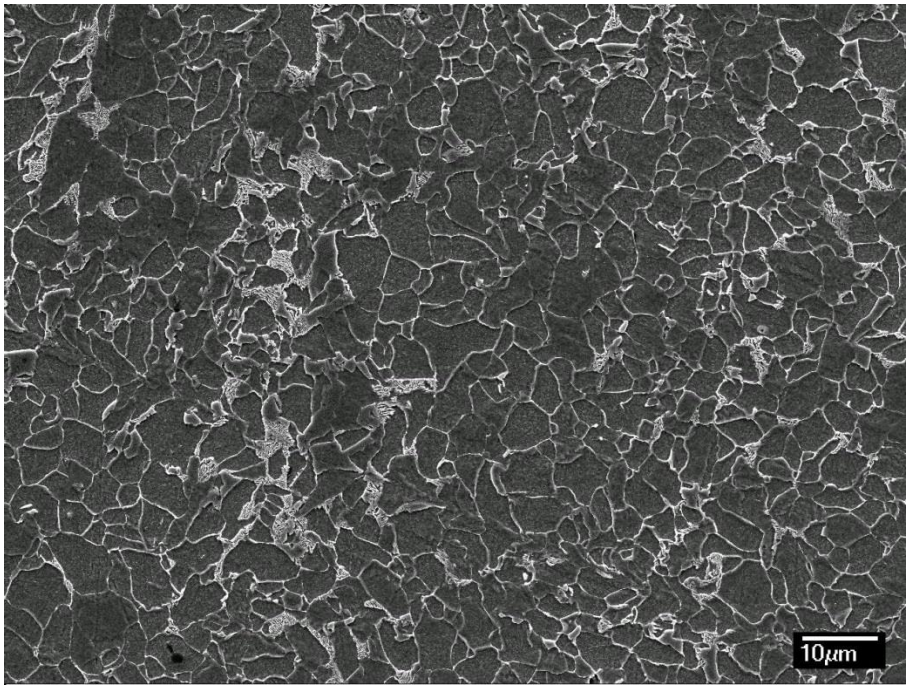

Figure 4.26 SEM micrograph (SEI mode) showing the microstructure at the centre of the FM sample (0.1 wt.% C) processed by HPT up to 1 turn and etched with 2% nital.

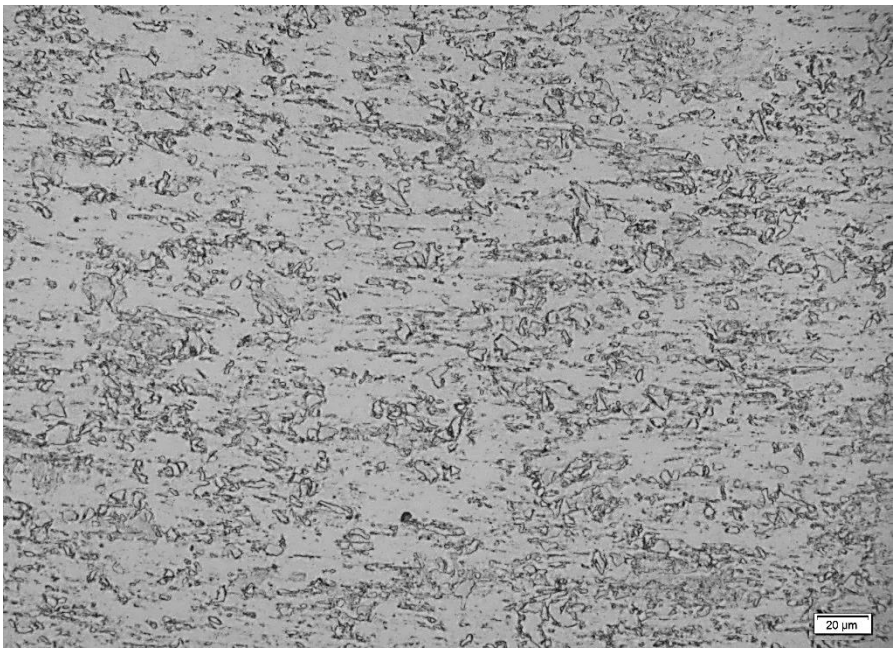

Figure 4.27 Optical micrograph showing the microstructure at the edge of the FM sample (0.1 wt.% C) processed up to 1 turn and etched with 2% nital.

The microstructure at the centre of the FM sample processed up to 4 turns is shown in Figure 4.28. The grain boundaries are not visible but the two phases can be readily distinguished. The second phase (martensite) is fragmented into irregular shapes. The microstructure at the edge of the FM sample processed up to 4 turns is illustrated in Figure 4.29 where the two phases can still be distinguished and the second phase is fragmented into about 4 μm fragments.

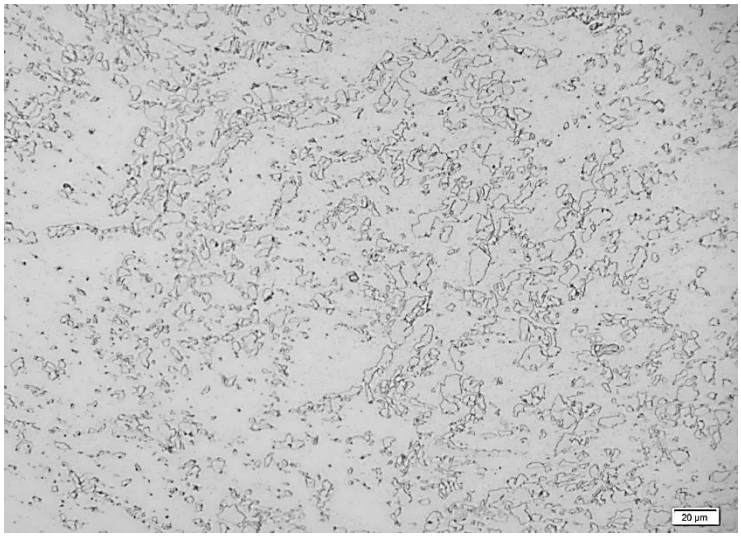

Figure 4.28 Optical micrograph showing the microstructure at the centre of the FM sample (0.1 wt.% C) processed up to 4 turns and etched with 2% nital.

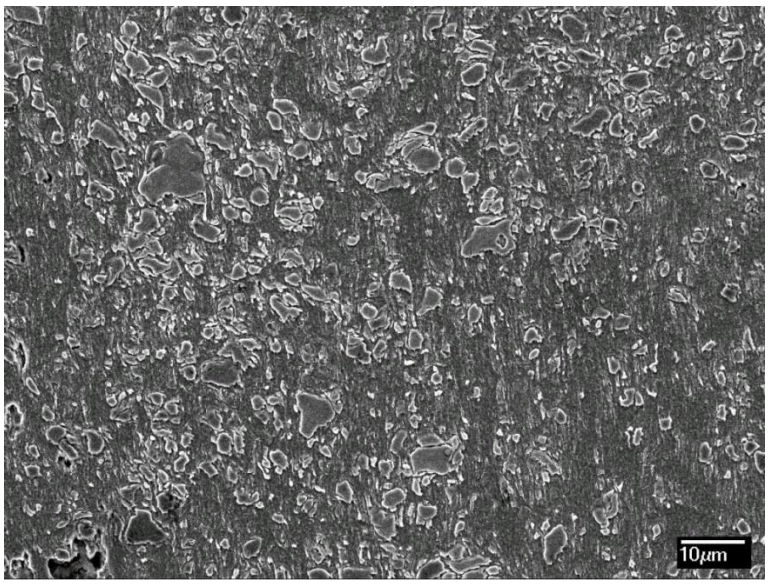

Figure 4.29 SEM micrograph (SEI mode) showing the microstructure at the edge of the FM sample (0.1 wt.% C) processed by HPT up to 4 turns and etched with 2% nital.

The microstructure at the centre and the edge of the FM sample processed up to 10 turns is shown in Figure 4.30 and Figure 4.31 At this high number of turns, it is believed that refinement continued to take place at the centre and the edge of the disk where martensite islands of about 3 μm and 1 μm size can be seen at the centre and the edge of the disk, respectively.

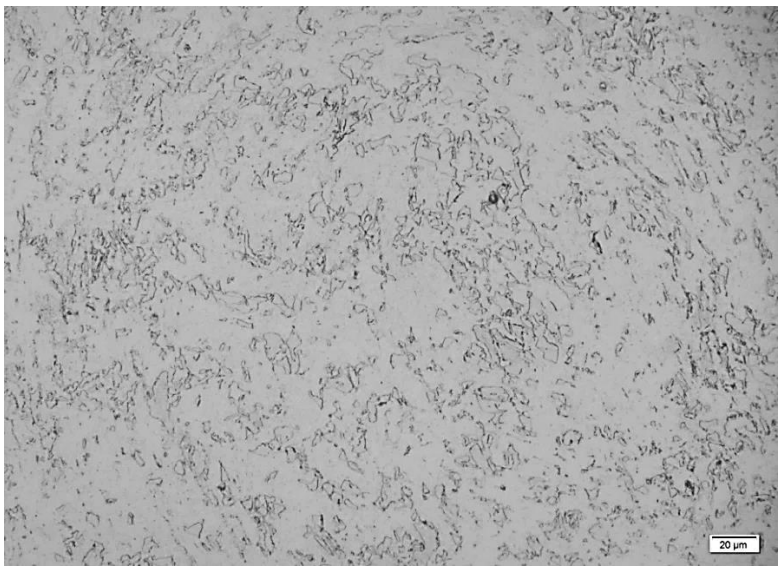

Figure 4.30 Optical micrograph showing the microstructure at the centre of the FM sample (0.1 wt.% C) processed up to 10 turns and etched with 2% nital.

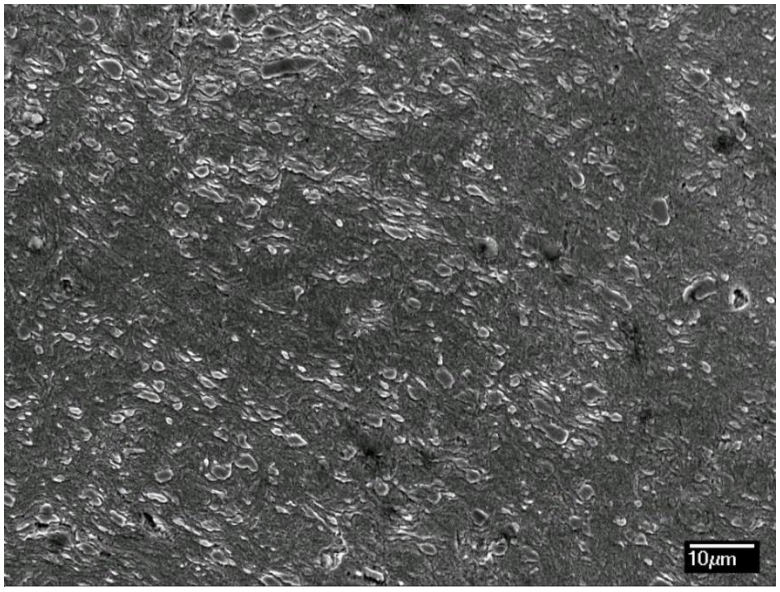

Figure 4.31 SEM micrograph (SEI mode) showing the microstructure at the edge of the FM sample (0.1 wt.% C) processed by HPT up to 10 turns and etched with 2% nital.

4.3.3. Optical microscopy and SEM results of the FM processed samples tempered at different temperatures

Tempering the FM sample processed up to 4 turns at 150°C and 250°C for 120 min did not result in any significant changes in the microstructure (e.g. Figure 4.32). The microstructure in Figure 4.32 consists of ferrite matrix and tempered martensite. It is well-known that martensite is supersaturated with carbon and decomposes when tempered. At 250°C and above, the diffusion coefficient of the carbon atoms in the martensite increases to values that allow some diffusion to occur, and consequently, the carbon atoms diffuse into the ferrite matrix leading to a gradual decomposition of the martensite. Investigating the microstructure of the FM sample processed up to 4 turns and tempered at 350°C and 450°C for 90 min by optical microscopy revealed that the microstructure consisted of temper martensite and ferrite matrix as shown in Figure 4.33 and Figure 4.34, respectively.

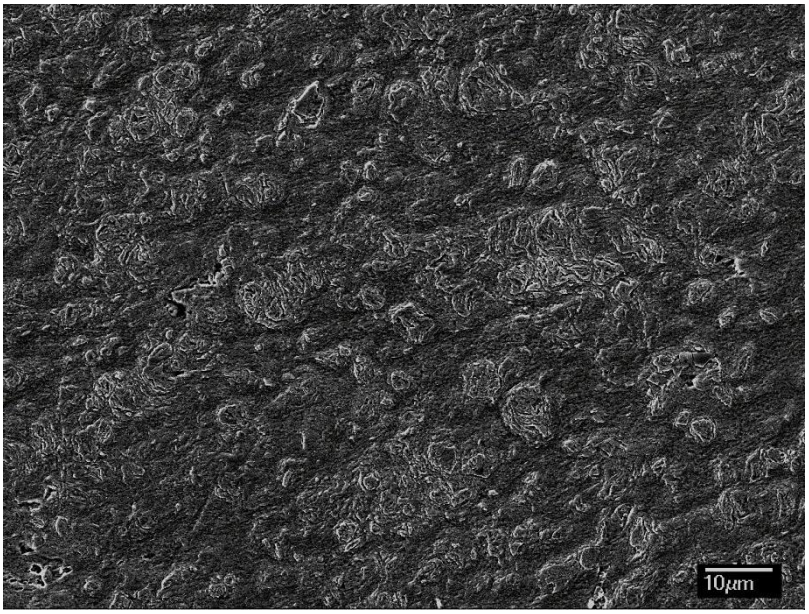

Figure 4.32 SEM micrograph (SEI mode) showing the microstructure at the edge of the FM sample (0.1 wt.% C) processed by HPT up to 4 turns and tempered at 250°C for 120 min and etched with 2% nital.

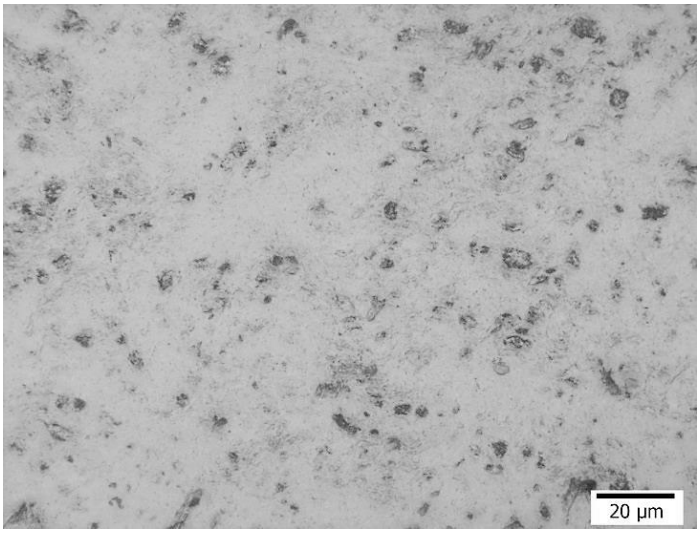

Figure 4.33 Optical micrograph showing the microstructure at the edge of the FM sample (0.1 wt.% C) processed up to 4 turns and tempered at 350°C for 90 min and etched with 2% nital.

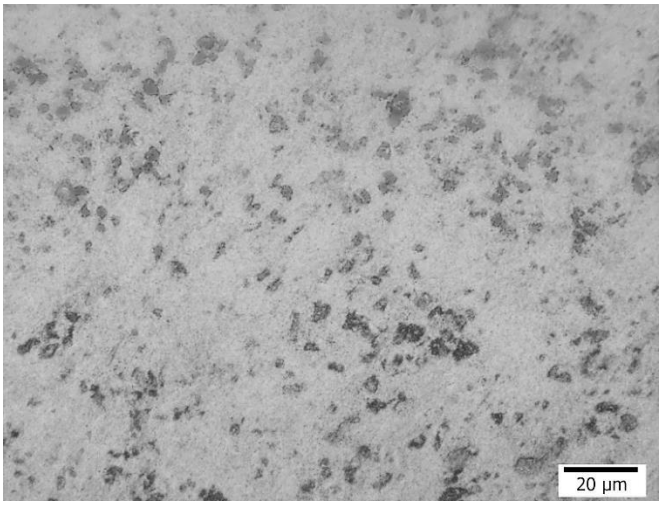

Figure 4.34 Optical micrograph showing the microstructure at the edge of the FM sample (0.1 wt.% C) processed up to 4 turns and tempered at 450°C for 90 min and etched with 2% nital.

Limited formation of cementite particles was observed (Figure 4.35) whereas extensive formation of cementite particles was observed in the sample tempered at 450°C as shown in Figure 4.36 and Figure 4.37. The cementite particles were mostly distributed homogeneously, with some limited local increases in number density, as shown in Figure 4.38. In general, the cementite particles have an equi-axed shape whist very few particles are elongated. The point count method was used to determine the volume fraction of the cementite particles in the sample tempered at 450°C (for details, see Appendix A). The volume fraction of cementite was determined as 0.05±0.01.

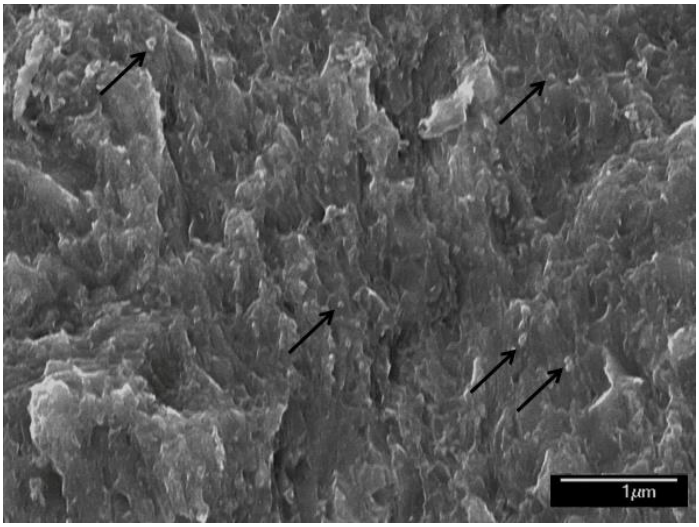

Figure 4.35 SEM micrograph (SEI mode) showing the microstructure at the edge of the FM sample (0.1 wt.% C) processed by HPT up to 4 turns and tempered at 350°C for 90 min and etched with 2% nital. Cementite particles are indicated by black arrows.

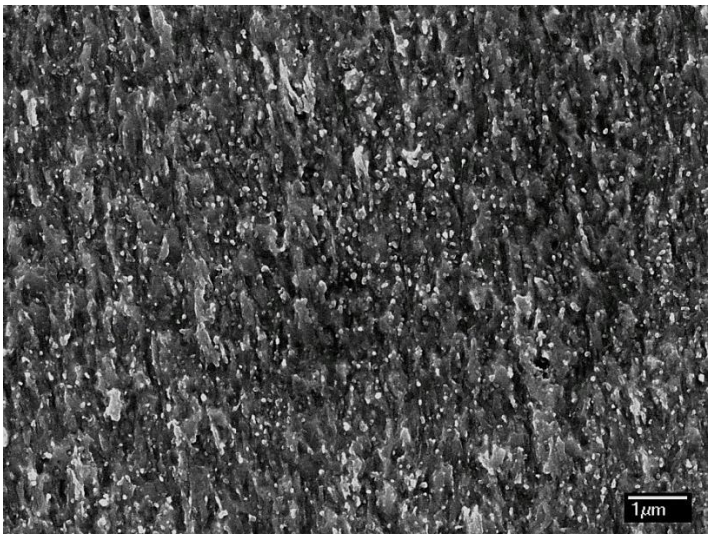

Figure 4.36 SEM micrograph (SEI mode) showing the microstructure (low magnification) at the edge of the FM sample (0.1 wt.% C) processed by HPT up to 4 turns and tempered at 450°C for 90 min and etched with 2% nital.

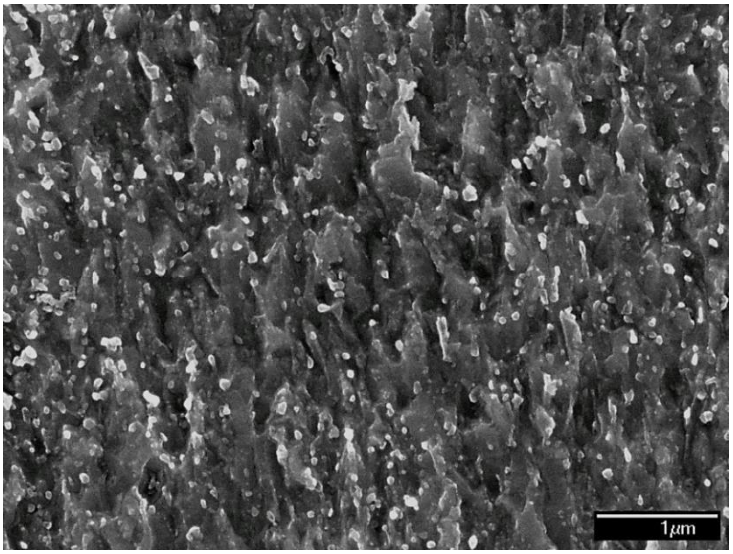

Figure 4.37 SEM image (SEI mode) showing the microstructure (high magnification) at the edge of the FM sample (0.1 wt.% C) processed up to 4 turns and tempered at 450°C for 90 min and etched with 2% nital.

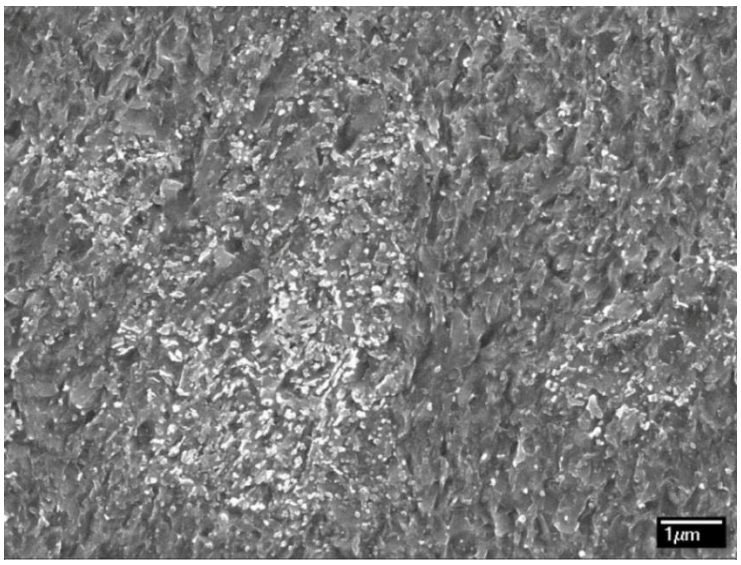

Figure 4.38 SEM image (SEI mode) showing the microstructure at the centre of the FM sample (0.1 wt.% C) processed up to 4 turns and tempered at 450°C for 90 min and etched with 2% nital.

Tempering the FM sample processed up to 4 turns at 550°C resulted in a microstructure consisting of recrystallized ferrite and coarse cementite particles as shown in Figure 4.39 to Figure 4.41. The recrystallized ferrite grain size was estimated

to be ~ 1 μm. Limited grain growth was observed at the centre of the tempered sample at this temperature.

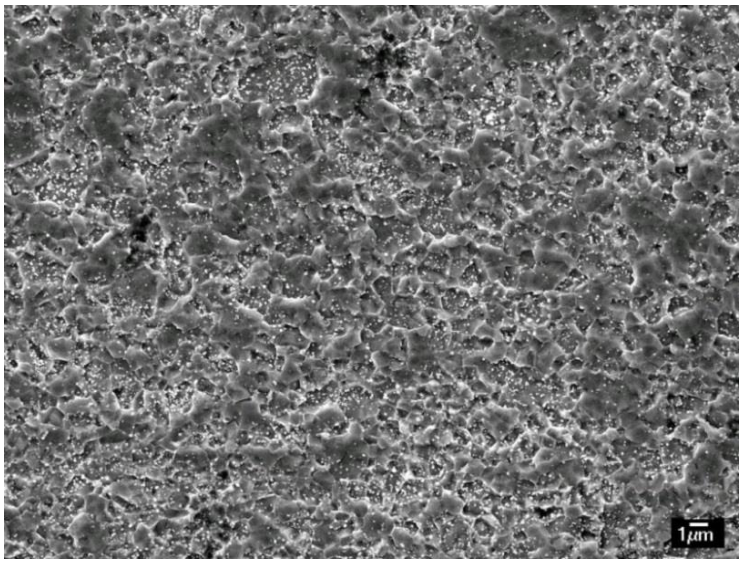

Figure 4.39 SEM image (SEI mode) showing the microstructure at the edge of the FM sample (0.1 wt.% C) processed up to 4 turns and tempered at 550°C for 90 min and etched with 2% nital.

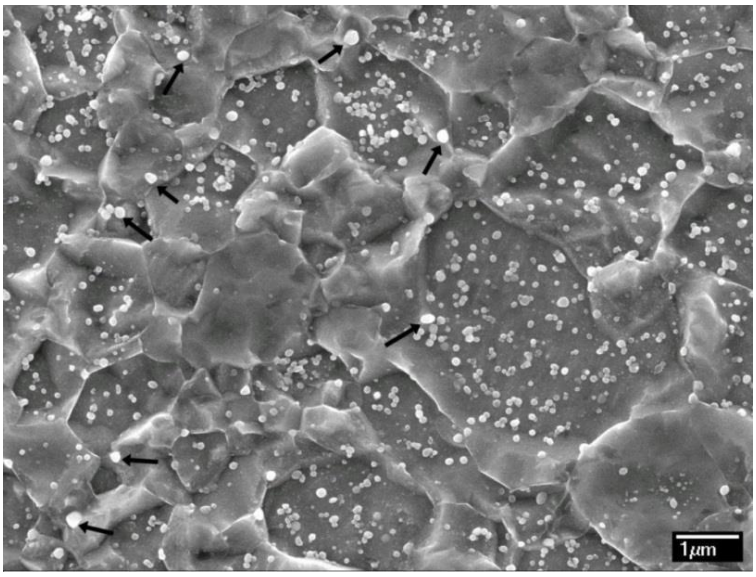

Figure 4.40 SEM image (SEI mode) showing the microstructure at the centre of the FM sample (0.1 wt.% C) processed up to 4 turns and tempered at 550°C for 90 min and etched with 2% nital.

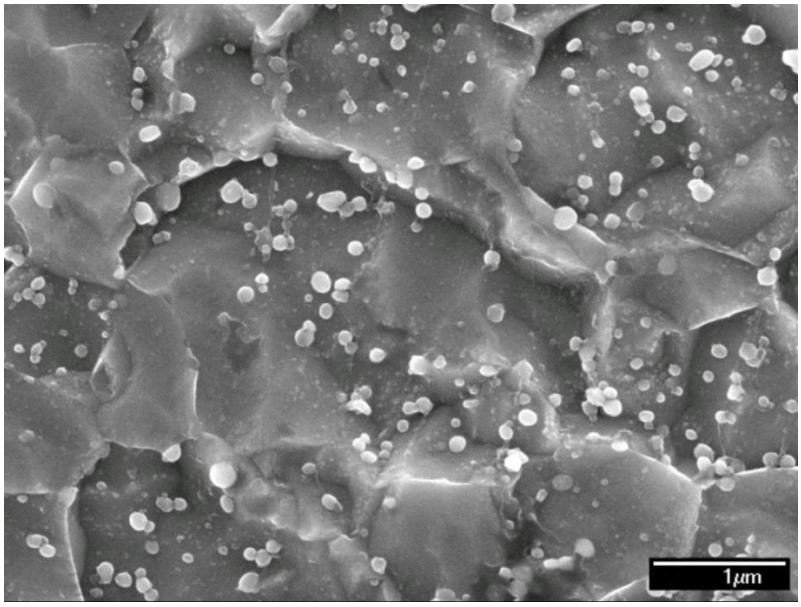

Figure 4.41 SEM image (SEI mode) showing the microstructure at the edge of the FM sample (0.1 wt.% C) processed up to 4 turns and tempered at 550°C for 90 min and etched with 2% nital.

4.3.4. TEM results of the FM samples

Figure 4.42a and Figure 4.42b are TEM bright-field images of the microstructure of the FM sample processed up to 1 turn at the centre and edge, respectively. The microstructures in Figure 4.42a and Figure 4.42b represents typical microstructures of severely plastically deformed steel where no well-defined grain boundaries can be seen but, instead, grains with high dislocation density are visible. The high magnification TEM image of a sample after one turn of HPT processing in Figure 4.43 shows one grain subdivided into several subgrains, as shown by the arrows. During the TEM investigation, indivual dislocations could not be detected while, in contrast, the clustered dislocations could be easily detected as shown in Figure 4.44.

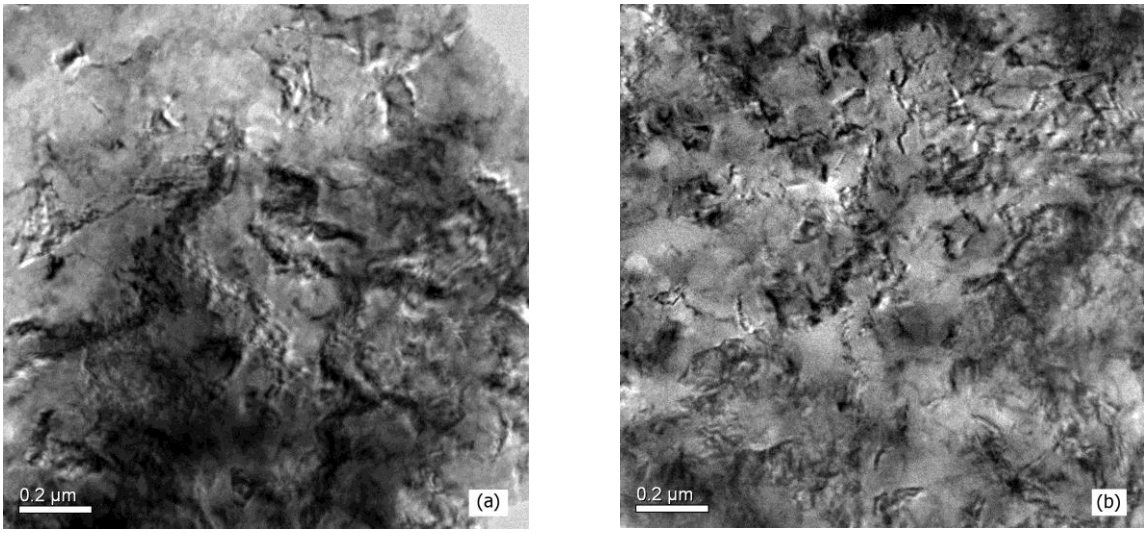

Figure 4.42 TEM image showing the microstructure of the FM sample processed by HPT up to 1 turn at (a) the centre and (b) the edge of the disk.

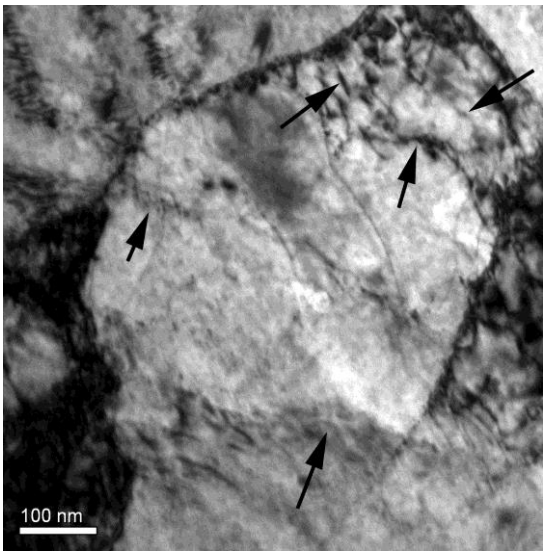

Figure 4.43 TEM bright field image showing the formation of new subgrains after 1 turn of HPT processing of the FM sample.

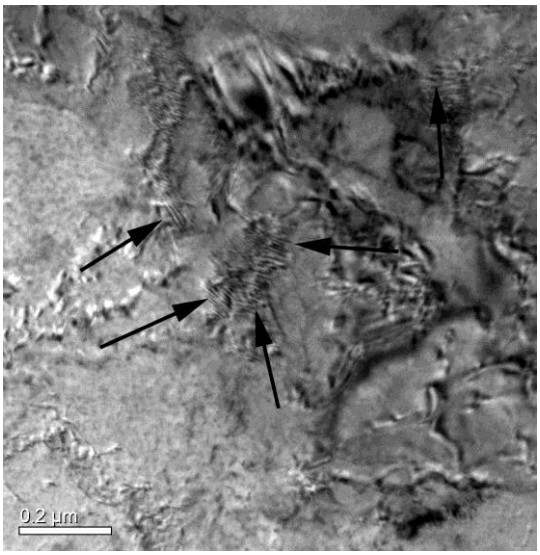

Figure 4.44 TEM bright field image showing clustered dislocations in the FM sample processed by HPT up to 1 turn.

Figure 4.45a and Figure 4.45b are TEM bright-field images showing the microstructure of the FM sample processed up to 4 turns at the centre and edge, respectively. The microstructures at the centre and the edge of the disk are, again, characterised by ill-defined grain boundaries. The SAD pattern in Figure 4.46 shows the presence of a high number of diffuse spots which suggests fine grains are present. Also for this location, clustered and elongated spots are present, indicating the presence of low angle grain boundaries. Figure 4.47a and Figure 4.47b are bright-field images showing the microstructure of the FM sample processed up to 10 turns at the centre

and the edge, respectively. Figures 4.47a and Figure 4.47b show a highly distorted microstructure in which individual features are difficult to resolve.

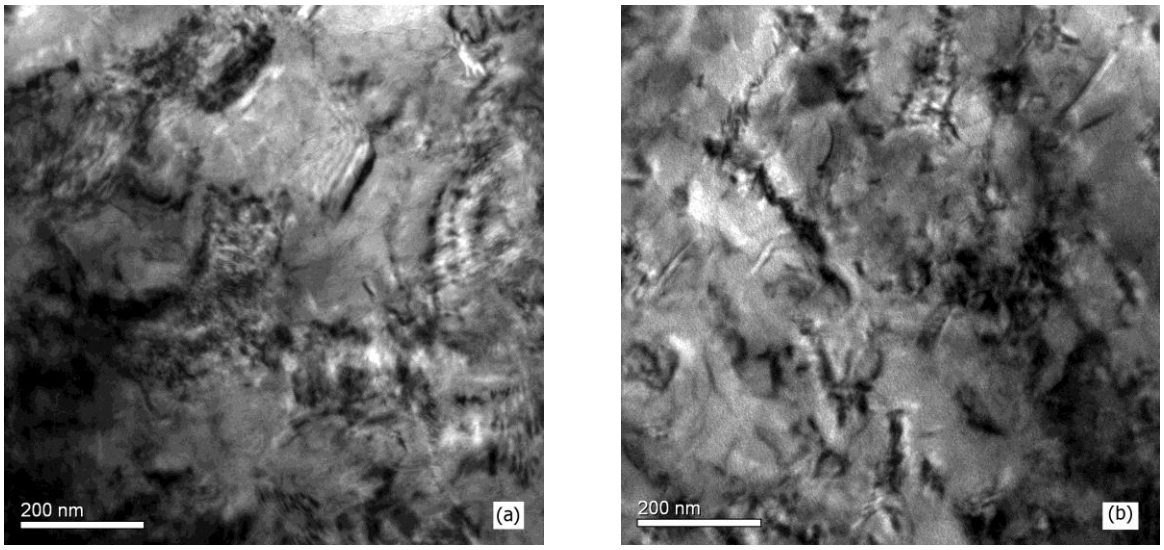

Figure 4.45 TEM bright field images showing the microstructure of the FM sample processed by HPT up to 4 turns at (a) the centre and (b) the edge of the disk.

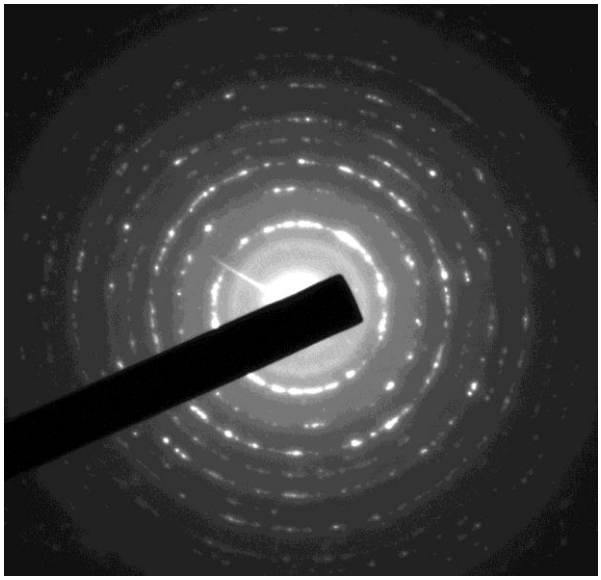

Figure 4.46 A selected area diffraction pattern at the edge of the FM sample processed up to 4 turns. The SAD area = 2.4 μm^2.

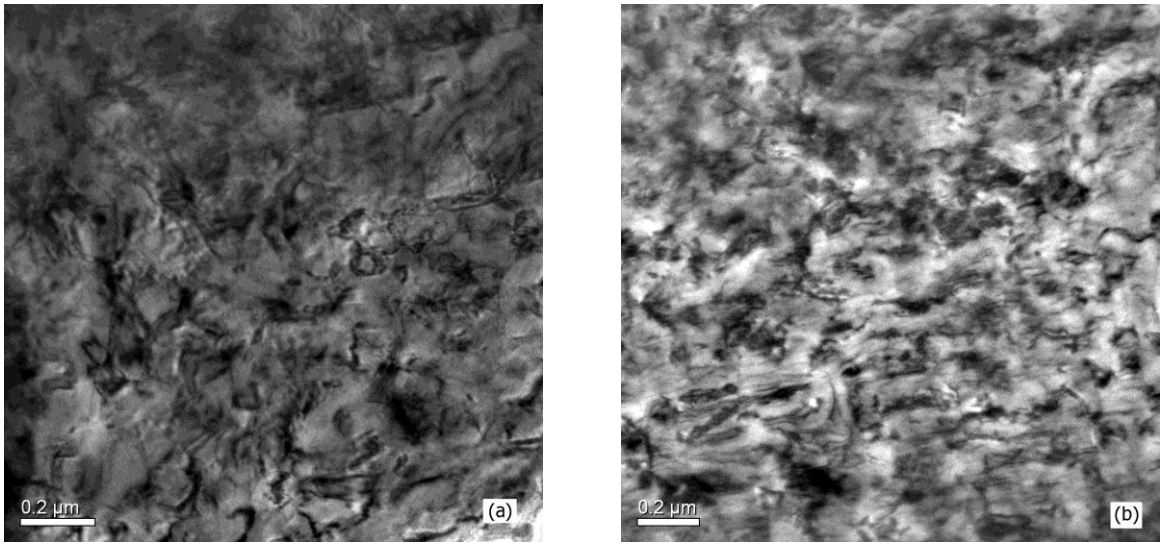

Figure 4.47 TEM bright field images showing the microstructure of the FM sample processed by HPT up to 10 turns at (a) the centre and (b) the edge of the disk.

4.4 XRD results

4.4.1. XRD results of the FP samples

XRD line profiles for the sample annealed at 1100^{o}C for 90 min (FP undeformed sample) and the FP processed samples were recorded and shown in Figure 4.48. The software Fityk 0.9.8 [158] and Origin 9.1 [159] were used to fit the line profiles, measure the full width at half maxima (FWHM), and for separating the overlapped peaks. Furthermore, several methods of line broadening analysis such as the modified Williamson-Hall and the Multiple Whole Profile-fit (MWP-fit) method were used in the current analysis. Due to the modern diffractometer (Rigaku SmartLab) used in the test and the substantial deformation of the samples, the instrumental broadening can be considered negligible in comparison to the line broadening caused by the sample.

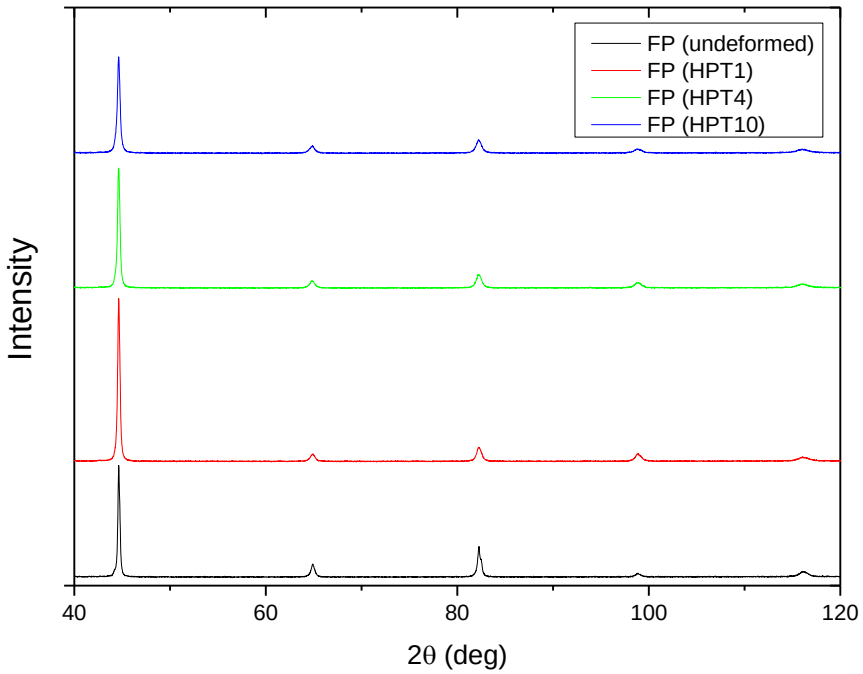

Figure 4.48 XRD line profiles of the sample annealed at 1100°C for 90 min (FP undeformed sample) and the FP samples processed by HPT up to 1, 4, and 10 turns.

Five peaks (110, 200, 211, 220, and 310) were included in the current XRD analysis. The lattice parameter (a) of the ferrite of the sample annealed at 1100°C for 90 min (FP undeformed sample) and the FP processed samples was calculated according to Cohen method [160]. Five values of the lattice parameter of the ferrite, corresponding to each individual peak, were obtained. The ferrite lattice parameter is taken as the average of these five values. Table 4.4 shows the calculation of the lattice parameter (a) of the ferrite of the sample annealed at 1100°C for 90 min, as an example. The lattice parameter of the ferrite does not show any systematic variation with θ which is an additional indication that the method and alignment is reliable. The lattice parameter values of the ferrite of the sample annealed at 1100°C for 90 min (FP undeformed sample) and the FP samples processed by HPT up to 1, 4, and 10 turns are shown in Table 4.5.

Table 4.4 Calculation of the lattice parameter (a) of the ferrite from XRD spectra for the sample annealed at 1100°C for 90 min (FP undeformed sample).

Peak no	**2θ**	***Sin*² θ**	***hkl***	$s=(h^2+k^2+l^2)$	$\frac{\sin^2\theta}{s}=\frac{\lambda^2}{4a^2}$	a **(nm)**
1	44.64	0.14423	110	2	0.072	0.2867
2	64.92	0.28806	200	4	0.072	0.2869
3	82.26	0.43266	211	6	0.072	0.2867
4	98.86	0.57701	220	8	0.072	0.2867
5	116.2	0.72075	310	10	0.072	0.2868

Table 4.5 The lattice parameter (a) values of the ferrite of the sample annealed at 1100°C for 90 min (FP undeformed sample) and the FP samples processed by HPT up to 1, 4, and 10 turns.

Sample	**Lattice parameter (nm)**
Annealed	0.2868 ± 0.0001
Ann+HPT1	0.2868 ± 0.0002
Ann+HPT4	0.2869 ± 0.0002
Ann+HPT10	0.2868 ± 0.0001

4.4.2. XRD results of the FM samples

XRD line profiles for the as-received and the FM processed samples were recorded and shown in Figure 4.49. Following the same procedures as in Section 4.4.1, (i.e. Cohen method [160]) the lattice parameter (a) of the ferrite of the as-received and the FM samples processed up to 1, 4, and 10 turns were determined and listed in Table 4.6.

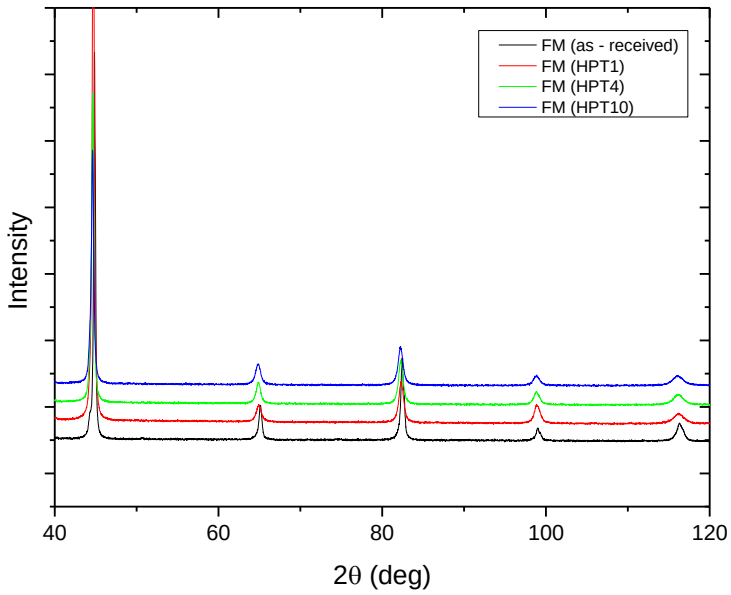

Figure 4.49 XRD line profiles of the as-received and the FM samples processed by HPT up to 1, 4, and 10 turns.

Table 4.6 The ferrite lattice parameter (a) values calculated for the FM samples processed by HPT up to 1, 4, and 10 turns.

Sample	Lattice parameter (nm)
As-received	0.2866±0.0005
FM (HPT1)	0.2867 ± 0.0003
FM (HPT4)	0.2868 ± 0.0002
FM (HPT10)	0.2870 ± 0.0002

Figure 4.50 represents one magnified *hkl* reflection (200) in the recorded patterns of the as-received and FM processed samples. It is clear from Figure 4.50 that the peak centre shifted to the lower angle side, on the 2θ-axis, as the number of HPT turns increased up to 10 turns (i.e. the ferrite lattice parameter (a) increased with HPT processing up to 10 turns). When solute atoms, such as carbon or nitrogen atoms, occupy the interstitial sites in the ferrite, expansion in the ferrite lattice parameter takes place. In the current study, it is unlikely that the solute atoms are nitrogen atoms due to the low nitrogen content in the current material (0.003 wt.% N). During the HPT processing, the large strain imposed on the processed sample and the small increase in the processing temperature may lead to partial decomposition of the metastable

martensite, (i.e. some carbon atoms may leave the supersaturated martensite and occupy the interstitial sites in the ferrite matrix). Another possible source of the interstitial carbon atoms may be a small amount of cementite present in the FM samples which decomposes during HPT processing, as several researchers have observed small amounts of cementite in FM steel [127, 134, 161]. It is believed that in the current study the dissolved carbon atoms, either from cementite dissolution or martensite partial decomposition, formed the supersaturated solid solution in ferrite during the HPT processing of the FM sample. However, further investigation is needed to confirm the source of the dissolved carbon atoms. It is worth to note that line broadening increases as the number of turns increases up to 10 turns (Figure 4.50).

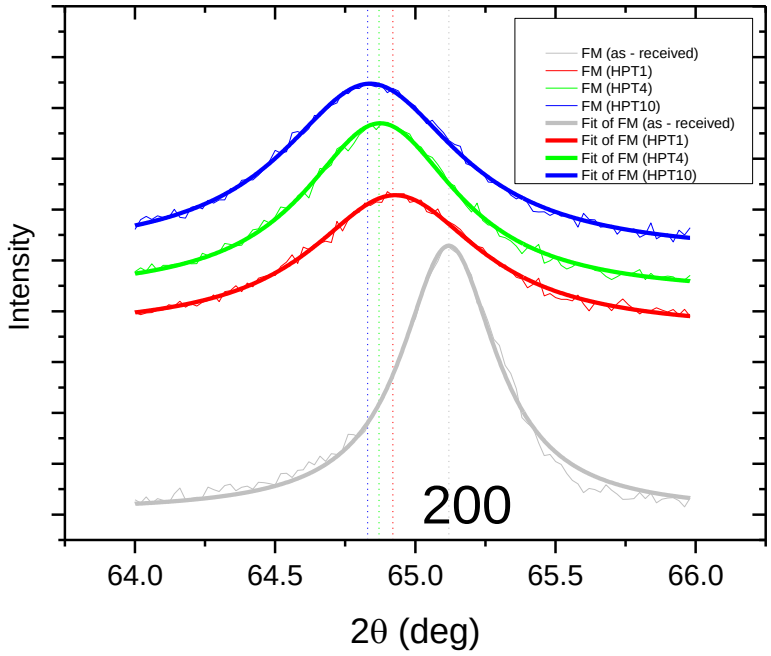

Figure 4.50 A magnified *hkl* reflection (200) in the patterns of the as-received and the FM samples processed up to 1, 4, and 10 turns. In this figure, the thin curves are the measured patterns while the thick (smooth) curves are the fitted curves. The Gauss function was used to fit the measured data. The dotted lines are the centre of the fitted curves.

Close Investigation of the XRD line profiles of the as-received and FM processed samples (Figure 4.49) reveals no martensite reflections. At the low carbon content in the current material, the martensite will possess a body-centred cubic (BCC) structure [50, 162] and consequently $a = c$ (according to [50]). Theoretically, both the ferrite and

martensite have the same crystal structure and very close lattice parameters (*a*) due to the low carbon content in the current material and hence heavily overlapped peaks of the ferrite and martensite are expected in case an appreciable fraction of martensite is present [50]. However, no overlapped peaks have been detected in the current group (FM samples) and this can be confirmed by the complete symmetry of the peaks recorded in the current group (FM samples). A plausible reason for the absence of the martensite reflections is the small volume fraction of martensite in the current material which is ~ 15%.

4.4.3. XRD results of the FM processed samples tempered at different temperatures

XRD line profiles of the FM sample processed up to 4 turns and tempered at different temperatures were recorded and are shown in Figure 4.51. Following the same procedures as in Section 4.4.1 (Cohen method [160]), the lattice parameter (*a*) of the ferrite of the FM sample processed up to 4 turns and tempered at different temperatures were determined and results are listed in Table 4.7.

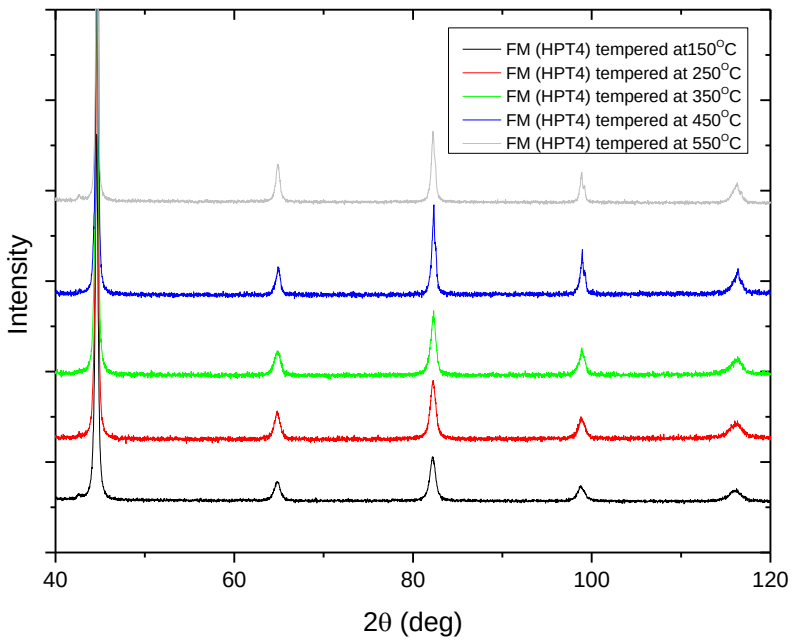

Figure 4.51 XRD line profiles of the FM sample processed by HPT up to 4 turns and tempered at different temperatures (150◦C to 550◦C).

Table 4.7 The ferrite lattice parameter (a) values calculated for the FM sample processed by HPT up to 4 turns and tempered at different temperatures (150°C to 550°C).

Sample	Lattice parameter (nm)
FM (HPT4) tempered at 150°C	0.2870 ± 0.0003
FM (HPT4) tempered at 250°C	0.2870 ± 0.0003
FM (HPT4) tempered at 350°C	0.2867 ± 0.0002
FM (HPT4) tempered at 450°C	0.2866 ± 0.0002
FM (HPT4) tempered at 550°C	0.2868 ± 0.0003

The centre of the peaks of the FM samples processed up to 4 turns and tempered at 150 and 250°C moved to the lower angles when compared with the as-deformed sample (as shown in Figure 4.52) which suggests an expansion in the ferrite lattice parameter took place. However, the peak centre of the FM sample processed up to 4 turns and tempered at 350°C was very close to the as-deformed sample. The peak centre of the FM sample processed up to 4 turns and tempered at 450°C was situated at a higher angle when compared with the as-deformed sample as shown in Figure 4.52. The peak for the FM sample processed up to 4 turns and tempered at 550°C is not shown to allow better comparison and analysis.

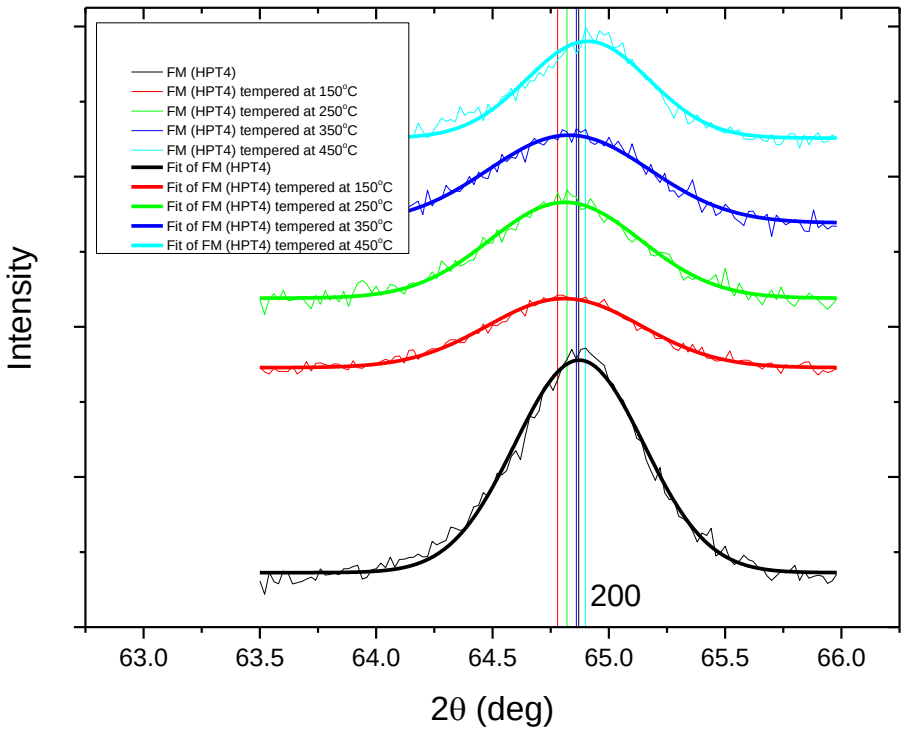

Figure 4.52 A magnified *hkl* reflection (200) in the patterns of the FM samples processed up 4 turns and tempered at different temperatures (150 to 450°C). In this figure, the thin curves are the measured patterns while the thick (smooth) curves are the fitted curves. The Gauss function was used to fit the measured data. The coloured straight lines are the centre of the fitted curves.

Investigating the XRD profile of the FM sample processed up to 4 turns and tempered at 450 and 550°C revealed the existence of Kα2 radiation effects. Figure 4.53 shows two overlapped peaks: the main peak due to Kα1 while the second peak is due to Kα2 radiation. The intensity of the peak due to Kα1 is about double that of the peak due to Kα2. Figure 4.54 shows the peak positions due to Kα1 and Kα2. It was possible to eliminate the Kα2 radiation effect (appeared in the patterns of the FM sample processed up to 4 turns and tempered at 450°C and 550°C) using the SmartLab diffractometer software during the scanning of the investigated samples. However, eliminating the Kα2 radiation using the SmartLab diffractometer software will reduce the measured intensity significantly and hence poor analysis will be expected. For samples tempered at 450°C and 550°C, the overlapped peaks due to Kα1 and Kα2 radiations were separated using one of the built-in functions in Origin 9.1 Software, the Lorentz function. The peaks due to Kα1 were used in the MWP fitting while those due to Kα2 were disregarded.

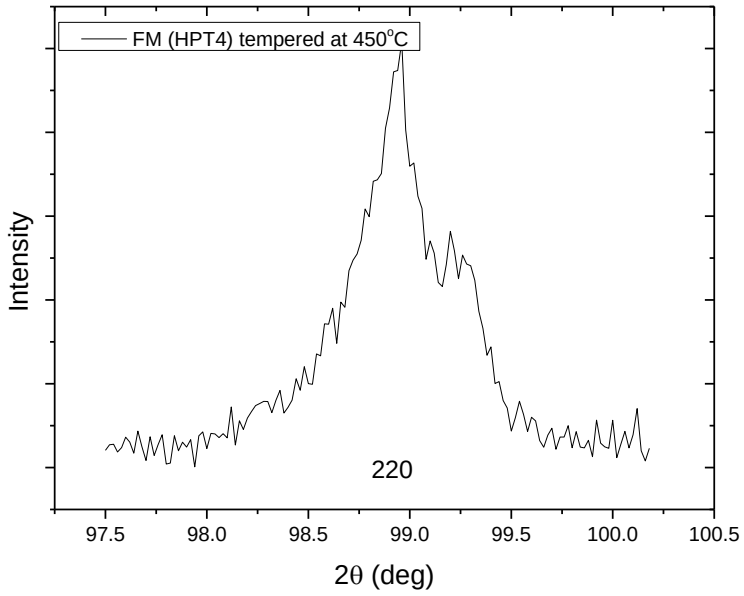

Figure 4.53 A magnified *hkl* reflection (220) in the pattern of the FM sample processed up to 4 turns and tempered at 450°C for 90 min.

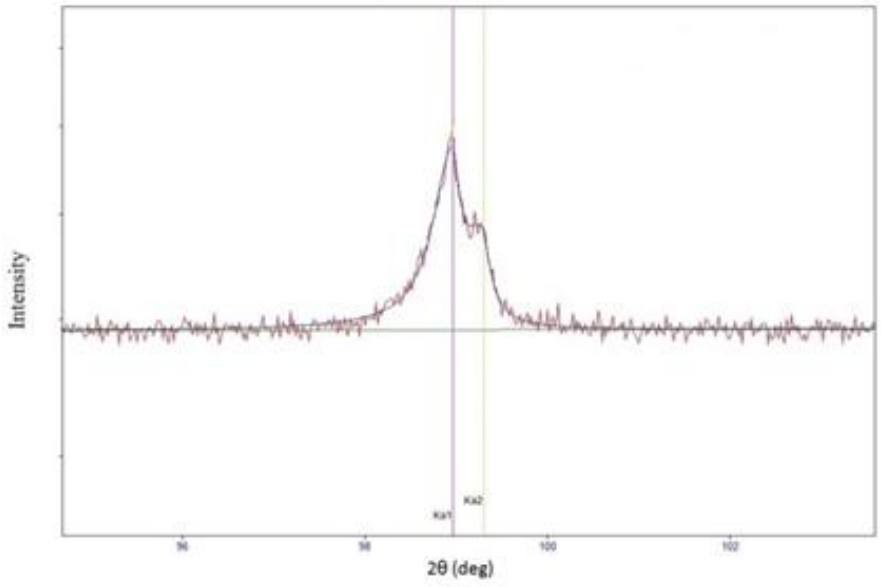

Figure 4.54 A magnified *hkl* reflection (220) in the pattern of the FM sample processed up to 4 turns and tempered at 450°C for 90 min with illustration of Kα1 and Kα2 peak positions obtained by the SmartLab diffractometer software.

CHAPTER 5

5. Discussion

5.1 HPT processing

It is very clear from the slippage investigation reported in Section 4.1 that indeed slippage took place during the first test. This can be due to several possible factors such as the relatively low applied pressure, the increased microhardness resulting from the high number of turns, and the insufficient grip (/friction) at the beginning of the rotation. The results of the second slippage test revealed that increasing the applied pressure from 1 to 6 GPa had a strong effect in eliminating slippage that occurred during the HPT process. It is believed that increasing the thickness of the HPT sample to 1 mm has minor role in eliminating the slippage during the HPT processing. Ensuring no slippage during the HPT process prior to the main experiment is an important factor to establish and maintain confidence in the results of this work.

5.2 Hardness

5.2.1. The microhardness of the FP samples

The overall microhardness of the FP samples increased due to processing up to 1, 4, and 10 turns, and this is in complete agreement with the general observations on microhardness of HPT-processed samples by many researchers, e.g. [17, 111, 118, 127]. There is a difference in the microhardness readings between the centre and the edge of the FP processed samples. After 10 turns, the microhardness increased to 3 times the microhardness of the initial state (the undeformed sample). A comparison between the microhardness results of the FP sample processed by HPT up to 4 turns in the current study and the microhardness results of FP samples processed by HPT up to 4 and 5 turns found in the literature was conducted and is presented in Table 5.1.

Table 5.1 Comparison between the microhardness results of the FP sample processed by HPT up to 4 turns, in the current study, and the microhardness results of FP sample processed by HPT up to 4 and 5 turns found in the literature.

Material used in the investigation (wt.%)	**Initial state**	**Processing condition**	**Hardness (GPa)**
(Current study) Low carbon steel 0.1 C, 0.1 Si, 1.55 Mn, 0.015 P, 0.005 S, 0.045 Al, and 0.003 N	Ferritic-pearlitic	HPT processing up to 4 turns under a pressure of 6 GPa	4.77
Low carbon steel 0.1 C, 1.12 Mn, 0.08 V, 0.07 Ti	Ferritic-pearlitic	HPT processing up to 5 turns under a pressure of 6 GPa [127]	6.44
09G2S Steel 0.12 C, 0.85 Mn, 0.030 P, 0.035 S	Ferritic-pearlitic	HPT processing up to 5 turns under a pressure of 6 GPa [111]	~ 6
10G2FT Steel 0.1 C, 1.12 Mn, 0.08 V, 0.07 Ti	Ferritic-pearlitic	HPT processing up to 5 turns under a pressure of 6 GPa [111]	~ 5
Low carbon-triple alloyed steel 0.2 C, 0.5 Cr, 0.6 Ni, 0.2 Mo	Ferritic-pearlitic	HPT processing up to 5 turns under a pressure of 6 GPa [118]	6.08

It is clear from Table 5.1 that the microhardness of the present FP sample is in broad agreement with the corresponding microhardness results listed in Table 5.1 when taking into consideration the difference in number of turns and the chemical composition. In Figure 4.2 (Section 4.2.1), the strain increases as the distance from the disk centre increases. It is worth noting that the difference in strain experienced by the centre and the edge of the HPT disc increases with number of HPT turns. In Figure 4.3 (Section 4.2.1), the microhardness increases with the strain regardless of the number of turns.

5.2.2. The microhardness of the FM samples

The microhardness of the as-received sample is ~ 206 Hv, and the microhardness of the FM samples increased due to the HPT processing as shown in Figure 4.4. The microhardness readings at the centre of all the FM samples processed up to 1, 4, and 10 turns are lower than the microhardness readings at the edge of these samples. There is a significant increase in the microhardness of the FM samples after 10 turns to reach 3 times the microhardness of the initial state. The microhardness results of the FM sample processed up to 4 turns, in the current study, are compared with other microhardness results of FM samples processed by HPT up to 4 and 5 turns under a pressure of 6 GPa and listed in Table 5.2. The data listed in Table 5.2 highlight that a high microhardness is achieved for a range of the ferritic-martensitic samples processed by HPT up to 4 and 5 turns. The microhardness results in the current study are broadly in agreement with the results listed in Table 5.2 when taking into consideration the difference in the number of turns and the additional particle strengthening resulting from the possible formation of carbides and carbonitrides caused by the presence of alloying elements such as vanadium and titanium. Plotting the strain vs. the distance from the disk centre according to Equation 2.4 (Figure 4.5) revealed that the strain increases as the distance from the disk centre increases. Again, the microhardness increased as the strain increased regardless of the number of turns as shown in Figure 4.6.

Table 5.2 Comparison between the microhardness results of the FM sample processed by HPT up to 4 turns, in the current study, and the microhardness results found in the literature of FM samples processed by HPT up to 4 and 5 turns.

Material used in the investigation (wt.%)	**Initial state**	**Processing condition**	**Hardness (GPa)**
(Current study) Low carbon steel 0.1 C, 0.1 Si, 1.55 Mn, 0.015 P, 0.005 S, 0.045 Al, and 0.003 N	Ferritic-martensitic	HPT processing up to 4 turns under a pressure of 6 GPa	~ 5
Low carbon steel 0.1 C, 1.12 Mn, 0.08 V, 0.07 Ti	Ferritic-martensitic (quenched from 950^{o}C)	HPT processing up to 5 turns under a pressure of 6 GPa [127]	7.22
Low carbon steel 0.1 C, 1.12 Mn, 0.08 V, 0.07 Ti	Ferritic-martensitic (quenched from 1180^{o}C)	HPT processing up to 5 turns under a pressure of 6 GPa [127]	8.63
09G2S Steel 0.12 C, 0.85 Mn, 0.030 P, 0.035 S	Ferritic-martensitic	HPT processing up to 5 turns under a pressure of 6 GPa [111]	6.5
10G2FT Steel 0.1 C, 1.12 Mn, 0.08 V, 0.07 Ti	Ferritic-martensitic	HPT processing up to 5 turns under a pressure of 6 GPa [111]	7.5

The second microhardness test involved indentations of specific phases (ferrite or martensite). It is clear from Table 4.1 that the microhardness of the individual phases are, in general, in good agreement with the microhardness results obtained from the first microhardness test. When the FM samples are processed up to 1, 4, and 10 turns, the microhardness of both phases increased at both the centre and the edge of the disk.

The microhardness results of the individual phases, ferrite or martensite, listed in Table 4.1, provide important information about the hardness (and strength) of the sample. The investigated FM samples contain hard martensite particles in a soft

continuous ferrite matrix. One can expect different behaviours of the two phases during the plastic deformation and this inhomogeneous deformation adds to the complexity of property and microstructure development [163]. During quenching from the two-phase (ferrite-austenite) region, an austenite to martensite phase transformation took place and residual stress fields are created in the areas close to the martensite. In the current investigation, it is observed that the dislocation density in the vicinity of the martensite is higher than the ferrite interiors and this was also confirmed by other researchers [61, 163]. The plastic deformation is initiated in the ferrite grain which is close to the martensite [164]. As the strain increases, the deformation moves inward to the ferrite grain's centre and then the martensite deformation starts at higher strain. In other words, at the initial stages of the deformation (at low strain), the ferrite grains deform plastically while the martensite deforms elastically [164]. After 1 turn, the microhardness of the ferrite in the present samples increased by 2.1 GPa while the microhardness of the martensite increased by 1.8 GPa. The microhardness of both phases continued to increase when HPT processing proceeds to 4 and 10 turns. After 4 and 10 turns of the HPT processing, the microhardness increment in the ferrite is still larger than the martensite even after 4 and 10 turns and it is thought that this can be due to a difference in the level of deformation and dislocation generation that can persist: dislocation generation in the martensite is lower than that in the ferrite. The increase in the microhardness after 1 turn is much larger than that in the subsequent 4 and 10 turns, and this is in agreement with the unique behaviour, high rate of work hardening at the initial stage of the deformation of the FM steel.

It is important to consider some of the limitations of the measurement of hardness of the two phases. It is noted that the martensite islands at the edge of the FM sample processed up to 10 turns were significantly refined to an approximate size of 1 to 2 μm. Placing the indenter on these refined islands using the optical microscope to perform the required indentation proved to be sometimes difficult. It is assumed throughout that during the microhardness measurements of the individual phases, ferrite or martensite, the indentation and subsurface deformation is all within one phase. As a result of limitations, the values obtained from this micrrohardness test can include some errors especially at high number of turns (10 turns) where the martensite islands were significantly refined at the edge of the sample.

Few studies exist in the literature that investigate the deformation mechanism of FM steel samples during tensile tests (e.g. [56, 164]). The average grain size of the FM samples in [56, 164] was 1 μm or above, with no studies found that investigated FM steel samples tensile tested with a grain size of less than 1 μm. Based on the above discussion, it is believed that the deformation mechanism of the FM steel HPT-

processed in the current study is similar to those that have been tensile tested in [56, 164] despite their differences in grain size. At low strains, ferrite deforms plastically, whereas martensite deforms elastically. At medium to high strains, both phases deform plastically.

5.2.3. The microhardness of the FM processed samples tempered at different temperatures

The microhardness of a material is strongly correlated to its microstructure. There was no significant change in the microhardness when tempering the FM processed samples at 250^{o}C (Figure 4.8) and this is consistent with the microstructure investigations of this sample which did not reveal significant changes. Increasing the tempering temperature to 350^{o}C resulted in a slight increase in microhardness, while microhardness was maintained when tempering at 450^{o}C. The high hardness preserved in the sample tempered at 450^{o}C is believed to be due to the following: first, a small reduction in the dislocation density (to be discussed in detail in Section 5.4.3), second, the formation of cementite particles, and third, no recrystallization and grain growth process took place at this high temperature (450^{o}C).

5.2.4. The nanohardness of the FP, FM, and FM processed samples tempered at different temperatures

Ghassemi-Armaki et al. [134] recorded a nanohardness of 2 GPa for the ferrite in a ferritic-martensitic steel (0.15 wt.% C). Hayashi et al. [133] measured a nanohardness of 2.8 GPa for the ferrite in ferritic-martensitic steel (0.16 mass.%C). Gadelrab et al. [165] recorded a higher value of nanohardness, 3.7 GPa, for the ferrite in austenitic-ferritic duplex stainless steel. In the current study, a nanohardness value of 3.16 GPa was measured for the ferrite in the sample annealed at 1100^{o}C for 90 min (as an example) which is comparable to the ferrite nanohardness measured in these previous studies [133, 134, 165]. However, the nanohardness measurements in the current study (Figure 4.12 and Figure 4.13) were somehow higher than the microhardness readings (Figure 4.1). This higher nanohardness can be attributed to two factors: first, the mechanical grinding and polishing processes during the nanohardness sample preparation added some degree of deformation and hence a hardened surface layer

might be created [166]; second, the so-called indentation size effect (ISE), i.e. the nanohardness increases as the indentation depth decreases [130].

The nanohardness of the ferrite in the FP samples increased as the number of turns increased up to 10 turns and this can be attributed mainly to the increase in the dislocation density, as will be explained later in Section 5.4.1, and other strengthening contributions such as solid solution. The nanohardness of the pearlite also increased as the number of turns increased up to 4 turns and this can be attributed mainly to the reduction in the lamellae spacing. However, the nanohardness of the pearlite is not a true quantitative measurement of the pearlite hardness during the HPT processing since the pearlite consists of lamellae structures of ferrite and cementite. The overall nanohardness of the FM samples increased as the number of turns increased up to 4 turns (Figure 4.16). The nanohardness of the ferrite in the FM sample processed up to 4 turns and tempered at 250^{o}C was 6.4 GPa and increased to 7.5 GPa when the sample was tempered at 350^{o}C. This increase in the nanohardness can be attributed to the limited formation of the cementite particles (Figure 4.35).

5.3 Microstructure

5.3.1. Optical microscopy and SEM of the FP samples

The microstructure of the sample annealed at 1100^{o}C for 90 min (Figure 4.17) represents a common microstructure of commercial steel consisting of a continuous ferrite matrix and hard pearlite particles. The pearlite colonies can be described as a composite structure comprising a very hard phase, cementite, and a soft ferrite phase arranged in lamellae form as shown in Figure 4.18.

The grain boundaries at the centre of the FP sample processed up to 1 and 4 turns are still visible and only slight refining took place since the centre region of the disk is exposed to the lowest strain during the HPT process according to Equation 2.4. At the edge of the FP samples processed up to 1 and 4 turns, no equi-axed pearlite colonies can be seen anymore. Instead, the cementite lamellae are heavily deformed and fragmented into small pieces of cementite in some regions whereas elsewhere they are elongated in the deformation direction. After 10 turns, the ferrite grain boundaries cannot be seen any more at the centre and the edge of the sample and this can be attributed to the further reduction in the ferrite grain sizes where it becomes very difficult to study this

kind of microstructure by means of optical or SEM microscopy. After 10 turns and at the edge of the disk, further cementite fragmentation took place where only small pieces of cementite (smaller than 1 μm) can be seen (Figure 4.24). Gavriljuk [167] observed cementite dissolution during cold working of pearlitic steel. The authors claimed that the cementite dissolution increased as the strain increased and saturated at high strain. Chakraborty et al. [150] deformed pearlitic steel by cold-drawing up to a strain of 1.4. The authors claimed that 50% of the cementite dissolved during the drawing process. Wetscher et al. [113] and Ivanisenko et al. [115] observed partial and complete dissolution of cementite, respectively, during the HPT processing of pearlitic steel (0.7-0.9 wt.% C). In the current study, no evidence of cementite dissolution was observed even after 10 turns. Furthermore, no appreciable expansion in the lattice parameter of the ferrite of the FP samples process by HPT up to 1, 4, and 10 turns (Table 4.5). The high carbon content (0.7-0.9 wt% C) in the investigated peralitic steels in [113, 115, 150, 167] had a major role in the cementite dissolution process during the deformation. In the current study, it is believed that the cementite did not dissolve in the FP samples during the HPT processing due to the low carbon content (0.1 wt% C).

5.3.2. Optical microscopy and SEM of the FM samples

The microstructure of the FM processed samples, Figure 4.26 to Figure 4.31, revealed that grain refinement took place during the HPT process even after 1 turn as shown in Figure 4.27. After 1 turn and at the centre of the FM sample, the grain boundaries are still visible and slight grain refinement took place because the centre region of the sample was exposed to the lowest strain according to Equation 2.4. After 4 and 10 turns of the HPT processing, further grain refinement (in both the ferrite and martensite phases) took place and no visible grain boundaries could be seen anymore. It can be seen from Figure 4.30 and Figure 4.31 that the martensite islands were refined to have an estimated average size of 4 and 1 μm, respectively.

5.3.3. Optical microscopy and SEM of the FM processed samples tempered at different temperatures

As mentioned earlier, tempering the FM sample processed up to 4 turns at 150^{o}C and 250^{o}C for 120 min did not result in marked changes in the microstructure. However, tempering the sample at these temperatures, 150^{o}C and 250^{o}C, resulted in formation of

supersaturated Fe-C solid solution in the ferrite matrix. Increasing the tempering temperature to 350°C resulted firstly in partial decomposition of the supersaturated Fe-C solid solution in the ferrite as revealed by the lattice parameter inspection; secondly, limited formation of cementite particles as revealed by the SEM investigation. Tempering the FM sample processed up to 4 turns at 450°C for 90 min, resulted in complete decomposition of the supersaturated Fe-C solid solution in ferrite as revealed by the lattice parameter inspection and the formation of fine-sized cementite particles (Figure 4.36 to Figure 4.48). In general, the cementite particles have spheroidized shapes and are distributed broadly homogeneously through the tempered sample (Figure 4.36 and Figure 4.37) with very limited clustering (Figure 4.38). The prior martensite structure has an effective role in developing such heterogeneous distribution of cementite and this dense distribution of cementite particles observed in Figure 4.38 is believed to be developed on one prior martensite block. It is worth to emphasise here that the HPT processing played an important role in producing high density of crystal defects which, in turn, helps in providing homogeneous nucleation sites for the formed cementite particles. At this tempering temperature, it is believed that recovery took place due to the existence of some recovered ferritic grains and the reduction in the dislocation density (see Section 5.4.3) while no recrystallization was detected. The point count method was applied to three different areas on the sample tempered at 450°C to determine the volume fraction of cementite (f) and the three values were averaged and considered as the average volume fraction of cementite (f) (for point count method procedures see Appendix A).For the sample tempered at 450°C for 90 min, this produced $f = 0.05 \pm 0.01$.

Tempering the FM processed sample at 450°C will result in grain growth in the ferrite matrix to reduce the total surface energy of the boundaries. During the grain growth process, large ferrite grains grow while smaller grains shrink, and hence, the mean grain size of the ferrite will increase [168]. However, in the presence of second phase particles in the ferrite matrix (such as cementite particles), the grain growth process can be partially or completely inhibited. In the FM sample tempered at 450°C, the cementite particles at the ferrite grain boundaries (Figure 4.36) retard the grain boundaries mobility by exerting forces on the grain boundaries [169].

Tempering the FM sample processed up to 4 turns at 550°C for 90 min, resulted in the formation of recrystallized equi-axed ferritic grains and coarsening of the cementite particles. The cementite particles formed either at the ferrite grain boundaries or at the prior austenite grain boundaries. The Ostwald ripening process was also observed where smaller cementite particles dissolved in order to provide carbon for other large particles to grow, (i.e. some large cementite particles, at the ferrite grain boundaries,

coarsened faster than those at the prior austenite boundaries as indicated by arrows in Figure 4.40).

5.3.4. TEM of the FM samples

The TEM images in Figure 4.42 to Figure 4.47 show that ill-defined grain boundaries are a common feature of the FM samples processed by HPT up to different number of turns. These ill-defined grain boundaries represent non-equilibrium boundaries with high-energy due to the existence of a high-density of trapped lattice dislocations [13]. After 1 turn, the original grains are subdivided into substructures or cells surrounded by cell walls as shown in Figure 4.43. In Figure 4.46, more diffuse spots were observed in the SAD pattern which suggests that further grain refinement took place after 4 turns. The clustered and elongated spots in the SAD pattern in Figure 4.46 suggest that the evolution of cells and subgrains continued after 4 turns.

5.4 XRD analysis

5.4.1. XRD of the FP samples

The XRD data in Figure 4.48 show that no new peaks appeared after the HPT processing of the FP samples up to 1, 4, and 10 turns, which indicates that no new phase was formed during the HPT processing. The fraction of the cementite phase in the present alloy at room temperature was determined using the lever rule and found to be ~ 1.3 wt.%. Due to this low fraction of cementite, no cementite reflections were detected during the XRD test even in the sample annealed at 1100^{o}C for 90 min (FP undeformed sample) and this is in agreement with the observations of other researchers [111, 118, 127]. However, the detection of weak cementite reflections is possible when scanning pearlitic steels (0.8-0.9 wt.% C) and this is due to the high volume fraction of cementite in these samples [76, 115, 150]. It is apparent from Table 4.5 that the lattice parameter of the sample annealed at 1100^{o}C for 90 min (FP undeformed sample) is larger than that of pure α-Fe (0.28664 nm [53, 54]). It is interesting to note that there was no appreciable increase in the lattice parameter after processing the FP samples up to 1, 4, and 10 turns. The maximum expansion in the α-Fe lattice parameter in our HPT

processed alloys was ~ 0.0001 nm which occurred for the FP sample processed up to 4 turns.

Investigation of the XRD line profiles of the FP processed samples revealed that line broadening increased with the number of turns (i.e. with increasing strain) as shown in Figure 5.1. The classical and modified Williamson-Hall method was used to determine the volume-weighted mean column-length, $\langle t \rangle_{\mathrm{vol}}$, and to study the nature of the dislocation types in the FP processed samples. In order to generate the Williamson-Hall plot, Equation 2.36 is used, and $\Delta K = \cos\theta . \Delta(2\theta)/\lambda$ is plotted against K=2sinθ/λ, producing a straight line. This method was applied for all the investigated samples as shown in Figure 5.2 to Figure 5.4. The intercept with the vertical-axis, ΔK axis in this case, is $(0.9/\langle t \rangle_{\mathrm{vol}})$.

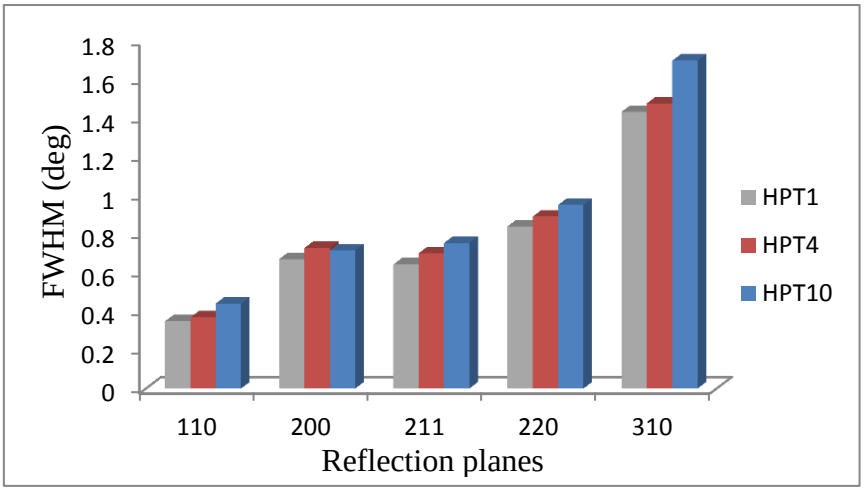

Figure 5.1 The broadening of the FWHM of the five *hkl* reflections after the HPT processing of the FP samples up to 10 turns.

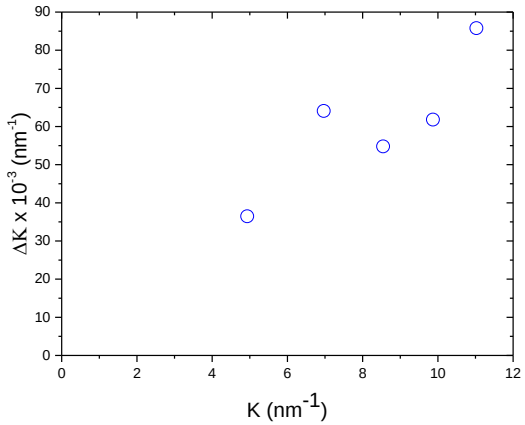

Figure 5.2 The classical Williamson-Hall plot of the FP sample processed by HPT up to 1 turn.

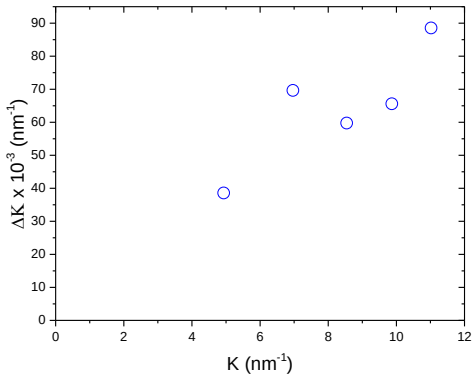

Figure 5.3 The classical Williamson-Hall plot of the FP sample processed by HPT up to 4 turns.

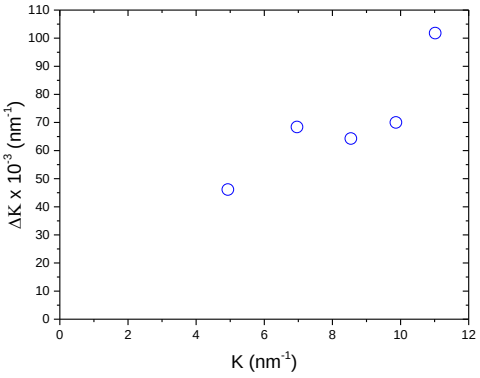

Figure 5.4 The classical Williamson-Hall plot of the FP sample processed by HPT up to 10 turns.

Figure 5.2 to Figure 5.4 clearly indicate the existence of a strong anisotropy where ΔK is not a monotonous function of K (K=2sinθ/λ). In order to account for this phenomenon (strain anisotropy), application of the modified Williamson-Hall method [144] becomes necessary. For steel, the average dislocation contrast factor $\bar{C}_{h00}$ is ~ 0.3 for both dislocation types (screw or edge) [146] while the parameter of the dislocation contrast factor (q) is 2.67 and 1.28 for screw and edge dislocations, respectively. Using these values of $\bar{C}_{h00}$ and q in Equation 2.38, the contrast factor was calculated for each individual diffraction plane. The plots of the modified Williamson-Hall method for the FP processed samples (assuming the presence of pure screw dislocations) are shown in Figure 5.5, Figure 5.7, and Figure 5.9 while the plots of the FP processed samples in the presence of mixed dislocations (proportions of 0.75 screw and 0.25 edge) are shown in Figure 5.6, Figure 5.8, and Figure 5.10. The strain anisotropy effect that was observed in

the classical Williamson-Hall plots (Figure 5.2 to Figure 4.4) almost disappeared when the contrast factor was introduced (Figure 5.5 to Figure 5.10), as is indicated by the calculated correlation coefficient, R^2, displayed in the figures. The modified Williamson-Hall plots of the FP processed samples in the case of mixed dislocations gave better linear dependencies and hence they were used in the analysis.

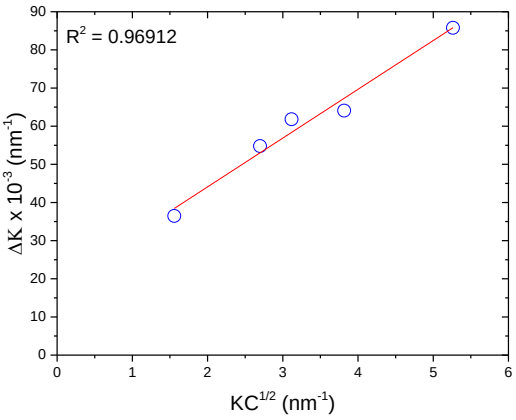

Figure 5.5 The modified Williamson-Hall plot of the FP sample processed up to 1 turn in the case of pure dislocations.

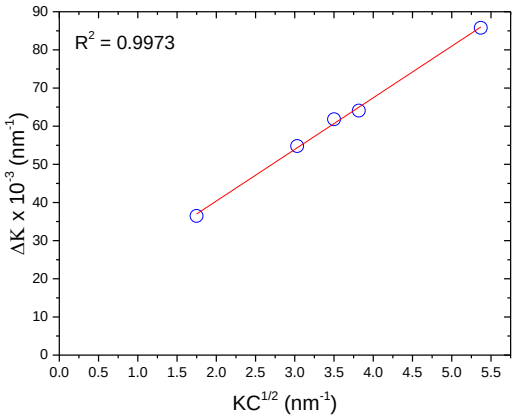

Figure 5.6 The modified Williamson-Hall plot of the FP sample processed up to 1 turn in the case of mixed dislocations (0.75 screw and 0.25 edge).

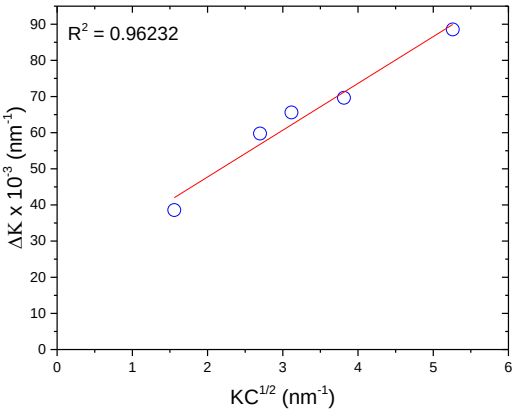

Figure 5.7 The modified Williamson-Hall plot of the FP sample processed up to 4 turns in the case of pure dislocations.

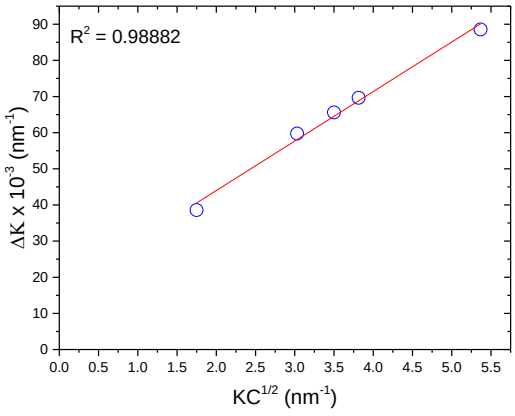

Figure 5.8 The modified Williamson-Hall plot of the FP sample processed up to 4 turns in the case of mixed dislocations (0.75 screw and 0.25 edge).

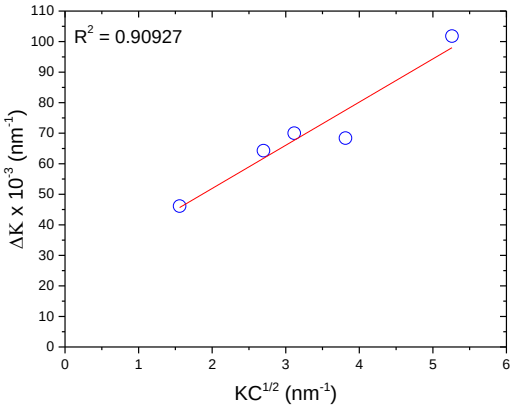

Figure 5.9 The modified Williamson-Hall plot of the FP sample processed up to 10 turns in the case of pure dislocations.

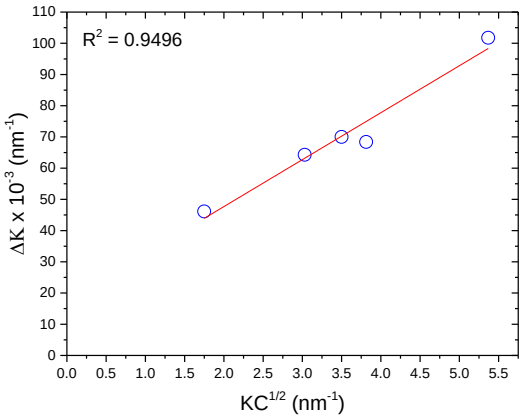

Figure 5.10 The modified Williamson-Hall plot of the FP sample processed up to 10 turns in the case of mixed dislocations (0.75 screw and 0.25 edge).

The volume-weighted mean column length ($\langle t \rangle_{\mathrm{vol}}$) of the FP samples processed up to 1, 4, and 10 turns is determined from the intercept with the vertical-axis, at $KC^{1/2} = 0$. The volume-weighted mean column lengths ($\langle t \rangle_{\mathrm{vol}}$) of the FP samples processed up to 1, 4, and 10 turns are listed in Table 5.3. Using Equation 2.40, the experimental q value can be determined when plotting $(\Delta K^2 - \xi)/K^2$ vs. H^2 where the intercept with the horizontal-axis (H^2) is $1/q$. This graphical method of determination of the experimental q value of the FP sample processed up to 1 turn is illustrated in Figure 5.11 (the FP sample processed up to 1 turn is analysed in this example). Table 5.4 shows the experimental q values of the FP processed samples obtained using this graphical method.

Table 5.3 The volume-weighted mean column lengths of the FP samples processed by HPT up to 1, 4, and 10 turns obtained by the modified Williamson-Hall method.

Sample	**The volume-weighted mean column length (nm)**
FP (HPT1)	68 ± 7
FP (HPT4)	54 ± 8
FP (HPT10)	51 ± 18

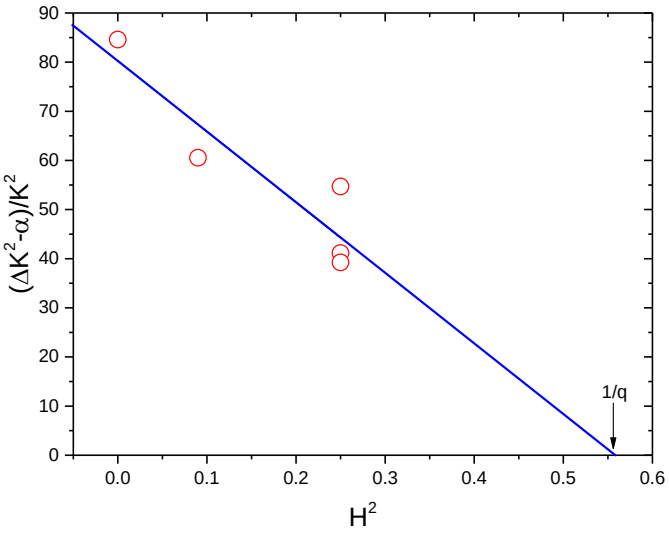

Figure 5.11 A plot of $(\Delta K^2 - \xi)/K^2$ vs. H^2 according to Equation 2.40 for the FP sample processed up to 1 turn.

Table 5.4 The values of the parameter of the dislocation contrast factor q obtained by the Williamson-Hall method of the FP processed samples.

Sample	***q***
FP (HPT1)	1.8 ± 0.6
FP (HPT4)	1.8 ± 0.5
FP (HPT10)	1.3 ± 0.9

Following the procedures described in Section 2.6.2, the input files necessary to run the Multiple Whole Profile-fit (MWP-fit) were prepared. The MWP-fit was applied to the FP samples processed by HPT up to 1, 4, and 10 turns. The result of the MWP-fit of the FP sample processed up to 1 turn is shown in Figure 5.12. In Figure 5.12, the Fourier transform of the measured and fitted profiles are plotted against L for the FP sample processed up to 1 turn, at which a good fit can be observed. A good fit was also observed in the results of the FP samples processed up to 4 and 10 turns (not shown here). The values of the dislocation contrast factor (q), and the dislocation density (ρ) obtained by the MWP-fit for the FP processed samples are listed in Table 5.5.

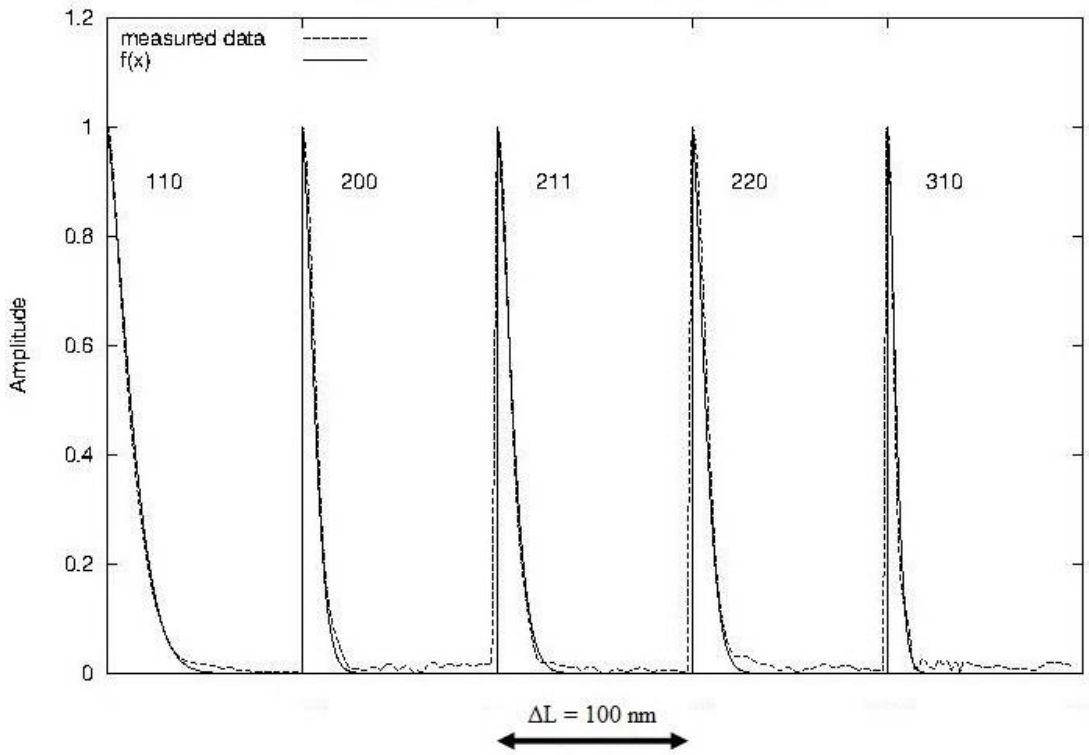

Figure 5.12 The Fourier transform of the measured and fitted profiles vs. *L*. The five peaks (110, 200, 211, 220, and 310) are plotted in sequence and in an independent range of ΔL. The range of ΔL extends from 0 to 100 nm.

Table 5.5 The parameter of the dislocation contrast factor (q) and the dislocation density (ρ) obtained by the MWP-fit of the FP processed samples.

Sample	q	$\rho \times 10^{15}$ **(m^{-2})**
FP (HPT1)	2.3 ± 0.04	2.4 ± 0.1
FP (HPT4)	1.57 ± 0.03	3.08 ± 0.03
FP (HPT10)	1.47 ± 0.04	3.7 ± 0.2

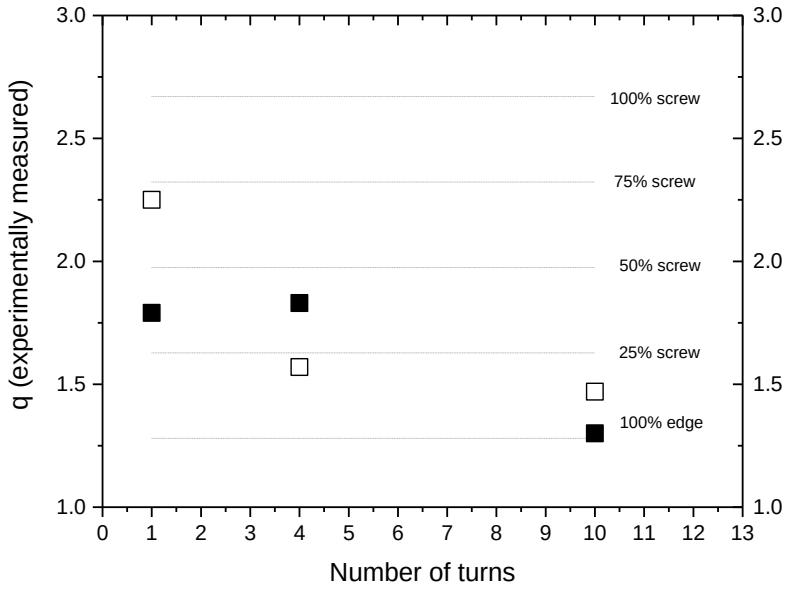

Figure 5.13 The nature of dislocations as a function of number of turns in the FP processed samples. Solid squares represent the *q* values obtained by the Williamson-Hall method while the open squares represent the *q* values obtained by the MWP-fit.

Figure 5.13 indicates that both screw and edge dislocations exist during the HPT processing of the FP samples up to 4 turns. However, at high number of HPT turns (10 turns), i.e. at very high strain, nearly 100% of the dislocations are edge type.

Dislocation density can be measured either by XRD or TEM techniques. Using TEM will lead to a measured dislocation density in a very small region while XRD analysis will produce an averaged dislocation density of a much wider region. Although dislocation densities measured by XRD are often somewhat higher than those measured by TEM, they are still comparable and in most cases within the same order of magnitude [170, 171]. Thus, measuring the dislocation density by XRD has an advantage over that measured by TEM since the sample preparation is easier in the case of XRD and this technique gives an average dislocation density while the TEM gives a dislocation density of a restricted area. Chen et al. [172] produced an Fe-C alloy by ball milling of iron and graphite and measured a dislocation density as $\sim 3.2\times10^{16}$ m^{-2} using XRD. Chakraborty et al. [150] used cold-drawing to deform a pearlitic steel (0.8 wt.% C) to total strain of 1.4. Chakraborty et al. [150] measured a dislocation density as 8×10^{15} m^{-2} in the deformed pearlitic steel using XRD. Zhang et al. [173] have cold-drawn pearlitic steel (0.8 wt.% C) to a strain of 2.67 and 3.68 and measured a dislocation density using TEM and high resolution electron microscopy (HREM) as 8.8×10^{15} and 2×10^{16}, respectively.

The dislocation densities obtained in the current study are equal to or less by one order of magnitude than those measured in the above investigations. The higher values of the dislocation densities in [150, 172, 173] may be attributed to the difference in the chemical composition, i.e. the very high carbon content (0.8 wt.% C). The MWP-fit method used in the current study has an advantage over the other XLPA methods due to its high accuracy [146].

5.4.2. XRD of the FM samples

The MWP-fit was applied to the FM samples processed by HPT up to 1, 4, and 10 turns following the same procedures as described in Section 2.6.2. The result of the MWP-fit of the FM sample processed up to 1 turn is shown in Figure 5.14. In Figure 5.14, the Fourier transform of the measured and fitted profiles are plotted against the Fourier length (L) for the FM sample processed up to 1 turn where good fit can be observed. Good fit was also observed in the result of the FM samples processed up to 4 and 10 turns (not shown here). The parameter of the dislocation contrast factor (q), and the dislocation density (ρ) obtained by the MWP-fit for the FM processed samples are listed in Table 5.6.

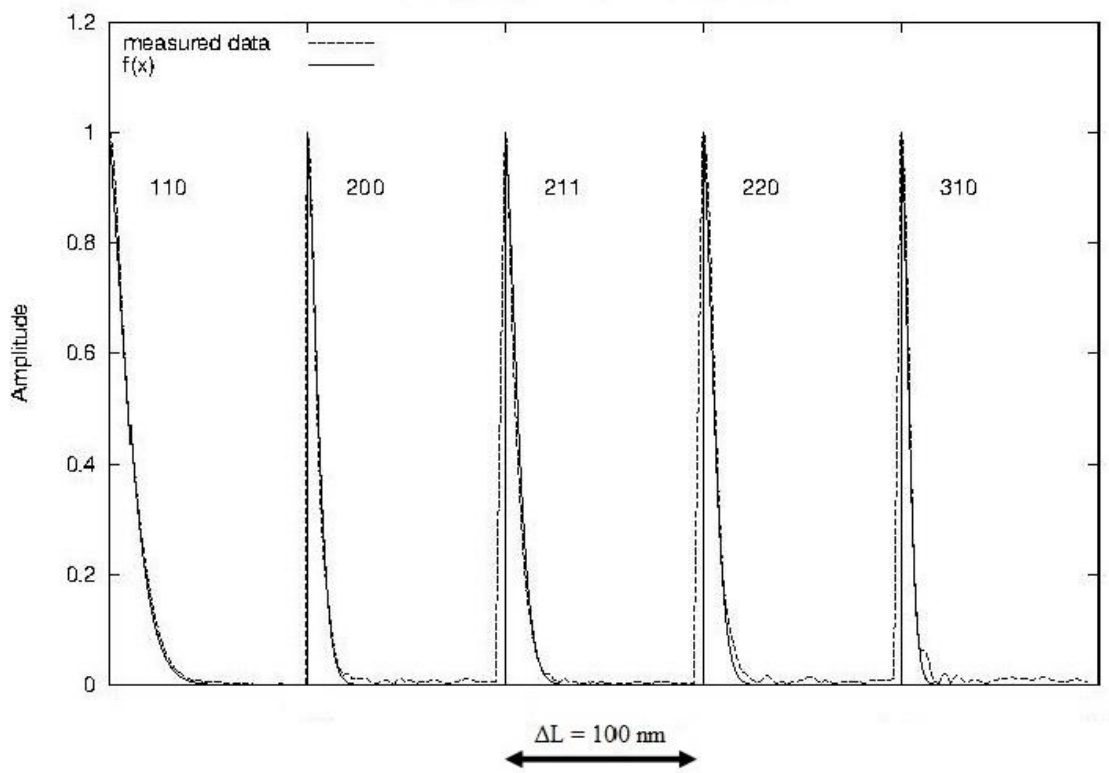

Figure 5.14 The MWP-fit result of the FM samples processed by HPT up to 1 turn (as an example). In this figure, a plot of the Fourier transform of the measured and the fitted (theoretically) vs. *L*. The five peaks (110, 200, 211, 220, and 310) are plotted in sequence and in an independent range of ΔL. The range of ΔL extends from 0 to 100 nm.

Table 5.6 The parameter of the dislocation contrast factor (*q)* and the dislocation density (*ρ)* obtained by the MWP-fit of the FM processed samples.

Sample	***q***	$\rho \times 10^{15}$ **(m^{-2})**
FM (HPT1)	2.07 ± 0.04	1.9 ± 0.3
FM (HPT4)	1.70 ± 0.03	2.09 ± 0.02
FM (HPT10)	1.87 ± 0.03	2.2 ± 0.2

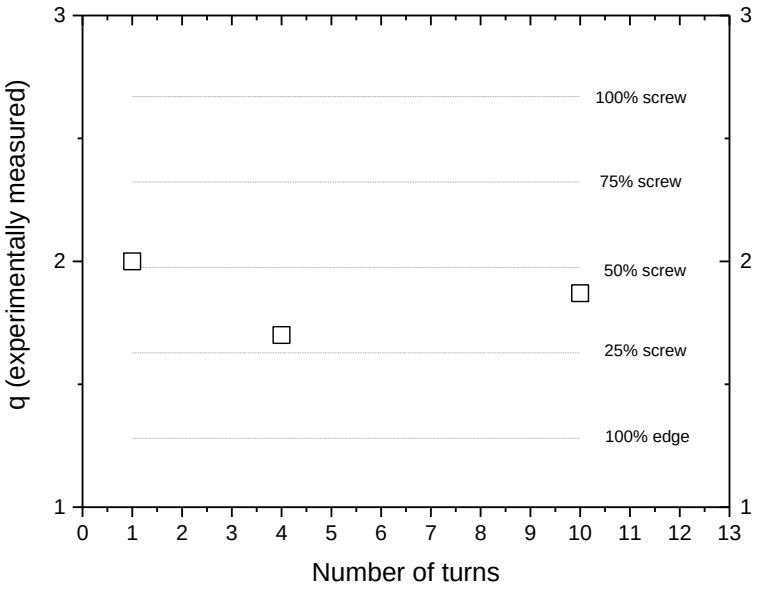

Figure 5.15 The nature of dislocations as a function of the number of turns obtained by the MWP-fit of the FM sample processed up to 1, 4, and 10 turns.

The comparison of measured q values with theoretical q factors for different relative fractions of screw and edge dislocations shown in Figure 5.15 indicates that both screw and edge dislocations exist during the HPT processing of the FM samples up to 10 turns.

Renzetti et al. [174] tempered ODS-Eurofer steel (0.07 wt.% C) at 750°C for 1h then cold-rolled it to a total reduction of 80%. Renzetti et al. [174] measured the dislocation density of the cold-rolled tempered steel using XRD as 8.0×10^{15} m^{-2}. Takebayashi et al. [170] measured the dislocation density in a martensitic steel (0.3 mass.% C) in the as-quenched initial state using XRD as 6.3×10^{15} m^{-2}. Takebayashi et al. [170] also measured the dislocation density of the same sample using TEM and obtained a value which was very close to the one obtained by the XRD. Nedjad et al. [151] measured the dislocation density of 18Ni (300) Maraging steel (ferritic-martensitic steel) pressed by ECAP up to 4 passes using XRD as 1.7×10^{16} m^{-2}. It is clear that the dislocation densities obtained in the current study are in the same or less by one order of magnitude when compared to those measured in the above investigations.

5.4.3. XRD of the FM processed samples tempered at different temperatures

In order to apply the MWP-fit to the FM sample processed up to 4 turns and tempered at 450°C for 90 min, it was necessary to separate the overlapped peaks (Figure 5.16). After the separation process of all overlapped peaks in the pattern, the peaks due to Kα1 were used when the MWP-fit was applied.

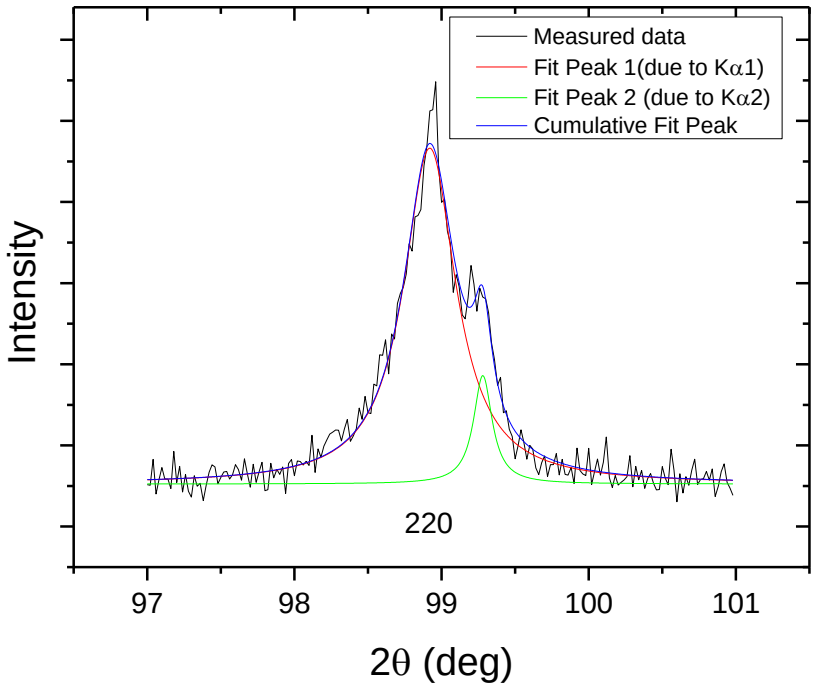

Figure 5.16 A magnified *hkl* reflection (220) of the FM sample processed up to 4 turns and tempered at 450°C for 90 min. In this figure, the peak due to Kα1 (red curve) was successfully separated from the peak due to Kα2 (green curve).

The MWP-fit was applied to the FM processed samples tempered at 250°C and 450°C following the same procedures as in Section 2.6.2. The result of the MWP-fit of the FM sample processed up to 4 turns and tempered at 250°C is shown in Figure 5.17. In Figure 5.17, the Fourier transform of the measured and fitted profiles are plotted against the Fourier length (L) for the FM samples processed up to 4 turns and tempered at 250°C where good fit can be observed. Good fit was also observed in the result of the FM sample processed up to 4 turns and tempered at 450°C (not shown here). The parameter of the dislocation contrast factor (q), and the dislocation density (ρ) obtained by the MWP-fit for the FM processed samples tempered at different temperatures

(250°C and 450°C) are listed in Table 5.7. The comparison of measured *q* values with theoretical *q* factors for different relative fractions of screw and edge dislocations shown in Figure 5.18 indicates that at high tempering temperature (450°C), the screw dislocations become dominant.

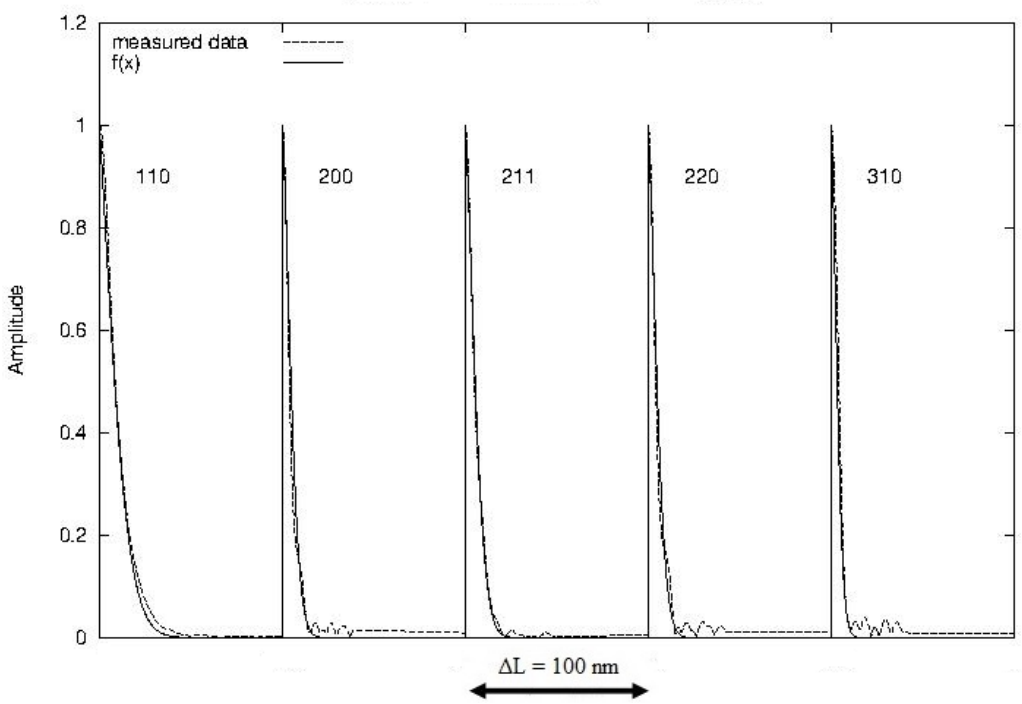

Figure 5.17 The MWP-fit result of the FM sample processed by HPT up to 4 turns and tempered at 250°C (as an example). In this figure, a plot of the Fourier transform of the measured and the fitted (theoretically) vs. *L*. The five peaks (110, 200, 211, 220, and 310) are plotted in sequence and in an independent range of *ΔL*. The range of *ΔL* extends from 0 to 100 nm.

Table 5.7 The parameter of the dislocation contrast factor (*q)* and the dislocation density (*ρ)* obtained by the MWP-fit of the FM processed samples tempered at 250°C and 450°C.

sample	***q***	$\rho \times 10^{15}$ **(m^{-2})**
FM (HPT4) tempered at 250°C	2.11 ± 0.05	2.41 ± 0.05
FM (HPT4) tempered at 450°C	2.50 ± 0.03	1.61 ± 0.03

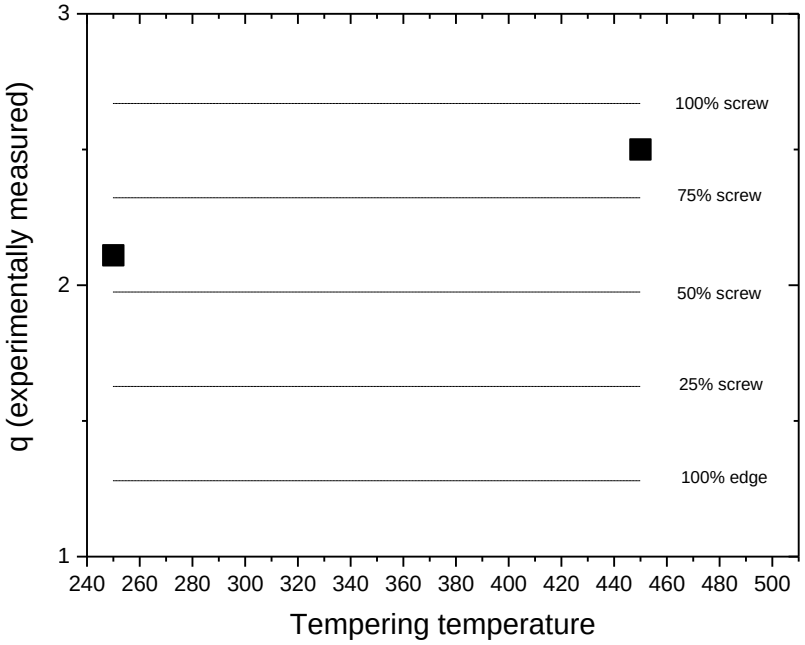

Figure 5.18 The nature of dislocations as a function of the tempering temperature obtained by the MWP-fit of the FM processed samples tempered at 250°C and 450°C.

Cheng et al. [175] processed Mo by HPT up to 6 turns under a pressure of 4 GPa and studied the relationship between the grain size and the density of the screw and edge dislocations. The authors observed that the density of the screw dislocations decreases as the grain size decreases, reaching zero when the grain size was less than 100 nm. The authors observed that both edge and screw dislocations exist when the grain size is between 100 and 300 nm. During the HPT processing of the FP samples, the fraction of the screw dislocation decreases as the number of turns increases (Figure 5.13 and Figure 5.15) or in other word as the grain size decreases. This is in agreement with Cheng et al.'s observations [175]. It is worth noting that no clear explanation was given in [175] for the dependency of the grain size and the fraction of the edge and screw dislocations.

In general, the screw dislocations were dominant in the FP sample processed up to 1 turn where the strain is relatively low (Figure 5.13). This observation is in agreement with the general notion that screw dislocations govern the deformation during the initial stages of the deformation in bcc metals such as steel alloys [175, 176]. After 4 and 10 turns of HPT processing of the FP and FM samples, dissociation of screw dislocation (1/2[111] into 3 {110} slip planes takes place (i.e. in 3 dimensions), and hence, slipping of the screw dislocation core becomes more difficult [175, 177]. In this case, the edge

dislocations moved much faster than screw dislocations, and consequently, multiplication of edge dislocations took place [178]. The difficult slipping of the screw dislocations and the multiplication of the edge dislocations resulted in high fraction of edge dislocations and low fraction of screw dislocations in these samples (Figure 5.13 and Figure 5.15) except for the FM sample processed up to 10 turns. XRD investigation revealed that the ferrite of the FM sample processed up to 10 turns has the largest content of carbon among all of the other processed samples. It is believed that the edge dislocations in the FM sample processed up to 10 turns have been pinned by the carbon since the carbon has an effective role in pinning edge dislocations, and hence, the multiplication process of the edge dislocations was reduced in this sample [179, 180] as shown in Figure 5.15. Tempering the FM sample processed up to 4 turns at 450°C for 90 min resulted in a reduction in the dislocation density from 2.09×10^{15} to 1.6×10^{15} m^{-2}. XRD analysis revealed that the lattice parameter of the ferrite of the FM sample processed up to 4 turns and tempered at 450°C was similar to that of pure α-iron (0.248 nm [53, 54]) which suggests that no solid solution was formed in this sample during tempering. Thus, edge dislocations are not pinned and can move freely since no carbon in solution presents in this sample. Furthermore, the screw dislocations dissociated into 3 slip planes after 4 turns of the HPT processing [177], which makes the edge dislocations are much faster than screw dislocations. At elevated temperature such as 450°C, edge dislocations of different signs on different glide planes annihilate each other by climb and glide processes which results in a reduction in the fraction of the edge dislocations and an increase in the fraction of the screw dislocations as shown in Figure 5.18 [181, 182].

Pesicka et al. [183] tempered a P91 martensitic steel (0.075 wt.% C) at 750°C for 15 min and measured the dislocation density as 0.79×10^{14} m^{-2} using XRD. In the current study, the dislocation density of the FM sample processed up to 4 turns and tempered at 450°C for 90 min was 1.6×10^{15} m^{-2}. The difference between the measured dislocation density in the current study and the one obtained by Pesicka et al. [183] can be attributed to the high annealing temperature used in [183] and the initial state in [183] being as-quenched martensitic steel while in the current study HPT-processed martensitic steel as the initial state was used. Astafurova et al. [127] tempered a martensitic steel (0.1 wt.% C) processed by HPT up to 5 turns at 500°C for 60 min. Astafurova et al. [127] measured a dislocation density as 2.1×10^{15} m^{-2} in the tempered martensitic steel. The measured dislocation density in the current study is very close to the one measured by Astafurova et al. [127]. This suggests that the XLPA results obtained in the current study are reliable and can be used to build up the required model with high confidence.

CHAPTER 6

6. The strength/hardness model

Predicting the strength of coarse-grained undeformed and deformed FP and FM samples has drawn the interest of many researchers. Karlsson and Linden [49] studied the yield strength and flow stress of a coarse-grained FP sample (0.2 wt.% C). The authors claimed the yield strength of the investigated FP sample to be about the same as the yield strength of ferrite with a similar grain size. The authors also claimed that the overall flow stress of the investigated sample could be satisfactorily described by the rule of mixtures of ferrite and pearlite. Similarly, Suh et al. [48] used FEM to predict the yield strength and flow stress of a coarse-grained FP sample (0.15 wt.% C). They ended with a result similar to that of Karlsson and Linden [49] where the yield strength of the FP steel is governed by the ferrite. Chen and Cheng [184] hypothesised that the tensile strength of FM steel can be described by the rule of mixtures of the ferrite and martensite. Speich and Wrlimont [124] proposed an empirical relation to predict the yield strength of coarse-grained FM steels with a carbon content of more than 0.013 wt.%. The empirical relation is a function of the square root of the carbon content (wt.%). Another empirical relation was proposed by Norstrom and Scand [185] to predict the yield strength of a coarse-grained FM steel that incorporates the following strengthening mechanisms : 1) the friction strength; 2) the carbon content; 3) strengthening due to substitutional solid solution such as Mn and Ni; 4) strengthening due to the dislocation density within the lath martensite; and 5) strengthening due to the martensite packet size. Recently, Fang et al. [63], Gunduz [64], and Salemi and Abdulla [65] studied the microstructural evolution and strength of FM steel samples tempered at 100^{o}C to 600^{o}C but no model was proposed in these studies to predict the strength/hardness of these tempered samples. Malik and Lund [99] proposed an empirical relation to predict the yield strength of a coarse-grained medium carbon steel (0.4 wt.% C) tempered at different temperatures. The authors incorporated strengthening due to dislocation density and strengthening due to second phase particles, but neglected strengthening due to grain boundary.

Researchers have extensively studied the ultrafine grain steels due to their attractive mechanical properties. Several studies have investigated the microstructural changes and microhardness of pearlitic steel (0.7-0.9 wt.% C) during different processing methods, including cold-rolling, cold-drawing, and HPT processing [113,

115, 150, 167]. In these studies, the authors observed cementite dissolution and hence tried to explain the mechanism behind it. Several studies can also be found that investigated the microstructural changes and microhardness of low-carbon steel during the equal-channel angular pressing process [21, 38, 109, 120]. Ivanisenko et al [115] and Wetscher et al. [113] studied the properties of pearlitic steel (0.6-0.9 wt.% C) during HPT processing. Astafurova et al. [127], Dobatkin et al. [111], and Cardona et al. [118] studied the microstructural evolution and microhardness of low-carbon steel during HPT processing. The principal concern of these studies [111, 118, 127] was simply the microstructural evolution and properties of the processed low-carbon steels and no attempt was made to predict the microhardness of the processed samples.

Qiao et al. [93] proposed a model to predict the strength/hardness of Al samples deformed by cold-rolling, ECAP, MDF, ARB, and embossing. Starink et al. [186] proposed a model to predict the hardness of pure metals processed by HPT. Miller [187] deformed low-carbon steels (0.053 wt.% C) containing Ni using cold-working in order to achieve a reduction in the samples thickness of 60 to 80%, which resulted in samples with different grain sizes (0.3 to 1.1 μm) being produced. He attributed the improvement in the yield strength to the grain size reduction, thereby neglecting the strengthening due to dislocation density. Valiev et al. [13] predicted the microhardness of Armco iron processed by HPT and claimed the hardness of the processed sample to be mainly due to grain boundary strengthening. It has also been documented that several strengthening mechanisms contribute to the overall strength of SPD-processed materials [93, 96, 186, 188]. Strengthening due to dislocation is considered to be the main mechanism, followed by strengthening due to the grain boundary when an SPD-processed material is investigated [189].

During HPT processing, the processed sample is exposed to large strain especially at a high number of turns. The HPT-processed materials are characterised by an ultrafine or nano structure and high dislocation density. The MWP-fit program was used in the current study to determine the dislocation density of the HPT-processed samples. Sarkar et al. [100] determined the dislocation density of an IF steel sample processed by ECAP using the Williamson-Hall method. They predicted the strength of the processed sample using the Taylor relation which considers the dislocation density to be the main strengthening contributor and so neglects other contributors to strengthening such as grain boundary strengthening.

The current model includes most of the strengthening mechanisms, which makes it consistent with the models that were previously proposed in the literature [93, 173, 186, 188], unlike the models that were proposed by Miller [187], Valiev et al. [13], and Sarkar et al. [100] which incorporated only one strengthening mechanism.

6.1 The model

In this section, a proposed strength/hardness model will be applied to predict the hardness of the FP and FM samples processed by HPT up to 10 turns. In addition, the model will be expanded to predict the hardness of the FM processed samples tempered at different temperatures.

Following the concepts outlined in [93], during HPT processing, the generated dislocation linelength (L_{gen}) in the ferrite matrix is either stored in grain (denoted as L_{ig}) or moved to the cell walls/grain boundaries (will be denoted as L_{gb}). The dislocations that have moved to the cell walls/grain boundaries are considered to be part of the grain boundary and are, consequently, subsumed in the grain boundary [93, 186]. Taking into account the possible annihilation of dislocations with opposite signs that glide on the same slip plane [190] will yield [186]:

$$L_{\text{gb}} + L_{\text{ig}} = (1 - f_{\text{an}})L_{\text{gen}} \qquad 6.1$$

where f_{an} is the fraction of the annihilated dislocations (temperature and material dependent). It is believed that the L_{ig} part makes a substantial contribution to the strength, while the L_{gb} part contributes to the reduction of the cell walls, as well as grain size reduction, and produces high angle grain boundaries.

In the current model, several contributors to the strength of the investigated samples will be accounted for: 1) the friction stress; 2) strengthening due to the solid solution (σ_{ss}); 3) strengthening due to dislocations (σ_{D}); 4) strengthening due to grain boundaries (σ_{GB}); and 5) strengthening due to second-phase particles (σ_P). In most treatments, it is accepted that the dislocation pile-up at the grain boundary is the basic mechanism behind the grain boundary strengthening [78]. Thus, the superposition of the grain boundary and dislocation strengthening (σ_{D}) in the quadratic form will be incorporated into the current model [186, 189, 191]:

$$(\sigma_{GB+D})^2 = (\sigma_{GB})^2 + (\sigma_D)^2 \qquad 6.2$$

It is also well accepted that the contributors to strengthening (mentioned above) are added linearly when predicting the overall strength of a material. Accordingly, the

following relation will be used to predict the overall strength of the investigated samples [93, 123, 192]:

$$\sigma = \sigma_{o} + \sigma_{SS} + \sigma_{GB+D} + \sigma_{P} \quad 6.3$$

6.2 Application of the model

All the essential equations that are used in the model are listed in this Chapter or else referenced if they are mentioned in the literature. Furthermore, all of the parameters used in the model are mentioned in the text and listed in Table 6.5 as well.

6.2.1. The friction stress

The friction stress of pure iron is as low as 34 MPa [94]. However, due to the existence of small amounts of alloying elements in the ferrite matrix of the investigated samples, the friction stress has been taken as 200 MPa [94] for all of the investigated samples.

6.2.2. Strengthening due to the solid solution

The strength due to the solid solution in the ferrite of the FP undeformed sample and FP processed samples can be determined using the following relation [67].

$$\sigma_{SS} = K_{C} X_{C} \quad 6.4$$

where K_{C} is the corresponding proportionality constant of carbon and it is taken as 5544 MPa per 1 wt% of carbon [67]. After substituting the lattice parameters of the ferrite of the FP undeformed sample and the FP processed samples obtained by XRD analysis (Table 6.1) in Equation 2.13, the carbon content in the ferrite of the FP undeformed sample and the FP samples processed up to 1,4, and 10 turns can be found. The results are listed in Table 6.1. The strength due to the solid solution in the ferrite of

the FP undeformed sample and FP processed samples is determined according to Equation 6.4, and the results are listed in Table 6.1.

The lattice parameters of both the ferrite of the as-received sample and the FM sample processed up to 4 turns and tempered at 450°C were found to be similar to those of the pure α-iron [53, 54] which suggests that no solid solution was formed in the ferrite of these samples (Table 6.1). The strengths due to the solid solution in the ferrite of the FM processed samples and the sample tempered at 250°C were determined by following the same procedures used when predicting the solution strengthening of the FP processed samples.

Table 6.1 The lattice parameters obtained by XRD, the carbon content in ferrite, and the strength due to the solid solution in the ferrite of the investigated samples.

Sample	**Lattice parameter (nm)**	X_C **(wt. %)**	σ_{SS} **(MPa)**
FP undeformed sample	0.2868 ± 0.0001	0.0195	108.0369
FP (HPT1)	0.2868 ± 0.0002	0.0195	108.0369
FP (HPT4)	0.2869 ± 0.0002	0.0451	250.1908
FP (HPT10)	0.2868 ± 0.0001	0.0195	108.0369
As-received	0.2866 ±0.0005	0.0000	0.0000
FM (HPT1)	0.2867 ± 0.0003	0.0041	15.5897
FM (HPT4)	0.2868 ± 0.0002	0.0195	108.0369
FM (HPT10)	0.2870 ± 0.0002	0.0708	392.3446
FM (HPT4) tempered at 250°C	0.2870 ± 0.0003	0.0708	392.3446
FM (HPT4) tempered at 450°C	0.2866 ± 0.0002	0.0000	0.0000

6.2.3. Strengthening due to dislocation density

Strengthening due to dislocation density was calculated according to Equation 6.5, which is another form of the Taylor relation (Equation 2.18). The values of the parameters used in Equation 6.5 are: the constant μ is 0.3 [93, 100, 189, 193, 194], the orientation factor M is 3 [100, 123, 193-195], the shear modulus G is 77 GPa [123], and the Burgers vector b of α-iron is 0.248 nm [100, 123, 188, 195]. The dislocation densities used in Equation 6.5 were obtained from an XRD line profile analysis except for the dislocation densities of the FP undeformed and as-received samples, which were taken from the literature [183, 196-198]. Table 6.2 details the dislocation densities of

the investigated samples as well as the calculated strength due to the dislocation densities (according to Equation 6.5) of these samples.

$$\sigma_D = \mu M G b \sqrt{\rho} \qquad 6.5$$

Table 6.2 Dislocation densities and the calculated strength due to the dislocation densities (according to Equation 6.5) of the investigated samples

Sample	$\rho \times 10^{15}$ (m^{-2})	σ_D (MPa)
FP undeformed sample	0.001 [183, 196]	17.2
FP (HPT1)	2.4 ± 0.1	854.1
Ann (HPT4)	3.08 ± 0.03	954
Ann (HPT10)	3.7 ± 0.2	1052.4
As-received	0.54 [197, 198]	399.4
FM (HPT1)	1.9 ± 0.3	749.1
FM (HPT4)	2.09 ± 0.02	786
FM (HPT10)	2.2 ± 0.2	799
FM (HPT4) tempered at 250°C	2.41 ± 0.05	842
FM (HPT4) tempered at 450°C	1.61 ± 0.03	687.4

6.2.4. Strengthening due to grain boundaries

It was not possible to determine the grain sizes of the deformed samples using TEM due to the high density of the dislocations, nor was it possible using EBSD due to the very low identification rate during the EBSD scan. According to [186], for metals processed by SPD at room temperature, the strengthening due to dislocation is generally much higher than strengthening due to the grain boundaries. In [186], a ratio (σ_{GB}/σ_D=0.52) was determined for Fe ferrite samples exposed to a strain higher than 1 during SPD processing at room temperature, and this ratio (σ_{GB}/σ_D=0.52) will be applied in the current model when calculating the grain boundary strengthening for the HPT-processed samples. Following this approach, the prediction of strengthening due to grain boundaries is possible even without measuring the grain size. The Hall-Petch relation (Equation 2.7) was applied when predicting the strength due to grain boundaries for the FP undeformed and as-received samples. Using the linear intercept

method [199], the average grain size of the FP undeformed and as-received samples was determined as 20 and 6 μm, respectively, while the Hall-Petch constant *k* was taken as 328 MPa $\mu m^{-1/2}$ [200]. Table 6.3 shows the calculated strength due to grain boundaries.

Table 6.3 The calculated strength due to the grain boundaries of the investigated samples

Sample	σ_{GB} **(MPa)**
FP undeformed sample	73.3303
Ann+HPT1	444.2
Ann+HPT4	496
Ann+HPT10	547.2
As-received	134
FM (HPT1)	390
FM (HPT4)	409
FM (HPT10)	415.3
FM (HPT4) tempered at 250°C	438
FM (HPT4) tempered at 450°C	357.4

6.2.5. Strengthening due to second phase particles

Although the essential relations used when predicting the strength due to second phase particles are stated in the literature review section, they will be deliberately restated here due to their importance and to make it easier for the reader to follow. The strength due to second phase particles can be found as [104]:

$$\sigma_{\text{part}} = \frac{\phi G b}{\pi D} ln \frac{D}{2b} \qquad 6.6$$

where ϕ is defined as in Section 2.3.3 and D is the interparticle spacing of the second phase particles, which can be found from the following relation [103]:

$$D = \left(\left(\frac{2\pi}{3f_{\text{part}}} \right)^{1/2} - \left(\frac{8}{3} \right)^{1/2} \right) . \frac{d_{\text{part}}}{2} \qquad 6.7$$

where f_{part} and d_{part} are the volume fraction and diameter of the second phase particles, respectively. The diameter of the second phase particles d_{part} can be found from the following relation [105]:

$$d_{\text{part}} = \frac{3f_{part}\lambda_{\text{part}}}{2(1 - f_{\text{part}})} \qquad 6.8$$

where λ_{part} is the mean free path (λ_{part} = 1-f_{part}/N_{L}) and N_{L} is the number of particles intercepted by unit length of a tested line. It will be assumed that pearlite, martensite, and cementite particles, as well as tempered martensite, are effectively non-shearable particles/inclusions. The strengthening due to non-shearable particles/inclusions will be determined by following the approach and procedures described above (Equation 6.6 to Equation 6.8) which is generally termed an Orowan-type approach. Optical and SEM images were used when calculating the volume fraction of the second phase particles of the investigated samples. The volume fraction of pearlite in the FP undeformed sample was determined as 0.1 using the point count method [157]. The volume fraction of the pearlite in the FP samples processed up to 1, 4, and 10 turns was assumed to be 0.1 since no cementite dissolution was evident. The volume fraction of the martensite in the as-received sample was determined as 0.15 using the point count method [157] and assumed to be constant after the HPT processing up to 1, 4, and 10 turns since no phase transformation was evident. The volume fraction of the tempered martensite in the FM sample processed up to 4 turns and tempered at 250^{o}C was assumed to be 0.15 (similar to the HPT-processed sample) since no significant change in the microstructure was observed. The volume fractions of the tempered martensite and the fine-sized cementite particles in the sample tempered at 450^{o}C were determined as 0.07 and 0.04, respectively, using the point count method [157]. Optical or SEM images were used when determining N_{L} (see Appendix A). When calculating strengthening due to second phase particles for the FM sample processed up to 4 turns and tempered at 450^{o}C, the linear addition of cementite and tempered martensite strengthening was assumed. The strengths due to second phase particles of the samples included in the model are listed in Table 6.4.

Table 6.4 The calculated strength due to second phase particles of the investigated samples

Sample	**σ_P (MPa)**
FP undeformed sample	13.07368
Ann+HPT1	10.66301
Ann+HPT4	30.39635
Ann+HPT10	28.38608
As-received	19.35067
FM (HPT1)	17.75349
FM (HPT4)	32.47252
FM (HPT10)	29.60848
FM (HPT4) tempered at 250°C	41.75602
FM (HPT4) tempered at 450°C	155.7981

Section 6.2.1 to Section 6.2.5 detailed the calculation of the individual contributors to the overall strength of the investigated samples. The overall strength is determined by the linear addition of these individual contributors of strengthening (Equation 6.3). Equation 2.24 ($Hv \approx C_T\sigma_y$) is used to convert the yield strength to hardness where a value of 3.5 was taken for the constant C_T in Equation 2.24 [123].

Table 6.5 Parameter values used in the model

Parameter	Value	References
σ_o	200 MPa	[94]
μ	0.3	[93, 100, 189, 193, 194]
M	3	[100, 123, 193-195]
G	77 GPa	[123]
b	0.248 nm	[100, 123, 188, 195]
γ_{PR}	0.33	[66]
k	328 MPa $\mu m^{1/2}$	[200]
K_C	5544 MPa/1wt.%	[67]
C_T	3.5	[123]
ρ (FP undeformed sample)	1.0×10^{12} m^{-2}	[183, 196]
ρ (as-received sample)	5.4×10^{14} m^{-2}	[197, 198]

The model was applied to predict all of the hardness data measured in the present work. The contributions of the different mechanisms to the strength as predicted by the model are shown in Figure 6.1 to Figure 6.3. It is clear from these figures that strengthening due to dislocation density has a strong effect on the overall strength, followed by strengthening due to grain boundaries, for all of the investigated samples. The strengthening due to the solid solution in the ferrite of the FP processed samples has a small effect as shown in Figure 6.1, whereas the strengthening due to second phase particles (pearlite in this case) was the smallest among all of the strengthening mechanisms. Strengthening due to the solid solution in the ferrite of the FM samples increased with the number of turns and reached a value close to that of the strengthening due to grain boundaries (Figure 6.2) in the FM sample processed up to 10 turns. In the FM sample processed up to 4 turns and tempered at 450°C, the strengthening due to second phase particles increased when compared to the sample tempered at 250°C. This can be attributed to the cementite particles in the sample tempered at 450°C, while there was no solid solution strengthening in this sample (Figure 6.3). Increasing the tempering temperature from 250°C to 450°C did not result in a significant reduction in the dislocation density. A comparison between the predicted and the measured hardness is presented in Figure 6.4. It can be seen from Figure 6.4 that the model captures the main hardening mechanisms well.

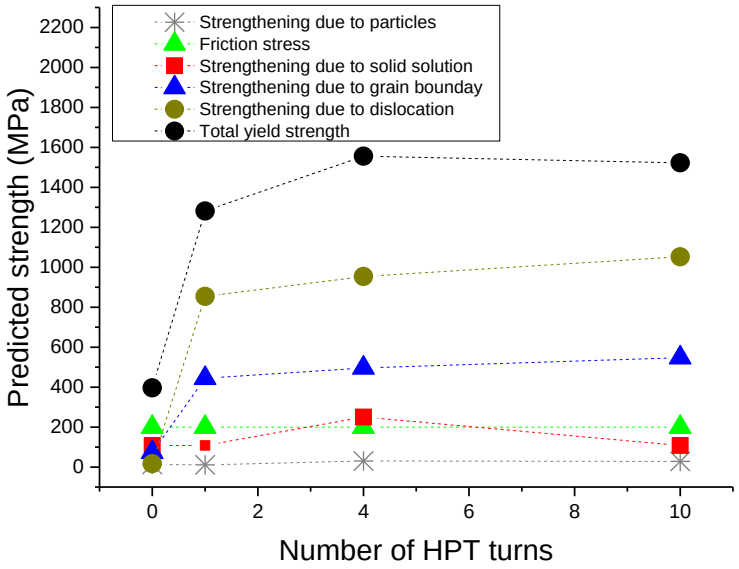

Figure 6.1 Prediction of the yield strength of the FP undeformed sample and the FP samples processed by HPT up to 1, 4, and 10 turns due to different strengthening mechanisms.

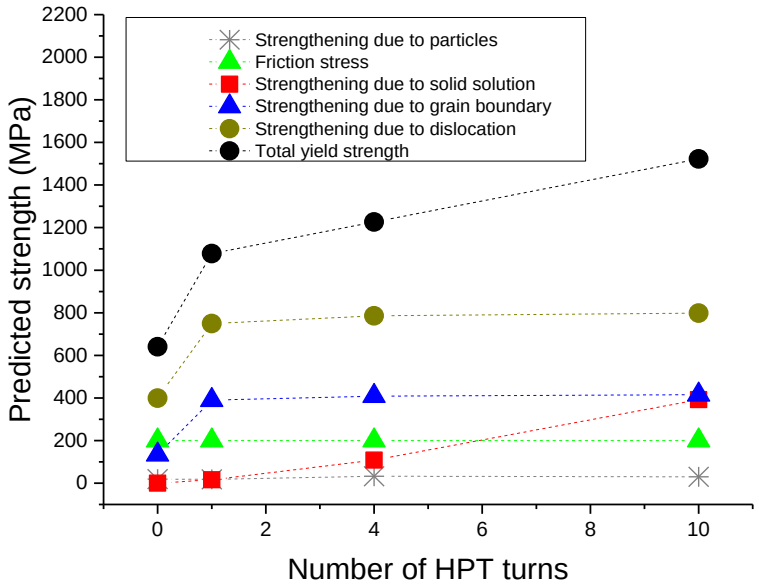

Figure 6.2 Prediction of the yield strength of the as received and FM samples processed by HPT up to 1, 4, and 10 turns due to different strengthening mechanisms.

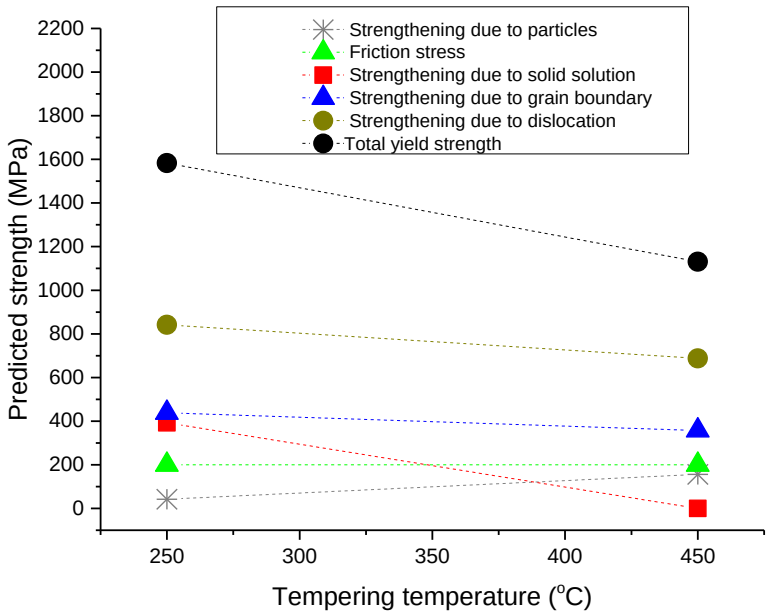

Figure 6.3 Prediction of the yield strength of the FM sample processed up to 4 turns and tempered at 250°C and 450°C due to different strengthening mechanisms.

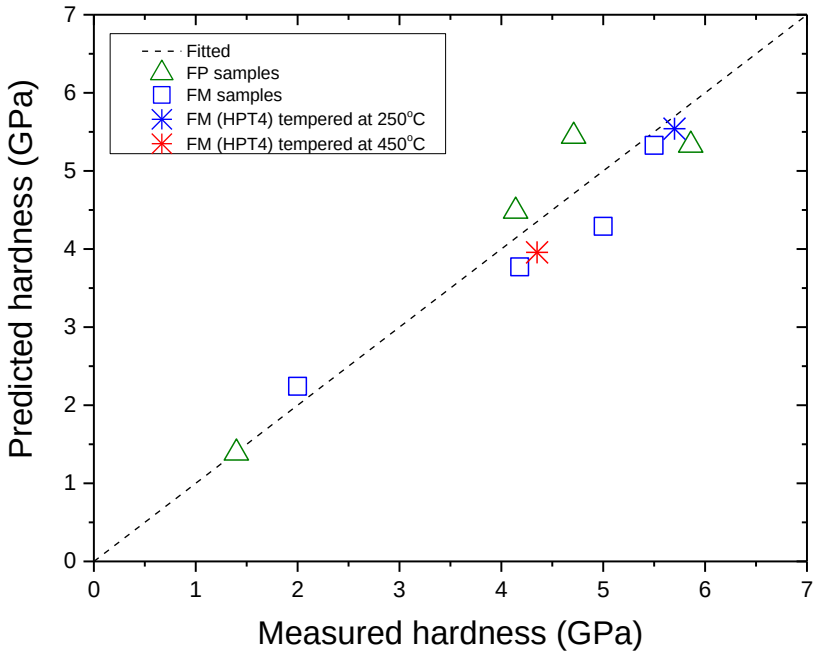

Figure 6.4 Predicted and measured hardness of the steel samples (undeformed, HPT-processed, and tempered samples).

6.3 Accuracy and applicability of the model

The model predicted the hardness of the investigated samples with an average error of ±8%. The model was applied to steel alloys in different initial states (ferritic-pearlitic and ferritic-martensitic). The model was also applied to undeformed steels (such as the FP undeformed and as-received samples) and HPT-processed samples (such as the FP and FM processed samples). The application of the model was further expanded to include FM processed samples tempered at different temperatures.

CHAPTER 7

7. Conclusions

During the HPT processing of low-carbon steel (0.1 wt.% C) in ferritic-pearlitic (FP) and ferritic-martensitic (FM) states, the microhardness monotonously increased with strain. After 10 turns, the microhardness increased up to 3 times compared to that of the initial state in both the FP and FM samples. The microhardness measurement of the individual phases, ferrite or martensite, in the FM samples processed up to 1, 4, and 10 turns showed a similar behaviour where each phase hardened with the increasing number of turns or strain. However, the ferrite had a higher hardening rate than the martensite. The nanohardness of the ferrite in the FP samples increased with the number of turns; this can be attributed to the increase in the dislocation density and the carbon-dislocation interaction. Similarly, the nanohardness of the pearlite increased with the number of turns up to 4 turns; this can be attributed to the decrease in the lamellae spacing. The nanohardness and the microhardness measurements of the FM samples processed by HPT had similar trend of increasing hardness with HPT deformation except for the FM sample processed up to 10 turns. The FM sample processed up to 4 turns and tempered at 350^{o}C had a higher nanohardness than that of the sample tempered at 250^{o}C.

Grain refinement of the ferrite and pearlite/martensite in the FP and FM samples took place during the HPT processing up to 10 turns. The ferrite grain boundaries were invisible at the edge of the FP and FM samples processed up to 4 turns when using optical microscopy or SEM. Cementite fragmentation in the FP samples started after 4 turns of HPT processing and increased with strain. Cementite dissolution was not observed even after 10 turns. Refinement of martensite islands was evident during the HPT processing reaching an estimated size of ~ 1 μm in the FM sample processed up to 10 turns. The FM samples processed up to 4 turns and tempered at 450^{o}C for 90 min have a microstructure consisting of ferrite, tempered martensite, and fine-sized cementite particles.

During the XRD investigation, only ferrite reflections were detected and this was due to the small volume fraction of pearlite, ~ 10%, and martensite, ~ 15%, in the FP and FM samples, respectively. No appreciable expansion in the lattice parameter (a) of the ferrite of the FP processed samples was observed. The lattice parameter (a) of the ferrite of the FM processed samples increased as the number of turns increased. The

lattice parameter of the ferrite of the FM sample processed up to 4 turns and tempered at 450°C for 90 min was similar to that of the pure α-iron (0.28664 nm) which suggests that the fine-sized cementite particles formed as a result of complete decomposition of the supersaturated solid solution in the ferrite matrix.

The volume-weighted mean column-length, $\langle t \rangle_{vol}$, of the FP processed samples determined by the modified Williamson-Hall method decreased with the number of turns. Using the modified Williamson-Hall method and the multiple whole profile-fit (MWP-fit), the fraction of the screw dislocation in the FP samples was found to decrease as the number of turns increased.

The strength/hardness model, proposed in the current study, is based on the assumption that the dislocations and grain boundaries strengthening are the main strengthening contributors to the strength of the HPT-processed steel samples. The strength/hardness model also accounts for other strengthening contributions such as solid solution and Orowan strengthening. The model was able to predict the strength/hardness of the HPT-processed samples and the FM processed samples tempered at different temperatures to a good accuracy with an average error of ±8%.

The novelties of this work are summarised below:

1. Producing a material with a novel microstructure from the ferritic-pearlitic or ferritic-martensitic initial state after only 10 turns of HPT processing. This material has a novel microstructure and possesses high microhardness of ~ 5.5 GPa.

2. Producing tempered ultrafine grained martensitic steel that is thermally stable up to 450°C. The key point in producing the thermally stable tempered martensitic steel is the HPT processing which provided dense crystal defects that acted as nucleation sites for the formed cementite particles which in turn retarded the grain growth at this high temperature.

3. Studying the character of the dislocation during the HPT processing of low-carbon steel in the ferritic-pearlitic, ferritic-martensitic, and FM processed samples tempered at different temperatures.

4. Proposing a model, using the dislocation densities obtained from the XRD line profile analysis (XLPA), to predict the strength/hardness of the FP processed samples, FM processed samples, and FM processed samples tempered at different temperatures. The model can be used to predict the strength/hardness of all the investigated samples to a good accuracy with an average error of ±8%.

CHAPTER 8

8. Future work and upscaling HPT sample size

8.1 Future work

In the current study, the thermal stability of FM samples processed by HPT up to different number of turns was investigated using optical microscopy, SEM, microhardness, TEM, and XRD. However, studying the thermal stability of the FP processed samples was not possible due to the limited time during the project, and hence, this is deemed a priority for future work.

The modified Williamson-Hall method and the MWP-fit were applied to the FP samples processed by HPT up to 1, 4, and 10 turns. In the future, other XLPA methods such as the Warren-Averbach and Convolutional Multiple Whole Profile (CMWP) fitting should be applied to investigate the reliability of the results obtained by the various XLPA techniques.

After the TEM investigation of the FM samples in the current study, it is believed that it is impossible, or at least difficult to a large extent, to measure the dislocation density in the HPT-processed samples using TEM due to the non-resolvable microstructure after the HPT processing. In the FM samples processed by HPT and tempered at different temperatures, the dislocation density decreased and the stress fields associated with the dislocations were relaxed to a large extent which enhances the opportunity to measure the dislocation density in these tempered samples by TEM. Measuring the dislocation density in the future by both the XLPA and TEM will provide a better reliability of the measured dislocation density.

The source of the carbon atoms that caused the interstitial solid solution in the ferrite matrix during the HPT processing of the FM samples can be determined when using the Atom Probe Tomography (ATP) since a 3D map is constructed during ATP tests. In the same regard, it is possible to study the carbon clustering when tempering the FM processed sample at 250^{o}C and the early stages of the cementite formation when tempering the FM processed samples at 350^{o}C and 450^{o}C.

Finally, conducting experiments to investigate high-strength low-alloy (HSLA) steel is another item for future work. It is well-known that neutron diffraction is very useful when studying multi-phase steels such as dual-phase and HSLA steels. It should be considered to use neutron diffraction in addition to XRD in further investigations. However, limited neutron diffraction centres can be found across the world.

8.2 Upscaling HPT sample size

The main disadvantage of the HPT processing is the size of the HPT sample. In most cases, the HPT sample has a diameter of 10 mm and a thickness of 1 mm. Accordingly, several attempts were made to upscale the HPT sample size and these will be explained. Sakai et al. [201] used a HPT sample, Al–3 wt.% Mg–0.2 wt.% Sc, in the cylindrical form with a diameter of 10 mm and a hight of 8.5 mm. Sakai et al. [201] had potential success when they successfully processed the cylindrical HPT sample up to 1 turn. Although there was a variation in the microhardness across the investigated central plane, the microhardness at the edge increased by a factor of >2 compared with the undeformed sample. Edalati and Horita [202] developed the so-called continuous high pressure torsion (CHPT) tool to overcome the main limitation of the HPT technique, the sample size. The CHPT tool consists of upper and lower anvils where the lower anvil has a ring-shaped area with high surface roughness while the upper anvil has a half ring-shaped groove with 0.5 mm depth, 3 mm width, and outer diameter of 20 or 30 mm. A U-shaped sample is placed in the upper anvil groove during the deformation. Edalati and Horita [202] processed a U-shaped sample of different materials using the CHPT tool up to 2 turns. The microstructure obtained by the CHPT was comparable to that obtained by the conventional HPT processing. Instead of using disk sample duirng the HPT processing, Harai et al. [203] used a ring sample having an inner and outer diameter of 14 and 20 mm. Harai et al. [203] processed a pure high aluminium sample up to 1 turn and concluded that using a ring or disk sample leads to comparable results.

It is clear from the above that upscaling the HPT sample size is an achievable target. Success of upscaling the HPT sample size will put HPT processing at front of SPD techniques.

In the current study, it was possible to produce ultrafine grained steels that are free microscopic and macroscopic defects. After 10 turns of HPT processing, the microhardness significantly increased to reach a value of ~ 5.5 to 5.8 GPa. A lot of industry applications require steels with high strength, such as the microhardness measured in the current study. It is important to stress here that the major limitation of the HPT is the sample size. This limitation should always be considered when talking about using HPT-processed samples in industrial applications. Three applications are identified here:

1. Armour plates: due to the high hardness obtained after the HPT processing of the FP and FM samples, the processed samples can be used in the military field in general and particularly as armour plates since the common armour plate, ARMOX 500T, has a microhardness of 540 HB (513 Hv) [204]. Using a processed low-carbon steel by HPT instead of ARMOX 500T in the armour plate industry will open a new window of producing low cost armour plate. The low carbon content in the current processed materials is another promising factor for this material to be used in the armour plate field since no problems will be anticipated during welding processes. In addition to the high strength that is required in any armour plate, impact toughness also required and should be studied further in the future.

2. Car body parts: upscaling the HPT sample size will allow the investigated processed samples to be used in the automotive industry. Steel is used to manufacture the different parts of the car such as the body, shafts, bearings and wheel rims among others. Nowadays, due to the global warming phenomena and the increasing oil prices, automotive manufacturers are keen to produce lightweight cars that also adhere to the strict safety specifications. These goals can be achieved by replacing mild steel sheets, used in the manufacturing of body parts, with high strength steel sheets [205]. The realisation of a microhardness of ~ 5.5 GPa in the investigated FP and FM samples is a first step towards the production of cars that are simultaneously lightweight and safe.

3. High temperature environment: some applications require steel with a microstructure stable at elevated temperatures in the range between 200^{o}C and 400^{o}C such as steam, chemical plants, and engine shafts in the aerospace sector. The thermally stable tempered martensitic steel produced in the current study will be a candidate for such applications taking into account the limitation of sample size.

Appendix A Metallography analysis and determination of carbon content in ferrite after HPT processing

A.1 Point count method

The point count method can be implemented by following the procedures that are mentioned in the ASTM E562 [157]. The point count method was used to determine the volume fraction of the pearlite, martensite, and cementite particles in the FP, FM, FM samples processed up to 4 turns and tempered at 450°C that were used in the current study. Here, the procedures that were followed to determine the volume fraction of pearlite in one area out of three in the FP undeformed smple will be demonstrated.

A grid consisting of 12 horizontal and 12 vertical lines is placed on an optical image representing the microstructure of the undeformed FP sample as shown in Figure A-1. The second phase (pearlite) should be clearly defined in the optical image. The points of intersection between the horizontal and vertical lines are the points of interest and they will be used in the point count method. The grid constructed in Figure A-1 yielded 12 grid points (P_o) and 12 fields (number of horizontal lines) and hence the total number of the grid points (P_T) is 12×12=144. If the point falls in the second phase (pearlite), its value is one while the value of the point tangent to the second phase (pearlite) is ½. The mean volume fraction of pearlite ($\overline{X}$) can be found by $\sum P_p/P_T$ (Equation A-1). However, conducting the analysis of each field individually and then taking the average will help us in performing further statistical analysis which is useful to a large extent [206].

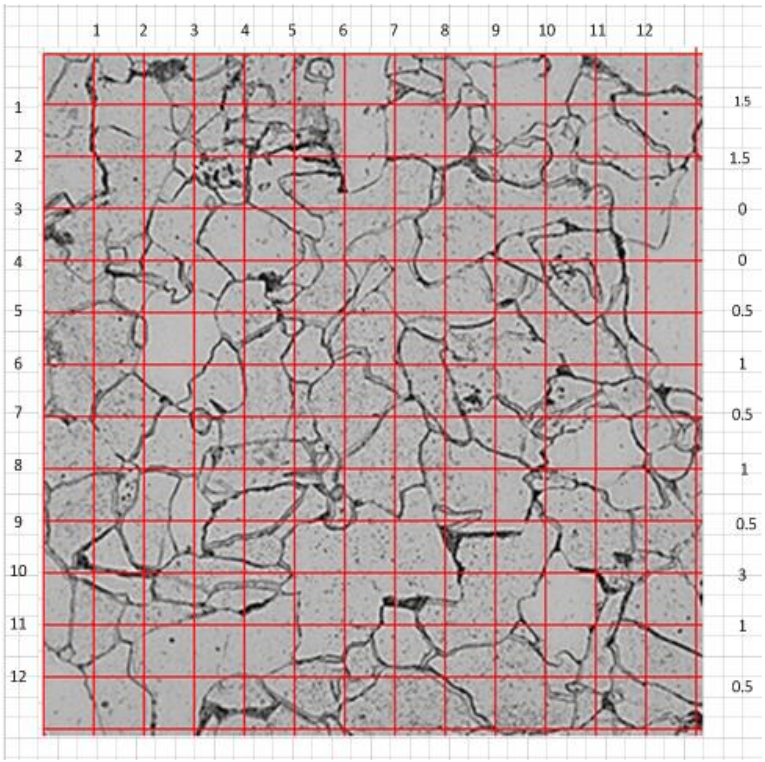

Figure A-1 A grid containing 144 points is placed on an optical micrograph representing the microstructure of the FP undeformed sample etched with 2% nital.

Table App-1 Illustration of the point count method statistical analysis

Field number	**Number of points in pearlite (P_p)**	$X_i=P_p/P_o$	$(X_i - \overline{X})^2$
1	1.5	0.125	0.002
2	1.5	0.125	0.002
3	0	0	0.005
4	0	0	0.005
5	0.5	0.041	0.001
6	1	0.083	4.822×10^{-5}
7	0.5	0.041	0.001
8	1	0.083	4.822×10^{-5}
9	0.5	0.041	0.001
10	3	0.25	0.030
11	1	0.083	4.822
12	0.5	0.041	0.001
	$\sum P_p = 11$		$\sum(X_i - \bar{X})^2$=0.0515

Again, the volume fraction of pearlite (V_p) can be found from the following relation [206]:

$$V_p(\%) = \frac{\sum P_p}{P_T} * 100 = \frac{11}{144} * 100 = 7.6\% \quad \text{A-1}$$

The standard deviation (sd) can be found from the following relations [206]:

$$sd = \left[\frac{\sum(X_i - \bar{X})^2}{N_f - 1}\right]^{1/2} = \left[\frac{0.0515}{12 - 1}\right]^{1/2} = 0.068 \quad \text{A-2}$$

where N_f is the number of fields. The 95% confidence limit (CL) can be found from the following relation [206]:

$$95\%\ CL = \frac{2s}{\sqrt{N - 1}} * 100 = \frac{2 * 0.06}{\sqrt{11}} = 4\% \quad \text{A-3}$$

A.2 Calculation of N_L

A test grid consisting of 25 horizontal and 25 vertical lines is placed on SEM image representing the microstructure of the FM sample processed up to 4 turns and tempered at 450°C for 90 min (Figure A-2) [207]. In Figure A-2, 28.5 mm equals 1 μm on the SEM image scale and accordingly each horizontal or vertical line has a length of 4.56 μm. The total length of the horizontal or vertical lines is 4.56×25=114 μm. The number of the particles intercepted per horizontal or vertical unit length (N_L) is illustrated on the left and bottom of Figure A-2, respectively. The average (N_L) was found to be ~ 0.49 μm^{-1}.

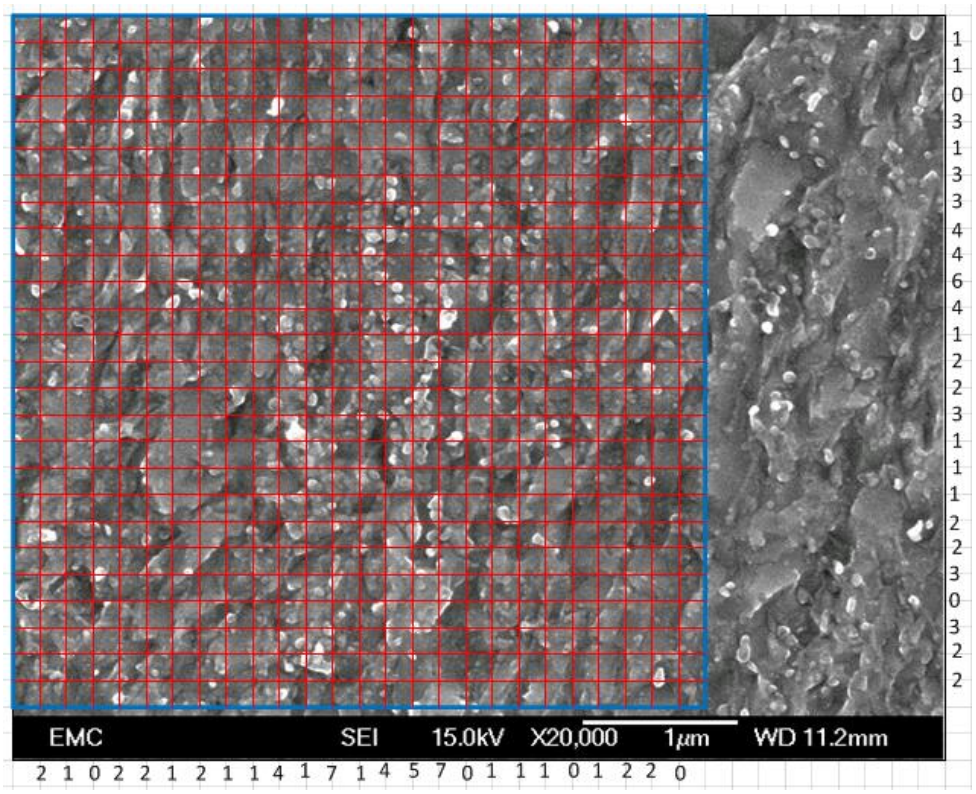

Figure A-2 A grid consisting of 25 horizontal and 25 vertical lines is placed on SEM image that represents the microstructure of the FM sample processed up to 4 turns and tempered at 450°C for 90 min.

References

[1] Y.T. Zhu, T.C. Lowe, T.G. Langdon, Scripta Materialia, 51 (2004) 825-830.
[2] H. Gleiter, Progress in Materials Science, 33 (1989) 223-315.
[3] C.C. Koch, Y.S. Cho, Nanostructured Materials, 1 (1992) 207-212.
[4] A.P. Zhilyaev, T.G. Langdon, Progress in Materials Science, 53 (2008) 893-979.
[5] T.G. Langdon, Journal of Materials Science, 42 (2007) 3388-3397.
[6] Y. Zhu, R.Z. Valiev, T.G. Langdon, N. Tsuji, K. Lu, MRS Bulletin, 35 (2010) 977-981.
[7] T.C. Lowe, R.Z. Valiev, JOM, (2004) 64-68.
[8] Y.T. Zhu, T.G. Langdon, JOM, (2004) 58-63.
[9] C. Xu, Z. Horita, T.G. Langdon, Acta Materialia, 56 (2008) 5168-5176.
[10] A.P. Zhilyaev, G.V. Nurislamova, B.-K. Kim, B.D. Baro, J.A. Szpunar, T.G. Langdon, Acta Materialia, 51 (2003) 753-765.
[11] A. Vorhauer, R. Pippan, Scripta Materialia, 51 (2004) 921-925.
[12] A.P. Zhilyaev, T.R. McNelley, T.G. Langdon, Journal of Materials Science, 42 (2007) 1517-1528.
[13] R.Z. Valiev, Y.V. Ivanisenko, E.F. Rauch, B. Baudelet, Acta Materialia, 44 (1996) 4705-4712.
[14] N.H. Polakowski, E.J. Ripling, Strength and structure of engineering materials, Prentice – Hall, Englewook cliffs, NJ, USA, 1966.
[15] M.V. Degtyarev, T.I. Chashchukhina, L.M. Voronova, V. Pilyugin, Phys. Metal. Metall, 90 (2000) 604-611.
[16] B. Efros, V. Pilyugin, A. Patselov, Y. Beygelzimer, N. Efros, in: Y. Zhu, T.G. Langdon, R. Mishra, S. Semiatin, M. Saran, T.C. Lowe (Eds.) Ultrafine grained materials II, TMS (The minerals, Metals and Materials Society), 2002.
[17] H. Jiang, Y.T. Zhu, D.P. Butt, I.V. Alexandrov, T.C. Lowe, Materials Science and Engineering A, 290 (2000) 128-138.
[18] M. Kawasaki, R.B. Figueiredo, T.G. Langdon, Acta Materialia, 59 (2011) 308-316.
[19] A.P. Zhilyaev, S. Lee, G.V. Nurislamova, R.Z. Valiev, T.G. Langdon, Scripta Materialia, 44 (2001) 2753-2758.
[20] R.Z. Valiev, T.G. Langdon, Progress in Materials Science, 51 (2006) 881-981.
[21] D.H. Shin, B.C. Kim, Y.-S. Kim, K.-T. Park, Acta Materialia, 48 (2000) 2247-2255.
[22] J. Zrnik, S.V. Dobatkin, I. Mamuzic, METABK, 47 (2008) 211-216.
[23] X. Nie, S. Xie, Physica B, 405 (2010) 1969-1972.
[24] P.B. Berbon, M. Furukawa, Z. Horita, M. Nemoto, T.G. Langdon, Metallurgical and Materials Transactions A, 30 (1999) 1989-1997.
[25] Y. Iwahashi, J. Wang, Z. Horita, M. Nemoto, T.G. Langdon, Scripta Materialia, 35 (1996) 143-146.

[26] B.S. Atlan, Severe plastic deformation: toward bulk production of nanostructured materials, Nova Science Publisher, New York, USA, 2006.
[27] M. Furukawa, Z. Horita, T.G. Langdon, Adv. Eng. Mat., 3 (2001) 121-125.
[28] M. Furukawa, Z. Horita, M. Nemoto, T.G. Langdon, Materials Science and Engineering A, 324 (2002) 82-89.
[29] M. Furukawa, Y. Iwahashi, Z. Horita, M. Nemoto, T.G. Langdon, Materials Science and Engineering A, 257 (1998) 328-332.
[30] V.M. Segal, Materials Science and Engineering A, 197 (1995) 157-164.
[31] K. Nakashima, Z. Horita, M. Nemoto, T.G. Langdon, Materials Science and Engineering A, 281 (2000) 82-87.
[32] G. Krallics, J.G. Lenard, Journal of Materials Processing Technology, 152 (2004) 154-161.
[33] N. Tsuji, Y. Saito, S.-H. Lee, Y. Minamino, Advanced Engineering Materials, 5 (2003) 338-343.
[34] Y. Saito, H. Utsunomiya, N. Tsuji, T. Sakai, Acta Materialia, 47 (1999) 579-583.
[35] E.O. Hall, Proc. Phys. Soc. B, 64 (1951) 747-753.
[36] N.J. Petch, J. Iron Steel Inst. , 173 (1953) 25-28.
[37] J.T. Wang, C. Xu, Z.Z. Du, G.Z. Qu, T.G. Langdon, Materials Science and Engineering A, 410-411 (2005) 312-315.
[38] K.-T. Park, Y.-S. Kim, D.H. Shin, Metallurgical and Materials Transactions A, 32 (2001) 2373-2379.
[39] J. Zrnik, R. Pippan, S. Scheriau, L. Kraus, M. Fujda, Journal of Materials Science, 45 (2010) 4822-4826.
[40] Z. Horita, T. Fujinami, M. Nemoto, T.G. Langdon, Metallurgical and Materials Transactions A, 31 (2000) 691-701.
[41] R.Z. Valiev, I.V. Alexandrov, Y.T. Zhu, T.C. Lowe, J. Mater. Res, 17 (2002) 5-8.
[42] V.V. Stolyarov, Y.T. Zhu, I.V. Alexandrov, T.C. Lowe, R.Z. Valiev, Materials Science and Engineering A, 343 (2003) 43-50.
[43] V. Latysh, G. Krallics, I. Alexandrov, A. Fodor, Current Applied Physics, 6 (2006) 262-266.
[44] R.Z. Valiev, R.K. Islamgaliev, I.V. Alexandrov, Progress in Materials Science, 45 (2000) 103-189.
[45] E.V. Bobruk, M.Y. Murashkin, V.U. Kazykhanov, R.Z. Valiev, Reviews on Advance Materials Science, 31 (2012) 109-115.
[46] A. Revesz, Z. Kanya, T. Verebelyi, P.J. Szabo, A.P. Zhilyaev, T. Spassov, Journal of Alloys and Compounds, 504 (2010) 83-88.
[47] D.H. Shin, B.C. Kim, Y. Kim, K. Park, Acta Materialia, 48 (2000) 2247-2255.

[48] D.-W. Suh, J.-H. Bae, J.-Y. Cho, K.H. Oh, H.-C. Lee, ISIJ International, 41 (2001) 782-787.
[49] B. Karlsson, G. Linden, Materials Science and Engineering A, 17 (1975) 209-219.
[50] L. Xiao, Z. Fan, Z. Jinxiu, Z. Mingxing, K. Mokuang, G. Zhenqi, The American Physical Society, 52 (1995) 9970-9978.
[51] G.V. Kurdjumov, A.G. Khachaturyan, Metallurgical Transactions, 3 (1972) 1069-1076.
[52] G.V. Kurdjumov, Metallurgical Transactions A, 7 (1976) 999-1011.
[53] R.E. Smallman, R.J. Bishop, Metals and Materials: Science, Processes, Applications, Butterworth Heineman, Oxford, UK, 1995.
[54] C.-M. Li, F. Sommer, E.J. Mittemeijer, Materials Science and Engineering: A, 325 (2002) 307-319.
[55] H.K. Bhadeshia, R.W. Honeycombe, Steels: microstructure and properties, Butterworth-Heinemann, Oxford, UK, 2006.
[56] J. Kadkhodapour, S. Schmauder, D. Raabe, S. Ziaei-Rad, U. Weber, M. Calcagnotto, Acta Materialia, 59 (2011) 4387-4394.
[57] V.B. Ginzburg, Metallurgical design of flat rolled steels, Marcel Dekker, New York, USA, 2005.
[58] D.A. Korzekwa, D.K. Matlock, G. Krauss, Metallurgical Transactions A, 15 (1984) 1221-1228.
[59] B.-C. Hwang, T.-Y. Cao, S.Y. Shin, S.-H. Kim, S.-H. Lee, S.-J. Kim, Materials Science and Technology, 21 (2005) 967-975.
[60] M. Pouranvari, MJoM, 16 (2010) 187-194.
[61] U. Liedl, S. Traint, E.A. Werner, Computational Materials Science, 25 (2002) 122-128.
[62] V.H.B. Hernandez, S.S. Nayak, Y. Zhou, Metallurgical and Materials Transactions A, 42 (2011) 3115-3129.
[63] X. Fang, Z. Fan, B. Ralph, P. Evans, R. Underhill, Journal of Materials Processing Technology, 132 (2003) 215-218.
[64] S. Gunduz, Materials Letters, 63 (2009) 2381-2383.
[65] A. Salemi, A. Abdollah-zadeh, Materials Characterization, 59 (2008) 484-487.
[66] G.E. Dieter, Mechanical Metallurgy, McGraw-Hill, USA, 1967.
[67] F.B. Pickering, Physical Metallurgy and the Design of Steels, Applied Science Publ., London, UK, 1978.
[68] F. Huyan, R. Larker, P. Rubin, P. Hedstrom, ISIJ International, 54 (2014) 248-250.
[69] E.J. Fasiska, H. Wagemblast, Trans. AIME, 239 (1967) 1818-1820.
[70] E.C. Bain, H.P. Paxton, Alloying elements in steel, American Society for Metals (ASM), Ohio, USA, 1961.
[71] A.R. Troiano, F.T. McGuire, Trans. Am. Soc. Met., 31 (1943) 340-359.

[72] B.L. Ferguson, in: G.E. Dieter (Ed.) ASM Handbook, Materials Selection and Design, ASM International, OH, USA, 1997.
[73] A.H. Cottrell, B.A. Bilby, Proc. Phys. Soc. , 62A (1949) 49-62.
[74] T.J. Rupert, J.C. Trenkle, C.A. Schuh, Acta Materialia, 59 (2011) 1619-1631.
[75] I. Matsui, T. Uesugi, Y. Takigawa, K. Higashi, Acta Materialia 61 (2013) 3360-3369.
[76] K. Hono, M. Ohnuma, M. Murayama, S. Nishida, A. Yoshie, T. Takahashi, Scripta Materialia, 44 (2001) 977-983.
[77] W. Lojkowski, M. Djahanbakhsh, G. Burkle, S. Gierlotka, W. Zielinski, H.-J. Fecht, Materials Science and Engineering A, 303 (2001) 197-208.
[78] J.D. Eshelby, F.C. Frank, F.R.N. Nabarro, The London, Edinburgh, and Dublin Philosophical Magazine and Journal of Science, 42 (1951) 351-364.
[79] A.H. Cottrell, Trans. AIME, 212 (1958) 192-203.
[80] M.A. Meyers, A. Mishra, D.J. Benson, JOM, (2006) 41-48.
[81] M.F. Ashby, Philosophical Magazine A, 21 (1970) 399-424.
[82] M.A. Meyers, E. Ashworth, Philosophical Magazine A, 46 (1982) 737-759.
[83] D.G. Morris, M.A. Morris, Acta Metallurgica, 39 (1991) 1763-1770.
[84] A.H. Chokshi, A. Rosen, Scripta Metallurgica, 23 (1989) 1679-1689.
[85] R.K. Guduru, R.O. Scattergood, C.C. Koch, K.L. Murty, S. Guruswamy, M.K. McCarter, Scripta Materialia, 54 (2006) 1879-1883.
[86] G.E. Fougere, J.R. Weertman, R.W. Siegel, Nanostructured Materials, 5 (1995) 127-134.
[87] D. Jia, K.T. Ramesh, E. Ma, Acta Materialia, 51 (2003) 3495-3509.
[88] J.C. Rawers, G. Korth, Nanostructured Materials, 7 (1996) 25-45.
[89] M. Zhu, H.-J. Fecht, Nanostructured Materials, 6 (1995) 921-924.
[90] A. Munitz, Z. Livne, J.C. Rawers, J.S. Adams, R.J. Fields, Nanostructured Materials, 11 (1999) 159-177.
[91] J.S.C. Jang, C.C. Koch, Scripta Metallurgica, 24 (1990) 1599-1604.
[92] K. Takeda, N. Nakada, T. Tsuchiyama, S. Takaki, ISIJ International, 48 (2008) 1122-1125.
[93] X.G. Qiao, N. Gao, M.J. Starink, Philosophical Magazine A, 4 (2012) 446-470.
[94] D.R. Lesuer, C.K. Syn, O.D. Sherby, Materials Science and Engineering A, 463 (2007) 54-60.
[95] N. Hansen, Scripta Materialia, 51 (2004) 801-806.
[96] N. Kamikawa, X. Huang, N. Tsuji, N. Hansen, Acta Materialia, 57 (2009) 4198-4208.
[97] J. Gubicza, N.Q. Chinh, T.G. Langdon, T. Ungar, in: Y.T. Zhu, T.G. Langdon, Z. Horita, M.J. Zehetbauer, S.L. Semiatin, T.C. Lowe (Eds.) Ultrafine Grained Materials IV, TMS (The Minerals, Metals & Materials Society), 2006.
[98] D.J. Dingley, D. McLean, Acta Metallurgica, 15 (1967) 885-901.
[99] L. Malik, J.A. Lund, Metallurgical Transactions, 3 (1972) 1403-1406.

[100] A. Sarkar, A. Bhowmik, S. Suwas, Applied Physics A, 94 (2009) 943-948.
[101] E. Orowan, Institute of Metals, London, (1948) 451-453.
[102] R.L. Fullman, Trans. AIME, 197 (1953) 447-452.
[103] L.M. Brown, in: P. Haasen (Ed.) Strength of metals and alloys, Pergamon Press, Oxford, UK, 1979.
[104] A. Kelly, R.B. Nicholson, Progress in Materials Science, 10 (1963) 151-311.
[105] W.M. Baldwin, B.I. Edelson, ASM TRANS Q, 55 (1962) 230-250.
[106] J. Moon, S. Kim, J. Jang, J. Lee, C. Lee, Materials Science and Engineering A, 487 (2008) 552-557.
[107] Y.-H. Zhao, X.-Z. Liao, S. Cheng, E. Ma, Y.T. Zhu, Adv. Mater, 18 (2006) 2280-2283.
[108] A.F. Zimmerman, G. Palumbo, K.T. Aust, U. Erb, Materials Science and Engineering A, 328 (2002) 137-146.
[109] Y. Fukuda, K. Oh-ishi, Z. Horita, T.G. Langdon, Acta Materialia, 50 (2002) 1359-1368.
[110] K.-T. Park, Y.-S. Kim, J.G. Lee, D.H. Shin, Materials Science and Engineering A, 293 (2000) 165-172.
[111] S.V. Dobatkin, S.V. Shagalina, O.I. Sleptsov, N.A. Krasil'nikov, Russian Metallurgy (Metally), 5 (2006) 95-104.
[112] E.G. Astafurova, G.G. Zakharova, E.V. Naydenkin, G.I. Raab, S.V. Dobatkin, The Physics of Metals and Metallography, 1 (2011) 62-71.
[113] F. Wetscher, R. Pippan, S. Sturm, F. Kauffman, C. Scheu, G. Dehm, Metallurgical and Materials Transactions A, 37 (2006) 1963-1968.
[114] M. Umemoto, Materials Transactions, 44 (2003) 1900-1911.
[115] Y. Ivanisenko, W. Lojkowski, R.Z. Valiev, H.-J. Fecht, Acta Materialia, 51 (2003) 5555-5570.
[116] K. Aoki, Y. Kimura, A. Azushima, in: I.S. Takaki, T. Maki (Eds.) International Symposium on Ultrafine Grained Steels, The Iron and Steel Institute of Japan (ISIJ), Tokyo, Japan, 2001.
[117] S. Bayramoglu, C.H. Gur, I.V. Alexandrov, M.M. Abramova, Materials Science and Engineering A, 527 (2010) 927-933.
[118] D.M.M. Cardona, J. Wongsa-Ngam, T.G. Langdon, J. Mater. Res. Technol., 3 (2014) 344-348.
[119] M. Calcagnotto, D. Ponge, Y. Adachi, D. Raabe, Proceeding of the 2nd International symposium on steel science (ISSS 2009), The Iron and Steel Institute of Japan (ISIJ), Japan, 2009.
[120] Y. Son, Y.K. Lee, K.-T. Park, C.S. Lee, D.H. Shin, Acta Materialia, 53 (2005) 3125-3134.
[121] D. Tabor, J. Inst. Metals, 79 (1951) 1-8.

[122] J.R. Cahoon, W.H. Broughton, A.R. Kutzak, Metallurgical Transactions, 2 (1971) 1979-1983.
[123] X. Zhang, N. Hansen, Y. Gao, X. Huang, Acta Materialia, 60 (2012) 5933-5943.
[124] G.R. Speich, H. Warlimont, J. Iron Steel Inst., 206 (1968) 385-392.
[125] N. Tsuji, R. Ueji, Y. Minamino, Y. Saito, Scripta Materialia, 46 (2002) 305-310.
[126] H.F. Lan, W.J. Liu, X.H. Liu, ISIJ International, 47 (2007) 1652-1657.
[127] E.G. Astafurova, S.V. Dobatkin, E.V. Naydenkin, S.V. Shagalina, G.G. Zakharova, F. Ivanov, Nanotechnologies in Russia, 4 (2009) 109-120.
[128] W.C. Oliver, G.M. Pharr, J. Mater. Res., 7 (1992) 1564-1583.
[129] W.C. Oliver, G.M. Pharr, J. Mater. Res. , 18 (2004).
[130] W.D. Nix, H. Gao, J. Mech. Phys. Solids, 46 (1998) 411-425.
[131] L. Qian, M. Li, Z. Zhou, H. Yang, X. Shi, Surface and Coatings Technology, 195 (2005) 264-271.
[132] E. Fereiduni, S.S.G. Banadkouki, Materials and Design, 56 (2014) 232-240.
[133] K. Hayashi, K. Miyata, F. Katsuki, T. Ishimoto, T. Nakano, Journal of Alloys and Compounds, 5775 (2013) 5593-5596.
[134] H. Ghassemi-Armaki, R. Maaβ, S.P. Bhat, J.R. Greer, K.S. Kumar, Acta Materialia, 62 (2014) 197-211.
[135] M.D. Taylor, K.S. Choi, X. Sun, Materials Science and Engineering A, 597 (2014) 431-439.
[136] T. Ungar, J. Gubicza, G. Ribarik, A. Borbely, Journal of Applied Crystallography, 34 (2001) 298-310.
[137] G.K. Williamson, W.H. Hall, Acta Metallurgica, 1 (1953) 22-31.
[138] B.E. Warren, B.L. Averbach, Journal of Applied Physics, 23 (1952) 497-512.
[139] G. Ribarik, T. Ungar, J. Gubicza, Journal of Applied Crystallography, 34 (2001) 669-676.
[140] http://www.renyi.hu/mwp, 02/07/2015.
[141] A. Guinier, X-ray diffraction, W. H. Freeman, CA, USA, 1963.
[142] A.R. Stokes, A.J.C. Wilson, Proc. Phys. Soc., 56 (1944) 174-181.
[143] T. Ungar, J. Gubicza, P. Hanak, I. Alexandrov, Materials Science and Engineering A, 319-321 (2001) 274-278.
[144] T. Ungar, A. Borbely, Applied Physics Letters, 69 (1996) 3173-3175.
[145] T. Ungar, G. Tichy, Physica Status Solidi A, 171 (1999) 425-434.
[146] J. Gubicza, X-ray line profile analysis in materials science, Engineering Science Reference, PA, USA, 2014.
[147] M. Wilkens, Physica Status Solidi, 2 (1970) 359-370.
[148] M. Wilkens, , in: J.A. Simmon, R. Wit, R. Bullough (Eds.) Fundamental aspects of dislocation theory, National Bureau Standards, Washington DC, USA, 1970.

[149] J. Goodisman, Journal of Applied Crystallography, 13 (1980) 132-134.
[150] J. Chakraborty, M. Ghosh, R. Ranjan, G. Das, D. Das, S. Chandra, Philosophical Magazine A, 93 (2013) 4598-4616.
[151] S.H. Nedjad, F.H. Nasab, M.R.M. Garabagh, S.R. Damadi, M.N. Ahmadabadi, Metallurgical and Materials Transactions A, 42 (2011) 2493-2496.
[152] S.N. Alhajeri, School of Engineering Science, University of Southampton, Southampton, UK, 2010.
[153] http://www.micromaterials.co.uk/the-nano-test/nanotest-vantage, 23/06/2015.
[154] http://www.micro.soton.ac.uk/JEM3010.php, 02/07/2015.
[155] http://ww1.prweb.com/prfiles/2013/06/04/10952219/smartlab.07_2005_10.jpg, 23/06/2015.
[156] http://www.isis.stfc.ac.uk/images/groups/support-laboratories/rigaku-inside13349.jpg, 23/06/2015.
[157] ASTM (E562-99), ASTM International, PA, USA, 2001.
[158] M. Wojdyr, Journal of Applied Crystallography, 43 (2010) 1126-1128.
[159] www.originlab.com, 02/07/2015.
[160] M.U. Cohen, Rev. Sci. Instrum, 6 (1935) 68-74.
[161] S.M. Hosseini, A. Najafizadeh, A. Kermanpur, Journal of Materials Processing Technology, 211 (2011) 230-236.
[162] G.R. Speich, W.C. Leslie, Metallurgical Transactions, 3 (1972) 1043-1053.
[163] Y. Bergstrom, Y. Granbom, D. Sterkenburg, Journal of Metallurgy, (2010) 1-16.
[164] M. Calcagnotto, Y. Adachi, D. Ponge, D. Raabe, Acta Materialia, 59 (2011) 658-670.
[165] K.R. Gadelrab, G. Li, M. Chiesa, T. Souier, J. Mater. Res., (2012) 1-6.
[166] Q. Furnemont, M. Kempf, Materials Science and Engineering A, 328 (2002) 26-32.
[167] V.G. Gavriljuk, Materials Science and Engineering A, 345 (2003) 81-89.
[168] L. Vanherpe, N. Moelans, B. Blanpain, S. Vandewalle, Computational Materials Science, 49 (2010) 340-350.
[169] C.S. Smith, Trans. AIME, 175 (1948) 15-51.
[170] S. Takebyashi, T. Kunieda, N. Yoshinaga, K. Ushioda, S. Ogata, ISIJ International, 50 (2010) 875-882.
[171] N. Guo, T. Liu, B. Luan, B. Wang, Q. Liu, Materials Research Innovations, 18 (2014) 249-254.
[172] Y.Z. Chen, A. Herz, Y.J. Li, C. Borchers, P. Choi, D. Raabe, R. Kirchheim, Acta Materialia, 61 (2013) 3172-3185.
[173] X. Zhang, A. Godfrey, X. Huang, N. Hansen, Q. Liu, Acta Materialia, 59 (2011) 3422-3430.
[174] R.A. Renzetti, H.R.Z. Sandim, R.E. Bolmaro, P.A. Suzuki, A. Moslang, Materials Science and Engineering A, 534 (2012) 142-146.

[175] G.M. Cheng, W.W. Jian, W.Z. Xu, H. Yuan, P.C. Millett, Y.T. Zhu, Materials Research Letters, 1 (2013) 26-31.
[176] C.W. Lung, J. Mater. Sci. Technol., 11 (1995) 133-136.
[177] V. Vitek, Philosophical Magazine, 84 (2004) 415-428.
[178] J. Chang, W. Cai, V.V. Bulatov, S. Yip, Computational Materials Science, 23 (2002) 111-115.
[179] E. Clouet, S. Garruchet, H. Nguyen, M. Perez, C. Becquart, Acta Materialia, 56 (2008) 3450-3460.
[180] M.N. Shetty, Dislocations and mechanical behaviour of materials, PHI Learning Pvt. Ltd., Delhi, India, 2013.
[181] A. Rollett, F.J. Humphreys, G.S. Rohrer, M. Hatherly, Recrystallization and related annealing phenomena, Elsevier, Oxford, UK, 2004.
[182] H. Strunk, H. Strecker, Materials Science and Engineering, 62 (1984) 265-269.
[183] J. Pesicka, R. Kuzel, A. Dronhofer, G. Eggeler, Acta Materialia, 51 (2003) 4847-4862.
[184] H.-C. Chen, G.-H. Cheng, Journal of Materials Science, 24 (1989) 1991-1994.
[185] L.A. Norstrom, J. Scand, J. Metall, 5 (1976) 159-165.
[186] M.J. Starink, X. Cheng, S. Yang, Acta Materialia, 61 (2013) 183-192.
[187] R.L. Miller, Metallurgical Transactions, 3 (1972) 905-912.
[188] B.Q. Han, F.A. Mohamed, E.J. Lavernia, Metallurgical and Materials Transactions A, 34 (2003) 71-83.
[189] M.J. Starink, S.C. Wang, Acta Materialia, 51 (2003) 5131-5150.
[190] U. Essmann, H. Mughrabi, Philosophical Magazine A, 40 (1979) 731-756.
[191] Z. Zhu, M.J. Starink, Materials Science and Engineering: A, 489 (2008) 138-149.
[192] B. Milkereit, M.J. Starink, Materials & Design, 76 (2015) 117-129.
[193] L. Wang, M. Li, J. Almer, Acta Materialia, 62 (2014) 239-249.
[194] H. Hosseini-Toudeshky, B. Anbarlooie, J. Kadkhodapour, G. Shadalooyi, Materials Science and Engineering A, 600 (2014) 108-121.
[195] M. Delince, P.J. Jacues, T. Pardoen, Acta Materialia 54 (2006) 3395-3404.
[196] S. Takaki, Materials Science Forum, Trans. Tech. Publ., 2003.
[197] T. Kunieda, M. Nakai, Y. Murata, T. Koyama, M. Morinaga, ISIJ international, 45 (2005) 1909-1914.
[198] J. Pesicka, A. Aghajani, C. Somsen, A. Hartmaier, G. Eggeler, Scripta Materialia, 62 (2010) 353-356.
[199] H. Abrams, in: G.E. Pellissier, S.M. Purdy (Eds.) Stereology and quantitative metallography, ASTM 504, ASTM, Pa, USA, 1972.
[200] D.-H. Shin, J.-J. Park, S.Y. Chang, Y.-K. Lee, K.-T. Park, ISIJ International, 42 (2002) 1490-1496.

[201] G. Sakai, K. Nakamura, Z. Horita, T.G. Langdon, Materials Science and Engineering A, 406 (2005) 268-273.
[202] K. Edalati, Z. Horita, Journal of Materials Science, 45 (2010) 4578-4582.
[203] Y. Harai, Y. Ito, Z. Horita, Scripta Materialia, 58 (2008) 469-472.
[204] http://www.ssab.com/en/Brands/Armox/Products/Armox-500T/, 02/07/2015.
[205] Y. Li, Z. Lin, A. Jiang, G. Chen, Materials and Design, 24 (2003) 177-182.
[206] G.F.V. Voort, Metallography: principles and practice, ASM International, OH, USA, 1999.
[207] J.J. Friel, Practical guide to image analysis, ASM International, OH, USA, 2000.